REPORT NO. RF4534-1
SEPT. 1984

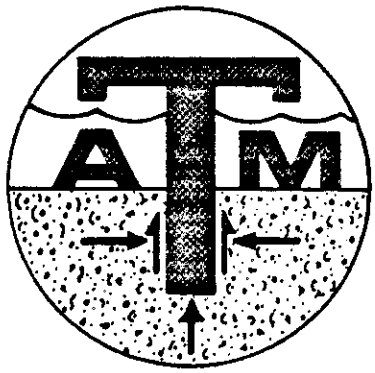

CENTER FOR MARINE GEOTECHNICAL ENGINEERING

THEORETICAL AND EXPERIMENTAL INVESTIGATION OF MUD FORCES ON OFFSHORE PIPELINES

FINAL REPORT
AGA PROJECT NO. PR-149-113

PROPRIETARY
STUDY
FOR THE
AMERICAN GAS ASSOCIATION

Texas Engineering Experiment Station
The Texas A&M University System

Department of Civil Engineering
Texas A&M University
College Station, Texas 77843

Report Distribution

AMERICAN GAS ASSOCIATION

PIPELINE RESEARCH COMMITTEE

R.J. Simmons, Jr., United Gas Pipe Line Company
R. Andsager, Northern Natural Gas Company
T.R. Baker, The Pipeline Authority
J.W. Bledsoe, Southern Natural Gas Company
R.C. Bonner, Consumers Power Company
H.E. Boomer, Natural Gas Pipeline Company of America
H.D. Church, Texas Eastern Gas Pipeline Company
W.F. Coates, Algonquin Gas Transmission Company
J.M. Craig, El Paso Natural Gas Company
S.H. Davis, ARCO Oil and Gas Company
M. Durnin, TransCanada PipeLines, Ltd.
J.J. Fratino, Columbia Gas Transmission Corporation
H.G. Gillit, Northwest Energy Corporation
E.H. Gilman, Colorado Interstate Gas Company
L.E. Hanna, Panhandle Eastern Pipe Line Company
J.E. Hansford, Florida Gas Transmission Company
V.L. Hayes, Phillips Petroleum Company
R.J. Judah, Transcontinental Gas Pipe Line Corporation
E.H. Kamphaus, Oklahoma Natural Gas Company
E.A. Milz, Shell Development Company
D.H. Nimmo, Pipelines Authority of South Australia
H.P. Prudhomme, Pacific Gas Transmission Company
J.M. Safran, Michigan Consolidated Gas Company
E.H. Shelton, NOVA, An Alberta Corporation
G.E. Strang, Southern California Gas Company
W. Such, Tennessee Gas Pipeline Company
L.J. Timms, Consolidated Gas Transmission Corporation
W.T. Turner, Jr., Texas Gas Transmission Corporation
E.L. VonRosenberg, Exxon Production Research Company
P.M.J. Wolfs, N.V, Nederlandse Gasunie
W.J. Woods, Jr., ANR Pipeline Company
F.R. Schollhammer, American Gas Association
J.M. Holden, American Gas Association
T.F. Murphy, American Gas Association

OFFSHORE SUPERVISORY COMMITTEE

G.E. Duffy, Northern Engineering International Company
D. Barlow, Sable Gas Systems, Ltd.
*L.J. Broussard, Tennessee Gas Pipeline Company
*D.W. Cross, Transcontinental Gas Pipe Line Corporation
D.A. Degenhardt, Natural Gas Pipeline Co. of America
C.V. Flint, Texas Gas Transmission Corporation
R.B. Harper, Florida Gas Transmission Company
J.C. Holder, United Gas Pipe Line Company

J. Keiser, Texas Eastern Gas Pipeline Company
P.S. Massey, Phillips Petroleum Company
H.D. Moy, Columbia Gulf Transmission Company
*J.D. Murff, Exxon Production Research Company
J.D. McNorgan, Southern California Gas Company
D.L. Price, Panhandle Eastern Pipe Line Company
P.T. Priesmeyer, Transcontinental Gas Pipe Line Corporation
*W.R. Wolfram (Ad Hoc Group Chairman), Exxon Production Research Company
C.A. Sellars, Shell Development Company
*G.L. Smith, ANR Pipeline Company
D.M. Young, Southern Natural Gas Company
F.R. Schollhammer, American Gas Association

*Project Ad Hoc Group members

THEORETICAL AND EXPERIMENTAL INVESTIGATION OF MUD FORCES ON OFFSHORE PIPELINES

(AGA Project No. PR-149-113)

ABSTRACT

A mathematical model for predicting mud loading on offshore pipelines is developed through a combined theoretical and experimental study. This loading is expressed in terms of the relationship of the resultant forces and torque per unit length to the local relative movement between the pipe and free-field sediment, pipe diameter and burial depth, and the sediment properties; numerous plots are given which can be used to estimate directly unit pipeline loads for specified conditions. A dimensional analysis of the problem is given first. The laboratory test equipment, consisting of three different sizes of drag boxes, is then described, followed by the test methods and results. Development of the theory and description of the solution technique are given next. Finally, experimental and theoretical results are compared.

The findings which have a direct bearing on pipeline analysis are discussed in the lead section "Summary of Results for Use in Pipeline Analysis". All of the primary conclusions based on the experimental work are listed in Section 3.5.

TABLE OF CONTENTS

TABLE OF CONTENTS (cont.)

TABLE OF CONTENTS (cont.)

LIST OF FIGURES

Figure

Figure

Figure Page

Figure Page

Figure Page

Figure

SUMMARY OF RESULTS FOR USE IN PIPELINE ANALYSIS

Quantities called "generalized force coefficients" are derived and plotted in this report. Many graphs of the coefficients, denoted by g_i ($i = 1, 2, 3, 4$), for wide ranges of parameters are collected in Appendix 5. They provide an important part of the information needed to predict response of pipelines to mudslides and other subsea disturbances. In particular, as illustrated later in this summary, the g_i enable calculation of the forces and torque per unit length exerted by the sediment on the pipe. In order to make a stress and deformation analysis of a pipeline one would normally have to combine this unit loading with other information, such as a differential equation of pipeline displacement, hydrodynamic forces, and the weight per unit length of the pipe.

Pipeline analysis is not within the scope of this project, but it is believed appropriate to comment on the applicability of the two cases, Sep = 0 and Sep = 1 (cf. Fig. 4.5), used to predict most of the curves in Appendix 5. The former case is for no separation of mud from the pipe, and it predicts an approximate upper bound to the horizontal unit force. Thus, a conservative approach would be to use the Sep = 0 case in predicting mud loads on pipes whenever the mud flows past the pipe. On the other hand, outside of a mudflow region the sediment would serve to anchor the pipeline, and one task of an analysis might be to predict the points which divide the pipe restraining zones from the region where the sediment acts to move the pipeline. Except for deeply buried pipes, $h/D > 4$ say (cf. Fig. 1 in Appendix 5), it may be instructive to use both the Sep = 1 and Sep = 0 cases to predict the soil restraining forces. From such comparisons one could gain

considerable insight into the response of pipelines to mudslides.

The generalized force coefficients are not limited to uses in mudslide problems. They have been developed for an arbitrary direction of motion, and thus one could address questions such as those related to the ability of the soil to support pipelines loaded only by their own weight and hydrodynamic forces.

Equations for Calculation of Unit Soil Loading

The comparisons between experimental and theoretical results discussed in Section 5 indicate that the nonlinear viscous model of sediment behavior is suitable for predicting mud forces on pipes. This loading is represented concisely through the generalized force coefficients g_i. The forces F_i' ($i = 1,2,3$) and moment M' about the pipe's axis (i.e., the torque) for a unit length of pipe are referred to the x_i coordinate system in Figs. 4.1 and 4.6. (The unit soil loading may vary along the pipeline due to, for example, variations in h/D and mud flow angle α (cf. Fig. 4.6).) Denoting quantities for a unit length of pipe with a prime, Eqs. (4.116) and (4.117) are rewritten to obtain

$$F_1' = k'g_1 , \quad F_2' = k'g_2 + F_B'$$

$$F_3' = k'g_3 , \quad M' = k'Dg_4 \tag{1}$$

where g_i may be obtained from graphs in this report and

$$k' = DC_o(V_R/D)^N \tag{2}$$

Also

D = pipe diameter

C_o = sediment strength for a standard vane rotation rate of 0.0143 rad/sec

V_R = resultant relative velocity between a short segment of the pipeline and adjacent sediment in the free field

N = exponent which defines the degree of nonlinearity of the sediment

F'_B = buoyant force per unit length

In the viscous model of soil behavior, N is equal to the strain rate exponent for strength, usually denoted by lower case n. Thus, n and N which appear in Sections 3 and 4, respectively, may be used interchangeably; for the lowest and highest strength sediments studied experimentally, N = 0.12 and N = 0.09, respectively. Inasmuch as vane rotation rate is expressed using seconds, the velocity V_R should be expressed using seconds and the same units employed for pipe diameter; hence, the units of V_R/D to be used in the calculations are diameters/sec.

According to the theory in Section 4.3.2, F'_B is the buoyant force of Archimedes' principle, which acts upward on a body in a liquid; it is equal to the weight per unit length of soil and water displaced by the pipe at its instantaneous location. However, experimental results in Section 3.4 (cf. Fig. 3.50) indicate that the direct effect of gravity is more complicated than this if $h/D > 1/2$. Guided by these results, if $1/2 < h/D \leq 2$ we recommend using for F'_B the expression

$$F'_B = F'_{Ba} - F'_{Bb} \qquad (3)$$

where

F'_{Ba} = total weight of sediment displaced by the lower one-half of the pipe's cross-section for a unit length of pipe

F'_{Bb} = total weight of sediment directly above the pipe less the weight of water displaced by this soil.

For $h/D > 2$, F'_{Bb} is probably less than the total submerged weight of sediment above the pipe (cf. Fig. 3.50). However, the value one should use in pipe loading is not known for a general loading and pressure state. For the important special case in which the magnitude of the local geostatic pressure is very large compared to sediment stresses due to pipe motion, so that the sediment behaves as a nonlinear viscous body without cracks, voids or separation, the theory in Section 4.3.2 implies Archimedes' principle may be used to calculate the total buoyant force F'_B, regardless of the value of h/D.

The only gravity-induced force discussed so far is the vertical buoyant force. There is also the effect of gravity due to vertical mudline displacements. An approximation for this effect is included in the plotted values of g_i when the "Grav" parameter in Eq. (5.1) is not zero. Another effect will be in the horizontal force when the sediment is not geometrically symmetric with respect to a vertical plane at the pipe's center. For example, such a situation exists if pipe motion creates a shelf behind the pipe, Sep = 1 in Fig. 4.5. The pipe then behaves like a dam, helping to resist a reduction in the elevation of the sediment in front of the pipe. In estimating the correction to F'_1 one should use the submerged unit weight of sediment $\Delta\gamma$. We believe an upper-bound estimate of this additional lateral force may be made by treating the sediment as a static fluid; for example, if $h/D \leq 1$ then add

$$F'_{1p} = h^2 \Delta\gamma/2 \qquad (4)$$

to the force F'_1 calculated from Eq. (1).

Finally, it should be mentioned that when the F'_i are interpreted as

forces exerted by the pipe on the sediment, they are positive if they act in the positive directions of the x_i coordinate axes in Figs. 4.1 and 4.6. The moment is positive when it produces a moment on the soil in the positive direction of pipe rotation shown in these figures. If we consider these same quantities to be the forces exerted by the sediment on the pipe, they are obviously positive when they act in just the opposite direction. If F'_B, Eq. (3), is positive it acts to lift the pipe.

Generalized Force Coefficients for Homogeneous Sediment

The coefficients g_i are functions of the exponent N and gravity parameter Grav. Also, they depend on the angles which define the movement of the pipe relative to the sediment, α and λ (cf. Fig. 4.6b), as well as the ratio of rotation rate to resultant velocity, $\dot{\theta}/V_R$. There are, in addition, different sets of g_i for the five different cases of sediment geometry shown in Fig. 4.5.

There are many figures in Section 3 which show experimental and theoretical generalized force coefficients. All theoretical curves in that section are for N = 0.12 and, unless stated otherwise, are for no gravity effect, Grav = 0. The majority of the experimental results in Section 3 for the horizontal force coefficient g_1 are bounded from below by the theoretical predictions for Sep = 1 without torque, and bounded from above by the predictions for Sep = 0 without rotation. For easy reference, several results for these two limiting cases are shown in Appendix 5. Except for Fig. 18, the curves in Appendix 5 are for λ = 0, and most are for the largest exponent that was measured, N = 0.12. Some curves are for N = 0.09, the smallest exponent measured, and they may be seen to differ only slightly from the others. The vertical force

coefficient g_2 for Sep = 0 is not plotted because it is zero, regardless of the values of flow angle α and h/D.

It is noteworthy that some of the experimental data for g_1 fall along a straight line on log-log paper, as in Figs. 3.78 and 3.79. This behavior implies g_1 obeys a power law in h/D, thus providing a simple formula that may be helpful for pipeline analysis.

Generalized Force Coefficients for Nonhomogeneous Sediment

Only a limited study of the effect of a nonuniform strength distribution has been made. Good agreement between theory and experiment is reported in Section 5.1 for the three cases investigated, each of which involved a relatively low strength top layer of sediment.

As a practical matter, it would be helpful to know if one can obtain g_i for nonhomogeneous sediment by using a suitably defined average strength in the theory for homogeneous sediment. For the laboratory tests using layered sediment, it was indeed found that horizontal and vertical force coefficients were approximately the same as those for homogeneous soil; this agreement was achieved by using an average of the strength from the mudline down to one radius below the pipe.

The use of an average strength is also examined in Appendix 6. In this case, a power-law modulus distribution is employed, and the soil is assumed to be a linearly viscoelastic material. We assume here that this modulus is proportional to the strength distribution, Eq. (4.172). The dimensionless ordinate in Fig. 2, Appendix 6, is approximately $(1+s)^{-1}$ for $0 \leq s \leq .5$ and small values of m; note that n is used instead of s in this Appendix. Next, it is observed that the average of

a power law strength distribution taken from the mudline to an arbitrary depth y_a is

$$C_{oa} = \frac{C_o}{1+s}\left(\frac{2y_a}{D}\right)^s \tag{5}$$

Considering Fig. 2, Appendix 6, the value of y_a/D is found to be

$$y_a/D = (h/D)^{.5} \tag{6}$$

Consequently, for the idealized problem in Appendix 6, in which $h/D \ll 1$, the horizontal force coefficient is the same as that for homogeneous sediment having the average strength C_{oa}; this strength is to be used in place of C_o in Eq. (2). The depth to which the average is taken is y_a, which is to be calculated from Eq. (6). This analysis thus gives a different rule than in the layered sediment problems (for which $h/D = 1/2$ and 1) which should be used for calculating an average strength.

It is mentioned in Section 4.6.2 that the computer program has an option for predicting coefficents g_i when Eq. (4.172) applies if $h/D = 1/2$ and the torque is zero. A limited study has been made assuming $\lambda = 0$, N = 0.12, and Grav = 0. As an excellent approximation for $0.1 \leq s \leq 1.5$, it was found that:

$$g_1 = (.23 + .093s)^{-1}, \quad (\alpha = 90°, \text{ Sep} = 0) \tag{7}$$

$$g_1 = (.36 + .14s)^{-1}, \quad (\alpha = 90°, \text{ Sep} = 1, c_1 = 0) \tag{8}$$

$$g_3 = (.41 + .15s)^{-1}, \quad (\alpha = 0°, \text{ Sep} = 0) \tag{9}$$

The strength to be used in Eq. (2) for calculating forces is that at the bottom of the pipe. For Sep = 0, the vertical force coefficient g_2 is zero, just as for homogeneous sediment. On the other hand, g_2 for the

same physical problem leading to Eq. (8) was surprisingly found to be essentially independent of s for $0 \leq s \leq 3$.

On the basis of these investigations of the effect of sediment nonhomogeneity, we conclude that there is no universal rule that permits utilizing the results for homogeneous soil; but it may be possible to develop simple rules for different ranges of h/D and different types of strength distributions. However, further study is needed before one can reliably extrapolate the present findings much beyond the specific cases investigated.

Example Problem

In order to illustrate the use of some of the results in this report for pipeline analysis, we shall solve a rather idealized problem.

Given Parameters

pipe diameter: $D = 2$ ft
recess depth: $h = 1$ ft
mudflow velocity (horizontal): $V_R = 0.5$ fps
flow angle: $\alpha = 90$ deg
mud strength: $C_o = 20$ psf (based on a vane rotation rate of 0.0143 rad/sec)
mudslide width: $L = 25$ ft
submerged unit weight of sediment: $\Delta\gamma = 36$ pcf
nonlinear or strain rate exponent: $N = 0.11$

Problem

For these given quantities, estimate the maximum bending moment in a pipeline which is assumed to be fixed at the edges of the 25 ft wide slide zone.

Solution

First, calculate the horizontal unit load, F_1.

Use Eq. (2): $k' = 2x20x(.5/2)^{.11} = 34.3$
Use Appendix 5, Fig. 1: $g_1 = 4.8$
Use Eq. (1): $F_1 = 34.3x4.8 = 164.6$ lb/ft

Next, calculate the maximum bending moment, M_b. For simplicity, assume

the ends of the pipe are fixed in position and the end moments are negligible (i.e., the pipe is essentially a pinned-ended beam). The maximum moment is at the center of the span and is given by [14],

$$M_b = F_1' L^2/8$$

Thus

$$M_b = 164.6 \times 625/8 = 12{,}859 \text{ ft-lb}$$

Discussion

1. Had clamped end conditions been assumed, instead of pinned, the maximum moment would be at the ends and equal to 2/3 of that calculated above. In reality, the end conditions depend on the restraints imposed by the soil as well as the pipe outside of the mud slide zone. Also, significant axial tension may develop due to large deflections, resulting in a lower bending moment unless the length of pipe participating in the bending action is increased.

2. Fig. 1, Appendix 5, is for N = 0.12 not 0.11. However, the force coefficients are not very sensitive to N, as may be seen by comparing Figs. 1 and 4.

3. The g_1 for no separation, Sep = 0 (cf. Fig. 4.5) was used in order to derive an upper bound on unit loading. In this case $g_2 = 0$, and also the correction in Eq. (4) is not used. On the other hand, if a lower bound were desired, one would use Fig. 7, Appendix 5, to find $g_1 = 2.5$ instead of 4.8. The correction due to gravity, Eq. (4), is

$$F_{1p}' = 1^2 \times 36/2 = 18 \text{ lb/ft}$$

Thus

$$F_1' = 2.5 \times 164.6/4.8 + 18 = 103.7 \text{ lb/ft}$$

After accounting for F_2' (using g_2 from Fig. 8 and assuming the pipe is

neutrally buoyant) the resultant moment is found to be approximately 0.9 of that for Sep = 0.

4. The calculations have neglected the effect of gravity on the vertical mudline displacement because Grav = 0 has been used. This dimensionless parameter, Eq. (5.1), is calculated as follows:

$$\text{Grav} = \frac{36 \times U_R}{20} \left(\frac{2 \times .0143}{.11}\right)^{.11} \left(.5/2\right)^{-.11} = 1.81\, U_R$$

where U_R is the free-field horizontal mud displacement in feet (relative to the pipe). The theory is not valid for displacements on the order of the pipe diameter or greater. However, considering the physical basis for this parameter, it is suggested at this time that $U_R = 2h$ be used whenever the actual displacement exceeds 2h. Hence, use U_R = 2 ft and obtain Grav = 3.62. From Fig. 16 for Sep = 0, g_1 = 7.3, and the bending moment becomes

$$M_b = 7.3 \times 12{,}859/4.8 = 19{,}556 \text{ ft-lb}$$

5. It is important that V_R be expressed in fps because diameter is in feet and the vane rotation rate used for C_o is in rad/sec. All curves of g_i plotted in this report should be used with C_o for the standard rotation rate of 0.0143 rad/sec. If the strength is measured using a different rate than this, one should correct the strength. Specifically, if $\dot{\theta}_t$ is the rotation rate in rad/sec and C_t the strength measured at this test rate, then the strength to be used in predicting soil loading is

$$C_o = C_t (0.0143/\dot{\theta}_t)^N$$

1.0 INTRODUCTION AND GENERAL SUMMARY

1.1 Approach

Large offshore river deltas may present formidable obstacles to submarine pipelines since fine grain soils are deposited at such rapid rates that very low strengths are developed. Strong wave action due to storms can trigger mudslides or produce other less severe but significant sea floor movement. The objective of this research was to derive a mathematical model by which one can make predictions of mud forces on pipelines. The pipeline analysis itself was not addressed. Rather, it is the relationship of the mud forces and torque per unit length exerted on the pipe to the local relative movement between the pipe and free-field sediment and various relevant parameters which was developed.

The approach was to use laboratory tests to guide the development of a theoretical model and to then check the accuracy of the model over a realistic range of physically-based dimensionless parameters.

Section 2 gives the basic dimensional analysis. It served as a guide to a systematic theoretical study and to the selection of test parameters so that the laboratory tests would be indicative of actual field conditions when practicable. The choice of the specific dimensional parameters which appear in this section was based on current understanding of relevant sediment deformation and failure behavior as well as on the need to define certain field and laboratory conditions.

For the experimental work, large, intermediate, and small "drag boxes" were employed. These boxes and the experimental work are described in Section 3. Also, all of the figures which compare experimental and theoretical results for forces and torque are given in

this section. The comparisons are made conveniently using so-called "generalized force coefficients", and therefore except for some representative force and torque diagrams, it is these coefficients that are plotted.

The theory is developed in Section 4, and the agreement between theory and experiment is discussed in Section 5. References to other work are in Section 6.

1.2 General Conclusions

Overall agreement between theory and experiment is good. In addition, through the closely coordinated theoretical and experimental study, much has been learned about the complex soil failure process that underlies the actual force-displacement behavior of a pipe and sediment system.

For all but deeply buried pipes, separation of mud from the pipe and mud cracking were significant. A maximum air pressure of 30 psi was applied to the soil, and therefore it is not known if higher sea floor water pressures would eliminate these phenomena. Several cases were studied theoretically, including one in which cracking and separation do not occur. In most comparisons, this latter case predicted horizontal forces which, as expected, exceeded the experimental values. Thus, although high pressures could not be imposed experimentally, the theory is believed to provide an upper bound to the horizontal force unless large deformation behavior of the type described in Section 1.3 develops.

The experimentally determined vertical mud force tended to be somewhat erratic, apparently due to the complex nature of the patterns of pipe-mud separation and internal mud cracking. Indeed, the

theoretically predicted vertical force was found to be sensitive to these patterns. However, as an important practical observation, it was found in a limited experimental study that the combined effect of sediment weight and deformation was such that the burial depth of freely floating pipes did not change appreciably with increasing imposed horizontal movement. An important finding from limited testing of freely rotating pipes (as well as from the theory) is that the horizontal force was practically the same as for pipes which were prevented from rotating in most cases.

The theoretical values of generalized force coefficients g_i were obtained by means of a personal computer using a program which is briefly discussed in Section 4.6. Curves of g_i are presented in this report for a wide enough range of conditions to make it unnecessary in most cases to use a computer to estimate unit pipeline loading. It was not an objective of this study to develop a computer program for general use.

1.3 Limitations of the Theory

For pipes which were only partially buried at the start of the test and then moved horizontally several diameters, the mud often fully covered the pipes. After full coverage was reached the horizontal force in some cases exceeded the upper bound prediction mentioned above. However, this is a bound using the initial depth of burial in the prediction. The theory is based on an assumption of small displacements, and thus is not sufficiently general for predicting an "effective" depth of burial and the effect of gravity with large displacements.

There are two other important limitations of the theoretical

analysis. One is concerned with strength gradient and the other with velocity gradient. At this time only certain special types of sediment nonhomogeneity can be treated, as discussed in Section 4.6.2. The theory in Section 4 allows for a general distribution of mud strength with depth, but the computer program is limited. The objective of the study of strength distribution effects was to obtain a preliminary experimental verification of the basic theory, which was accomplished. The lead section, p. xv, gives some of the particular findings of this project on soil nonhomogeneity that should be helpful in pipeline analysis; however, a more extensive experimental and theoretical study of nonhomogeneity is really needed. One important experimental result for sediment whose strength increased with depth is that the increase in effective depth of burial with large movements was greater than for homogeneous soil. This type of behavior could have been expected since there is more resistance to the sediment flowing under the pipe than over it, compared to the homogeneous case.

Finally, it has been assumed that there is no gradient in sediment velocity with depth other than that due to interaction with the pipeline. A significant gradient would exist, for example, near the bottom of a layer of mud flowing over stronger, stationary sediment. If such a gradient exists across a pipe, it may have a significant effect on the generalized force coefficients.

2.0 DIMENSIONAL ANALYSIS

2.1 Approach

The complete basic set of dimensional variables and associated independent dimensionless ratios is given in Table I. Nominal numerical values and ranges of variation are given in Table II. It should be noted that the field values were taken from information provided by Exxon Production Research Company from a survey of AGA members; these data are collected in Appendix 1.

The total number of independent dimensionless ratios that can be formed from a set of N-parameters is equal to N minus the number of basic physical units employed. Inasmuch as there are three units, force (F), time (t), length (L), this restriction was met by associating independent dimensionless ratios (π_i) with all but three of the dimensional parameters. The latter three quantities are designated as "primary variables" in Table I. Many of the parameters cannot be varied in the tests or their values are not known or are not needed. However, for comparison purposes, Table II has been arranged so that each line corresponds to a line with the same parameter in Table I.

Not all dimensionless parameters which are used later are given in the tables. Depending on the situation of interest, it will be desirable to use other parameters which are formed from those in the tables. Also, there are other nondimensional quantities which affect behavior, such as exponents used in describing behavior of soil in terms of power laws (cf. Section 4.1); these parameters are not considered basic to a dimensional analysis and therefore have been omitted here.

2.2 Discussion of Tables I and II

Pipe: The pipe variable that received most attention in the

TABLE I

Summary of Variables

Source	Variable Name	Symbol	Units	Dimensionless Ratio
Pipe	diameter	D	L	primary variable
	length	L	L	$\pi_1 = L/D$
	unit weight	γ_p	FL^{-3}	$\pi_2 = \gamma_p/\gamma_w$
	roughness	a_p	L	$\pi_3 = a_p/D$
Soil	shear strength	C	FL^{-2}	primary variable
	time constant for time/rate dependence	t_c	T	primary variable
	shear modulus	G_R	FL^{-2}	$\pi_4 = G_R/C$
	time constant for soil fabric changes	t_d	T	$\pi_5 = t_d/t_c$
	intrinsic fracture changes	Γ	FL^{-1}	$\pi_6 = \Gamma/(G_R a_s)$
	defect scale	a_s	L	$\pi_7 = a_s/D$
	*unit weight	γ_s	FL^{-3}	$\pi_8 = \gamma_s D/C$
	permeability	k_h	LT^{-1}	$\pi_9 = k_h t/D$
	coefficient of consolidation	c_v	L^2T^{-1}	$\pi_{10} = c_v t/D^2$
	compression index	C_c	—	$\pi_{11} = C_c$
	swelling index	C_s	—	$\pi_{12} = C_s$
	coefficient of lateral earth pressure	K_o	—	$\pi_{13} = K_o$
	soil mass size	L_s	L	$\pi_{14} = L_s/D$
	soil inhomogeneity scale (defined by strength gradient)	L_c	L	$\pi_{15} = L_c/D$

*Solids plus the water, not to be confused with unit weight of only the solids.

TABLE I
(cont.)

Source	Variable Name	Symbol	Units	Dimensionless Ratio
Water	unit weight	γ_w	FL^{-3}	$\pi_{16} = \gamma_w D/C$
	depth	h_w	L	$\pi_{17} = \gamma_w h_w/C$
	mudline pressure	p_w	FL^{-2}	$\pi_{18} = p_w/C$
Pipe Location and Movement	pipe recess depth	h	L	$\pi_{19} = h/D$
	rest time	t_o	T	$\pi_{20} = t_o/t_d$
	test time	t	T	$\pi_{21} = t/t_o$
	*resultant velocity	V_R	LT^{-1}	$\pi_{22} = V_R t_c/D$
	*flow angle	α	—	$\pi_{23} = \alpha$
	*penetration angle	λ	—	$\pi_{24} = \lambda$
	pipe rotation rate	$\dot{\theta}$	T^{-1}	$\pi_{25} = \dot{\theta}D/V_R$
Dynamic Effects	gravitational constant	g	LT^{-2}	$\pi_{26} = V_R/(G_R g/\gamma_s)^{1/2}$
**Reactions	soil force/length on pipe	F_i' (i=1,2,3)	FL^{-1}	$\pi_{27i} = F_i'/(DC)$
	soil moment (torque)/ length on pipe	M'	F	$\pi_{28} = M'/(D^2C)$

*See Fig. 4.6

** The generalized force coefficients g_i are more useful quantities for characterizing mud force than the dimensionless π-ratios, and therefore the former quantities are used in this report. (The π-ratios depend on resultant velocity, while the g_i do not.)

TABLE II

Values and Ranges of Parameters

Variable	Field Values (from Survey)		Laboratory Values	
	Dimensional Parameter	π-ratio	Dimensional Parameter	π-ratio
D(in)	8 → 43		3/8 → 6	
L(ft)	50 → 4000 (mudflow width)	1) $L/D >> 1$	1.0 → 3.5 (pipe length)	$L/D = 7 \rightarrow 32$
γ_p(lb/ft^3)		2) $\gamma_p/\gamma_w = 1.1 \rightarrow 1.8$		$\gamma_p/\gamma_w \leq 8$
a_p		3)	smooth → rough	
C(lb/ft^2)	10 → 3000 (undrained)		9.5 → 55 (undrained)	
t_c(min)				
G_R		4)		$G_R/C < 125$
t_d		5)		
Γ		6)		
a_s		7)		
γ_s(lb/ft^3)	75 → 130	8) $(\gamma_s-\gamma_w)D/C < 6$	90 → 100	$\gamma_s D/C = 0.06 \rightarrow 5$
k_h(in/sec)		9)	$\simeq 10^{-9}$	
c_v(in^2/sec)		10)	$2\times10^{-6} \rightarrow 2\times10^{-5}$	
C_c		11)		$\simeq 0.3$
C_s		12)		$\simeq 0.1$
K_o		13)		$\simeq 0.6$
L_s(ft)		14)	2x2x.5→6x6x6	
L_c		15)		$L_c/D = 0.5 \rightarrow 1$
γ_w(lb/ft^3)	64	16)	62	
h_w(ft)	0 → 1000	17) $h_w/D = 0, >> 1$		0
p_w(psi)		18) $p_w/C = 0, >> 1$	0 → 30 (air pressure)	$p_w/C = 0 \rightarrow 220$

TABLE II
(cont.)

Variable	Field Values (from survey)		Laboratory Values	
	Dimensional Parameter	π-ratio	Dimensional Parameter	π-ratio
h(in)	0 → 133	19) $h/D = 0 \rightarrow 12$		$h/D = 0 \rightarrow 18$
t_o(min)		20)	1080	
t(min)		21)	1 → 1200	$t/t_o = 10^{-3} \rightarrow 1$
V_R(ft/min)	10 → 200 (mudflow velocity)	22) $V_R t_c/D = 3t_c \rightarrow 300t_c$	$V_R = 3\times10^{-3} \rightarrow 2$	$V_R t_c/D = .05t_c \rightarrow 12t_c$
α(deg)		23)	0 → 90 deg	
λ(deg)		24)	0 → 90 deg	
$\dot{\Theta}$		25)		$\dot{\Theta}D/V_R = 0 \rightarrow 2$
g(ft/sec^2)	32	26) $V_R/(G_R g/\gamma_s)^{1/2} < .1$	32	$V_R/(G_R g/\gamma_s)^{1/2} < .001$
F_i' (i=1,2,3)		27)	Principal Results	$\pi_{27i} = \pi_{27i}(\pi_{19}, \pi_{21\rightarrow25})$
M′		28)		$\pi_{28} = \pi_{28}(\pi_{19}, \pi_{21\rightarrow25})$

experimental work is the diameter. The length was great enough to preclude significant effects of length; this point was checked by doing a limited amount of testing with different lengths. A few tests of pipes with different amounts of roughness indicated it may have an effect. For experimental and theoretical reasons, most testing was done under controlled translation and rotation of the pipe; in these cases the unit pipe weight does not directly affect the soil forces. Unit weight is taken into account in the theory. The pipe was permitted to move vertically and rotate without external restraint in some tests in order to examine the range of validity of the theory and to study complex deformation phenomena not treated theoretically.

Soil: This project is concerned with pipes in soils with very low strengths and therefore only weak soils were used in the tests. The undrained strength C is an increasing function of strain rate $\dot{\gamma}$; all of our experimental data on weak marine sediment indicates $C \sim \dot{\gamma}^n$, where n is small and typically close to 0.1 [1-5]. This power law behavior provided the basis for modeling the mud as a nonlinear viscous material in Phase I [1]. A more general representation is discussed in Section 4.1, in which the soil is modeled as a nonlinear viscoelastic material.

The parameters t_c and G_R are used in this generalized model. The time constant t_d, which is associated with thixotropy, was not studied experimentally. In the power law model of behavior employed, t_c and G_R are always grouped together (as in the prediction of strength), and therefore their individual values cannot be found from existing data. The quantities Γ and a_s influence the changes in fabric and growth of large defects such as cracks [6].

An objective of part of the work has been to study the effect of gravity. The parameter relevant to soil-pipe forces is $\pi_8 = \gamma_s D/C$

without water, and $\pi_8^* \equiv (\gamma_s - \gamma_w)D/C$ with water. This effect is discussed in Section 4.4, in which the modulus G_R is used instead of C because it arises naturally in the analysis; without drainage, the ratio $\pi_4 = G_R/C$ does not appear to change significantly with soil strength or test time [2, 4], and thus the form of relationships using modulus as a nondimensionalizing parameter is the same as when the strength is used.

The effect of gravity was studied without water in the experiments by using a very low strength mud and pipe diameters up to 6 inches. Testing at reduced pipe speeds increases π_8 and π_8^* because of the strain rate dependence of strength, and therefore this is one way of increasing gravity effects in the laboratory. Table II indicates that we reached values of π_8 up to 5 in the laboratory, which were achieved through a combination of low speeds and low strength mud. This value is large enough to account for the effect of gravity with full-scale pipes in weak sediment in all but one of the responses in Appendix 1; in one case a slightly larger value of $\pi_8 \approx 6$ is calculated for mud with the lowest strength and density (cf. page A.5).

Testing at very low speeds with laboratory scale pipes may result in significant pore water diffusion during the test. This stress-induced flow depends on soil parameters which determine the ease with which water can flow through the soil skeleton (permeability) and the ability of the skeleton to change volume (coefficient of consolidation, compression and swelling indices, and coefficient of lateral earth pressure, K_o) [7]. As a local change in water content affects the soil's deformation response and strength, laboratory tests at low speeds may not produce pipe force-time behavior which can be scaled up to full-size pipes. A rough estimate of the test time for significant

diffusion or drainage can be made using the ratio D^2/c_v; thus, for a 1-inch diameter pipe, and using the largest value of c_v shown in Table II,

$$t \simeq D^2/c_v \simeq 14 \text{ hours} \qquad (2.1)$$

As this time scales with the square of the diameter, no significant drainage is expected with full-size pipes. In the laboratory it is therefore important to test at speeds which are at least high enough to preclude effects of drainage on force-time behavior. For the tests conducted with 6-inch diameter pipes (primarily to study effects of gravity) the time for drainage is $t \sim 14 \times 6^2$ hours from Eq. (2.1). A test lasting no longer that 14 hours is not expected to be affected by changes in soil properties due to drainage. Results from some of our tests with small diameter pipes using ultra-low rates appear to exhibit effects of drainage or thixotropy.

The earth pressure coefficient K_o influences the initial state of stress in the sea bottom. At rest, the horizontal effective stress (the stress acting on the soil skeleton) is K_o times the vertical effective stress [8]. With $K_o < 1$, the total principal stresses in the mud, consisting of the effective stresses plus the pore water pressure, are not exactly equal. Although in Section 4.1 we assume the total initial principal stresses are the same (cf. Eq. (4.8)), the error is very small because the major component of the total stresses is the pore pressure in the weak, underconsolidated clays under study.

The soil mass size parameter, π_{14}, is large enough to preclude boundary effects in the laboratory mud boxes, as indicated by the agreement between test data from three different size boxes. Most testing involved essentially homogeneous soils. However, a few tests

were made in which a strength gradient existed in order to check theoretical predictions of the effect of the relevant parameter, π_{15}.

Water and Dynamic Effects: All tests were without water above the soil. External air pressure was applied in order to simulate the effect of moderate mudline pressures. As noted above, the effect of gravity on mud deformation is included in the theory of Section 4, and with water the parameter $\pi_8^* = (\gamma_s - \gamma_w)D/C$ is used in place of π_8. Dynamic pressures in the water do not cause significant changes in mudline pressure for realistic pipe speeds, as shown in Appendix 2. The parameter π_{26} is the ratio of horizontal pipe speed to shear wave speed in the mud; at V_R = 2 fpm, this quantity is negligible ($\pi_{26} \simeq 0.001$) in even the lowest strength mud tested.

Pipe Location and Movement; Reactions: The principal results consist of characterizing the relationship of forces, $_{27i}$, and torque, or moment, π_{28}, to h/D, angles α and λ, and velocity. The resultant normalized velocity V_R/D serves to define the strain rate in the mud, apart from pipe rotation. The range of values used in the laboratory, $05 < V_R/D < 12$ min^{-1}, is large but is not high enough to include the field values given in one response to the survey (page A.7). This is not believed to be a problem because the strain rate appears in the equations through a power law relationship, and it has been estimated using experimental results from an earlier study [5] that this relationship holds for strain rates which bracket the field values. The laboratory tests have indicated that when h/D exceeds approximately 6 the depth of burial is large enough to eliminate mud surface effects, and therefore the tests covered as wide a range of h/D as needed to simulate very shallow to very deep burial in the sea floor.

3.0 EXPERIMENTS

3.1 General Overview

The experimental portion of the previous work (Phase I) was a brief program designed to supplement and aid the theoretical development of pipeline drag forces. It was heavily based on the earlier program by Marti [3] concerning drag forces on vertical piles, and, in fact, utilized Marti's equipment which had been modified to hold horizontally oriented pipes. Tests were conducted on deeply buried pipes at atmospheric pressure and at pressures simulating shallow water depths in the ocean. Partially- and shallow-buried pipes were also tested, but only at atmospheric pressures owing to the limitations of the Marti equipment. At several depths of burial, tests were performed with the pipes oriented at various angles to the direction of flow, thereby providing both normal and axial drag components on the pipe. Whereas the tests in Marti's equipment were performed on rigidly held pipes, additional tests were performed in a separate device which allowed the pipes to move vertically as the sediment flowed horizontally past the pipe. These latter tests were conducted both at 0 and 30 psi pressure, but only on pipes oriented normal to the direction of sediment flow.

It became obvious during the analysis of the Phase I experimental data that many gaps remained to be filled in the experiments, both to verify the theory which had been developed and to assist in the extension of the theory to other cases. First of all, the initial experiments regarding oblique flow effects were incomplete with respect to the range of flow angles, the depth of burial and the influence of total pressure. Discrepancies occurred between theory and experiment, particularly at small and large flow angles (near 0° and 90°) which

may have been caused by instrumentation deficiencies or perhaps by the uncorrected effects of the finite length of the pipes. Buoyancy and scale effects were not examined during Phase I, again the result of equipment limitations. The vertical movement of the pipes under sediment flow conditions was scarcely examined, and drag forces in the vertical direction were not measured at all. Another condition which was not fully investigated but which can be an important design aspect, was the effect of pipe rotation. The influence of surface texture (roughness) of the pipe and the effects of vertical variation in sediment strength on the drag forces were not investigated, although both are obviously factors of significant practical importance.

Perhaps one of the most significant experimental findings during Phase I was the visual observation of sediment separation at the pipe-sediment interface, and sediment cracking near the pipes and in the far field away from the pipe. This phenomenon - which played an important role in the theoretical development - appeared to be influenced by the applied pressure, thereby demanding a study of pressure effects.

Finally, the influence of pipe velocity - although apparently well-handled by the Phase I theoretical developments - was a factor which needed further investigation.

The proposal for Phase II experimental studies outlined the tests to be conducted to fill in the gaps as discussed above and extend the knowledge of pipe drag forces. However, the proposed test program was considered as a point of departure rather than a rigorous test schedule. For the most part, theory was modified or developed contemporaneously with the experimental program, and tests were made as necessary to aid in the theoretical development. In some types of experiments, the number of original tests was reduced from those proposed and in several

cases new tests were added which were not anticipated in the original test program. This pragmatic approach served to eliminate repetitive or meaningless tests and placed the emphasis on development of worthwhile data.

3.1.1. Equipment Used in the Research

To perform the various types of tests envisioned for Phase II research required more versatile equipment than the two "drag boxes" used for the Phase I program. In fact, the demand for testing large diameter pipes precluded the use of either of the small-sized drag boxes previously used. But at the same time, it was neither practical nor economical to develop a single drag box to handle all tests. For example, a drag box adequate in size to test large diameter pipes would need unrealistically thick walls to withstand the internal pressures required for the pressurized tests. The most feasible approach was to use separate drag devices, each one capable of performing specific types of tests, but all of them able to perform some common tests to allow comparison between the test devices. This approach also accelerates test time by permitting simultaneous testing in the various drag boxes. Ultimately, three drag boxes were used as described below:

a. Large drag box. Examining scale and buoyancy effects required pipes with diameters up to 6 in., which resulted in the design and fabrication of a drag box which was 6 ft. square and contained a 4 ft. depth of sediment. This drag box also permitted the use of much longer pipes than the other two drag boxes, thereby insuring that pipe end effects were kept to a minimum. It also had the capability of simultaneously controlling both vertical and horizontal pipe movement which allowed tests to be performed with the pipe plunging into or

rising out of the sediment at any angle with any initial burial depth. Horizontal and vertical drag forces, as well as torque induced on the pipe, could be measured. Although this was the most versatile of the three drag boxes, it could not be pressurized, thus, all tests were performed at atmospheric pressure.

b. Intermediate drag box. This was the original box developed by Marti [3] for drag tests on vertical piles. It was modified for the Phase I pipe studies to allow the use of horizontal pipes. In its original state, the box could only be pressurized when completely filled with sediment, which limited the Phase I pressurized tests to deeply buried pipes. For the Phase II tests, the device was further modified to permit it to be pressurized when the box was partially filled with sediment thus allowing tests to be performed on shallow and partially buried pipes. This box had two important advantages: it was easy to adjust the pipe orientation to allow sediment flow at various angles to the direction of pipe movement, and the instrumentation was relatively simple and maintenance-free. The major disadvantage was that the pipe was fixed in the vertical direction, thereby preventing tests with both freely floating and freely rotating pipes.

c. Small drag box. This box was originally designed to hold a simple shear apparatus [4]. Because the box was capable of sustaining internal pressures of 30 psi and could be actuated by a closed-loop servo-controlled testing machine, it was modified to become a drag box for these studies. The pipe support system in this box was developed to permit the pipe to freely move in the vertical direction and to freely rotate. In addition, the pipe could be oriented at different angles to the direction of sediment flow. The main limitation of this drag box was the limited depth of sediment which prevented pipes from being

tested at burial depths greater than twice the pipe diameter.

3.1.2 Sediment Used in the Research

The sediment used in the experiments was obtained from the South Pass region of the Mississippi Delta at a location where water depth was 200 ft. Large box coring equipment was used to collect the sediment from a zone of approximately 0-5 ft. below the mudline. The sediment was immediately transferred to metal drums for shipment and storage. This material is typical of the sediments producing pipe-damaging mudslides in the Mississippi Delta. It is a highly plastic, low shear strength soil with a high-clay content.

3.2 Description of Test Equipment

3.2.1 Large Drag Box

3.2.1.1 General Design Requirements: The objectives of the experimental program required the development of a drag box to measure horizontal and vertical forces on model pipes ranging in diameter from 1-1/2 to 6 in. The following requirements were considered during the design stage:

1. The apparatus must be of adequate size to reduce end effects even with the large diameter pipe.
2. The pipe must be capable of travelling both horizontally and vertically as it moves in the sediment.
3. The equipment must provide a wide range of pipe velocities in both directions of movement.
4. Horizontal and vertical forces, and torque induced on the pipe, must be measured simultaneously, without any one of these affecting the other measurements as the pipe moves through the sediment.

5. The sediment used in the testing program must have uniform engineering properties, and a plane surface precisely parallel to horizontal pipe movement.

To achieve these requirements, a large drag box, 6-ft. x 6-ft. in plan view and 4 ft. high, was fabricated. Even these dimensions were not considered adequate for the 6 in. diameter pipe, but this problem was solved by designing the pipe with a special instrumented center section. The drag device consists of several components, described in detail below.

3.2.1.2 Large Drag Box Description: The side and front views of the large scale drag box with supporting equipment are shown in cross section in Figs. 3.1 and 3.2, respectively. The drag box, constructed of 3/16 in. mild steel plates reinforced with steel angles, was designed to withstand an internal mud pressure of 500 psf with minimal deflection. Care was taken to ensure that the box was constructed perfectly square to eliminate complications when installing support equipment.

The 6 ft. wide box provided approximately 1 ft. clearance between the edge of the box and the end of the pipe, thereby allowing nearly 4 ft. of pipe length. This provided a length:diameter ratio of nearly 28 for the 1.5 in. diameter pipe used most frequently in the drag box. Previous tests had shown that this ratio was adequate to reduce pipe end effects to only a few percent of the total drag force.

A 1/2 hp motor (B) drives a variable speed gearbox (C) which, in turn, drives a chain (D) connected to two leadscrews (Q) mounted on top of the drag box. Rotation of the leadscrews is translated into linear motion of a platform (H) mounted on the leadscrews; this provides the

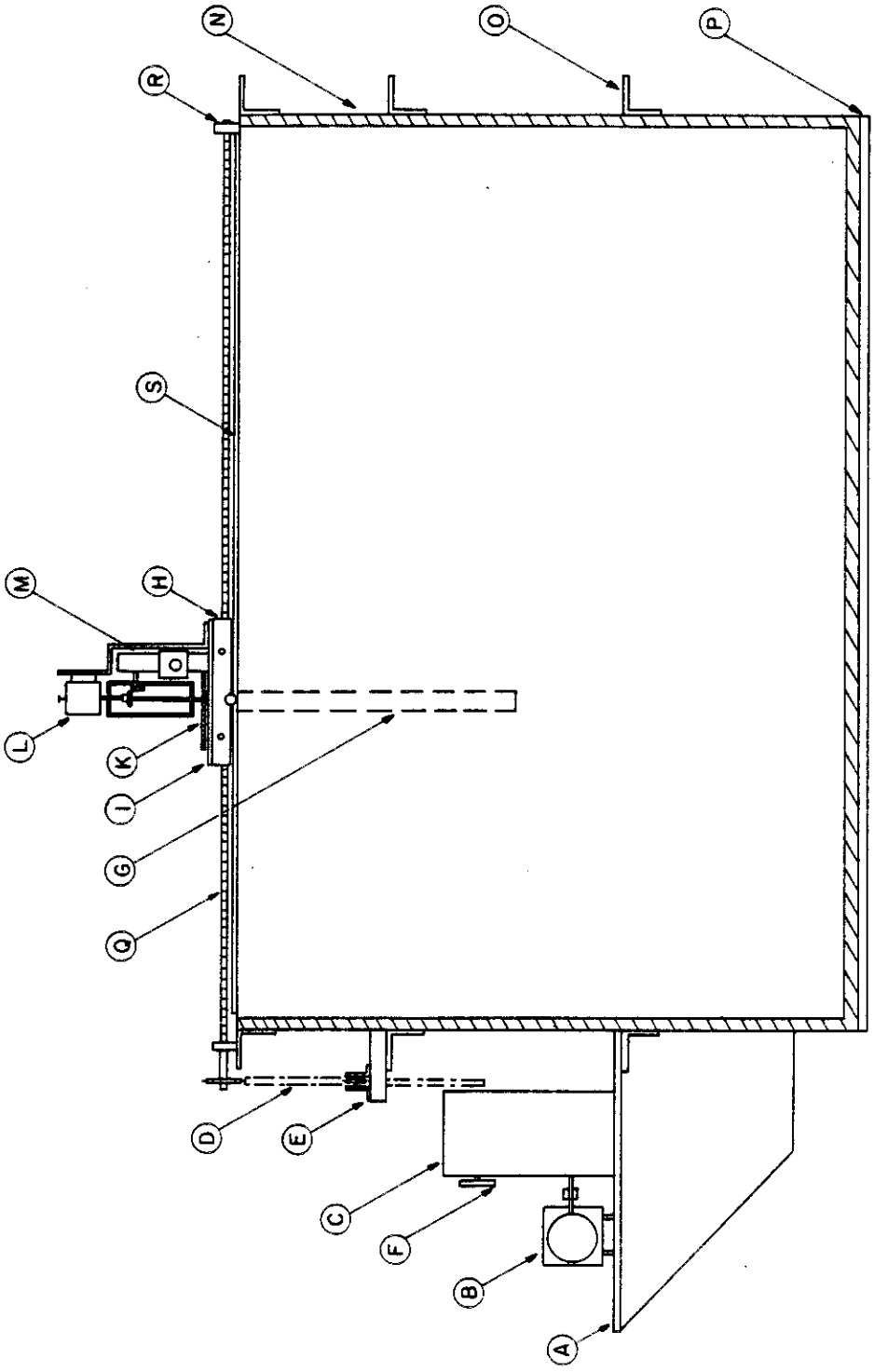

FIG. 3.1 - Cross Section Side View of the Large Scale Drag Box.

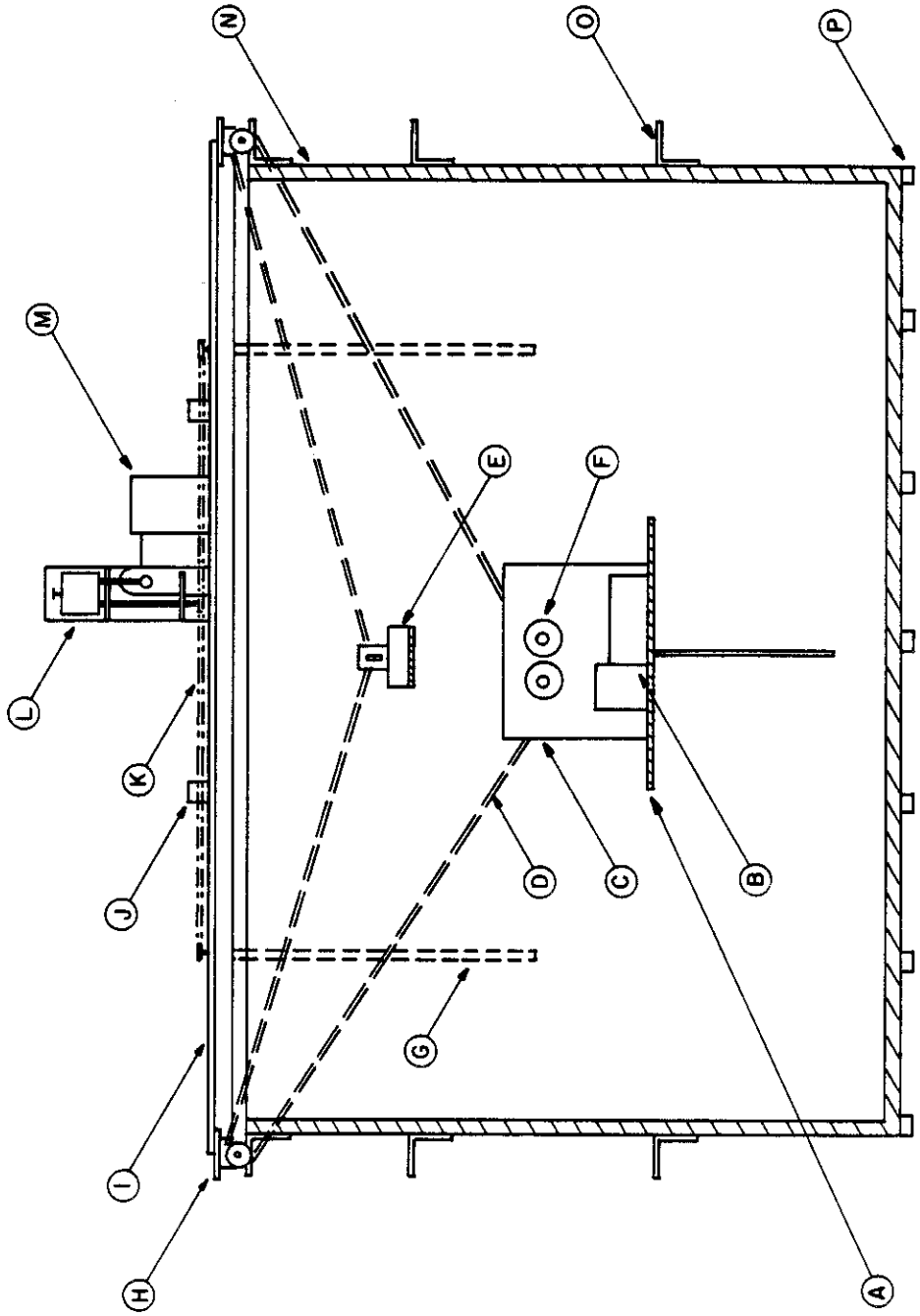

FIG. 3.2 - Cross Section Front View of the Large Scale Drag Box;

LEGEND FOR FIGS. 3.1 AND 3.2

A. Supporting Platform for Horizontal Movement Equipment

B. Horizontal Drive Motor

C. Horizontal Drive Gear Box

D. Horizontal Drive Chain

E. Idler Assembly for Horizontal Movement

F. Change Gears for Variable Horizontal Speed

G. Unislide for Vertical Movement

H. Pillow Block

I. Platform

J. Idler Assembly for Vertical Movement

K. Vertical Drive Chain

L. Step Function Speed Reducer

M. Variable Speed Drive Motor

N. 6-ft. x 6-ft. x 4-ft. (1.83-m. x 1.83-m. x 1.22-m.) Steel Tank

O. Reinforcement Angle

P. Supporting Wood Block

Q. Lead Screw for Horizontal Movemement

R. Bearing

S. Guide Rail

horizontal movement of the pipe. The gear box can drive the platform at velocities ranging from 5.0×10^{-2} in. per minute to 3.6 in. per minute by changing the gears in the gear box. Two unislides (G) are mounted on the underside of the platform to provide vertical pipe movement. The basic idea behind the unislides is the same as the horizontal leadscrews. A variable speed motor (M) drives the shafts of the unislides through a step function speed reducer (L). This system provides vertical velocities ranging from 1.87×10^{-4} in. per minute to 1.5×10^{-1} in. per minute. Figure 3.3 shows the drag box equipped with the supporting equipment and Fig. 3.4 shows the unislides, installed under the platform.

3.2.1.3 Force and Torque Transducers: One of the most important requirements of the design was to independently measure the drag forces, both vertical and horizontal, and the torque caused by sediment reaction on the moving pipe. Since commercial transducers meeting these requirements (as well as space limitations) could not be located, transducers were designed and fabricated locally. As shown in Fig. 3.5, two horizontal strain gaged members connected with the outer frame of the transducer measure the vertical drag force, while two vertical members connected to the inner frame measure the horizontal drag force. The horizontal gaged members are 0.18 in. thick and 0.625 in. long, whereas the vertical members are 0.18 in. thick and 0.5 in. in length; the transducer is 1.0 in. wide, but the gaged members have been reduced to 0.75 in. width. At the strain gage locations, the transducer material, 7075-T6 aluminum, develops approximately 500 microstrains per 100 pounds-force. When connected to the recording instrumentation the transducer system can resolve forces to 0.07 lbs.

The simplest and most direct way to measure torque is with strain

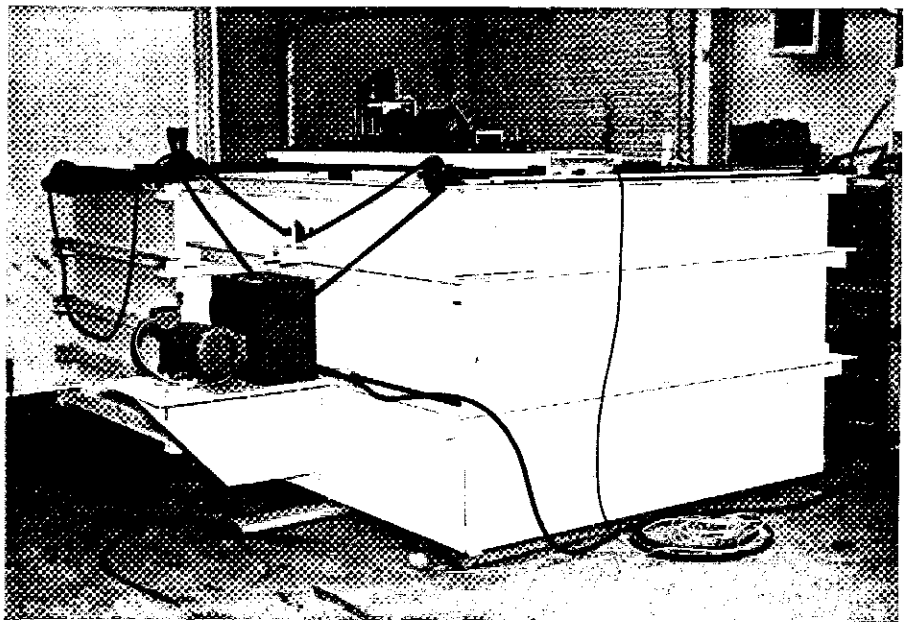

FIG. 3.3 - Large Scale Drag Device.

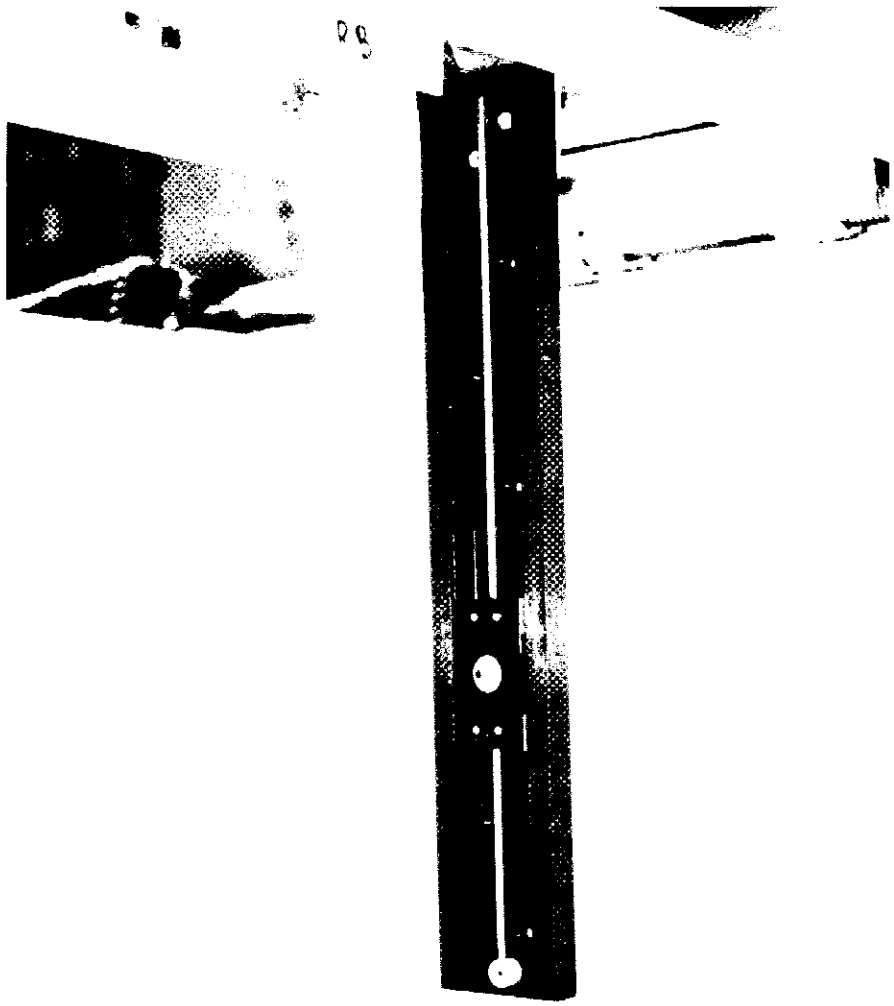

FIG. 3.4 - Unislide Assembly Mounted Under the Platform.

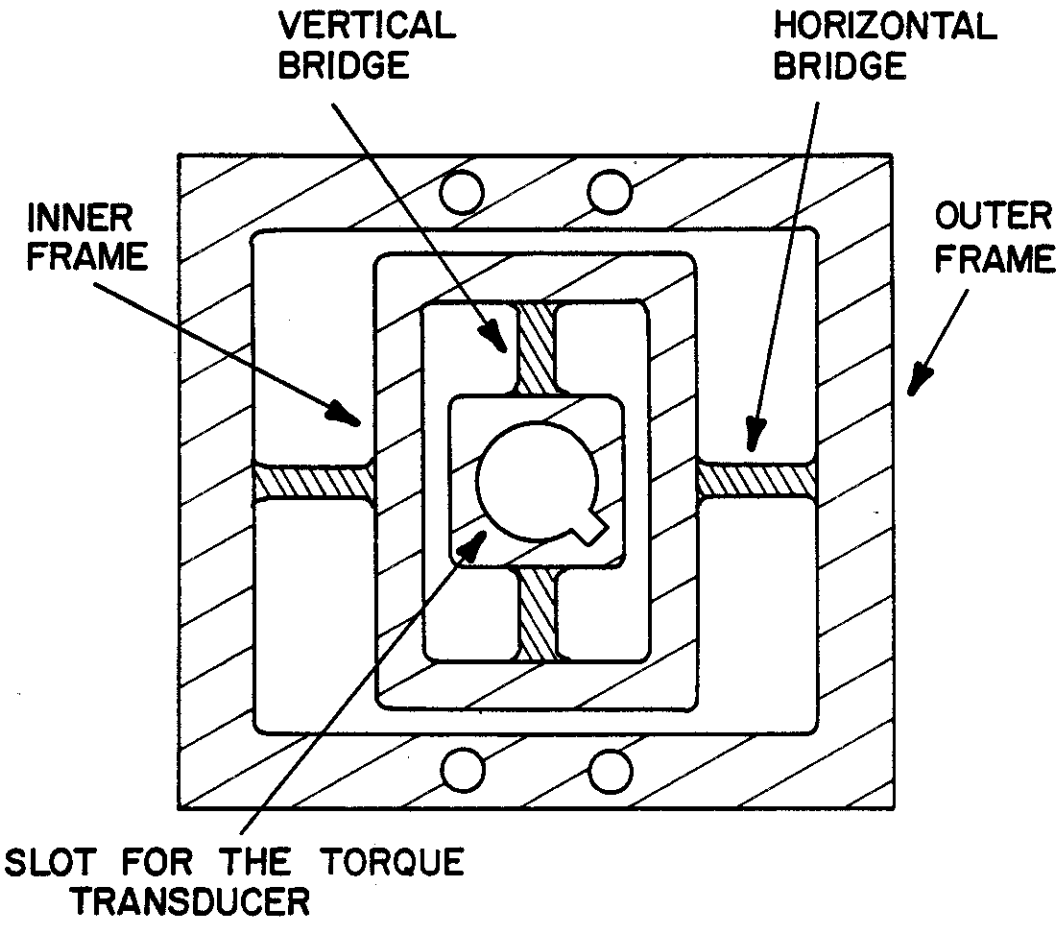

FIG. 3.5 - Schematic Diagram of the Force Transducer.

gages mounted on a shaft, using two sets of gages arranged at 45° to the longitudinal axis. A shaft machined to 0.75 in. length with a diameter of 0.406 in. was utilized as shown in Fig. 3.6. Using 7075-T6 aluminum the shaft develops approximately 100 microstrains per 1.39 in.-lbs. of torque. The transducer system can accurately resolve torques to 0.015 in.-lbs. Each torque transducer was fitted into a hole in the force transducer and secured by a key.

After the strain gages were placed on the transducers, they were coated to provide mechanical protection and waterproofing. The force transducers were further protected by covering them with plates on each side which were sealed to the the transducer frame. The force and torque transducers are shown in Figs. 3.7 and 3.8, respectively. The completed set of force and torque transducers ready for installation on the pipes is shown in Fig. 3.9.

3.2.1.4 Sediment Leveling System: A removable sediment leveling system was installed inside the tank. It consists of a scraper which runs on two rails and is equipped with adjustable vertical supports on both sides of the scraper to adjust the level of the scraper. Using one person on each side of the scraper, it is pulled back and forth several times to level the sediment in the tank. A schematic diagram of the leveling system is shown in Fig. 3.10.

3.2.1.5 Instrumentation and Recording Equipment: A schematic diagram of the instrumentation system is shown in Fig. 3.11. The basic components of the instrumentation were the two force and torque transducers as discussed above. The transducers were connected to signal conditioners which provided excitation current to each transducer and also contained the zeroing circuitry for each channel. The output

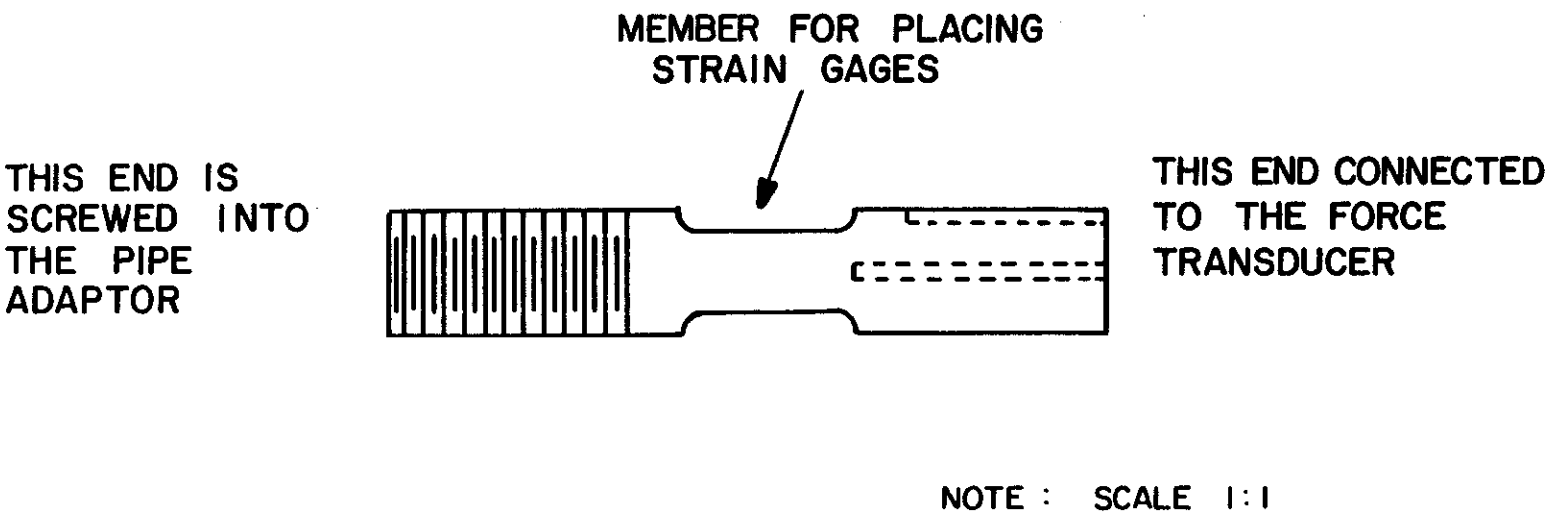

FIG. 3.6 - Schematic Diagram of the Torque Transducer.

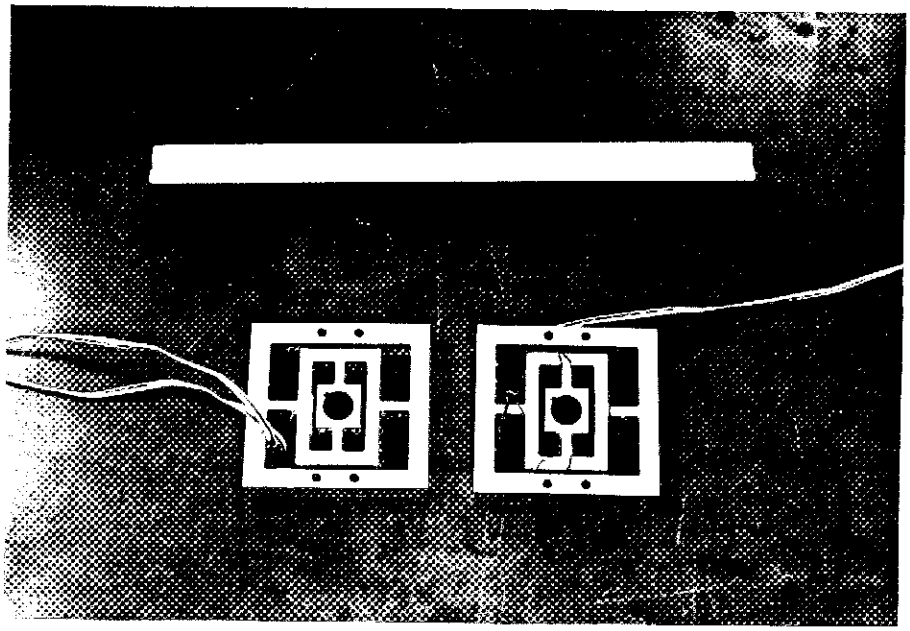

FIG. 3.7 - Force Transducers for Measuring Vertical and Horizontal Drag Forces.

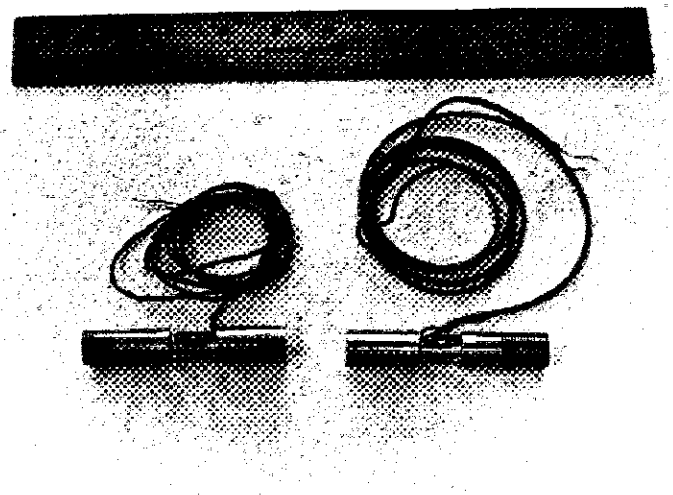

FIG. 3.8 - Transducers for Measuring Torque.

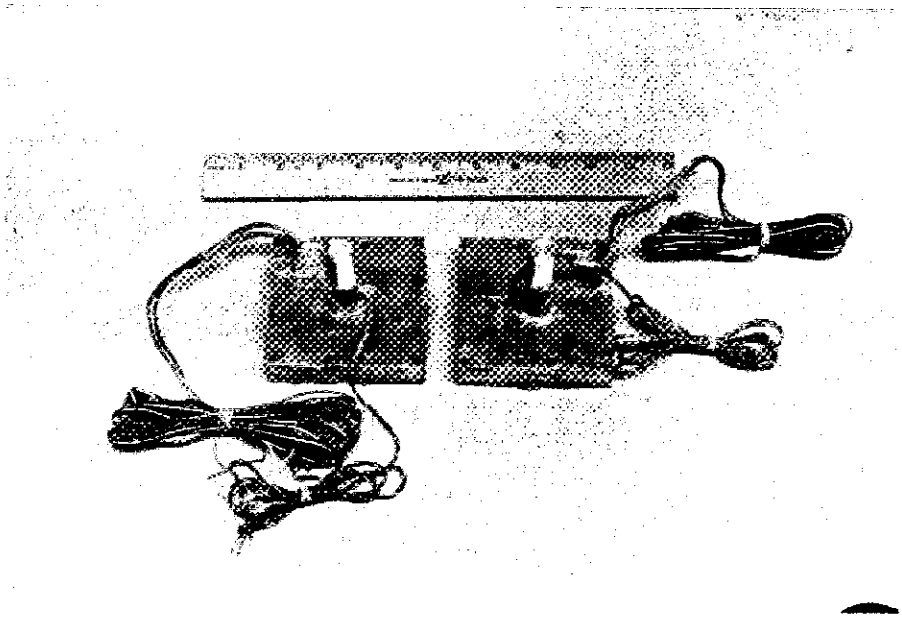

FIG. 3.9 - The Completed Set of Force and Torque Transducers.

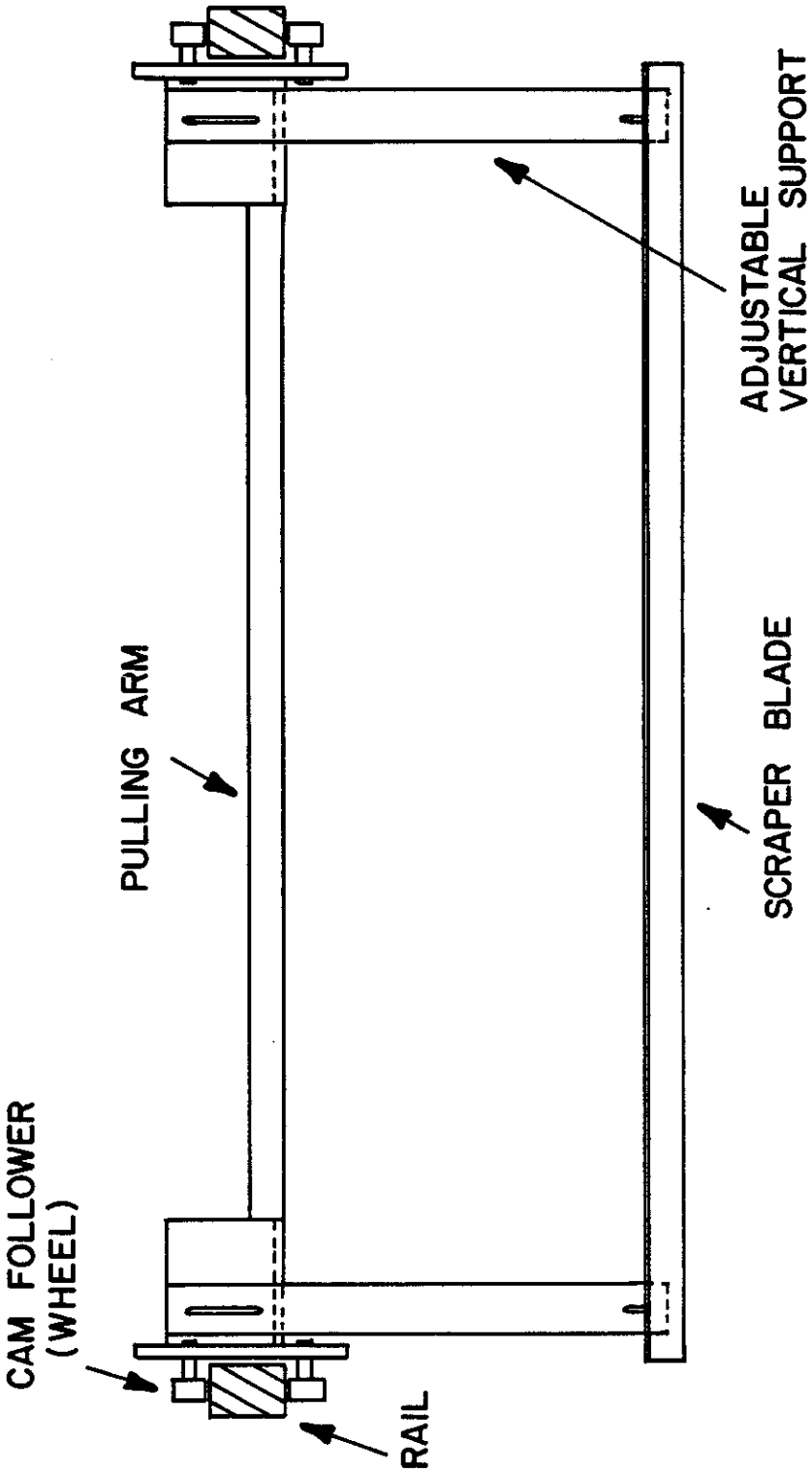

FIG. 3.10 - Schematic Diagram of the Leveling System Installed on the Large Drag Box.

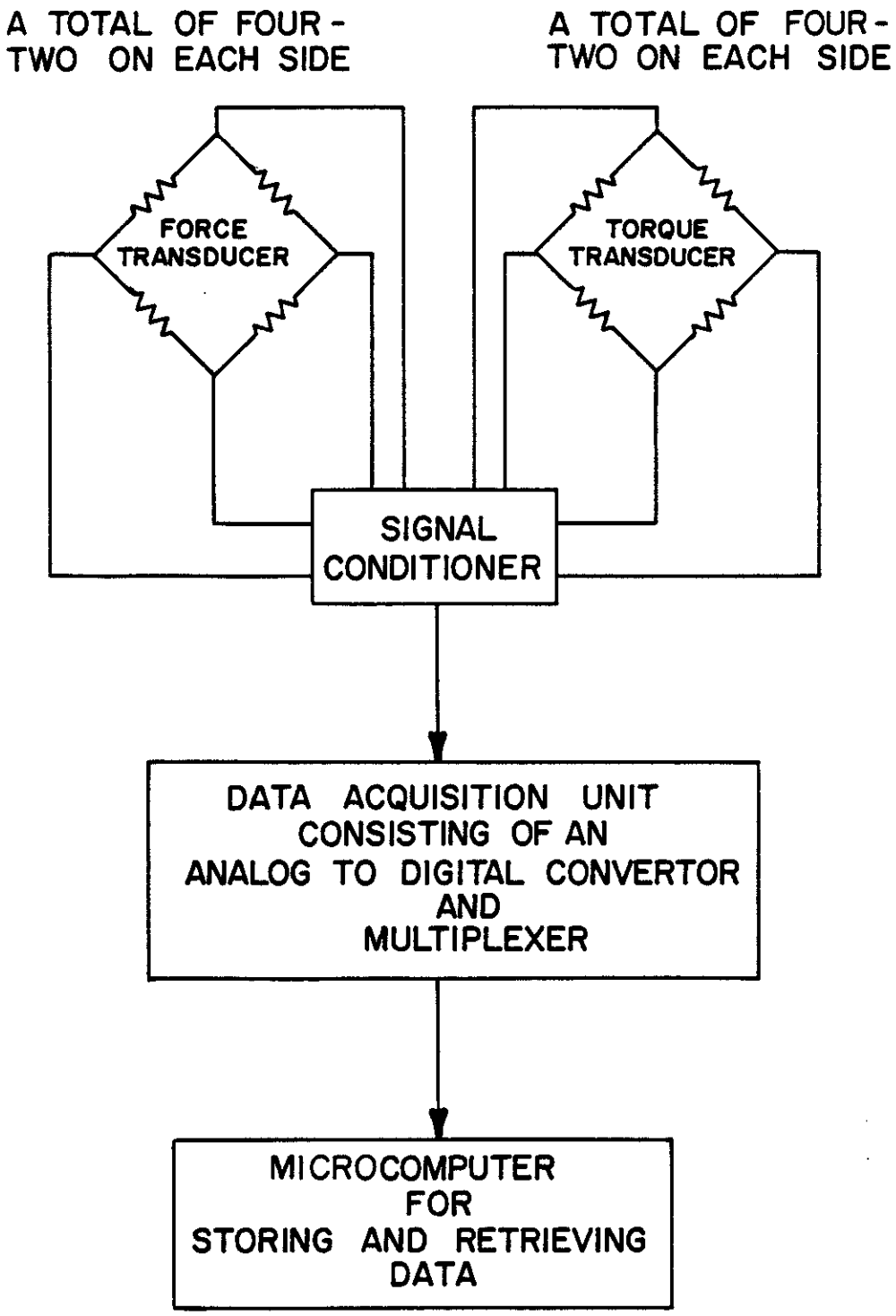

FIG. 3.11 - Schematic Diagram of Force and Torque Instrumentation

signals from the transducers were transmitted to a data acquisition unit consisting of an analog-to-digital converter and multiplexer (HP 3497A). This data acquisition unit could obtain six channels of data at a sampling rate of 0.25 secs. Digital data were transmitted to an HP-85 computer for processing and storage on magnetic tape or floppy disc. The processed data could be output in engineering units only moments after completion of a test. The data recording equipment is shown in Fig. 3.12.

3.2.1.6 The Pipes: Three different pipes were used during the test program. The first tests were done using a solid steel bar, 0.75 in. diameter and 41.875 in. long, for the purpose of checking the equipment and comparing results to previous tests conducted on pipe of the same diameter. These results are considered preliminary and are not reported herein; however, the results were identical to earlier tests in the intermediate box, within the limits of experimental error.

Most of the tests were performed using a 1.50 in. diameter, 41.875 in. long steel pipe which weighed 4.10 lbs. including the end caps. The pipe exterior was not machined, and the surface roughness was that of a normal exposed pipe.

Several tests were performed using a 6.0 in. diameter pipe. If fabricated with the same length as the smaller pipes, this pipe would have had a length:diameter ratio of 7:1, which could have resulted in significant end effects. To eliminate this problem, the pipe was fabricated with an active or instrumented 12 in. long center section. This was accomplished by suspending the center section on the force and torque transducers which were installed in the two outer sections of pipe as shown in Fig. 3.13. To prevent friction between the active section and the adjoining pipes a slight crack was left which was sealed

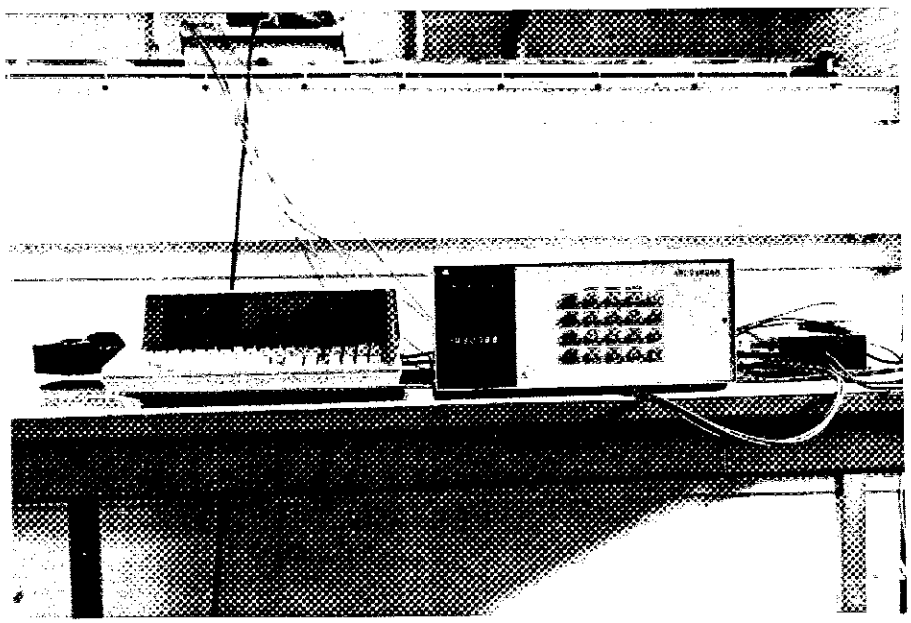

FIG. 3.12 - Data Acquisition and Recording Equipment Used with Large Drag Box.

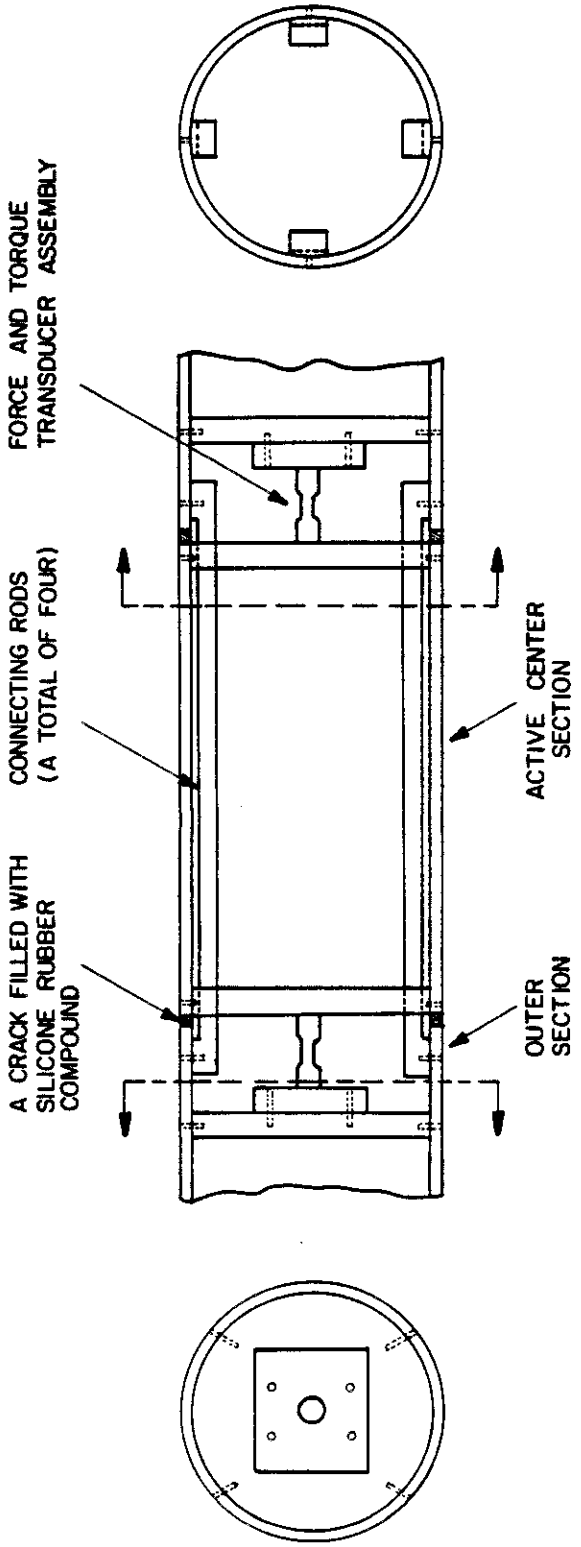

FIG. 3.13 - Schematic Diagram of the Instrumented Center Section of the 6 in. Pipe.

with silicone rubber compound.

The 6 in. pipe worked very well, but it did require precise installation to insure that the force transducers were aligned vertically and horizontally, and it precluded the use of rotating pipe.

3.2.2 Intermediate Drag Box

3.2.2.1 General Requirements: The primary requirements for this equipment were:

1. It must be capable of measuring the axial and normal drag forces on model pipes oriented at different angles to the sediment flow direction for burial depths, h/D, ranging from 0.25 to at least 9 (infinitely deep).

2. It must have the ability to pressurize the pipe-sediment system to total pressures of at least 30 psi.

3. It must provide a wide range of pipe velocities for purposes of examining rate effect on pipe drag forces.

4. The sediment container must be large enough to accomodate model pipes of adequate dimensions without producing boundary effects.

3.2.2.2 Intermediate Drag Box Description: The requirements above were met with the simple shear/drag device developed by Marti [3]; this device was also used in Phase I of the research. As shown in cross section in Fig. 3.14, this consists of a heavy metal box with inside dimensions of 3 ft. by 3 ft. by 14 in. high. The sediment is placed in a rubber bag - which just fits into the interior of the box - through a large opening in the top of the bag. After sealing this opening with a cover, the sliding lid of the box is clamped in place (Fig. 3.15). Two large rubber bladders on either side of the box can be pressurized to produce the desired total pressure in the sediment. A vertical rod,

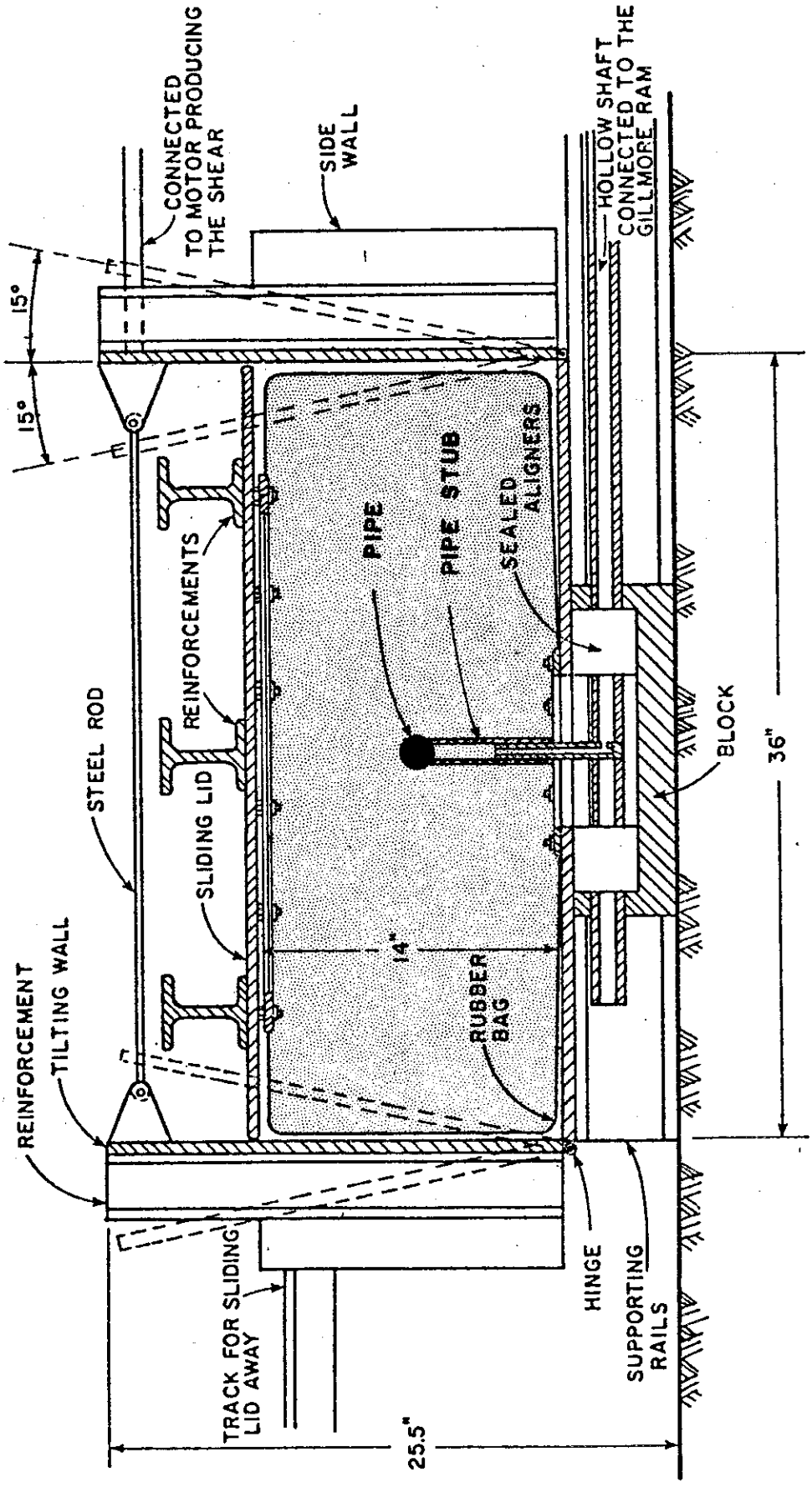

FIG. 3.14 – Cross Section Side View of the Intermediate Scale Drag Box.

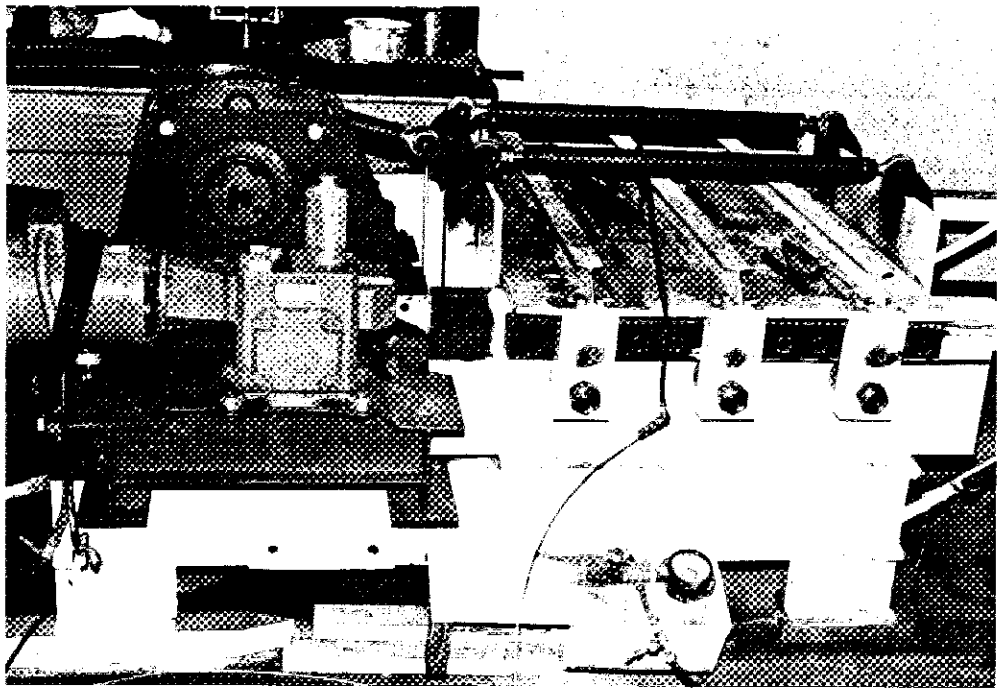

FIG. 3.15 - Intermediate Scale Drag Box with Sliding Lid Clamped in Place Prior to Performing Drag Test.

herein termed the "pipe stub", extends from the bottom of the box through a special seal into the interior cavity. Outside of the box, this stub is connected to the hydraulic ram of a closed-loop servo-controlled testing machine which can be programmed to move the pipe stub back and forth through a wide range of velocities.

The model pipes are mounted on top of the pipe stub using specially tooled adapters termed "pipe mounters" (Fig. 3.16). The top of each mounter was machined with a concave surface of appropriate radius to receive the horizontally mounted pipes, while the bottom of the mounter was machined with a slot to engage a mating projection on the pipe stub. By machining the slots at various angles, the orientation of the pipe with respect to the direction of movement could be controlled. The flow angle, α, was varied from 0° (pipe moving axially) to 90° (pipe oriented normal to flow direction) in 10° increments and at 45°. Measured angles of α sometimes varied from the desired values by 1-2°; the measured values are plotted herein.

Attached to the vertical stub are strain gages, one strain gage bridge oriented normal to the direction of flow and the other at right angles to the flow direction. The strain gage bridges were calibrated using known weights and moment arms to produce a calibration curve between bridge output voltage and moment. With the available data acquisition equipment, a moment of 0.005 in.-lbs. could be resolved for both strain gage bridges.

By knowing the measured moments and the moment arm to the center of the model pipe, drag forces on the pipe in the two directions (normal and perpendicular to the direction of flow) could be calculated. Simple trigonometric relations allowed these forces to be translated into axial and normal forces on the pipe.

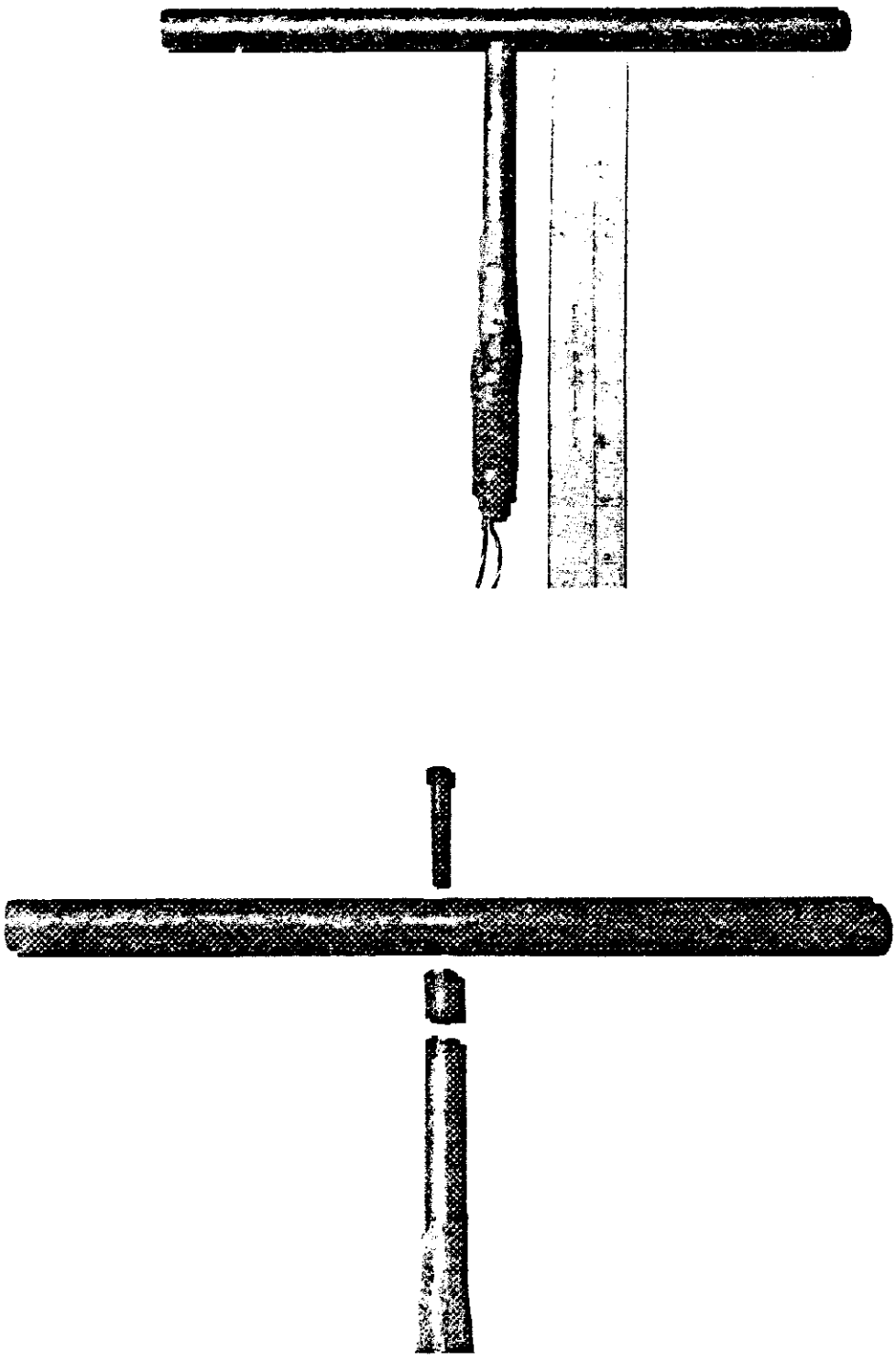

FIG. 3.16 - Exploded View of Pipe, Stub and Pipe Mounter Used in Intermediate Scale Drag Box.

The intermediate drag box was initially designed for deeply buried piles and was modified for this research to handle deeply buried pipes. For shallow and partially buried pipes, it was a simple matter to lower the sediment level in the box to achieve the desired burial depth. However, this left a void over the pipe which rendered the pressurization system useless, and tests could be performed only at atmospheric pressure. Some tests at atmospheric pressure were required in the test plan, but it was necessary to modify the drag box for tests requiring pressure on shallow and partially buried pipes. This was accomplished by removing the pressure bladders from the box and manufacturing a new sealed lid for the top of the rubber bag which held the sediment (Fig. 3.17). This lid contained a pressure inlet which allowed the entire contents of the bag to be pressurized once the sliding top of the drag box was clamped in place.

Most of the tests in the intermediate box were conducted on a 0.75 in. diameter by 12 in. long steel pipe. However, in one series of tests conducted to study end effects this pipe was replaced by a 1.5 in. diameter, 12 in. long pipe, and by a 0.375 in. diameter, 12 in. long pipe. This also necessitated the fabrication of new pipe mounters to match the pipe diameters.

In all tests performed in the intermediate drag box the pipe was rigidly held, i.e. it could not rotate or move in the vertical direction during the conduct of the test.

The data acquisition equipment used for the intermediate drag box was essentially the same as for the large drag box with the following exceptions: electrical signals from the strain gage bridges were conditioned and amplified before being transmitted to the A-D converter,

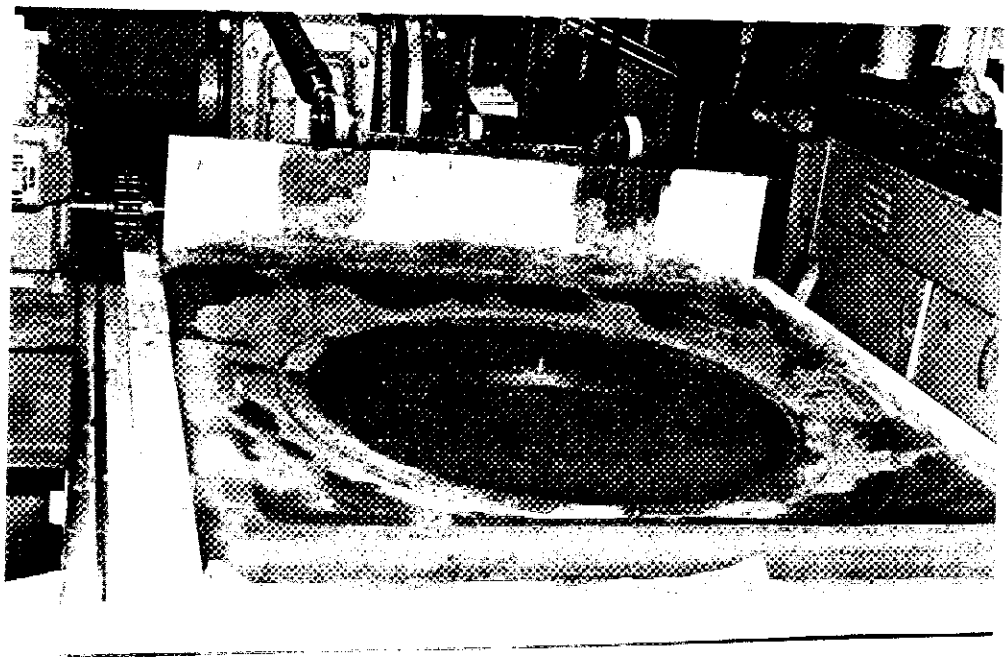

FIG. 3.17 - View of Sealed Lid with the Pressure Inlet Used in Intermediate Scale Drag Box.

and the output data were also displayed on an X-Y_1Y_2 plotter. Horizontal displacement of the pipe was measured with an LVDT, whose output was transmitted to both the plotter and the A-D converter.

It should be noted that the sides of this box can be rotated to produce a state of simple shear in the sediment. In an extensive set of experiments, Marti [3] measured drag forces on stationary vertical piles with the sediment moving past the piles in cyclic simple shearing, and compared these values to the drag forces on the pile when it moved back and forth in the stationary sediment. He found that both conditions produced the same drag forces. From a mechanical viewpoint, it is easier to move the pipe in the stationary sediment, and this procedure was used in the experiments reported herein. If the alternative approach had been used, it would have been impossible to determine the relative displacement between the pipe and the sediment, a measurement which was important to the theoretical development.

3.2.3 Small Drag Box

3.2.3.1 General Requirements: At the time this drag box was designed, many tests had already been performed in the large and intermediate boxes, and the specific tasks for the small box were well understood. This greatly simplified the design. These tasks required the following capabilities:

1. The pipe must be capable of being oriented at different angles to the sediment flow direction, and the instrumentation must be able to measure axial and normal drag forces on the pipes.

2. Pipe burial depths must be adjustable from h/D of 0.25 to 2.

3. Pipes must be capable of being tested either fixed against vertical movement or allowed to freely float, and they should be controllable to allow free rotation or to be clamped against rotation.

4. Tests must be performed under conditions of pressure ranging from atmospheric to 30 psi.

5. The driving mechanism should be capable of providing pipe velocities comparable to those utilized in the other two drag boxes.

3.2.3.2 Small Drag Box Description: The primary difficulty, that of obtaining a large pressure vessel capable of withstanding 30 psi pressures, was solved by using the pressurization chamber for the large scale simple shear device developed by Riggins [4]. This chamber is 3 ft. by 3 ft. by 20 in. high and is constructed of 1/2 in. plate reinforced to keep deflections to a minimum. It is equipped with a pair of machined rods on the inside bottom which serve as tracks for linear ball bushings attached to a moveable carriage (Fig. 3.18). A 2 ft. by 2 ft. by 4.5 in. deep container holding the sediment fits onto the carriage (Fig. 3.19). The carriage and sediment container move practically friction-free on the linear ball bushings. The movement of the carriage is accomplished by connecting it to a piston which penetrates through a pressure seal in the wall of the chamber. This piston is in turn connected to the actuator of a closed-loop servo-controlled testing machine, thus the total movement and rate of movement of the sediment box can be carefully controlled. Riggins installed a load transducer between the actuator piston and the carriage to measure the load applied to his simple shear specimens; he was able to calibrate the friction from the linear ball bushings out of his measurements. After several pipe drag tests had been performed using this approach, it was found that the results were erratic and that this could be attributed to the variations in frictional forces in the linear ball bushings. This required the development of a new transducer which directly measured the

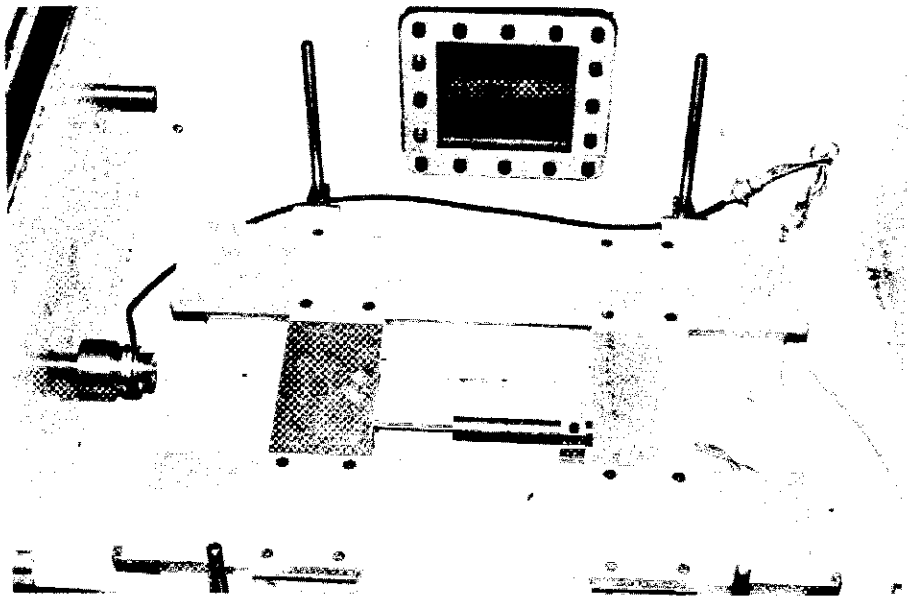

FIG. 3.18 - Pressure Container and Carriage in Small Scale Drag Box.

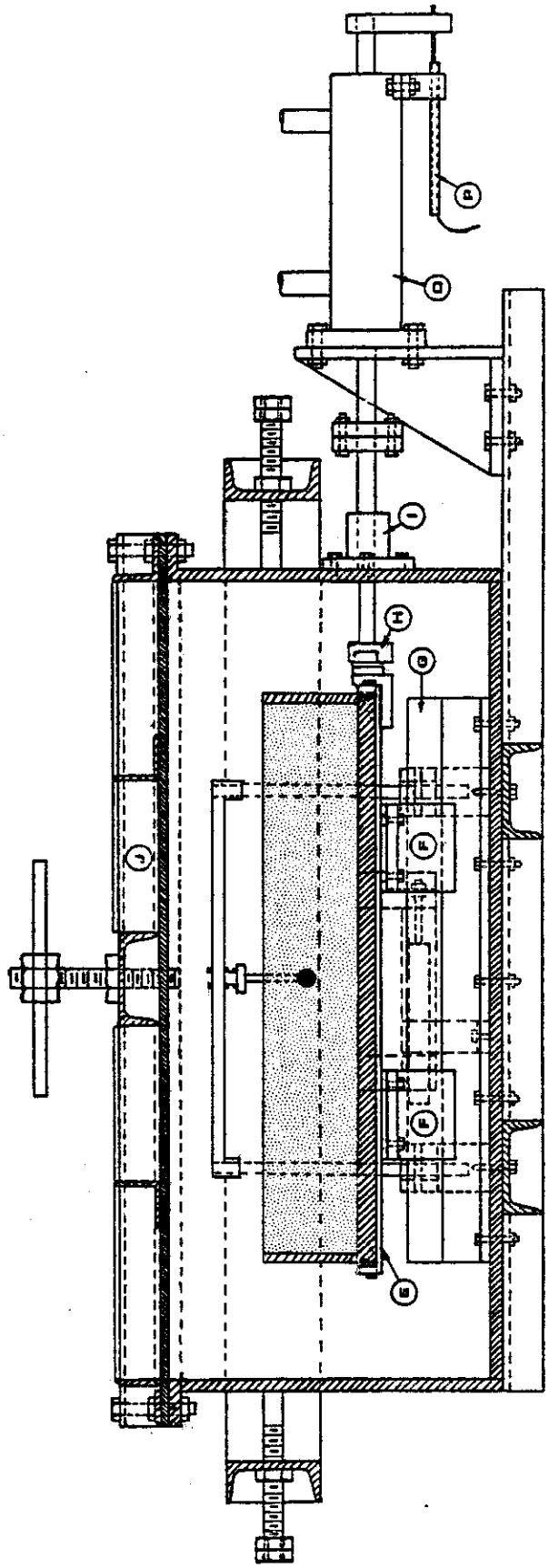

FIG. 3.19 - Cross Section Side View of Small Scale Drag Box.

forces on the model pipes.

This new transducer was designed to measure moments in two directions, normal and axial to the pipe, and it was insensitive to torsion and vertical loads. In concept, it is similar to the approach used in the intermediate box except the transducer is located above the sediment surface rather than in the sediment. The transducer is a thin-walled hollow tube, 1.00 in. outside diameter with wall thickness of 0.015 in., machined from 7075-T6 aluminum and instrumented with two full strain gage bridges oriented at 90° to each other. When connected to the instrumentation system, it is capable of resolving moments of 0.005 in-lbs. It basically joins together two frames: one frame holds the pipe, while the other frame is rigidly attached to supports in the pressure chamber.

The frame which supports the pipe has two rods extending down from it to which the pipe is attached, similar in concept to the unislides used in the large drag box. These rods can be adjusted to raise and lower the pipe to change the recess depths, h/D. The rods are also slotted at the bottom end to allow the pipe to freely float if desired, or the pipe can be fixed to prevent vertical movement.

Several pipes were used in the drag box, but all were nominally 3/4 in. in diameter and 12 in. long. To attach the pipe, small studs extending from the ends of the pipe fit into the slots in the rods described above. One pipe contained ball bearings in the ends of the pipe to allow the pipe to freely rotate during the drag tests.

With this design, the pipes could be clamped against vertical movement or allowed to freely float vertically, and they could be fixed against rotation or allowed to freely rotate.

Data acquisition equipment utilized was exactly the same as for the

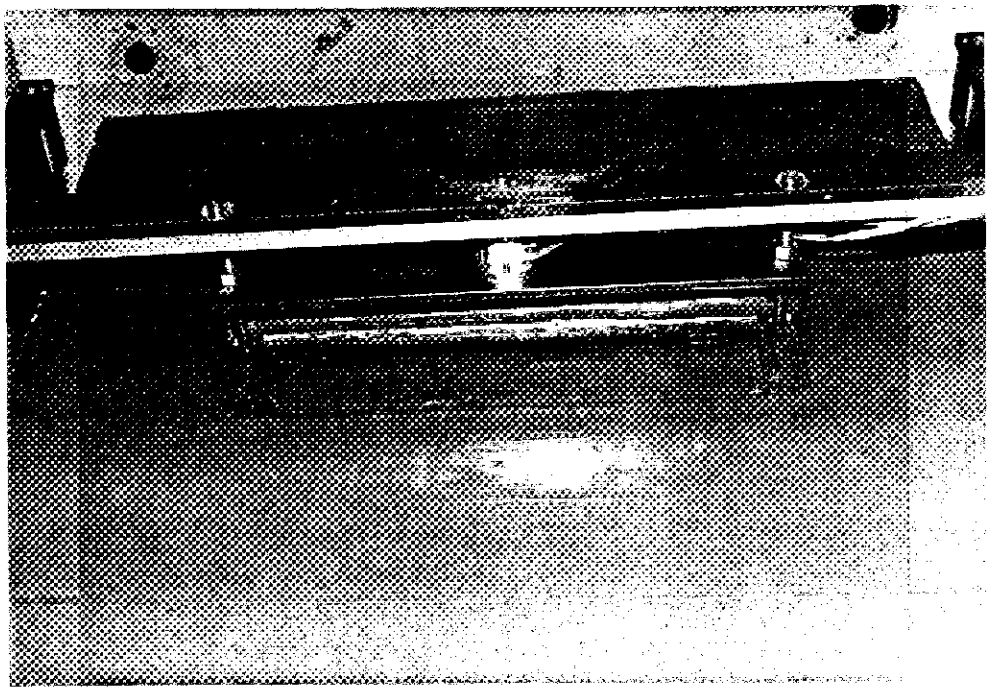

FIG. 3.20 - View of Pipe Support Frames and Transducer Used in Small Scale Drag Box.

intermediate box.

Sediment velocities were controlled by the rates of movement of the sediment container which was attached to the closed-loop servo-controlled testing machine.

This was the only drag box in which the sediment moved past the pipe as opposed to the pipe moving in the stationary sediment. The sediment thickness was limited and the largest h/D which could be safely used without boundary effects was 2. However, problems involving deeply buried pipes had been settled when this box was designed, and only partially buried and shallow buried pipes needed to be tested.

3.3 Experimental Tests

3.3.1 Tests on Sediment

3.3.1.1 Engineering Properties: The sediment had a liquid limit of 115, a plastic limit of 49, and a plasticity index of 66. Grain size analysis showed that there was a trace of sand-sized particles (mostly shells), 75 percent clay size (<0.002 mm), with the remainder being silt size. The plasticity index suggests that the sediment contains a high concentration of montmorillonite clay.

During the testing program the sediment in each drag box was continually reused so that uniformity of the soil properties was carefully controlled. Whenever it was necessary to add water to modify the strength or make up for evaporation losses, only distilled water was added.

Sediment shear strength was measured during the test program with a motorized miniature vane and a hand-held vane. The purpose of the motorized miniature vane test was to accurately determine the undrained shear strength, C_{uo},* of the very soft sediment. The strength was

*The subscript, u, refers to the ultimate or peak strength.

measured under standard conditions (rotation rate of 0.0143 rad/sec) using the vane shear device developed by Stevenson [2], which is geometrically similar to the vanes used by McClelland Engineers for their in situ measurements. The motorized miniature vane shear device is shown in Fig. 3.21.

Although there was a great deal of confidence in these shear strength measurements, they were made on samples packed into molds and not on the sediment in the drag boxes. For this reason, a hand-held vane device was used to determine strength in the drag boxes. This device was also capable of determining the shear strength at depth in the boxes, a task that could not be performed with the motorized miniature vane.

3.3.1.2 Determination of Rate-Dependent Properties: Research performed by Stevenson [2] and subsequent research by Marti [3] and Riggins [4] documented the strain-rate dependence of soft marine sediments such as the sediment used in this research. Stevenson developed a test procedure using a specially designed laboratory miniature vane shear device for examining the strain rate dependence and characterized the sediments as nonlinear viscoelastic materials. The time-dependent exponent, n, was found to be related to sediment water content and liquidity index. During Marti's research on pile drag forces, it was observed that the drag forces were proportional to the pile (or sediment) velocity as a function of the value of n. This was confirmed during the Phase I studies on pipe drag forces. This provided another means, although somewhat indirect, of determining n.

To completely characterize the sediment for this study, and to aid in selecting sediment moisture contents for the experiments, a test

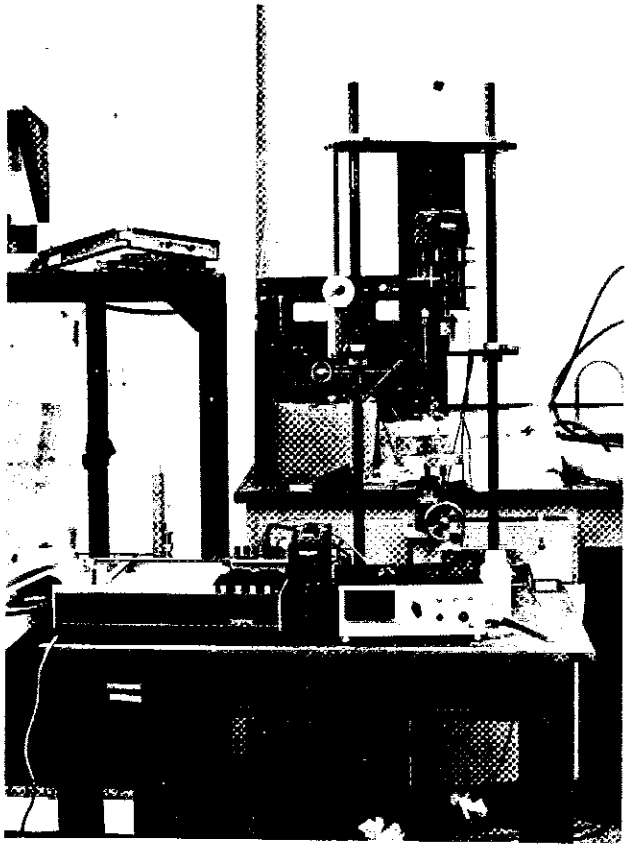

FIG. 3.21 - Motorized Miniature Vane Shear Device.

series was conducted to determine the relationship between n, water content and undrained shear strength of the sediment using the Stevenson miniature vane apparatus. In anticipation of problems concerning thixotropic behavior of the sediment, tests were performed after rest times of 24, 48 and 72 hours. The sediment samples were packed into molds, capped to prevent evaporation, and after the desired rest times, the tests were conducted. The test procedure involved rotating the vane in the sediment at a minimum of four different rates (using fresh locations in the sediment for each rate) recording the torque-rotation angle curve, and then obtaining the moisture content.

Fig. 3.22 shows the relationship between C_{uo}, the undrained shear strength at the standard vane rotation rate of 0.0143 rad/sec, and sediment moisture content, plotted on a semi-logarithmic scale. This relationship is roughly linear, as might be expected for this type of soil, and there are no distinct effects of resting time. Undrained shear strength is plotted versus strain rate exponent in Fig. 3.23. This figure shows that within the range of strengths which were tested, there was only slight dependency of n on the shear strength. Also, there is little diference between the 48 and 72 hr. results. There is some indication that for equal shear strengths the n-values for 24 hr. curing times are slightly less than those for the longer curing times.

The relationship between C_{uo} and n was further developed for lower strengths by later drag tests.

3.3.2 Test Procedure for Large Drag Box

One of the major problems ivolved in the tests conducted in the large drag box was processing the significant amount of sediment necessary to fill the box. The sediment needed to be homogeneous and also at the proper water content to achieve the desired undrained shear

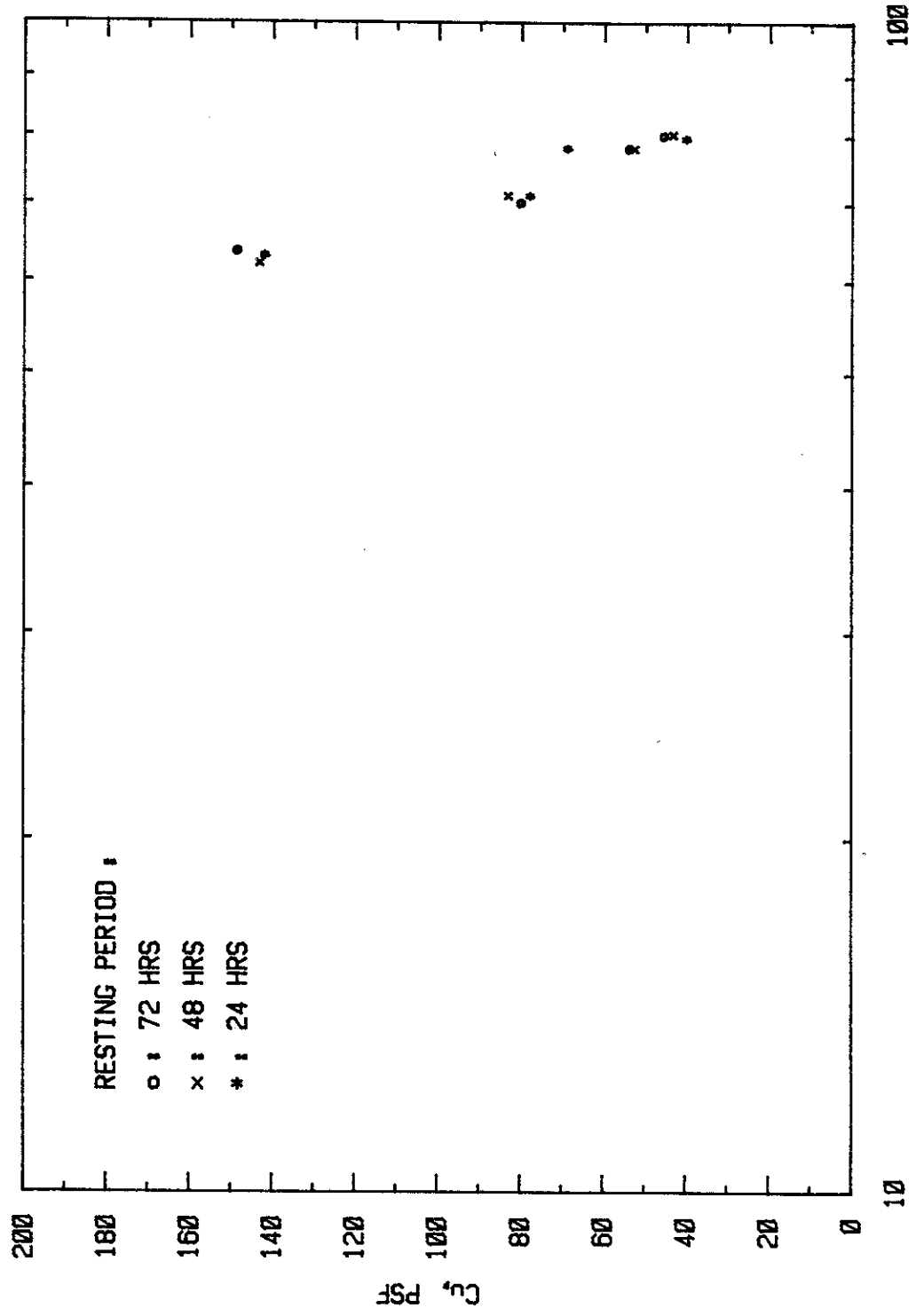

FIG. 3.22 – Relationship Between Undrained Shear Strength and Moisture Content for Sediment.

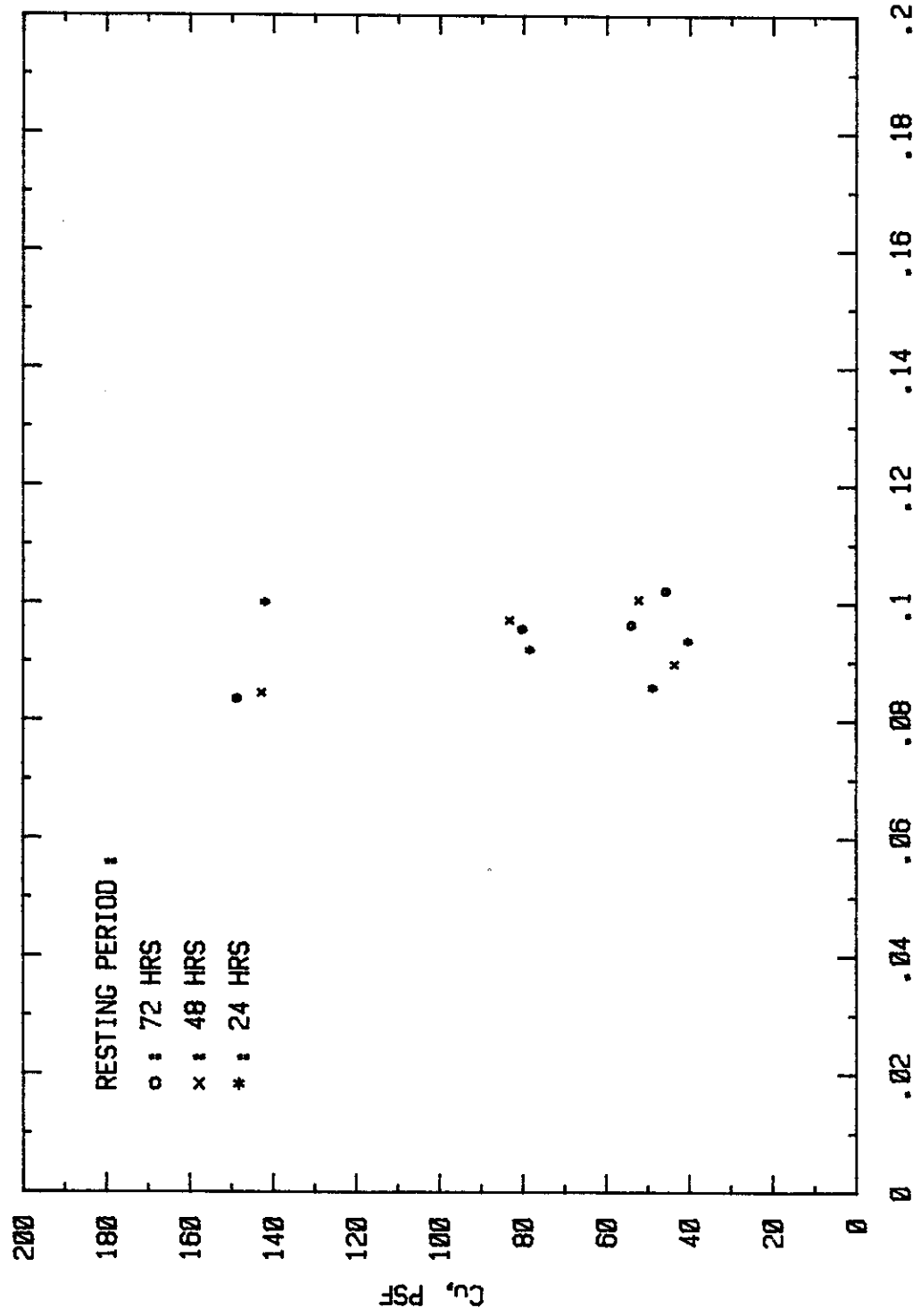

FIG. 3.23 – Relationship Between Undrained Shear Strength and Strain Rate Exponent for Sediment.

strength of 20 psf. Initial mixing was achieved by placing small amounts of the sediment in a large wooden tank, adding distilled water to produce a slurry, then mixing with a hand-held mixer. The slurry was then transferred to the large drag tank. After the drag tank was filled, a Vulcan pump was used to circulate the sediment between the drag tank and the wooden storage tank over a period of several weeks. The mixing homogenized the sediment, and natural evaporation reduced the water content to the point where sediment strength was nominally 20 psf.

It was planned to recirculate (mix) the sediment after each test in the large drag box, but at the final water content the pump could not maintain suction owing to the thixotropic properties of the sediment. This made it necessary to resort to hand-mixing of the sediment for each test.

The procedure utilized for preparation and performance of the drag tests is described below:

1. The sediment was thoroughly mixed in the large scale drag device using a hand-held mixer. Although care was taken to eliminate air trapped in the sediment, some air voids were created by the mixer. These were eliminated by using a trowel or by rearranging the sediment by hand. Fig. 3.24 shows the sediment being mixed by the mixer.

2. The sediment was leveled with the screeding system installed in the drag device.

3. With the pipe in air, all force and torque measuring channels were adjusted to zero using the excitation and zeroing circuit unit. This eliminated the pipe weight from subsequent measurements.

4. A trench was dug to the anticipated recess depth, and the pipe was lowered to the desired position. The recess depth of the pipe was

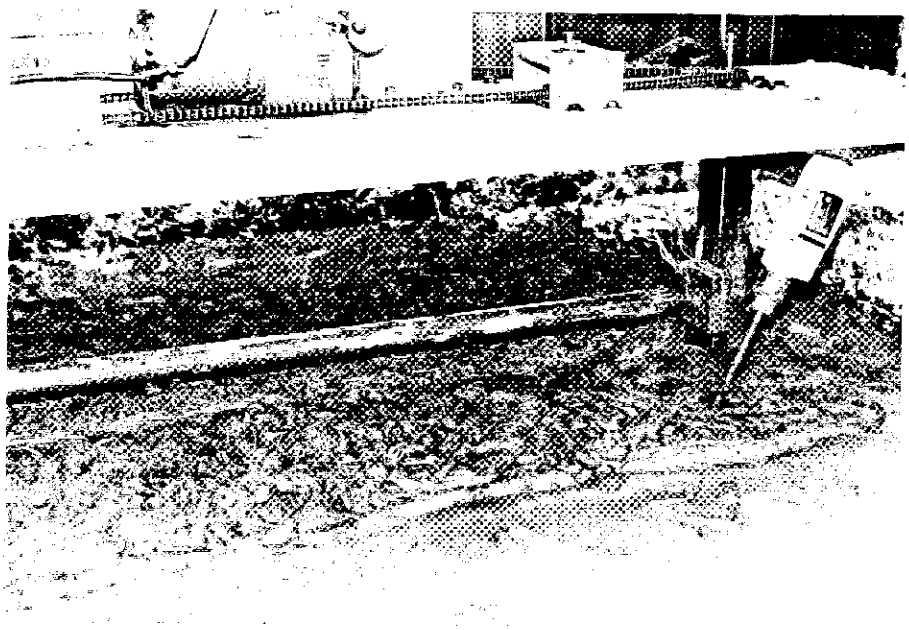

FIG. 3.24 - Mixing the Sediment with a Hand-held Electric Mixer.

accurately obtained by measuring from the platform to the sediment surface and to the top of the pipe.

5. After the pipe was set to the required depth, the sediment was packed by hand around the pipe to close the trench. This was done carefully to eliminate excessive residual stresses from acting on the pipe, especially in the horizontal direction. The sediment around the pipe was then leveled with a trowel and left undisturbed for a two hour healing or rest period before testing. Fig. 3.25 shows a close-up view of the pipe after installation.

6. After the rest period, the experiment was performed by simultaneously triggering the data acquisition apparatus and pipe drive mechanisms.

The technique of placing the pipe in a pre-formed trench seemed preferable to pushing the pipe into the sediment to the desired recess depth. Large residual stresses, particularly in the vertical direction, would result from the latter approach, and the buoyancy force could not be separated from the vertical drag force.

Shear strength and moisture content determinations were done immediately before the actual drag test was performed. Samples for determining the time-dependent exponent, n, were taken after step 1. and tested immediately after the drag test so the healing period was also two hours. Hand-held vane shear tests performed after the two hour healing period indicated that some variation in strength occurred with depth, possibly due to consolidation of the sediment. The variation with depth was small, less than 10 percent at a depth of 8 in. and the sediment can safely be considered as homogeneous.

3.3.2.1 Tests Conducted in Large Drag Box: Several different types of drag tests were conducted during the program, as described below:

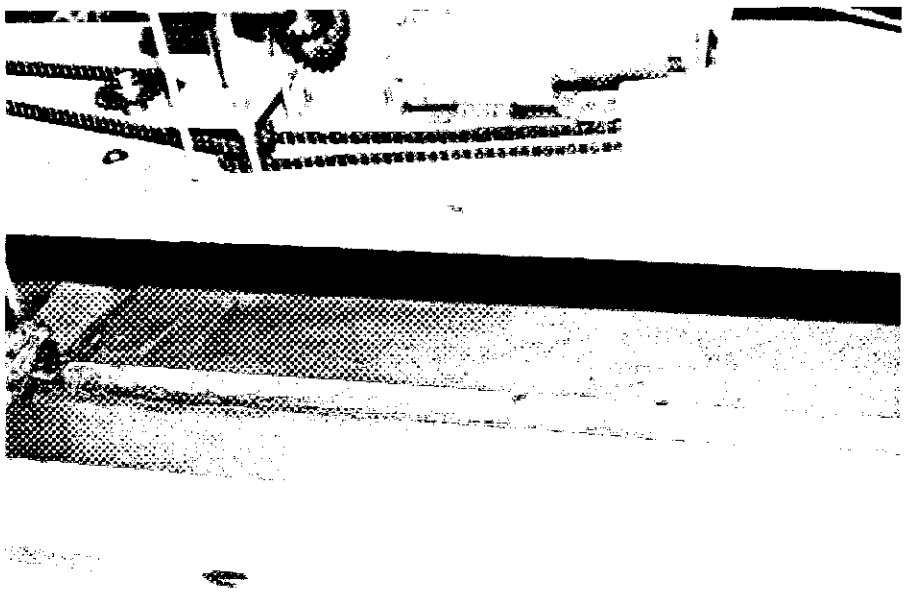

FIG. 3.25 - A Close-up View of the Pipe Set to the Required Recess Depth for a Test.

1. Fixed-Ends Horizontal Drag Tests (1.5 in. O.D. Pipe).

In these tests, the pipe was rigidly held to prevent rotation and vertical movement. These tests were performed to compare values of the horizontal force coefficient with those obtained in the other drag boxes, and to obtain values of vertical force coefficient and torque coefficient which could not be otained in the other boxes. Recess depths, expressed in terms of h/D, ranged from 0.25 to the maximum obtainable value of 5.2. The pipe was pulled through the sediment with a horizontal velocity of 0.09 in./sec.; i.e., V_1/D of 0.06 dia./sec. Figure 3.26 shows the pipe in the sediment prior to a drag test and Fig. 3.27 shows the pipe after completion of the test. In all of these tests, the pipe underwent a total horizontal displacement of 16.5 in.

2. Pushed-Down Vertical Tests (1.5 in. O.D. Pipe).

These tests were performed with vertical movement only and no pipe rotation. The tests simulate a very practical field condition, but the results were also important in the development of the theory. Initial recess depths in the tests ranged from h/D of 0.0 (pipe just touching the sediment surface) to 1.0. Four different velocities, ranging from V_2/D of 0.00118 to 0.0133 dia./sec. were utilized. Figure 3.28 shows the changes in the sediment surface during a test.

3. Pushed-Down Angle Tests (1.5 in. O.D. Pipe).

These tests consisted of forcing the pipe into the sediment at two different ratios of horizontal to vertical velocity, namely 10:1 and 1:1. Equipment constraints limited the actual ratios, expressed as the angle of movement from the horizontal, λ, to 4.8° and 43.2°, respectively. Three initial recess depths were chosen for the 43.2° tests: h/D of 0.0, 0.25, and 1.0. For 4.8° angle tests, recess depths

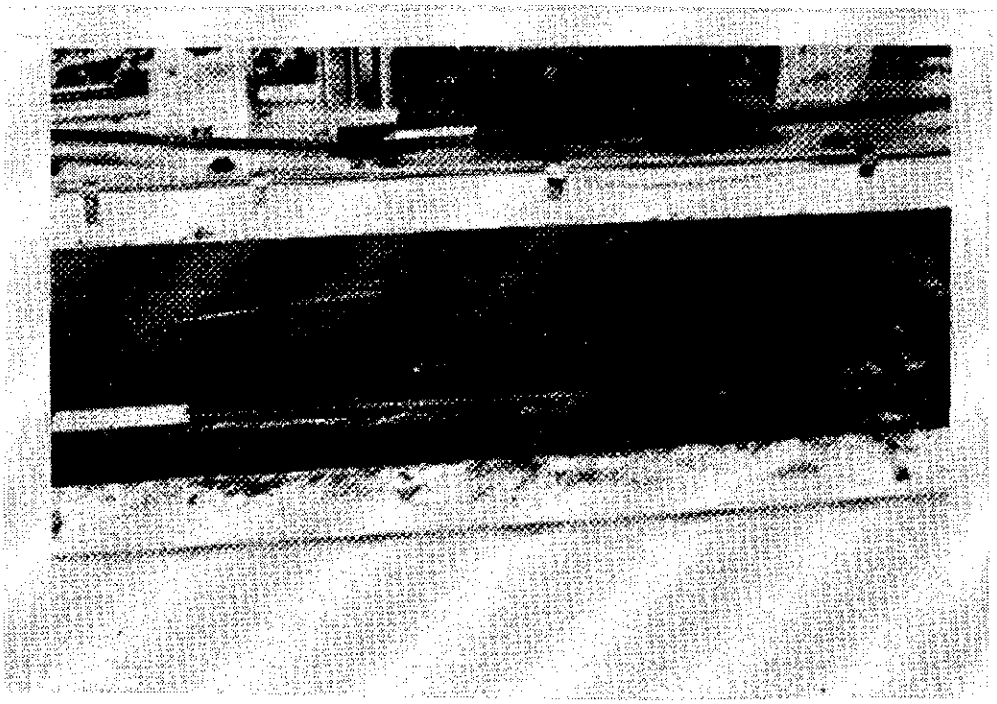

FIG. 3.26 - The Pipe in the Sediment Prior to a Fixed-Ends Horizontal Drag Test with h/D = 0.5

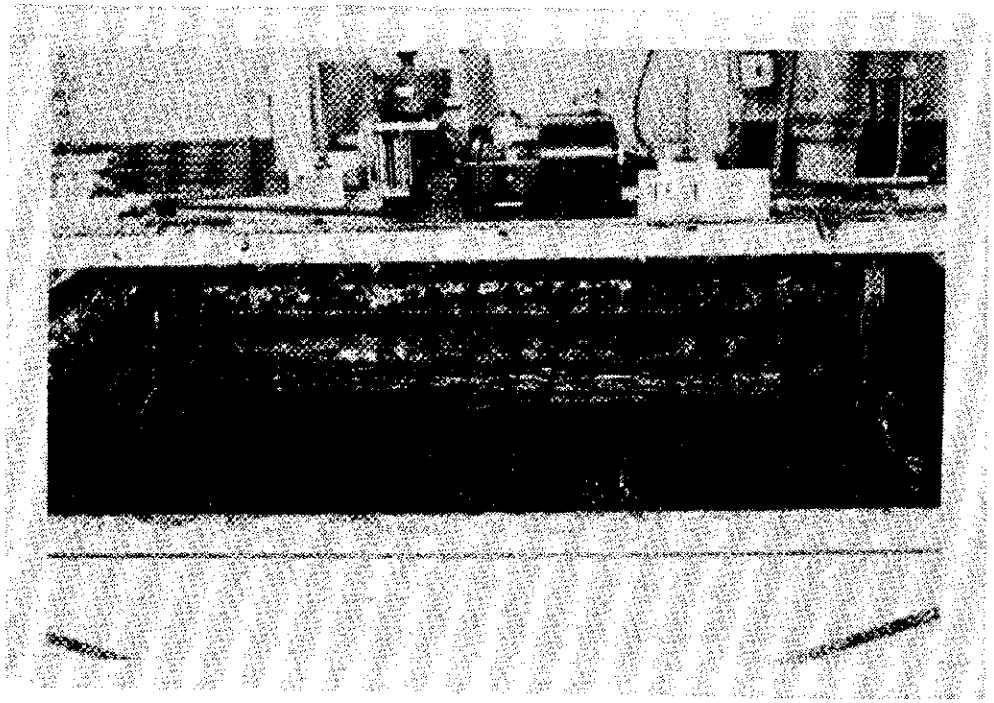

FIG. 3.27 - The Pipe Buried by the Sediment After the Completion of a Fixed-Ends Horizontal Drag Test with h/D = 0.5.

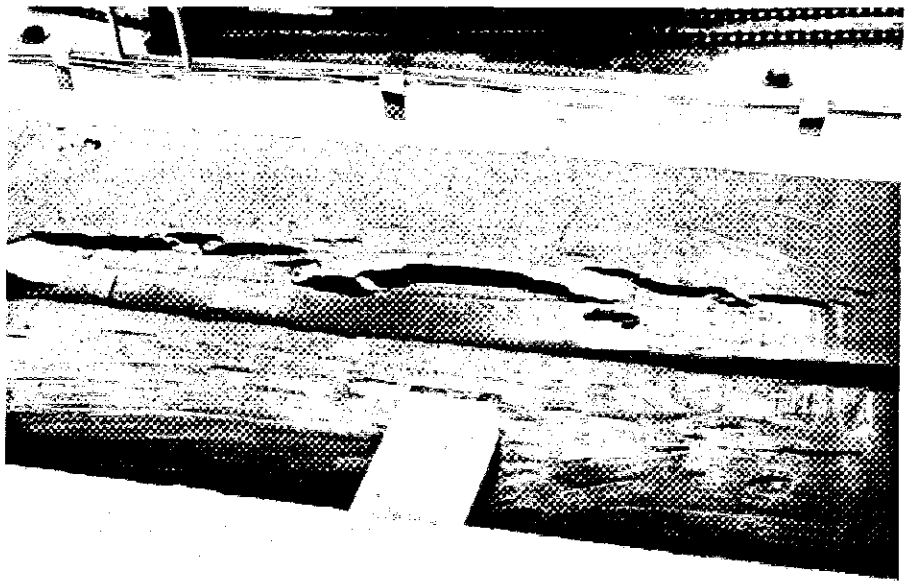

FIG. 3.28 - Changes in the Sediment Surface During a Pushed-Down Vertical Test Starting at h/D = 0.

ranged from h/D of 0.0 to 3.0. Figure 3.29 and Fig. 3.30 show a 4.8° and 43.2° angle test respectively.

4. Pulled-Up Angle Tests (1.5 in. O.D. Pipe).

These tests were basically the same as above except the pipe was pulled up to the surface of the sediment from the initial recess depths which ranged from h/D of 0.25 to 4.0. Figures 3.31 through 3.33 show a series of changes in the sediment surface during a 43.2° pulled-up angle test. Figure 3.34 shows sediment clinging to the pipe at the end of the test. This created a vertical (downward) force on the pipe even when it was clear of the sediment.

5. Freely-Rotated Horizontal Drag Tests (1.5 in. O.D. Pipe).

These tests were basically the same as the earlier horizontal drag tests except the pipe was allowed to rotate freely on two Teflon bearings installed at the ends of the pipe. Some friction existed in the bearings and the term "freely rotating" should not be taken to mean frictionless. Recess depths ranged from h/D of 0.25 to 4.0 and the pipe was pulled through the sediment horizontally with a velocity of 0.09 in./sec. This test simulated a possible field condition, and it provided important insight into sediment cracking patterns.

6. Fixed-Ends Horizontal Drag Tests (6.0 in. O.D. Pipe).

The 6 in. O.D. pipe with a 12 in. long instrumented or "active" section was mounted rigidly to prevent rotation. The horizontal pipe velocity was 0.09 in./sec., i.e., V_1/D = 0.015 dia./sec., and h/D values of 0.25 and 0.5 were used. Three replicate tests with h/D of 0.5 were performed to check the effectiveness and validity of this large scale model pipe. The main reason for performing these tests was to determine whether scale and buoyancy effects were important.

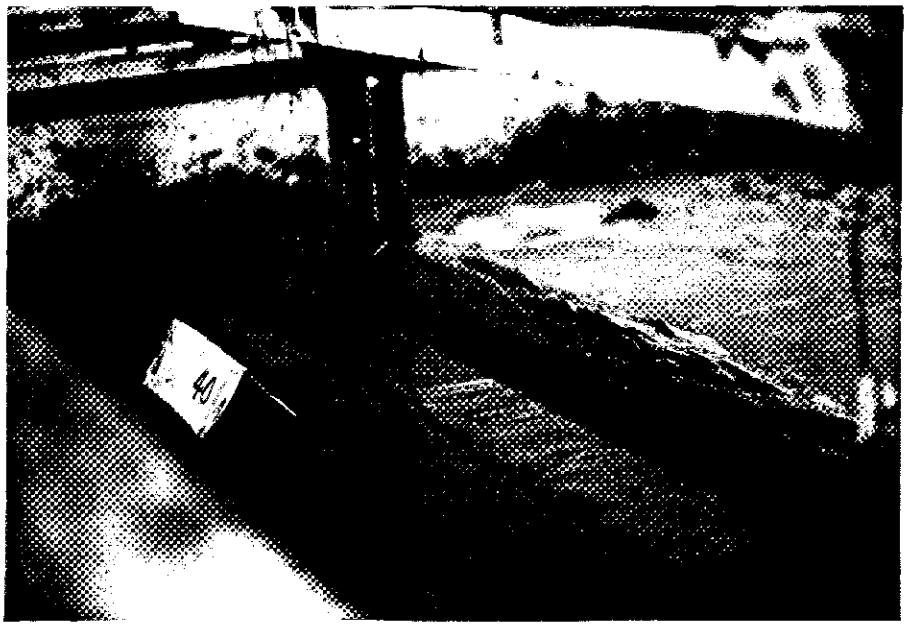

FIG. 3.29 - A 4.8° Pushed-Down Angle Test.

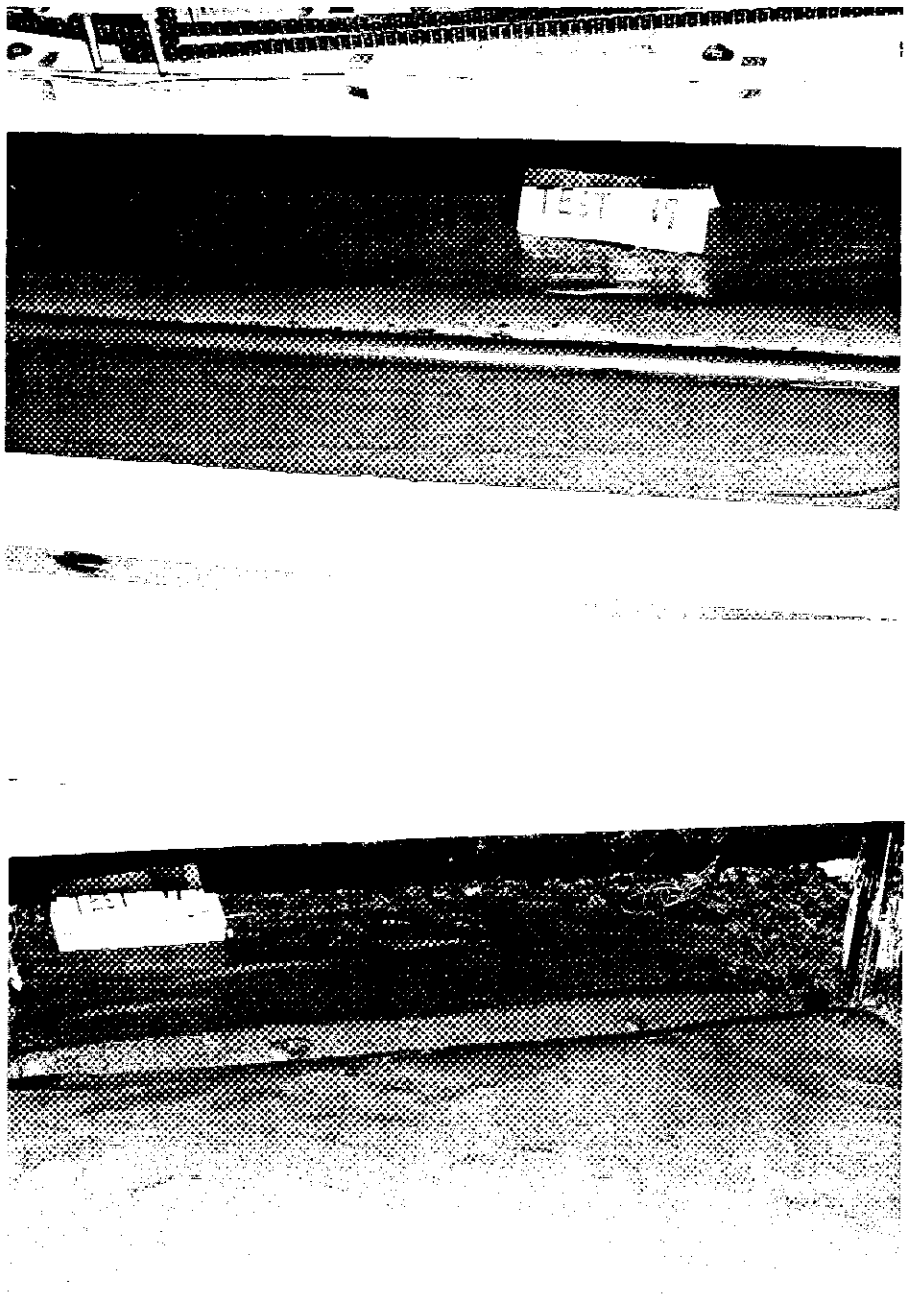

FIG. 3.30 - A 43.2° Pushed-Down Angle Test with Initial h/D = 0.

FIG. 3.31 - Initial Changes in Sediment Surface During a 43.2° Pulled-Up Angle Test with Initial h/D = 4.

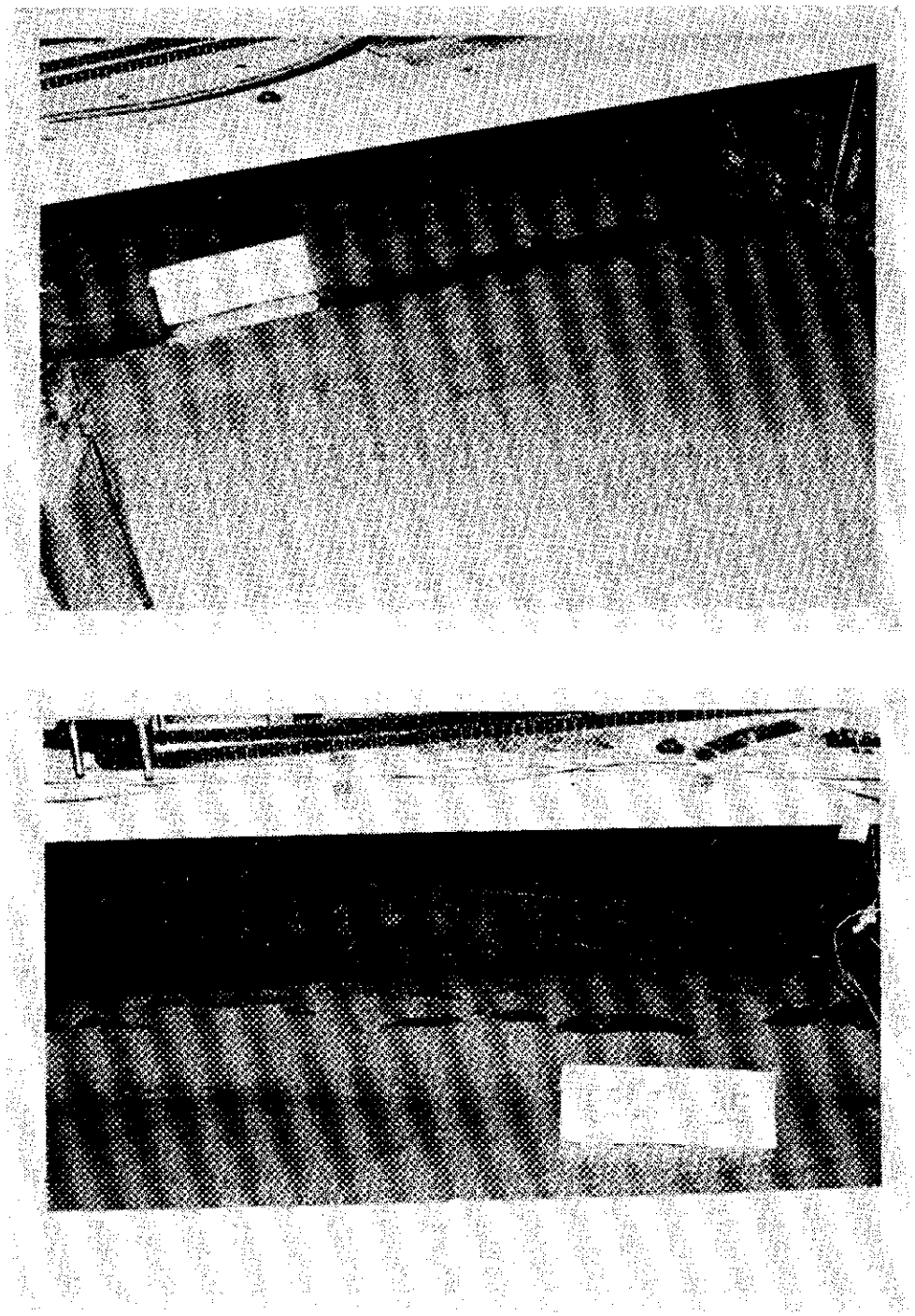

FIG. 3.32 - Continued Pipe Movement Caused Cracks to Propagate to the Sediment Surface During a 43.2° Pulled-Up Angle Test with Initial h/D = 4.

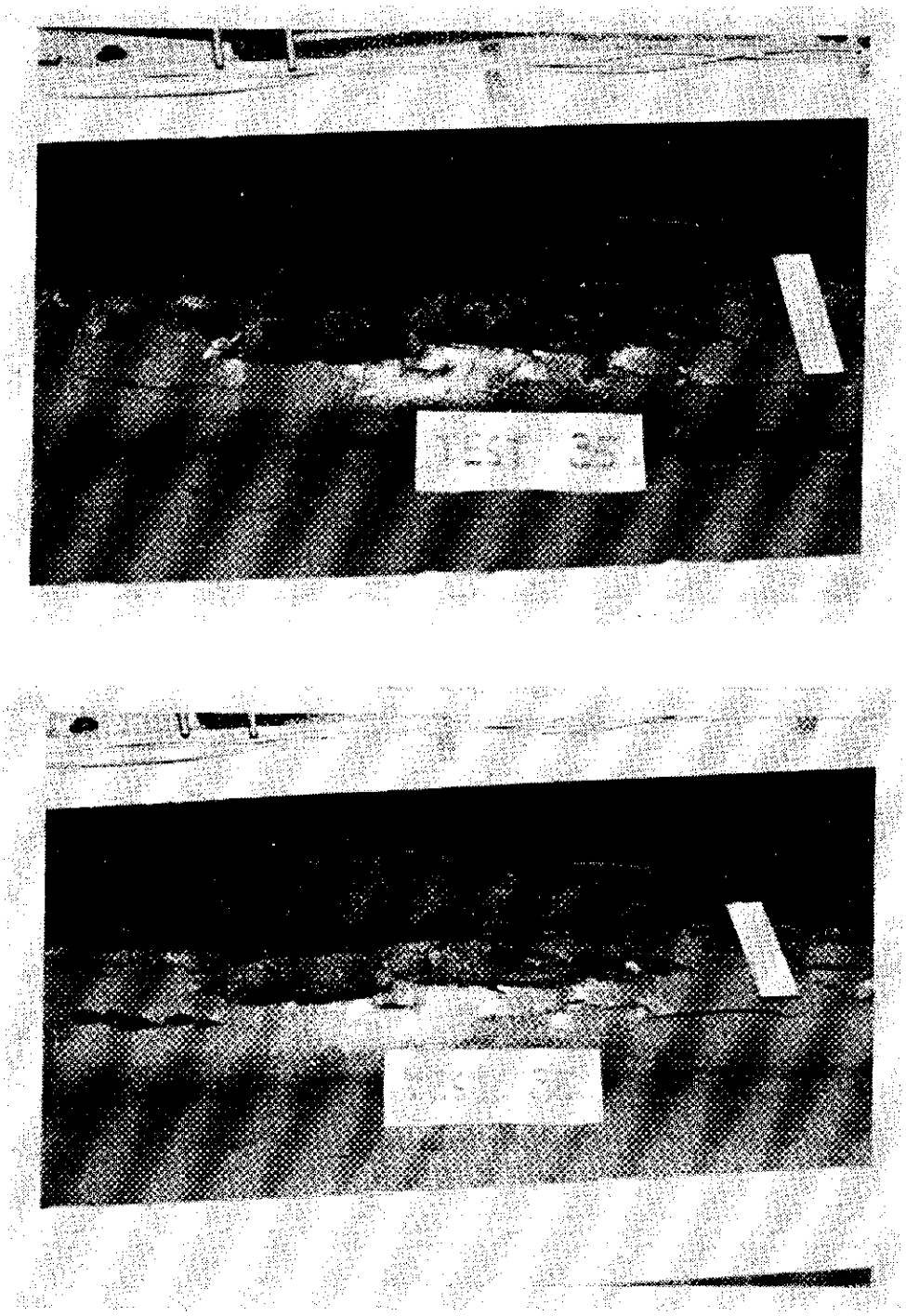

FIG. 3.33 - Cracks Opened Up During the Final Stages of a 43.2° Pulled-Up Angle Test with Initial h/D = 4.

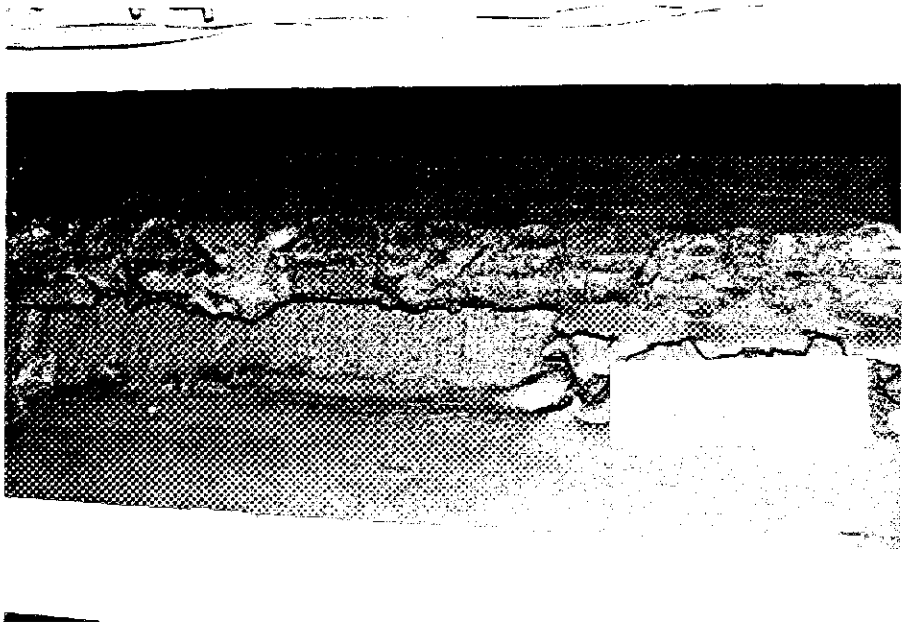

FIG. 3.34 - Sediment Clinging to the Pipe at the End of a 43.2° Pulled-Up Angle Test.

7. Fixed-Ends Layered Horizontal Drag Tests (6.0 in. O.D. Pipe).

These special tests were conducted on layered sediment where the surface material was weaker than the underlying sediment. This necessitated somewhat different sediment preparation techniques. The first two tests were conducted with h/D = 0.5 and with the upper 3 in. of sediment (i.e. to the bottom of the pipe) being composed of weaker sediment. The only difference in these two tests was in the strength of the top layer. In these tests, the top 3 in. of sediment was removed and the remaining sediment was mixed and repacked in the same way as described in the standard procedure. The removed sediment was mixed with distilled water until the desired undrained shear strength was obtained. At this point the pipe was set to the desired recess depth and the weaker sediment was placed over the underlying stronger sediment. Figures 3.35 through 3.37 show the sequence of preparation for this type of test.

A third test was performed with h/D = 1 and with the top 4.5 in. of sediment being weaker, i.e. the bottom 1.5 in. of pipe protruded into the stronger sediment. Figures 3.38 through 3.41 were taken at various stages of this drag test.

Table 3.1 is a summary of the tests performed in the large drag box, listed according to the type of test.

3.3.3 Test Procedure for Intermediate Drag Box

This drag box contained nearly 1/2 cubic yards of sediment, and although the problem of mixing and preparing the sediment for a test was not as difficult as for the large box, it was by no means an insignificant task. To obtain the desired shear strength, the contents of the box were removed and mixed with distilled water, or exposed to the atmosphere if drying were necessary. Uniformity of the sediment was obtained by mixing in small batches using a large motor-driven mixer.

FIG. 3.35 - Top 3 in. of Sediment After Being Removed by the Sediment Scraper During Preparation of a Layered Sediment Test.

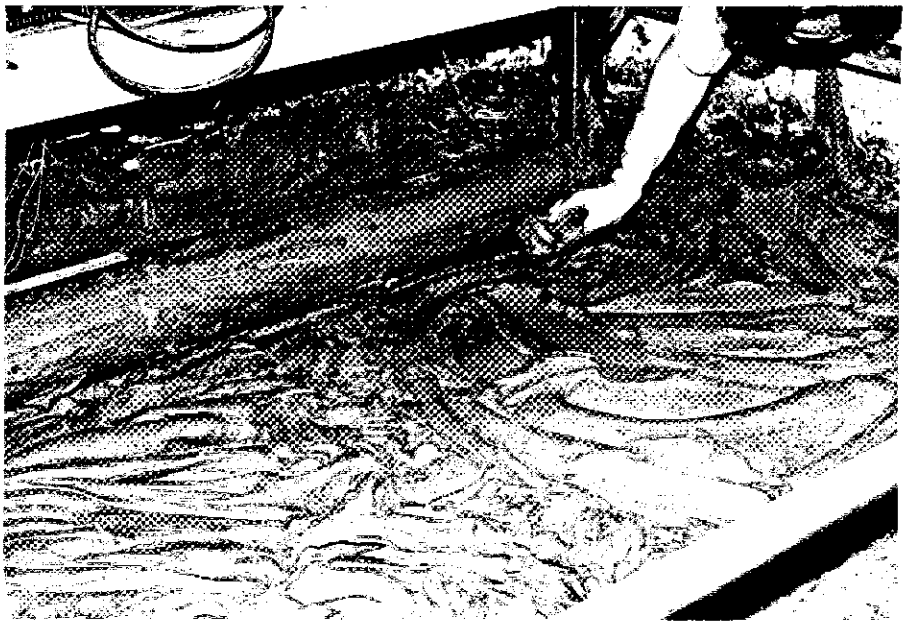

FIG. 3.36 - Packing the Weak Sediment by Hand Around the Pipe During Preparation of a Layered Sediment Test.

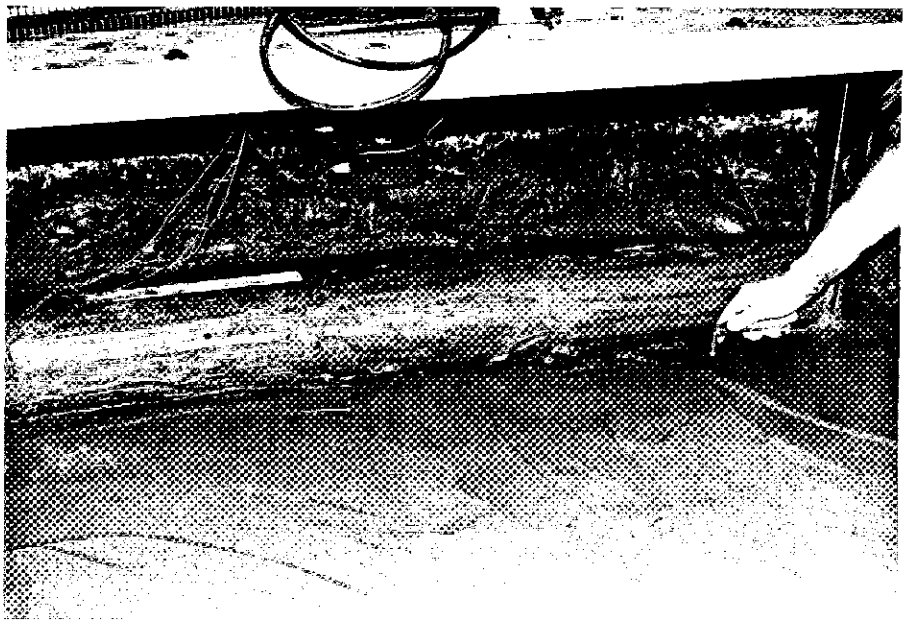

FIG. 3.37 - Leveling the Sediment Around the Pipe with a Trowel During Preparation of a Layered Sediment Test.

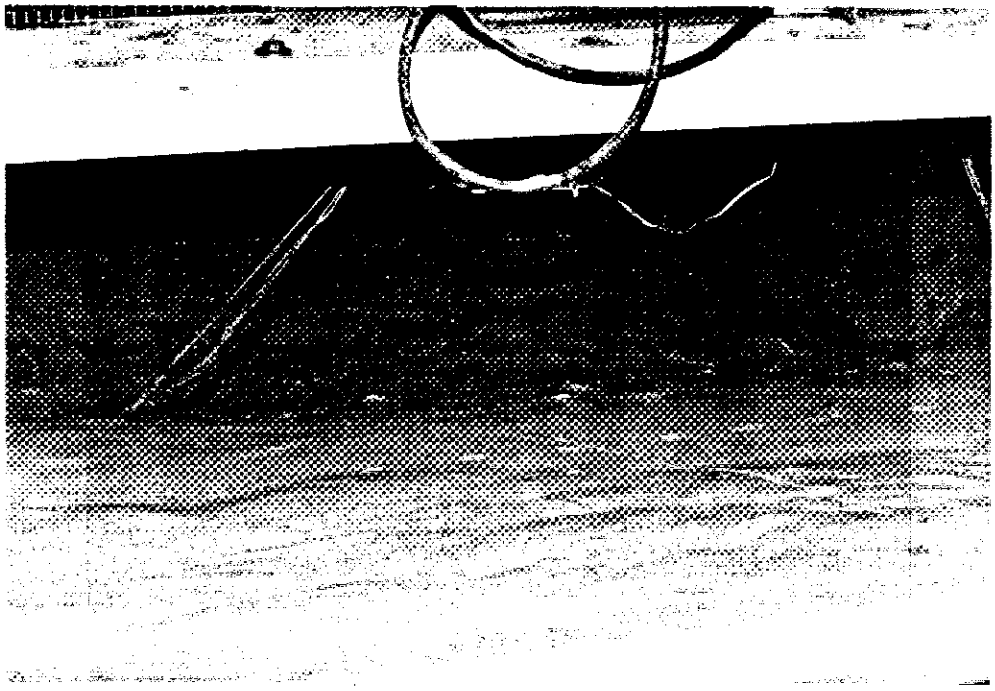

FIG. 3.38 - View of Sediment Rolling Over 6 in. Diameter Pipe During Layered Test with h/D = 1.

FIG. 3.39 - View of Cavity Left Behind 6 in. Diameter Pipe During Layered Test with h/D = 1. Right Side.

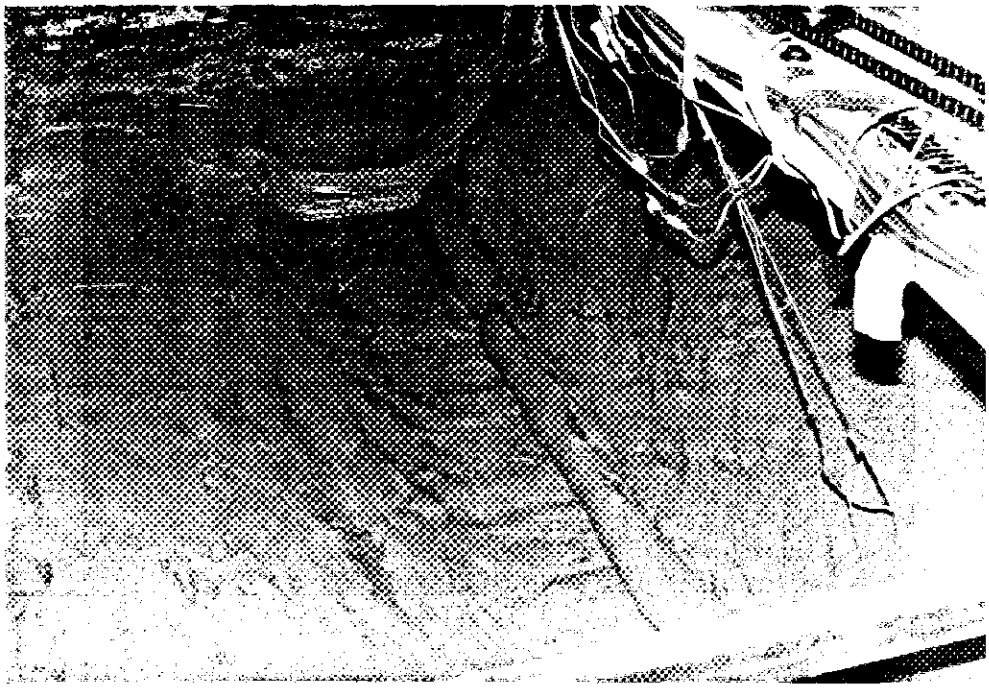

FIG. 3.40 - View of Cavity Left Behind 6 in. Diameter Pipe During Layered Test with h/D = 1. Left Side.

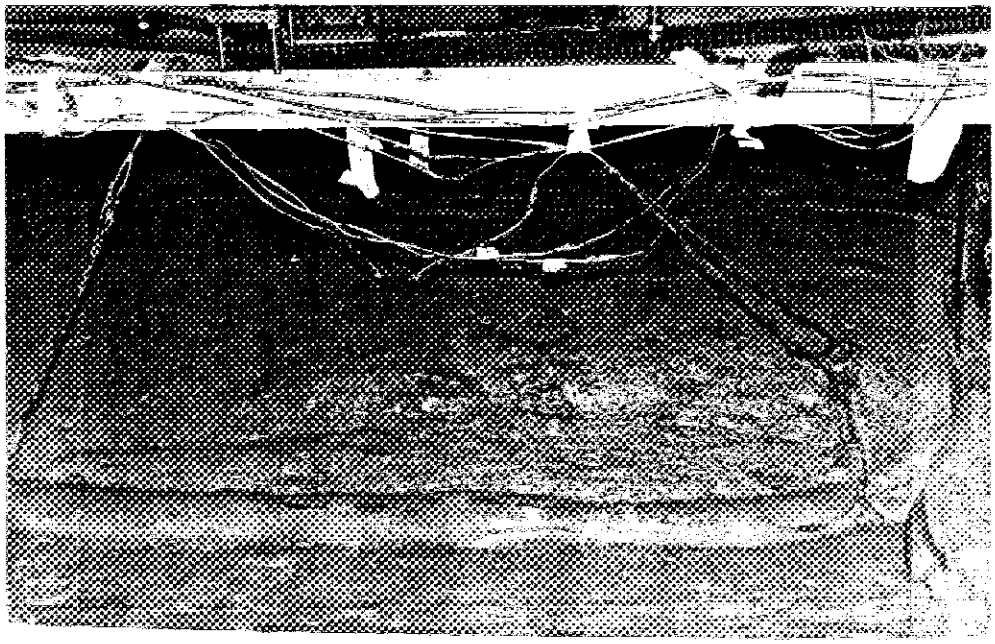

FIG. 3.41 - View from Behind 6 in. Diameter Pipe During Layered Test with h/D = 1.

TABLE 3.1 - Summary of Drag Tests Performed in Large Drag Box

TEST	RECESS DEPTH (h/D)	PIPE DIAMETER,D (in.)	PIPE LENGTH,L (in.)	VELOCITY, (V/D) (dia/sec)	LAMBDA (deg.)	TYPE OF TEST	UNDRAINED SHEAR STRENGTH (PSF)
RTEST 4	0.25	1.5	41.875	0.06	0	a	23.0
TEST 27	0.25	1.5	41.875	0.06	0	a	21.0
RTEST 2	0.5	1.5	41.875	0.06	0	a	22.95
TEST 21	0.5	1.5	41.875	0.06	0	a	24.4
RTEST 3	1.0	1.5	41.875	0.06	0	a	23.0
TEST 28	2.0	1.5	41.875	0.060	0	a	21.0
TEST 59	4.0	1.5	41.875	0.06	0	a	20.0
TEST 60	4.0	1.5	41.875	0.06	0	a	20.0
TEST 6	5.2	1.5	41.875	0.06	0	a	24.0
TEST 8	0.0	1.5	41.875	0.009	90	b	24.0

TABLE 3.1 - (Continued)

TEST	RECESS DEPTH (h/D)	PIPE DIAMETER,D (in.)	PIPE LENGTH,L (in.)	VELOCITY, (V/D) (dia/sec)	LAMBDA (deg.)	TYPE OF TEST	UNDRAINED SHEAR STRENGTH (PSF)
TEST 4	0.5	1.5	41.875	0.00118	90	b	23.0
TEST 3	1.0	1.5	41.875	0.0133	43.2	b	22.0
TEST 7	0.0	1.5	41.875	0.0133	43.2	c	24.0
TEST 18	0.0	1.5	41.875	0.0133	43.2	c	24.0
TEST 34	0.0	1.5	41.875	0.0133	43.2	c	21.0
TEST 37	0.0	1.5	41.875	0.0133	43.2	c	20.6
TEST 31	0.25	1.5	41.875	0.0133	43.2	c	20.8
TEST 39	0.0	1.5	41.875	0.06021	4.76	c	20.8
TEST 44	0.0	1.5	41.875	0.06021	4.76	c	19.5
TEST 36	0.25	1.5	41.875	0.06021	4.76	c	20.8
TEST 45	0.25	1.5	41.875	0.06021	4.76	c	19.5
TEST 40	0.5	1.5	41.875	0.06021	4.76	c	20.6
TEST 46	0.5	1.5	41.875	0.06021	4.76	c	19.5

TABLE 3.1 - (Continued)

TEST	RECESS DEPTH (h/D)	PIPE DIAMETER,D (in.)	PIPE LENGTH,L (in.)	VELOCITY, (V/D) (dia/sec)	LAMBDA (deg.)	TYPE OF TEST	UNDRAINED SHEAR STRENGTH (PSF)
TEST 38	1.0	1.5	41.875	0.06021	4.76	c	20.6
TEST 47	1.0	1.5	41.875	0.06021	4.76	c	19.5
TEST 50	1.0	1.5	41.875	0.06021	4.76	c	19.5
TEST 48	2.0	1.5	41.875	0.06021	4.76	c	19.5
TEST 49	3.0	1.5	41.875	0.06021	4.76	c	19.5
TEST 32	0.25	1.5	41.875	0.0133	43.17	d	20.8
TEST 30	0.5	1.5	41.875	0.0133	43.17	d	20.8
TEST 51	0.5	1.5	41.875	0.0133	43.17	d	20.8
TEST 29	1.0	1.5	41.875	0.0133	43.17	d	20.8
TEST 33	2.0	1.5	41.975	0.0133	43.17	d	20.8
TEST 35	4.0	1.5	41.875	0.0133	43.17	d	20.8
TEST 12	0.25	1.5	41.875	0.0582	4.92°	d	25.0
TEST 14	0.5	1.5	41.875	0.0582	4.92°	d	25.0
TEST 10	1.0	1.5	41.875	0.0130	22.5°	d	24.4

TABLE 3.1 - (Continued)

TEST	RECESS DEPTH (h/D)	PIPE DIAMETER,D (in.)	PIPE LENGTH,L (in.)	VELOCITY, (V/D) (dia/sec)	LAMBDA (deg.)	TYPE OF TEST	UNDRAINED SHEAR STRENGTH (PSF)
TEST 13	2.0	1.5	41.875	0.0582	4.92	d	25.0
TEST 15	4.0	1.5	41.875	0.0582	4.92	d	24.4
TEST 9	0.25	1.5	41.875	0.00118	90	d	23.0
TEST 9	0.5	1.5	41.875	0.009	90	d	23.0
RTEST10	0.5	1.5	41.875	0.00118	90	d	21.5
TEST 1 + TEST 2	1.0	1.5	41.875	0.00118	90	d	23.0
TEST 55	0.25	1.5	41.875	0.06	0	e	21.0
TEST 52	0.5	1.5	41.875	0.06	0	e	20.0
TEST 53	1.0	1.5	41.875	0.06	0	e	21.0
TEST 58	1.0	1.5	41.875	0.06	0	e	20.0
TEST 54	2.0	1.5	41.875	0.06	0	e	19.0
TEST 57	4.0	1.5	41.875	0.06	0	e	19.5
TEST 6	4.0	1.5	41.875	0.06	0	e	19.5
TEST 63	0.25	6.0	12*	0.015	0	e	20.0

TABLE 3.1 - (Continued)

TEST	RECESS DEPTH (h/D)	PIPE DIAMETER,D (in.)	PIPE LENGTH,L (in.)	VELOCITY, (V/D) (dia/sec)	LAMBDA (deg.)	TYPE OF TEST	UNDRAINED SHEAR STRENGTH (PSF)
TEST 64	0.5	6.0	12*	0.015	0	f	20
TEST 65	0.5	6.0	12*	0.015	0	f	20
TEST 66	0.5	6.0	12*	0.015	0	f	20
TEST 67	0.5	6.0	12*	0.015	0	g	xx
TEST 68	0.5	6.0	12*	0.015	0	h	xxx
TEST 69	1.0	6.0	12*	0.015	0	i	xxxx

Note: 1 in. = 25.4 mm, 1 psf = 0.048 kPa

*. Active Center Section

a. Fixed Ends Horizontal Drag Test (1.5 in. O.D. pipe)

b. Pushed Down Vertical Test

c. Pushed Down Angle Test

d. Pulled Up Angle Test

e. "Freely" Rotated Horizontal Drag Test

f. Fixed Ends Horizontal Drag Test (6.0 in. O.D. pipe)

g. Fixed Ends Horizontal Layered Drag Test xx (Top 3" Sediment - C_u = 12.9 psf
Beyond 3" Sediment - C_u = 20 psf)

h. Fixed Ends Horizontal Layered Drag Test xxx (Top 3" Sediment - C_u = 9.5 psf
Beyond 3" Sediment - C_u = 20 psf)

i. Fixed Ends Horizontal Layered Drag Test xxxx (Top 4.5" Sediment - C_u = 9.5 psf
with 1.5" of Pipe Diameter Intruded Into Beyond 4.5" Sediment - C_u = 20 psf)
Stiffer Layer

The small batches were combined in a larger container and the entire batch was mixed together to obtain uniformity. Fortunately, it was not necessary to perform this mixing process prior to every test since the sediment was totally enclosed in the rubber bag inside the shear box and moisture evaporation was slow. Instead, approximately one-third of the sediment - that portion within the zone of influence of the pipe - was removed and mixed prior to each test. The total amount of sediment in the bag was mixed every so often to maintain uniformity or when moisture changes were necessary to vary the shear strength.

The procedure utilized for preparation and performance of the drag tests is described below:

1. The pipe was adjusted to the proper orientation angle and the closed-loop servo-controlled testing machine was set for the desired loading rate and displacement. At the same time, all data acquisition equipment was adjusted, calibration checks were made and initial readings were obtained.

2. The drag box was filled by throwing small quantities of the previously mixed sediment into the box with sufficient force to remove entrapped air. This was done to insure that the mixture would be saturated when the confining pressure was applied. For deeply buried pipe, the sediment was placed in this manner until the rubber bag was completely filled. Since the pipe in this box could not be adjusted in the vertical direction, it was necessary in the tests on shallow or partially buried pipes to bring the sediment to the desired level where it was then smoothed by hand with a trowel. Measurements were made from the top of the box to control the elevation of the sediment, thereby insuring that the proper recess depth of the pipe was obtained.

3. The pressure-tight cover was then bolted to the top of the rubber bag, the sliding top of the shear box was positioned and the confining pressure was applied to the sediment.

4. After the desired rest period, which was 21 hrs. in most cases but 2 hrs. in some tests, the test was started by simultaneously triggering the controls to the closed-loop servo-controlled testing machine and the data acquisition equipment.

5. When the test was completed, the box was disassembled and several shear strength measurements were made in the sediment away from the area disturbed by the pipe using the hand-held vane shear device described earlier. Moisture content determinations were also made.

3.3.3.1 Tests Conducted in the Intermediate Drag Box: The different types of tests conducted in the box are discussed below:

1. Rate Effects on Drag Factors.

The normalized drag factors, by use of the term $(V/D)^n$, should take into account the effects of varying pipe or sediment velocity, i.e. the drag factor should be constant regardless of velocity. A comprehensive series of tests were conducted in the intermediate drag box to determine whether this premise was correct.

In the first series of tests, the pipe was oriented normal to the direction of flow with h/D of 9 and with six different pipe velocities, ranging from fast to extremely slow. A subsequent series of tests were performed at two burial depths ($h/D = 0.25$ and 2), at two pipe speeds (V/D = 0.08 and 0.0008 dia/sec), but at various pipe orientation angles, α, ranging from 0° to 90°. In all cases, the sediment rest time was 21 hrs. prior to performing the test.

2. Pipe Angle Tests.

In the Phase I testing program, some tests were performed to

determine the normal and axial drag forces on pipes oriented at various angles, α, to the direction of movement. There were insufficient tests and the instrumentation lacked enough resolution, to totally define the angle effect at various recess depths. Thus, a detailed series of tests were performed in the intermediate drag box with the flow angle, α, ranging from 0° to 90° at angular increments of 10° and also at 45°. Pipe burial depths, h/D, of 0.25, 0.50, 1, 2 and 9 (considered infinitely deep) were used. The sediment was pressurized to 21 psi, undrained shear strength of the sediment was approximately 55 psf, and the tests were conducted at a fast rate of speed (V/D = 0.08 dia/sec).

3. Effects of Pressure on Drag Characteristics.

It is well-known that when soils are sheared under conditions of no drainage, their shear strength will remain constant regardless of the magnitude of the outside pressure. It is this premise which allowed drag testing to be performed at atmospheric pressure rather than actual total pressures that might be expected at the ocean bottom. However, other aspects of sediment behavior are not so clearly defined under conditions of pressure versus nonpressure. A submerged pipe moving in sediment may leave a trailing void under conditions of no pressure, but the application of total pressure could cause a collapse of the void and change the drag force on the pipe accordingly, even though the strength remained constant for both cases. The observation of significant crack patterns both in the sediment and around the pipe during early stages of testing led to the conclusion that the effect of pressure on the drag forces must be experimentally examined.

Pressure effects were studied in the intermediate box and the small box although the majority of the testing was performed in the former. A

large number of tests were performed with the pipe oriented normal to the direction of movement ($\alpha = 90°$) and at recess depths, h/D, ranging from 0.25 to 9. Undrained shear strength was nominally 20 psf and pressures of 0 and 30 psi were used. Two pipe velocities, V/D of 0.08 and 0.0008 dia/sec, were studied. The effect of pipe velocity on the sediment cracking pattern and drag forces had been observed in previous tests and velocity variations were considered important in this test series.

4. End Effects Study.

It was not known whether the ends of the finite length of model pipe used in the tests had an effect on the test results. The dimensions of the box limited the length of pipe which could be used, and for the 0.75 in. diameter pipe, a length of 12 in. was used. This produced a length: diameter ratio of 16. One approach to determining the effects of the pipe ends was to perform tests with other model pipes which were also 12 in. long, but which had different diameters and therefore different length: diameter ratios. If the ends had no effect, then the force coefficients for all pipes should be the same for the same flow angles. Two new pipes were fabricated for this study with diameters of 3/8 in. and 1-1/2 in. which resulted in length: diameter ratios of 32 and 8, respectively.

Tests were conducted on these pipes at a pipe velocity of 0.08 dia/sec in sediment having a shear strength of 55 psf, and at a total pressure of 21 psi. The pipes were tested over a range of flow angles from 20° to 70°, and the pipes were deeply buried.

3.3.4 Test Procedure for Small Drag Box

Compared to the other drag boxes, the small drag box contained a small amount of sediment, about 1.5 cubic ft., and the sediment

preparation technique was relatively simple. The data acquisition and loading equipment were the same as used in the intermediate drag box, thus only a brief description of the procedure is given below:

1. All of the sediment was removed from the sediment container and mixed to achieve uniformity. The moisture content was adjusted to obtain the desired undrained shear strength either by adding distilled water or allowing moisture evaporation.

2. The pipe was installed in the drag box, oriented in the desired direction, and the pipe supports were adjusted to achieve the desired pipe recess depth. This was easily accomplished by measuring to the top of the pipe from a straight edge placed across the top of the sediment container.

3. The sediment container was filled by throwing the sediment into the container in the manner used for the intermediate drag box. The sediment around the pipe was carefully placed by hand, then the entire sediment surface was screeded flush with the top of the sediment container.

4. The cover was bolted to the top of the box and the confining pressure was applied to the box.

5. After the desired rest period, which ranged from 2 to 21 hrs. depending on the type of test, the test was started by triggering the test machine and data acquisition equipment.

6. Upon completion of the test, the top of the box was removed and shear strength/moisture content determinations were made in the sediment.

It was observed in the early tests that the sediment surface was drying slightly during the tests with long resting times, probably a

result of the large amount of dry air supplied to the box to pressurize the pipe-sediment system. This problem was remedied by humidifying the air as it entered the box.

3.3.4.1 Tests Conducted in the Small Drag Box

1. Pipe Angle Tests.

These tests were similar to those conducted in the intermediate drag box, and they were performed primarily to verify the relationship between the flow angle and the normal and axial force coefficients. Only three angles, 0°, 45° and 90° were tested. The tests were conducted under total confining pressures of 30 psi and after rest times of 2 hrs., rather than 21 hrs. as in the intermediate drag box. Also, the pipes were allowed to freely rotate whereas they were fixed in the intermediate drag box.

These tests also served to illustrate some important effects of pipe-sediment behavior. Fig. 3.42 illustrates the sediment rolling up behind the pipe owing to the pipe being able to freely rotate, whereas a similar test with the pipe clamped against rotation (Fig. 3.43) shows a different pattern of sediment behavior behind the pipe.

Figs. 3.44 and 3.45 are views of two similar tests with $h/D = 1$ after 21 hrs. rest time. Both tests show distinct separation at the pipe-sediment interface, but the weaker sediment (Fig. 3.44) exhibits more cracking behind the pipe. Tests with $h/D = 0.50$ are shown in Figs. 3.46 and 3.47. Different rest times were utilized. After 21 hrs. rest time a sharp distinct separation occurred at the pipe-sediment interface, whereas after 2 hrs. of rest time a more gradual separation was observed.

2. Effects of Shear Strength/Pressure Combinations.

The purpose of these tests was to determine whether two different

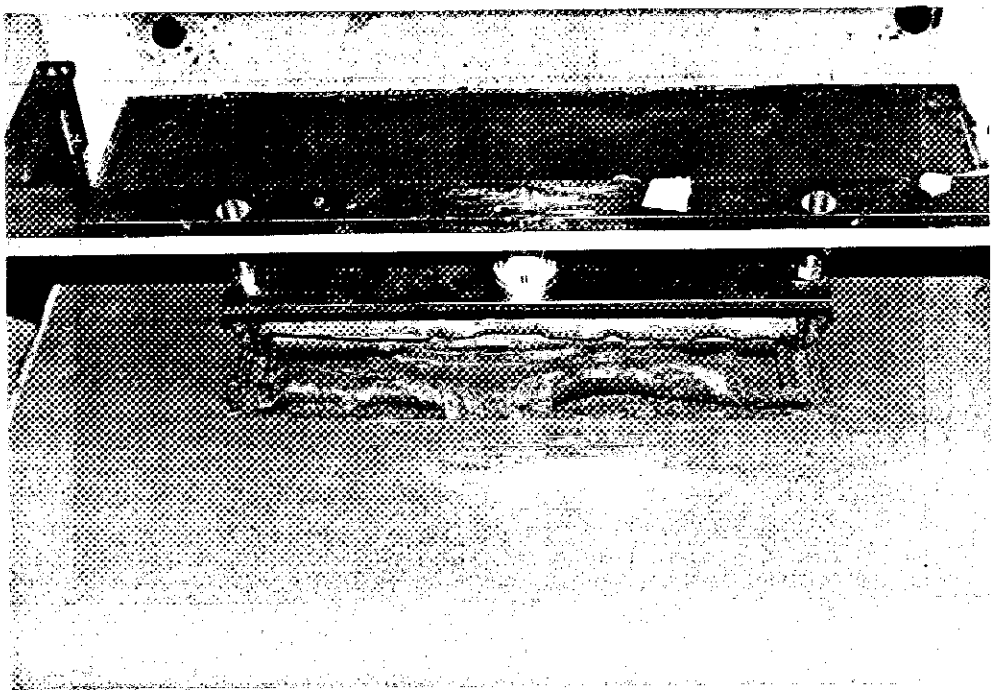

FIG. 3.42 - Sediment Rolling Up Behind a Freely Rotating Pipe

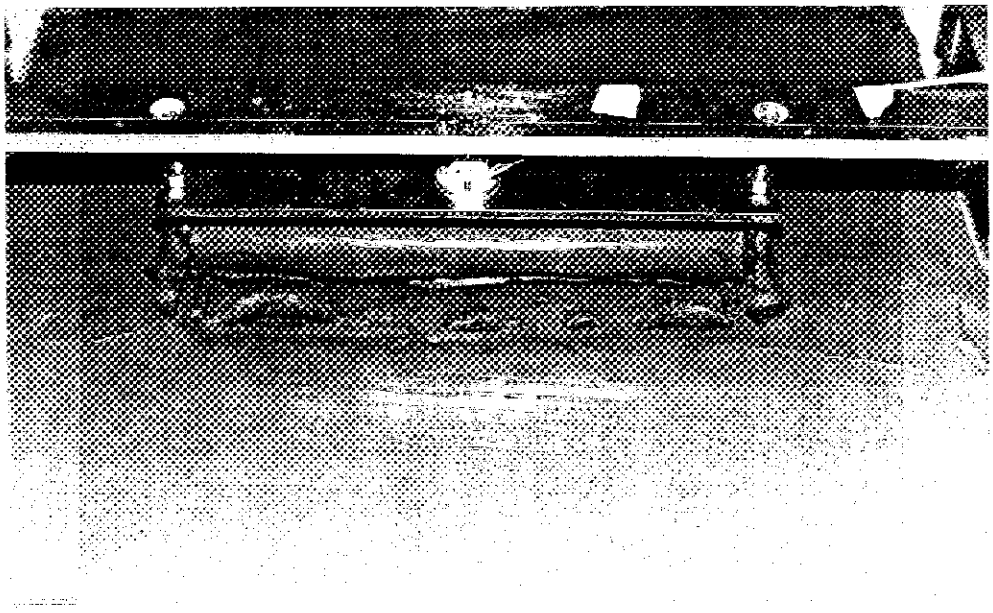

FIG. 3.43 - Test Similar to that Shown in Fig. 3.42 but with Nonrotating Pipe.

FIG. 3.44 - Test with Clamped Pipe and 20 psf Sediment after 21 hrs Rest Time for h/D = 1.

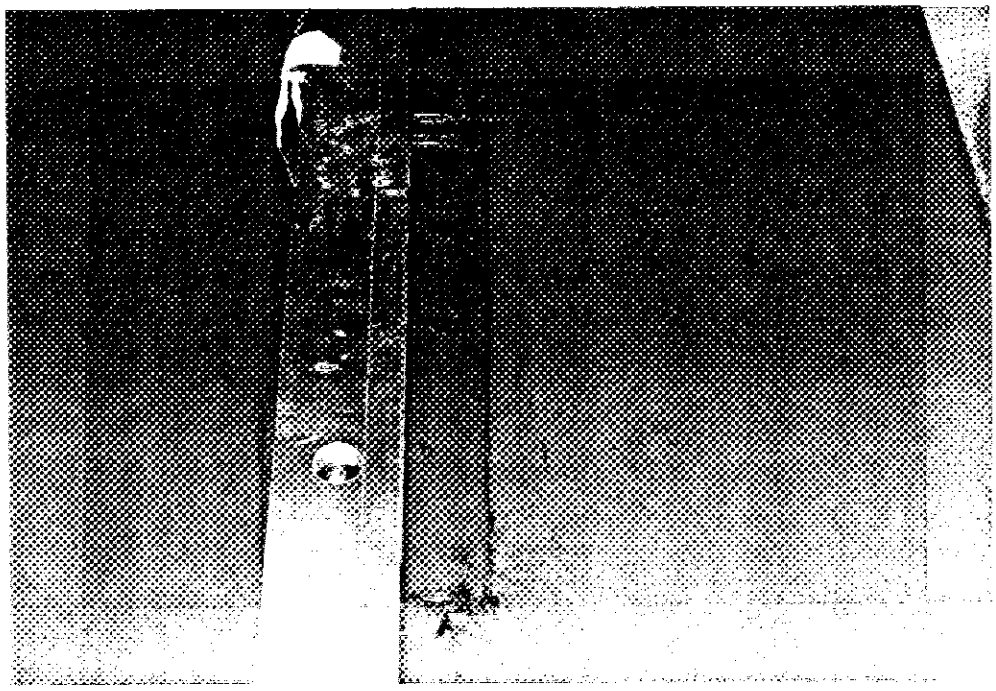

FIG. 3.45 - Test with Clamped Pipe and 42.5 psf Sediment after 21 hrs Rest Time for h/D = 1.

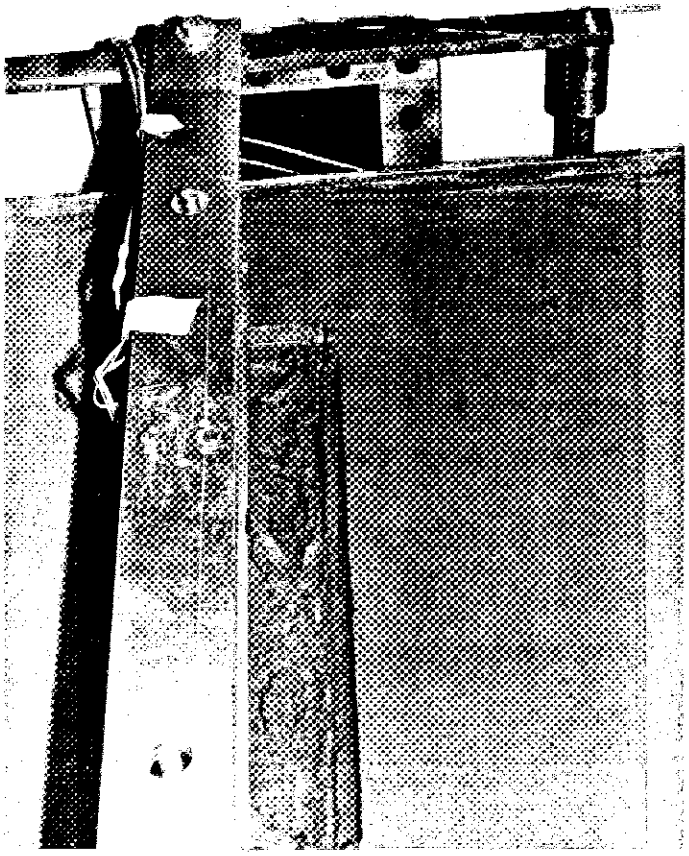

FIG. 3.46 - Test with Clamped Pipe and 20 psf Sediment after 21 hrs Rest Time for h/D = 0.50.

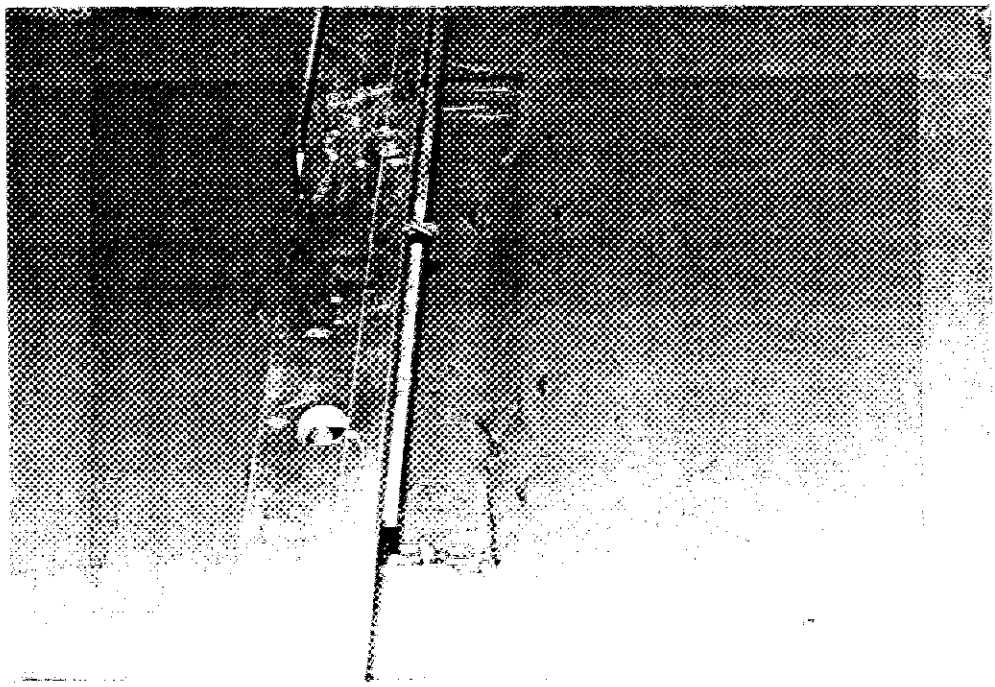

FIG. 3.47 - Test with Clamped Pipe and 20 psf Sediment after 2 hrs Rest Time for h/D = 0.50.

shear strengths of sediment - 20 and 42.5 psf - would produce different force coefficients or different shapes of force versus displacement curves under conditions of constant confining pressure. The pressure used was 21 psi, the flow angle was 90°, and pipes were tested at recess depths of h/D = 0.25, 0.50, 1 and 2.

3. Effect of Pipe Surface Roughness.

Full-size pipelines may range in surface roughness from relatively smooth to rough. Furthermore, the surface texture may change with time owing to chemical or biological attack. It would be impractical - perhaps impossible - to attempt to model surface roughness in laboratory experiments on drag forces. However, since this is an effect which may have a bearing on the drag factors, a brief study of surface roughness was made in the small drag box using 3/4 in. diameter by 12 in. long pipes. Three different roughnesses were used:

a. Smooth pipe. This pipe was turned to the proper diameter in a lathe and the surface was then polished. The drag tests were performed over a short time period, and there was no rust or other visible change of the pipe surface during the test period.

b. Standard pipe. The pipe used for the majority of tests performed was termed the standard pipe. It was fabricated from mill finished rod, free from scale, with no surface finishing. The surface stayed essentially the same throughout the test series.

c. Rough pipe. To produce this pipe, a sheet of wet-or-dry sandpaper was glued to the pipe surface. The sandpaper, manufactured by 3M Company, was listed as 80 grit paper.

A quantitative measure of the surface roughness of the pipes was obtained by comparing the surface finish with a GAR visual surface

roughness comparator. The surface roughness, expressed as the arithmetic average (AA) in microinches is given below.

Smooth Pipe - AA = 32

Standard Pipe - AA = 200

Rough Pipe - AA = 500

Tests were performed at two recess depths, $h/D = 0.50$ and 1 with the pipe free to rotate and without pressure. A few tests were performed at $h/D = 0.50$ with the pipe clamped to prevent rotation. All tests were performed after a 2 hr. resting period and at a flow angle of 90°.

Fig. 3.49 is a view of a test performed on the rough pipe in the clamped mode. This showed a very smooth separation behind the pipe with no cracking of the sediment.

4. Miscellaneous Tests.

Several miscellaneous tests were performed to aid in development of theory or check previous observations. Some tests were performed in which the elevation of the sediment mound over the pipe was measured as the sediment was moved past the pipe. Obviously, these tests were conducted at atmospheric pressure.

Other tests, also at atmospheric pressure, were performed on freely floating pipes buried at various depths to determine the vertical movement of the pipes as the sediment flowed past the pipes.

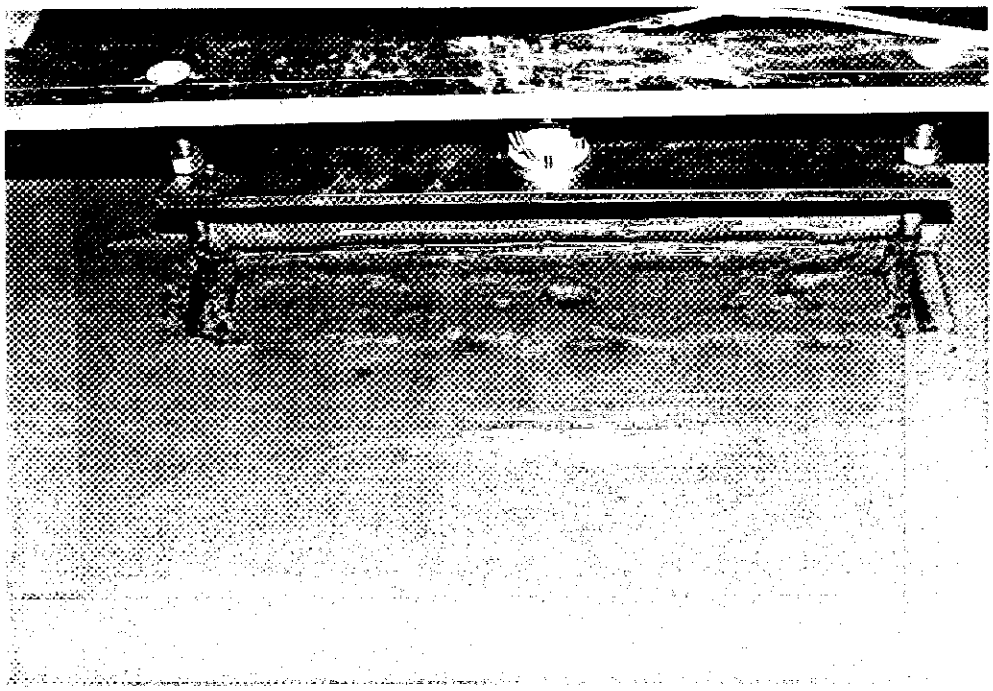

FIG. 3.48 - Test with Clamped Pipe and 42.5 psf Sediment after 2 hrs Rest Time for h/D = 0.50

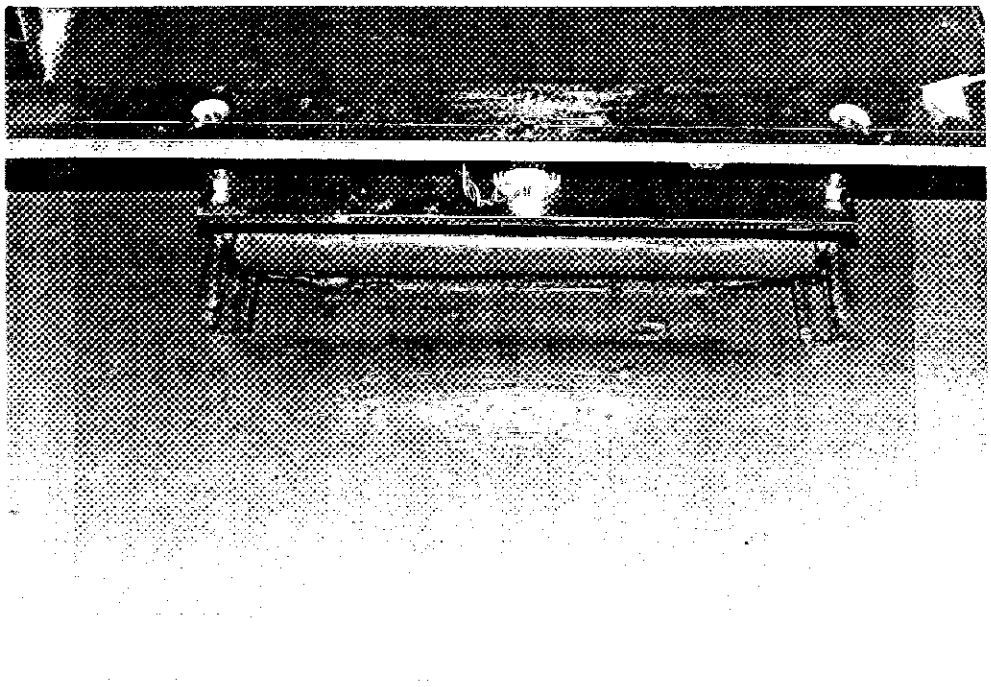

FIG. 3.49 - Test with Rough Pipe Surface after 2 hrs Rest Time

3.4 Test Results

Many different types of tests were performed for this research and some types of tests were performed in more than one type of drag box. Although there may be some advantage in reporting similar types of tests together, it is believed that it might be less confusing to the reader if the results are grouped according to the type of drag box used. This approach is followed below by reporting results of the large box first, followed by results from the intermediate drag box and then the small drag box.

Many of the curves to be presented will have experimental data plotted as points, and theoretical results plotted as lines. The theoretical results and comparison between theory and experiment will be discussed in Section 5, but to eliminate the duplication of experimental results in Section 5, the theory curves are shown in this section. See the first page of Section 5 for a key to the different theories plotted on the experimental results. Note also that the same results are often presented on both arithmetic and log-log scales.

3.4.1 Test Results in Large Drag Box

As mentioned earlier in the report the pipe in the large drag box was equipped with transducers at each end. Under ideal conditions, each transducer should record half of the total load and torque applied to the pipe. This design has the advantage of detecting electronic and mechanical problems in the transducers by comparing the load-displacement or torque-displacement curves for each transducer. Data obtained from this study confirm that some malfunctions did occur. In these few circumstances close examination of the data from each channel usually allowed the selection of a good working channel, and the total force was obtained by multiplying the results from this channel by two.

Results from duplicated tests were also used for comparison.

All tests showed some initial horizontal and vertical force on the pipe even though all six recording channels were adjusted to zero prior to placing the pipe in the sediment. The initial horizontal loads were small and random in direction; they were probably the result of slight variations of technique when packing the sediment around the pipe, and they should not influence the horizontal force-displacement curves. For this reason, no adjustments were made to these curves, nor was any compensation made in the calculation of the horizontal force coefficients due to the initial forces. Initial vertical forces, on the other hand, present a more complicated situation. It was expected that an initial buoyant (positive) force would occur on the pipes, and this was found to be the case for partially buried pipes. But for pipes with h/D greater than one, the initial force (that force which was measured just before movement was initiated) was negative, i.e. the overlying sediment actually pushed the pipe downward. Figure 3.50 compares the measured vertical forces with several calculated forces. One set of forces was obtained by assuming that the weight of the vertical column of sediment directly above the pipe pushed down on the pipe. Another approach is shown in which the calculated buoyant force, which remains constant for h/D greater than one, is subtracted from the vertical force. The measured data show closer comparison to this latter force, labeled Combined Buoyant and Vertical Mud Force.

Calculation of the various force coefficients, termed g_1, g_2 and g_3, was based on Eq. (4.116), presented below for convenience (i refers to direction in Fig. 4.6):

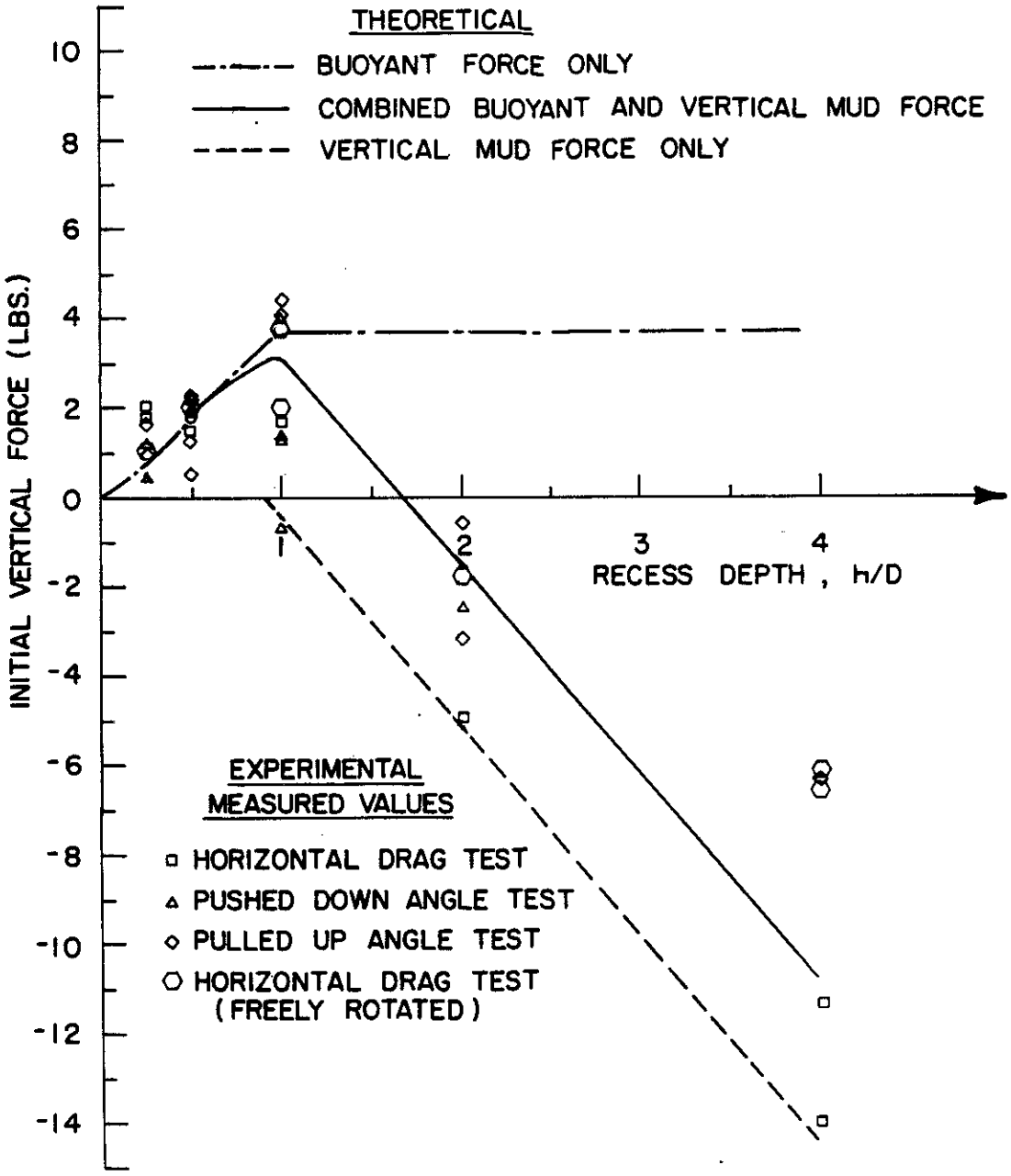

FIG. 3.50 - Comparison of Theoretical and Measured Initial Vertical Forces

$$g_i = \frac{F_i}{LDC_{uo}(V_R/D)^n} \qquad (i = 1,2,3)$$

In tests where the pipe did not move vertically, such as horizontal drag tests, the horizontal V/D was used in the calculation of the vertical force coefficient. When the pipe was pulled through the sediment at an angle, the resultant velocity, V_R/D, was used for calculating both horizontal and vertical force coefficients.

The values of undrained shear strength, C_{uo}, which varied from test to test, the values of V_R/D, and other information pertinent to the tests, were shown in Table 3.1. The strain rate exponent, n, was found to be 0.12 for the low sediment strengths utilized in the large box.

It was mentioned earlier in this report that several different types of tests were conducted during the entire program. Below, each type of test will be examined and discussed separately.

1. Fixed-End Horizontal Drag Tests (1.5 in. O.D. Pipe).

Nine tests with h/D ranging from 0.25 to 5.2 were performed with horizontal motion only. Tests with h/D of 0.25, 0.5 and 4.0 were replicated to determine the reproducibility of the results. Results of two tests with h/D of 0.25 are compared in Figs. 3.51 through 3.53. These results show good agreement between replicate tests with respect to peak or initial values, but the curves were not always reproducible at large displacements.

The horizontal drag force for these tests often exhibited an initial peak at small displacements followed by a decrease in force (see Test 27, Fig. 3.51). This was associated with initial separation of the sediment at the pipe-soil interface or with cracking of the sediment at the trailing edge of the pipe. As the pipe continued to move forward,

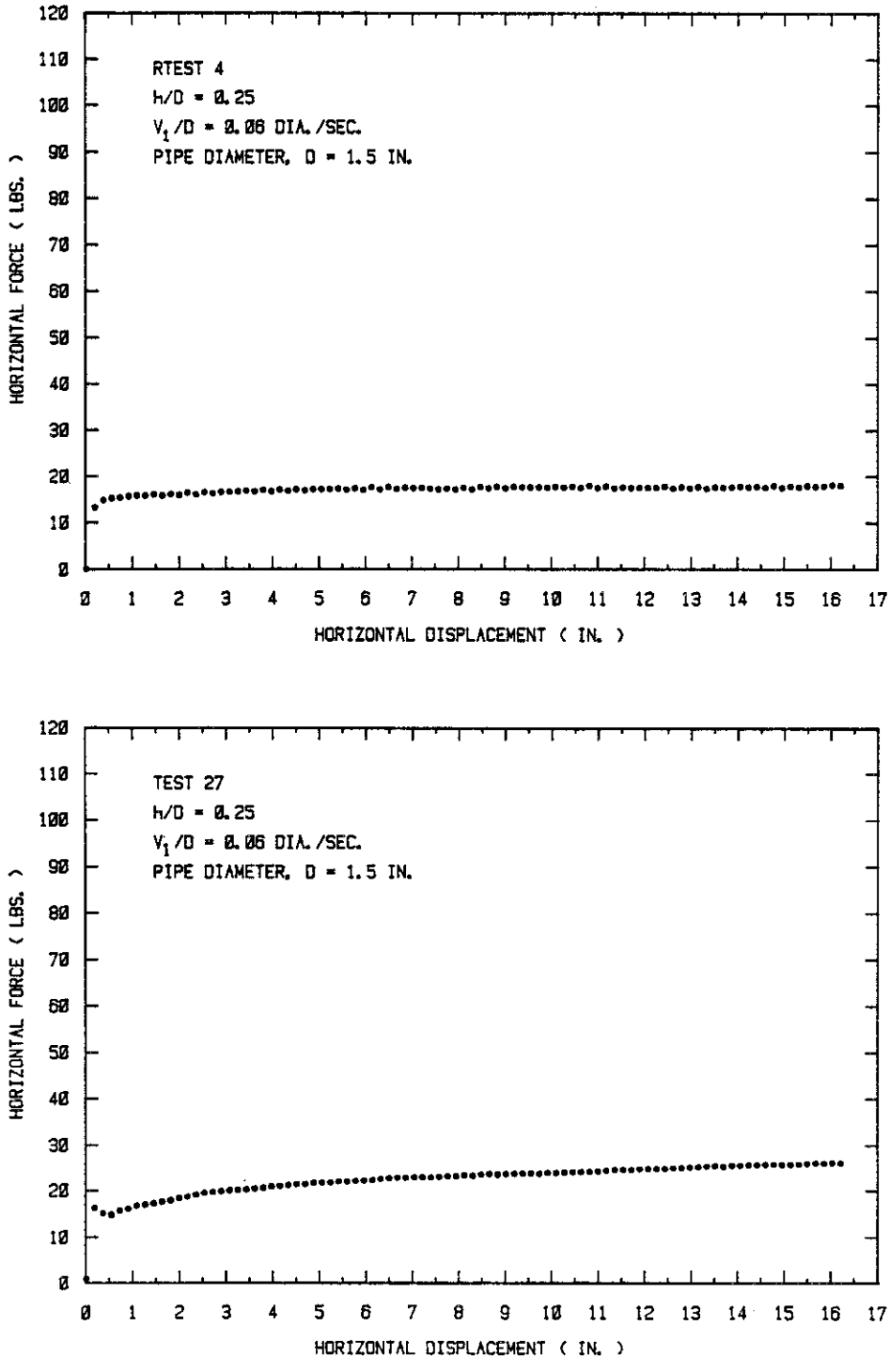

FIG. 3.51. - Comparison of Horizontal Drag Forces for Replicate Tests

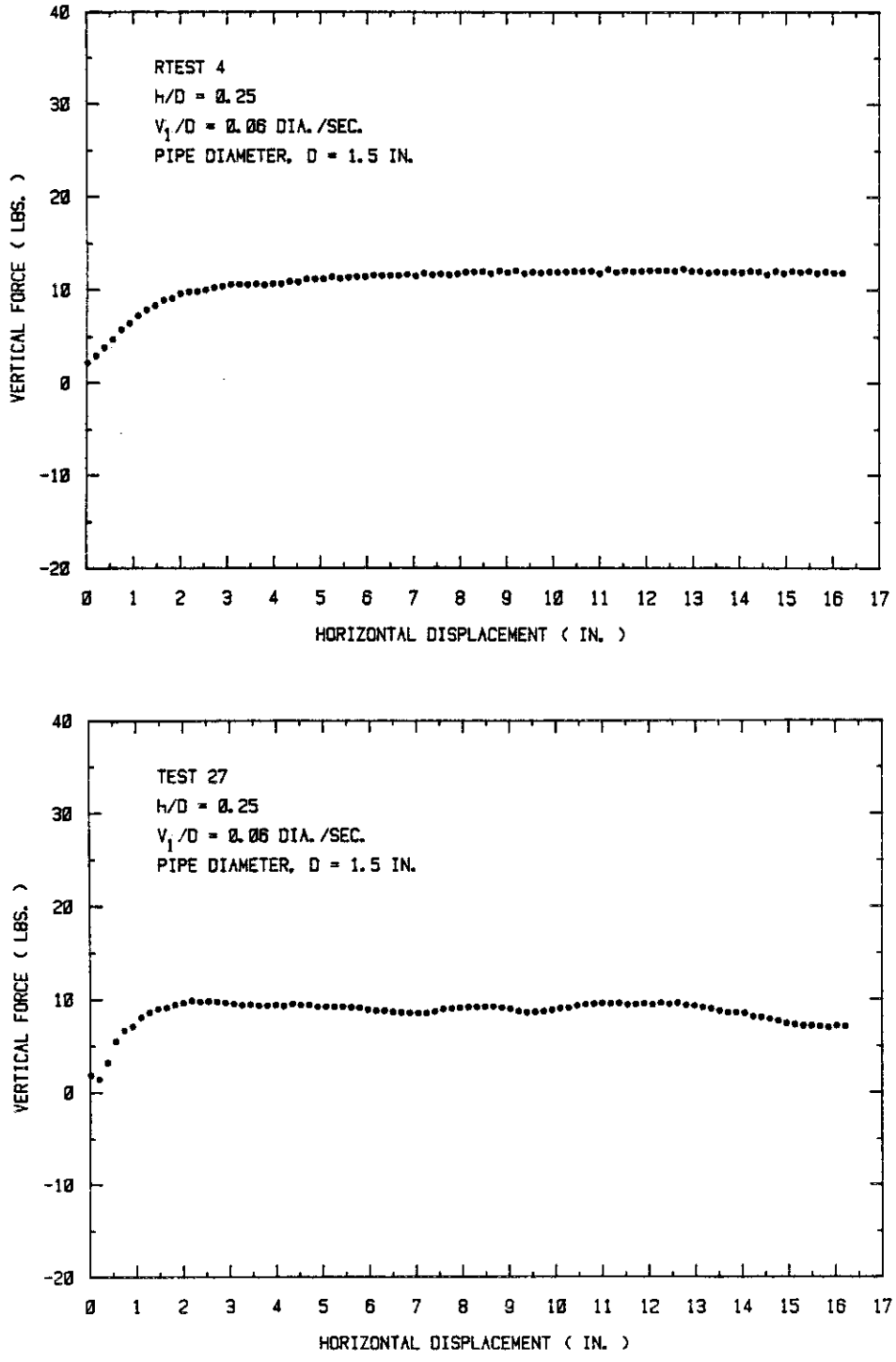

FIG. 3.52. - Comparison of Vertical Drag Forces for Replicate Tests

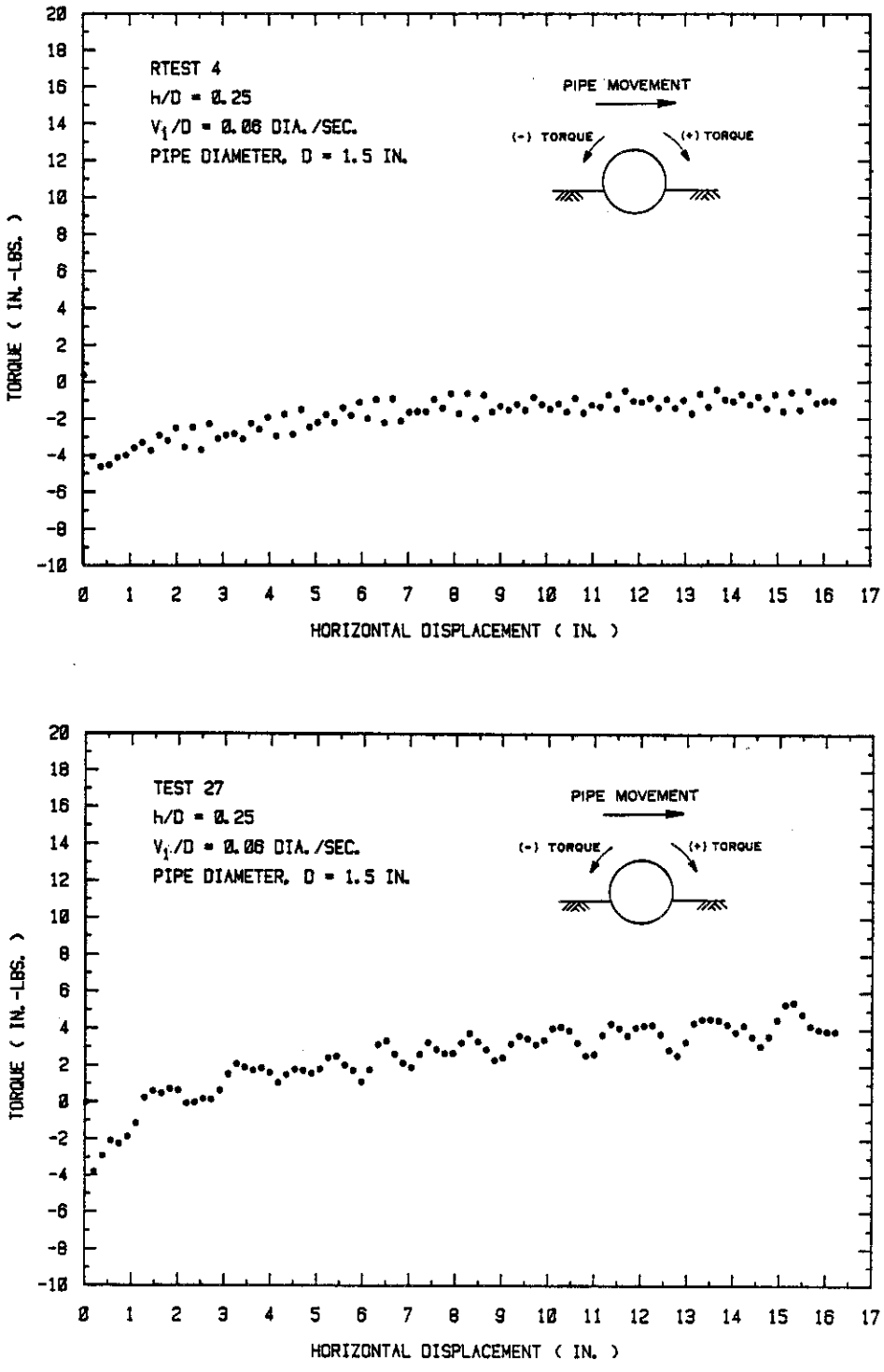

FIG. 3.53. - Comparison of Torques for Replicate Tests

sediment accumulated in front of the pipe and the horizontal force gradually increased. For cases of complete burial, a mound appeared on the sediment surface which moved with the pipe.

The theoretical developments associated with this research are concerned in part with the soil failure or "breakaway" forces. When a definite peak did not exist (RTEST 4, Fig. 3.51), there was usually a definite break in the slope of the curve, and this point was selected. These are termed the "failure" points. The corresponding horizontal force coefficients, g_1, are plotted versus initial recess depth in Fig. 3.54. For another part of the theory, forces at large displacements are appropriate, and for this case, force coefficients were determined at a normalized displacement, U/D, of 3. Values of g_1 determined at this point are plotted in Fig. 3.55.

The general pattern of vertical forces varied depending on the initial burial depth (see Fig. 3.56). For shallow burial depth ($h/D < 0.5$), the vertical forces gradually increased with displacement, always remaining positive (buoyant). For $h/D = 1$, the force rose to a maximum and then began decreasing as the weight of the sediment over the pipe overcame the lift force on the pipe. At h/D of 2 and 4, the vertical forces initially decreased and then increased somewhat with additional displacement, but they were always negative, presumably due to the weight of the overlying sediment pushing down on the pipe.

The analysis for vertical force coefficients is more complex than for the horizontal case, owing to the complicated interaction which exists between the buoyant force and sediment loading once pipe movement is initiated. The initial force discussed earlier becomes an important variable. Two different approaches were used to calculate the vertical force coefficient. In one case, the difference between the initial

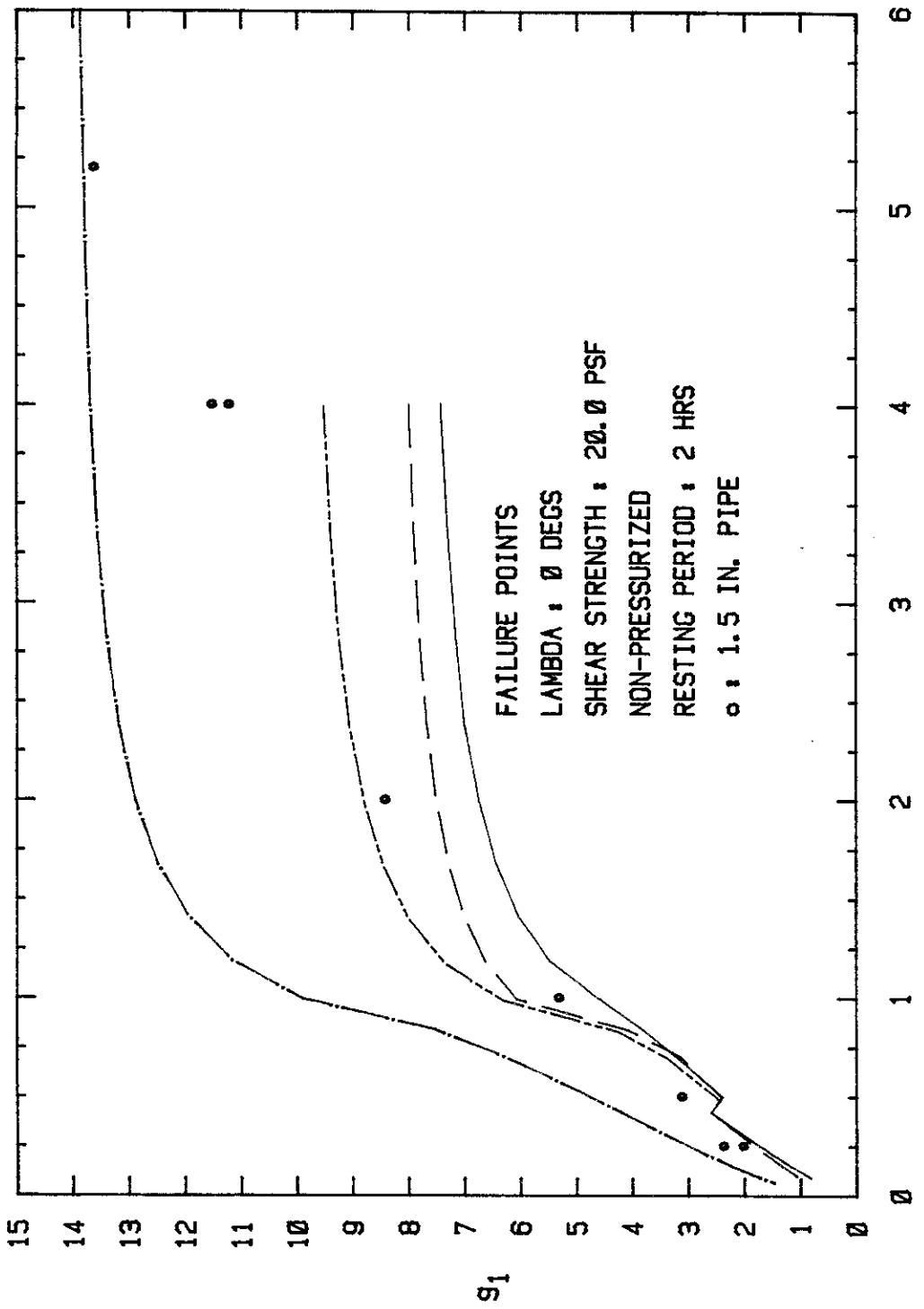

FIG. 3.54a - Horizontal Force Coefficient at Failure Points Versus Recess Depth for Fixed-Ends Horizontal Drag Tests. Arithmetic Scale.

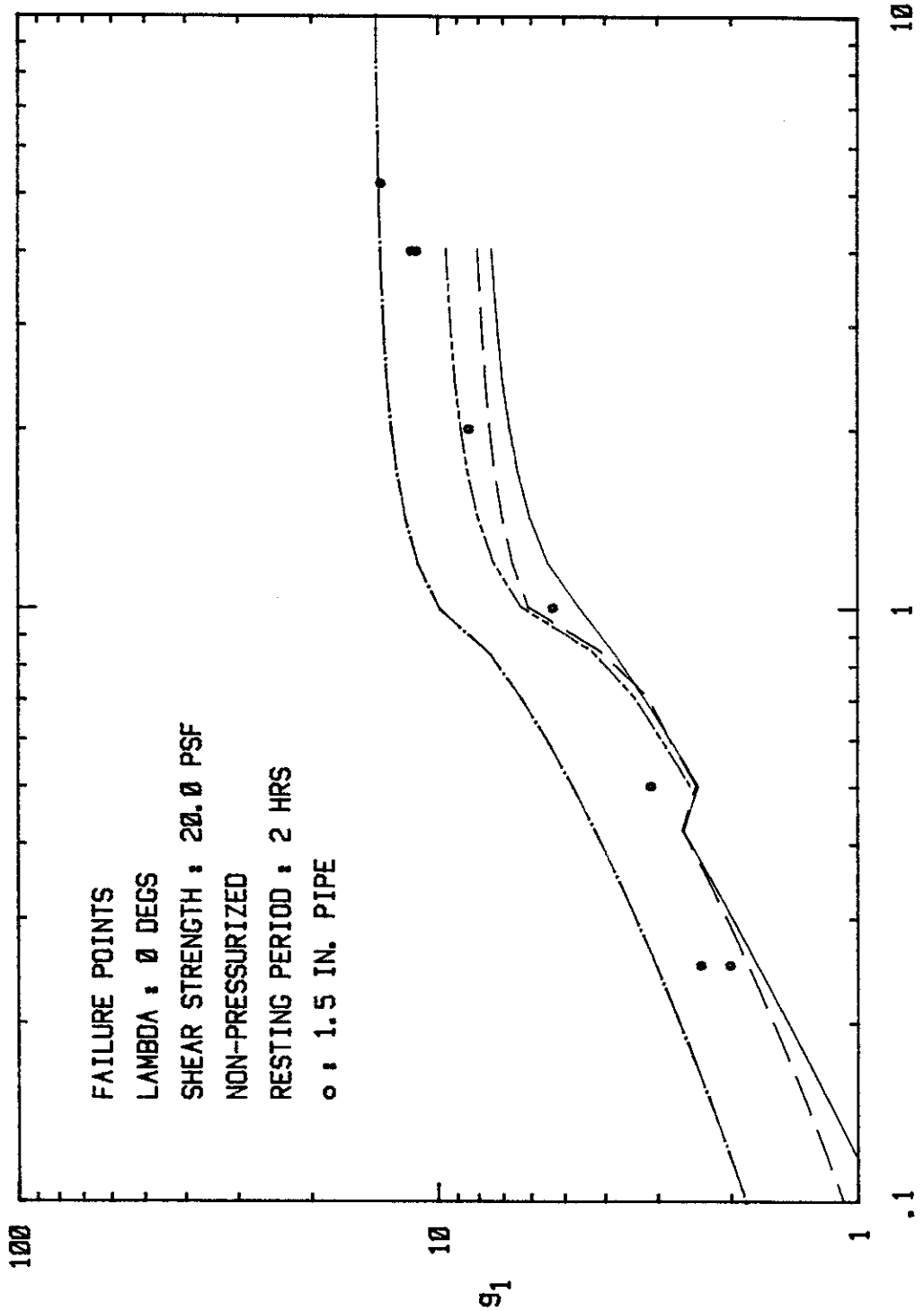

FIG. 3.54b - Horizontal Force Coefficient at Failure Points Versus Recess Depth for Fixed-Ends Horizontal Drag Tests. Logarithmic Scale.

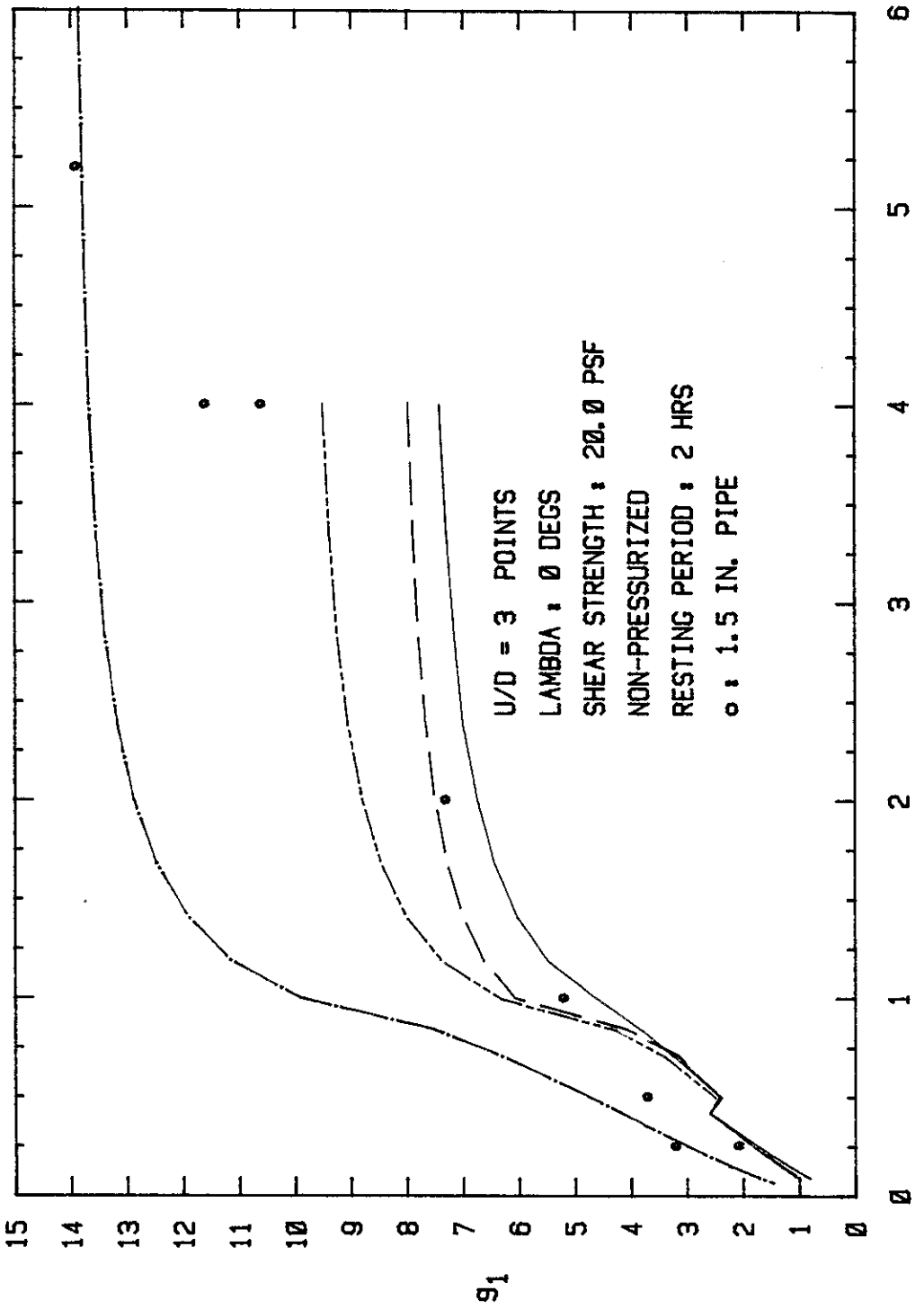

FIG. 3.55a - Horizontal Force Coefficient at U/D = 3 Points Versus Recess Depth for Fixed-Ends Horizontal Drag Tests. Arithmetic Scale.

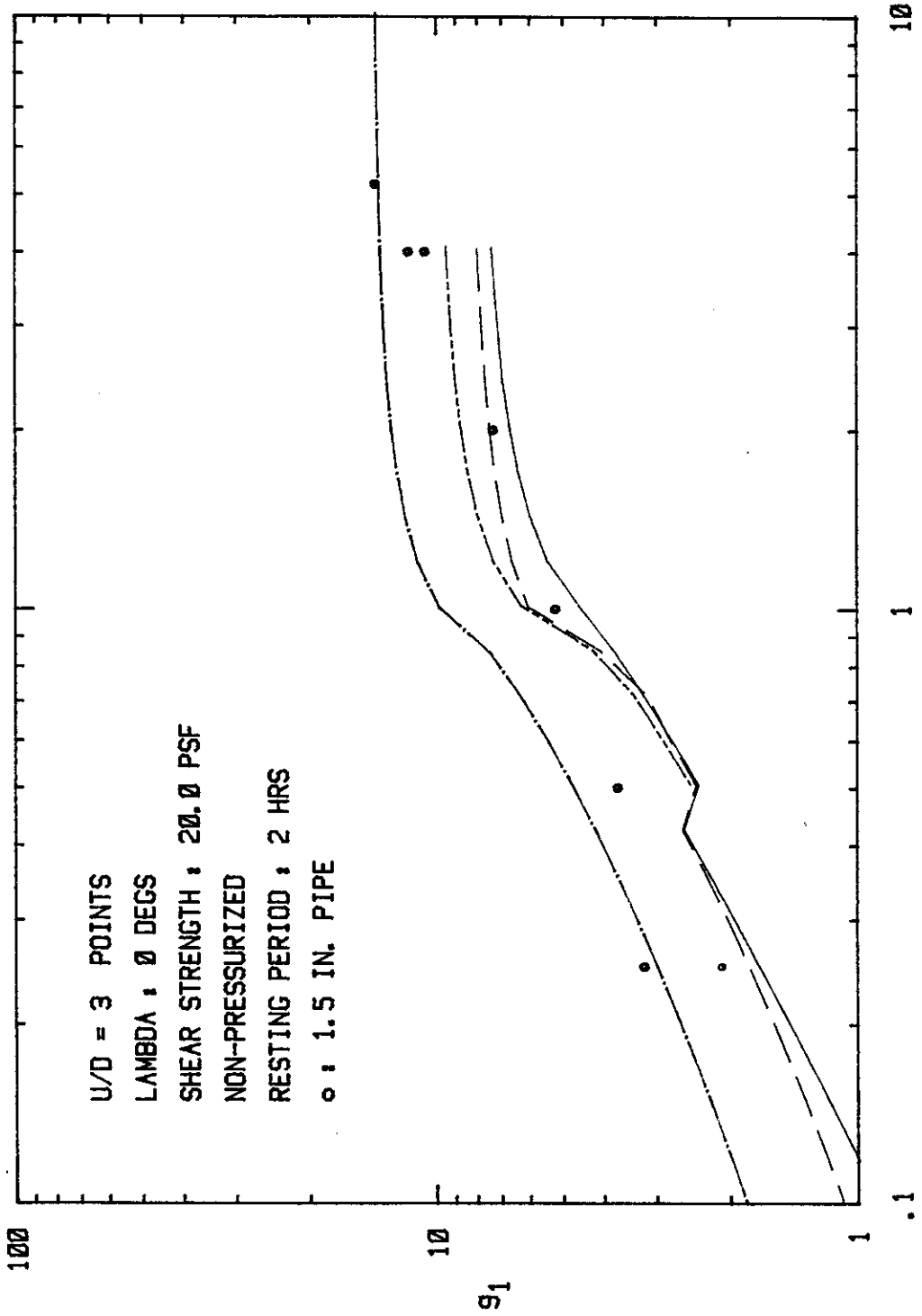

FIG. 3.55b – Horizontal Force Coefficient at U/D = 3 Points Versus Recess Depth for Fixed-Ends Horizontal Drag Tests. Logarithmic Scale.

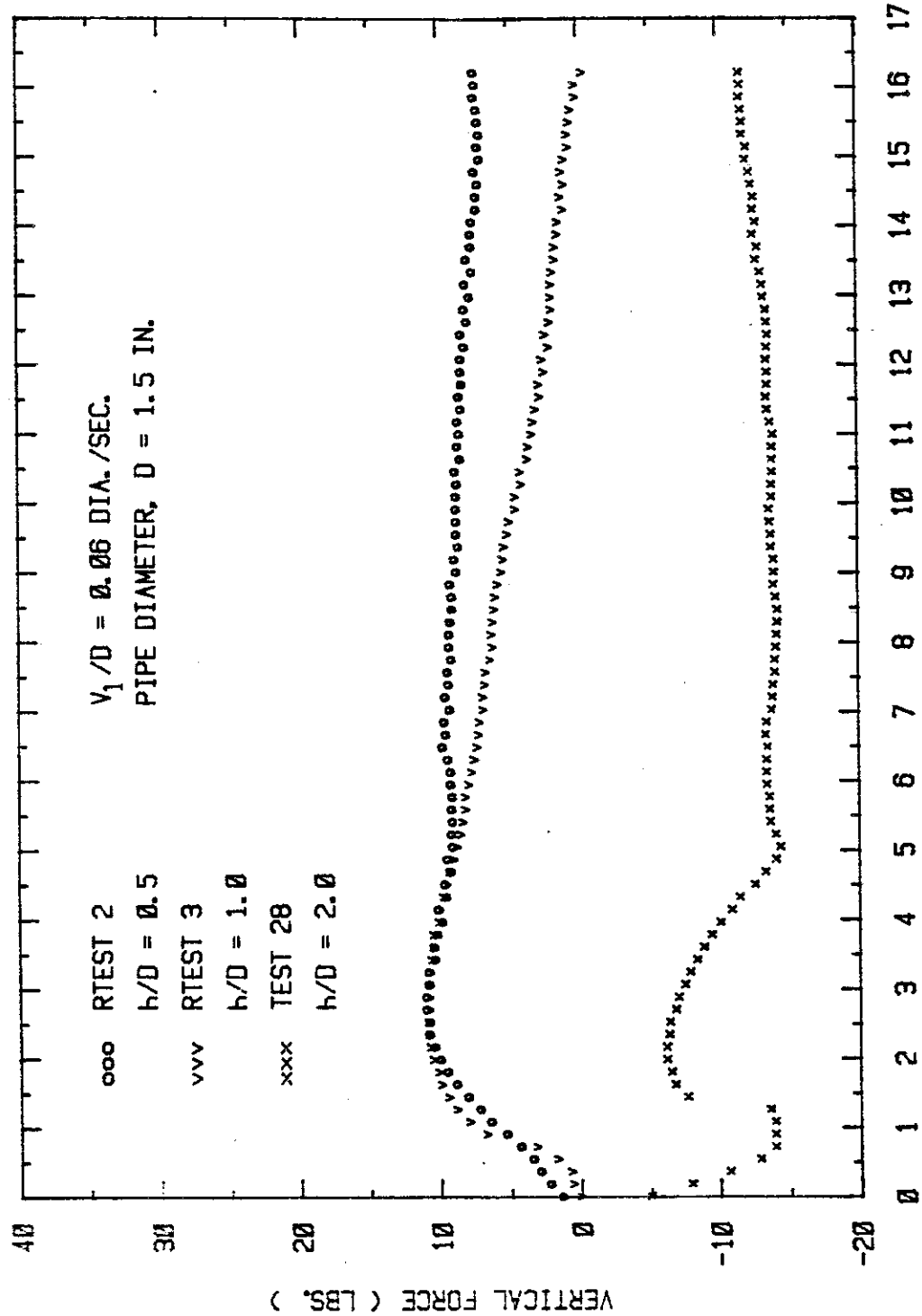

FIG. 3.56 - Comparison of Vertical Forces for Various Depths of Burial for Fixed-Ends Horizontal Drag Tests.

and maximum force was used. The other approach used a corrected initial force based on the theoretical combined buoyant and vertical mud force from Fig. 3.50. Based on these two different approaches, the vertical force coefficients, g_2, versus recess depths are shown in Fig. 3.57.

The vertical force coefficients might be indicative of the vertical direction of movement for freely floating pipes. Pipes should tend to rise up out of the soil when the initial recess depth, h/D is less than or equal to 1 since g_2 is positive. At initial h/D of 2, pipes should tend to stay down in the sediment (g_2 is negative). For deeply buried pipes (h/D = 4.0), no significant upward or downward movement should occur (g_2 approximately 0).

The torque measurements can be utilized to determine the torsional resistance required for full scale pipe, but they can also offer insight into the complicated aspects of pipe-soil interaction. To illustrate this, torque-displacement curves for h/D of 0.5 and 1.0 are shown in Figs. 3.58 and 3.59. For h/D = 0.5, the pipe initially tried to rotate backward (counterclockwise), but as movement continued the pipe then attempted to rotate into the oncoming sediment (clockwise). For deeper recess depths, this action was reversed, with the pipe initially attempting to rotate into the oncoming sediment and then attempting to rotate in the reverse direction. At large displacements, the torque was positive for both recess depths.

Figures 3.60-3.64 show the relationship between the torque coefficient, g_4, and the normalized displacement, U/D, for several horizontal drag tests.

2. Pushed Down Vertical Tests (1.5 in. O.D. Pipe).

For this series, three tests with initial recess depths, h/D, of 0.0,

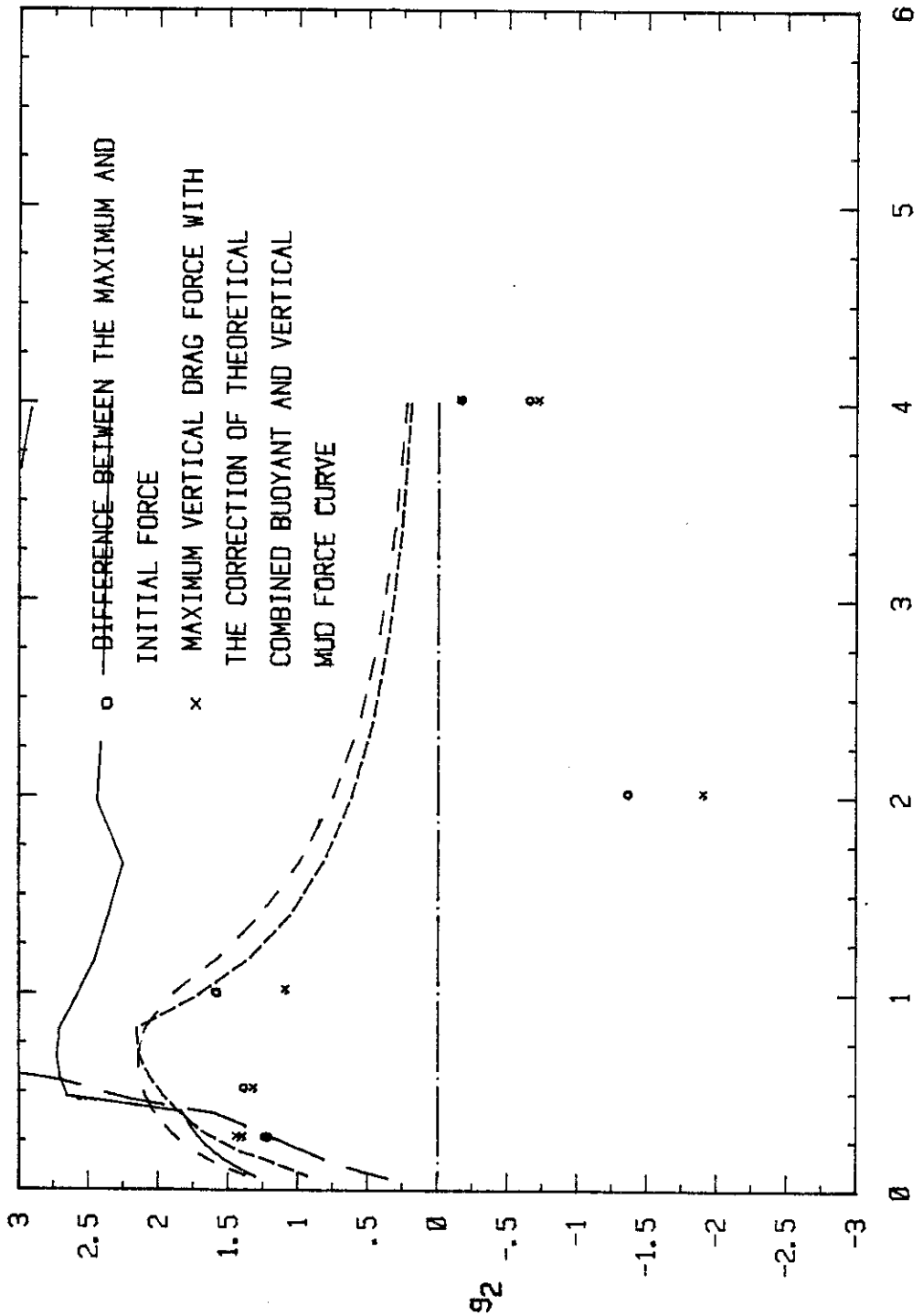

FIG. 3.57 - Vertical Force Coefficient Versus Recess Depth for Fixed-Ends Horizontal Drag Tests.

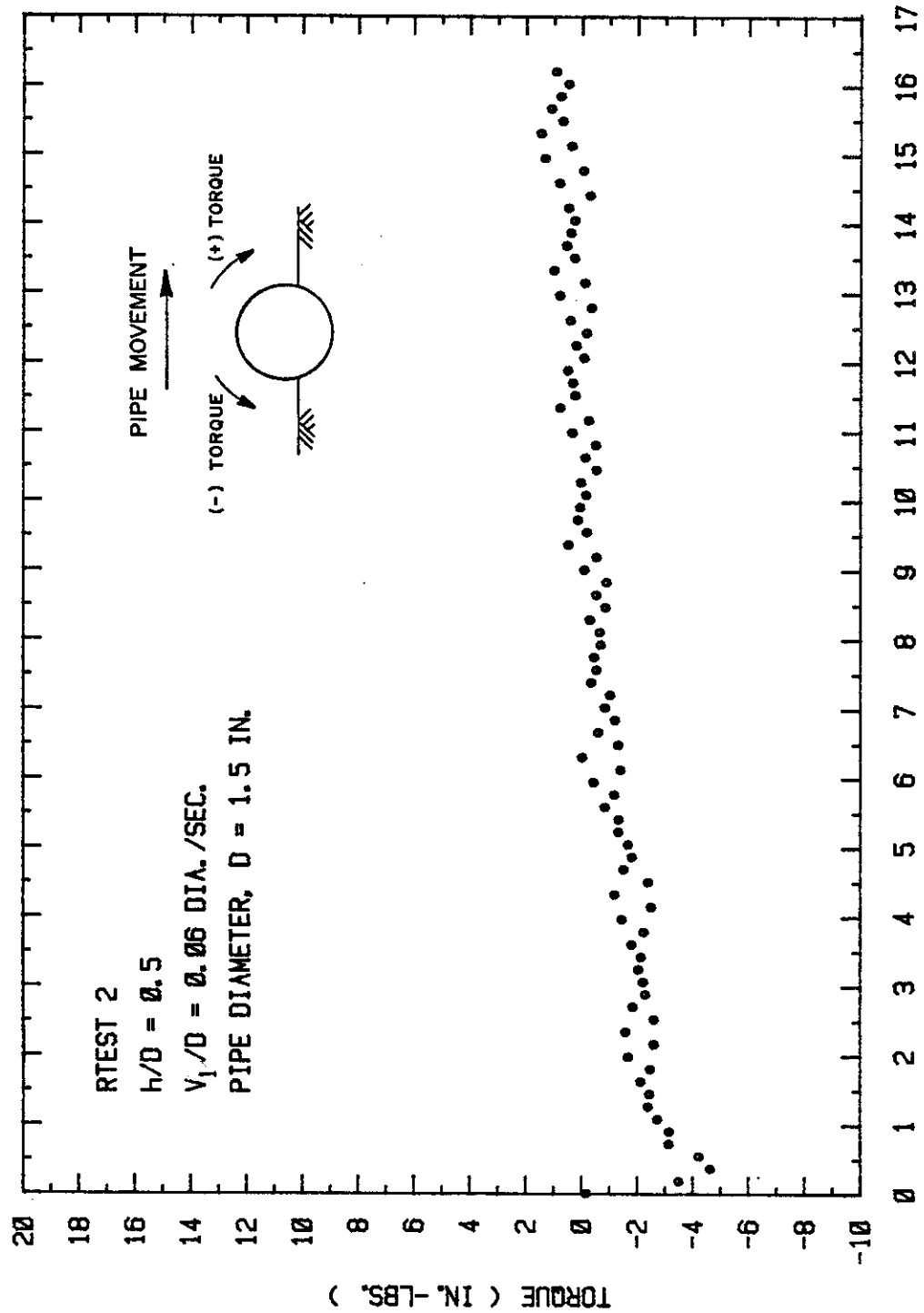

FIG. 3.58. - Torque Versus Displacement for h/D of 0.5. Fixed-Ends Horizontal Drag Test.

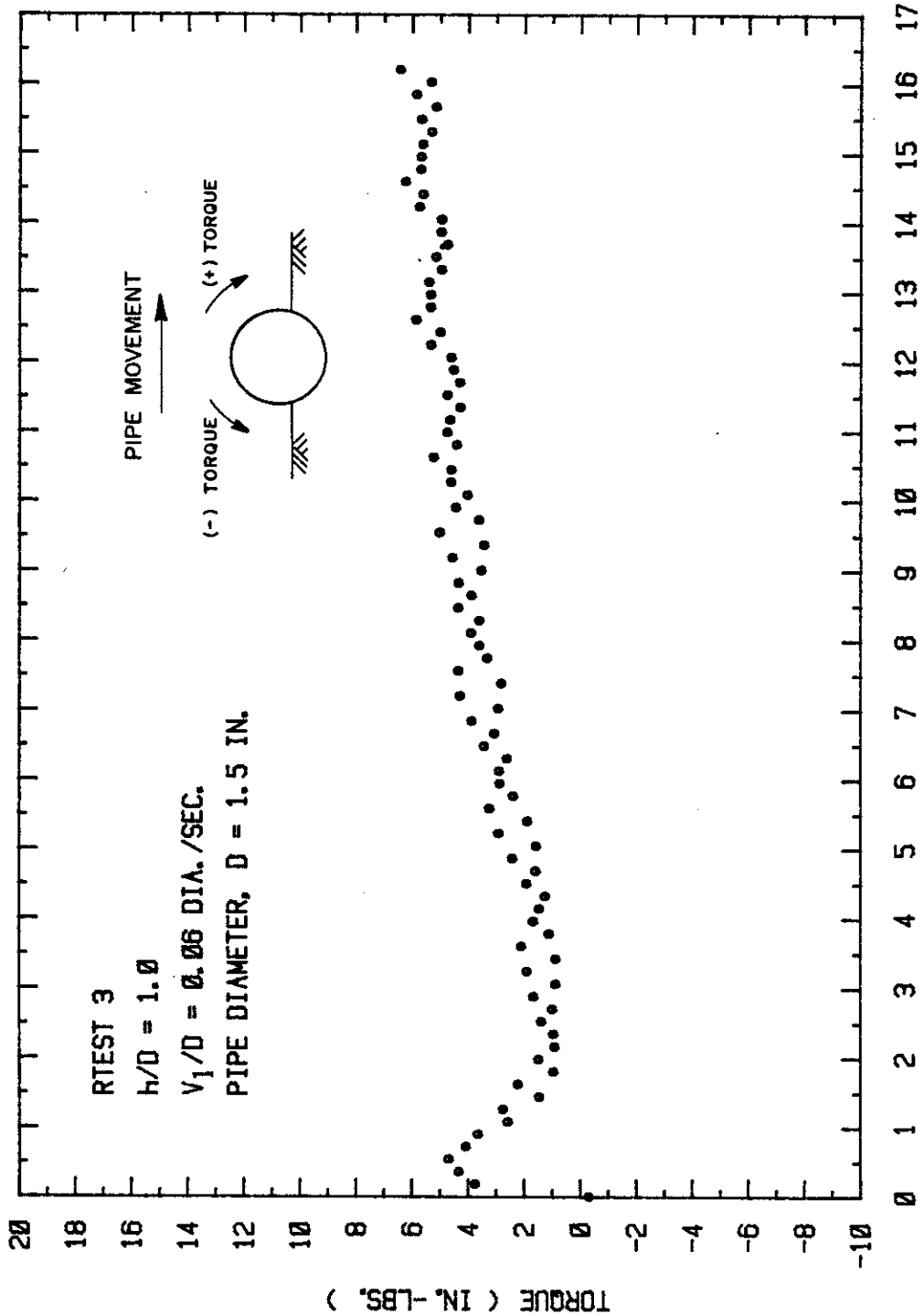

FIG. 3.59. - Torque Versus Displacement for h/D of 1.0. Fixed-Ends Horizontal Drag Test

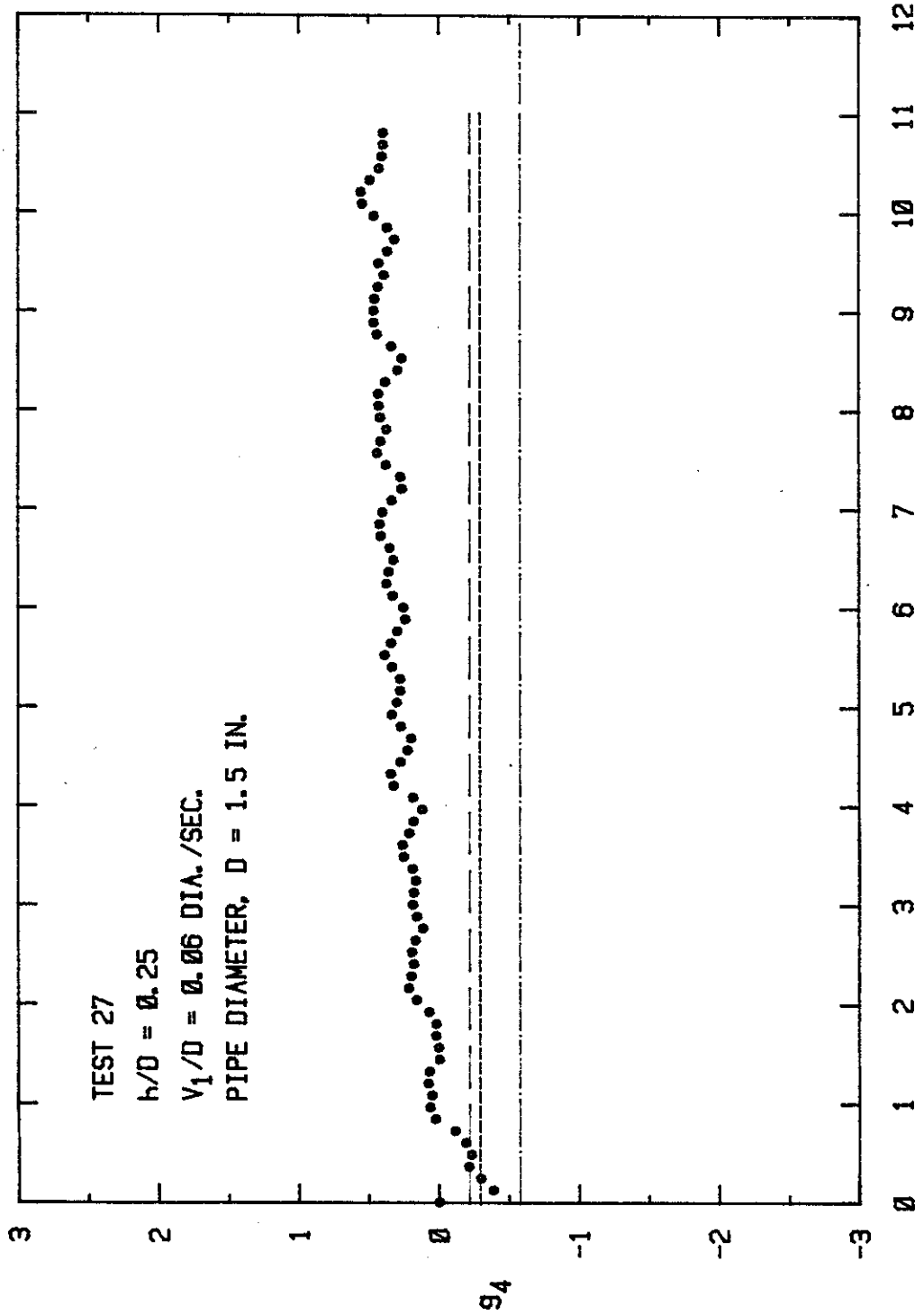

FIG. 3.60 – Torque Coefficient Versus Displacement for h/D of 0.25 Fixed-Ends Horizontal Drag Test.

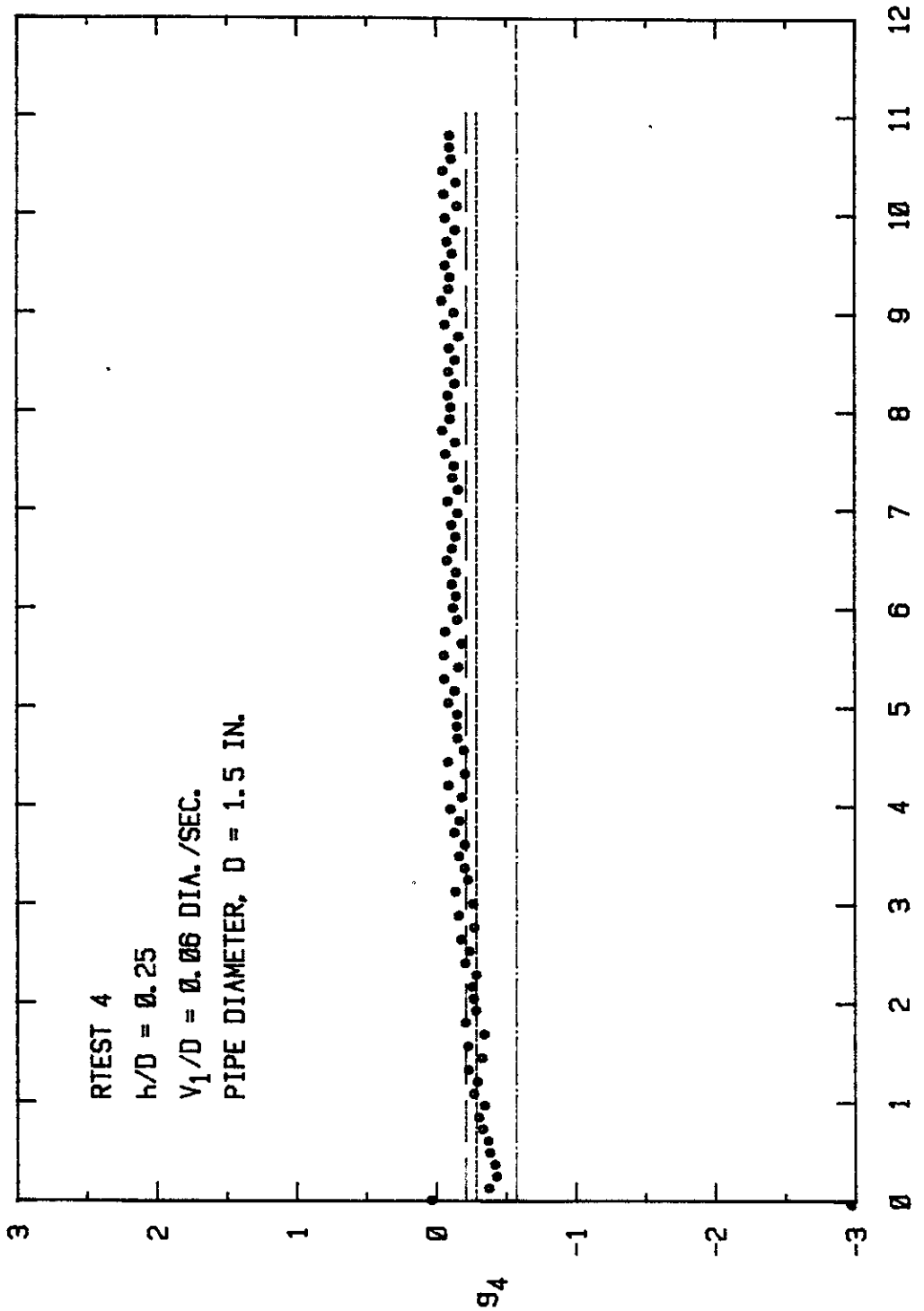

FIG. 3.61 - Torque Coefficient Versus Displacement for h/D of 0.25 Fixed-Ends Horizontal Drag Test.

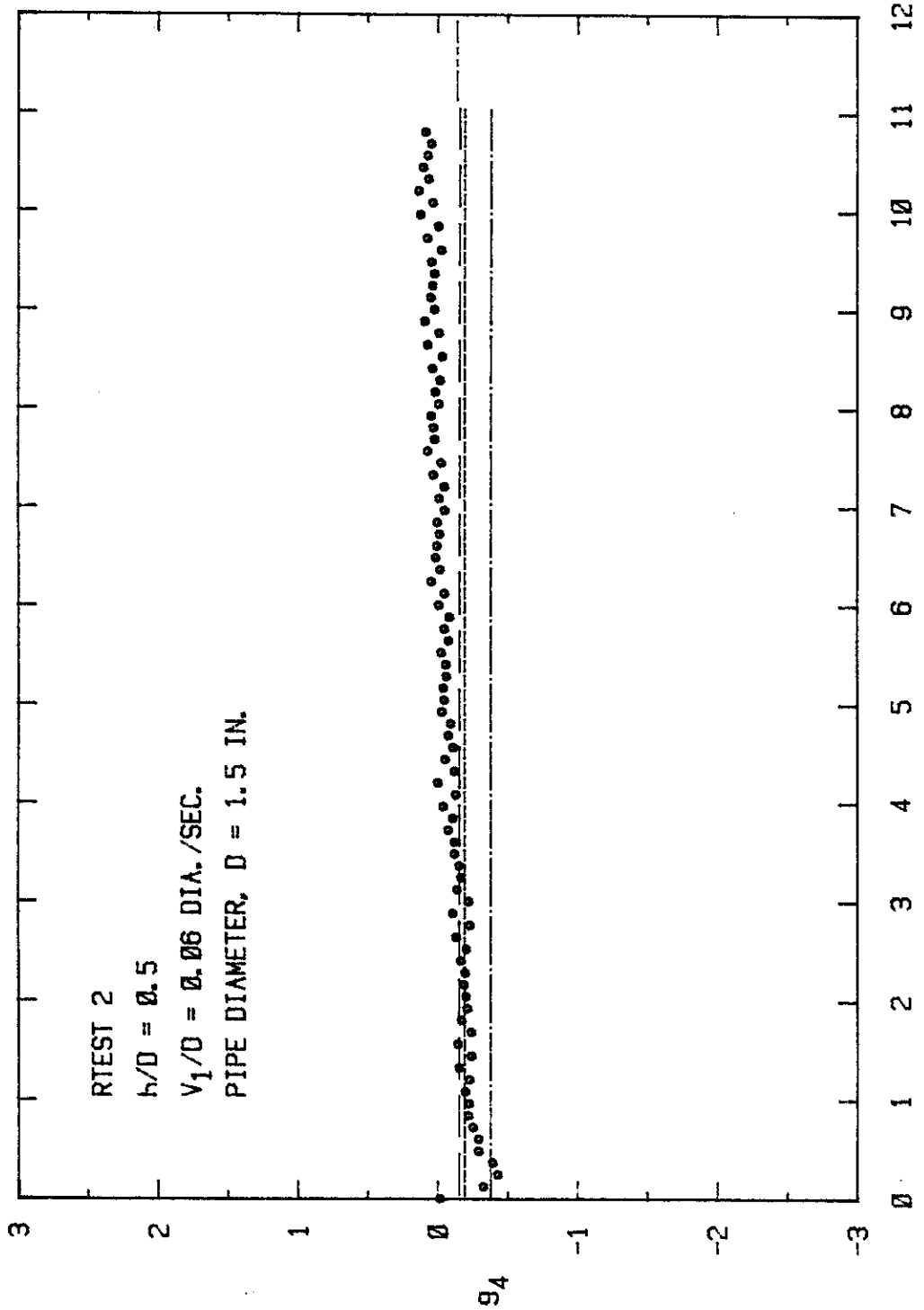

FIG. 3.62 - Torque Coefficient Versus Displacement for h/D of 0.5 Fixed-Ends Horizontal Drag Test.

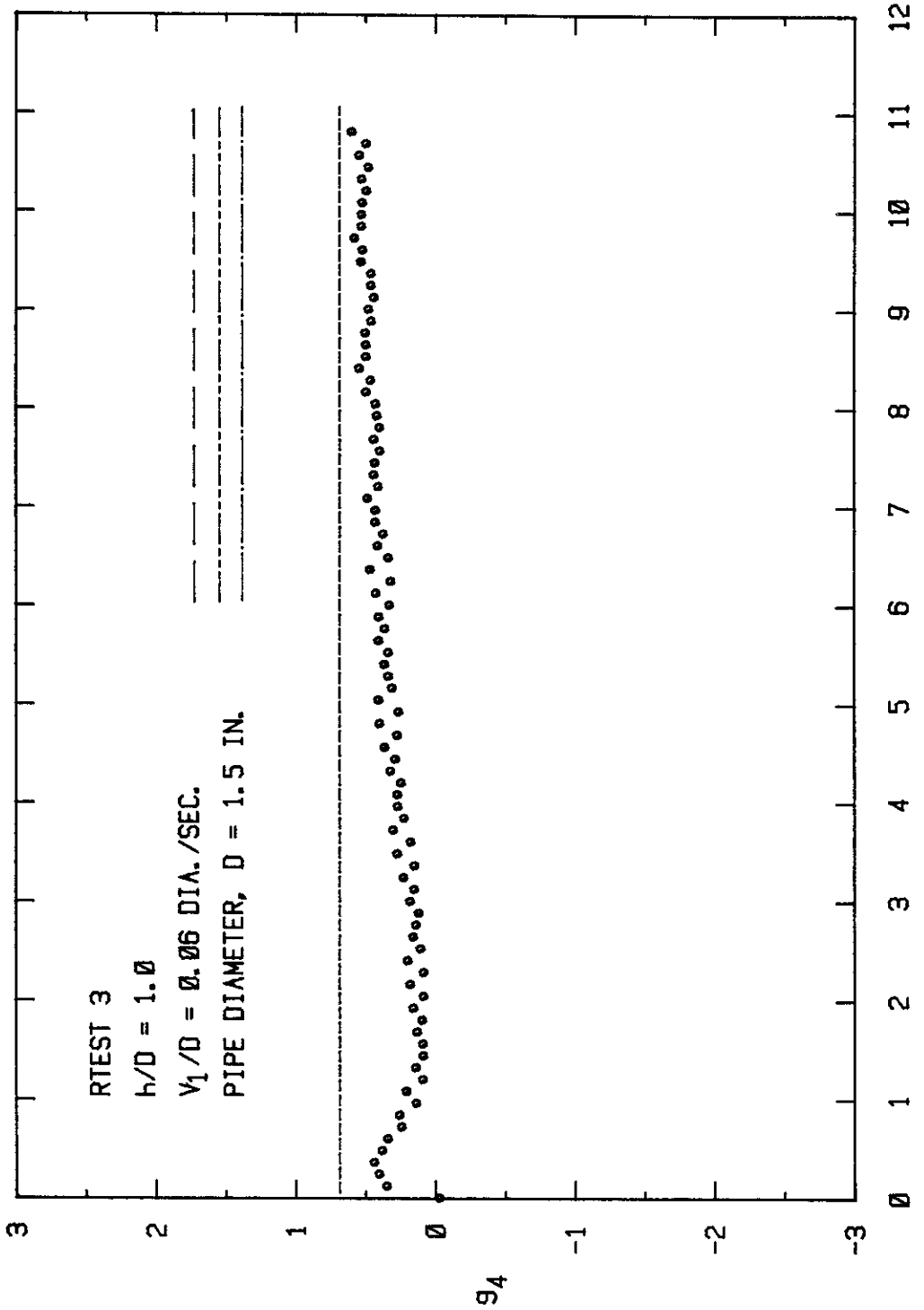

FIG. 3.63 - Torque Coefficient Versus Displacement for h/D of 1.0 Fixed-Ends Horizontal Drag Test.

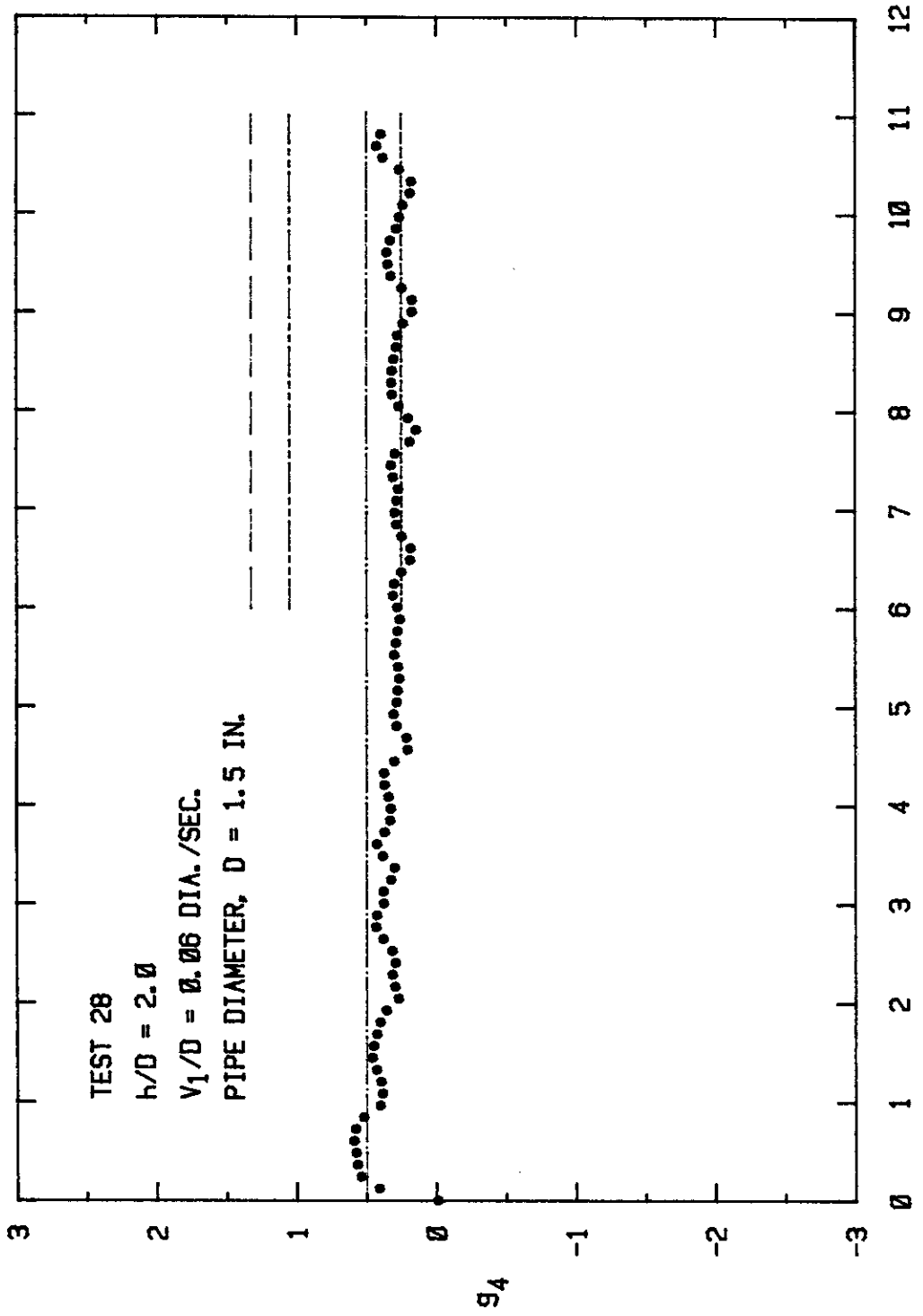

FIG. 3.64 - Torque Coefficient Versus Displacement for h/D of 2.0 Fixed-Ends Horizontal Drag Test.

0.5 and 1.0 were performed to determine the vertical force as the pipe was pushed straight down into the soil. A typical test result is shown in Fig. 3.65. The curve shows that the vertical force continued to increase with depth of penetration, but became nearly constant at approximately 6.5 in. of penetration. Observations showed that surface cracks began to appear adjacent to the cavity as the pipe penetrated deeper, and that the opening nearly closed as sediment fell into the deepening cavity (see Fig. 3.28).

Figure 3.66 is a plot of vertical force coefficient g_2 versus h/D for all three tests. The curves coincide at a recess depth, h/D, of approximately 3. The maximum value obtained for g_2 was 13.4 at h/D of 5, but the trend of the curve indicates that g_2 will reach a value of approximately 14 for deeper recess depths.

3. Pushed Down Angle Tests (1.5 in. O.D. Pipe).

Two types of these tests were performed: one type where the pipe was pushed down at a shallow angle (4.76° measured from the horizontal) and the other at a steep angle (43.17°). Again, a number of tests were repeated for verification purposes. Minor differences in results existed among some of the duplicated tests. However, in this type of test, the results are very dependent on the cracking pattern which develops in the mud and which allows the mud to fall in on top of the pipe. It is likely that a series of tests would develop a band of results rather than a well-defined curve. Nevertheless, the overall results showed consistency in the general behavior among the replicate tests.

Horizontal drag force curves for shallow angle (4.76°) drag tests showed that the forces peaked at small displacements (except for h/D of 0.25, which showed a gradual increase), decreased, and then gradually

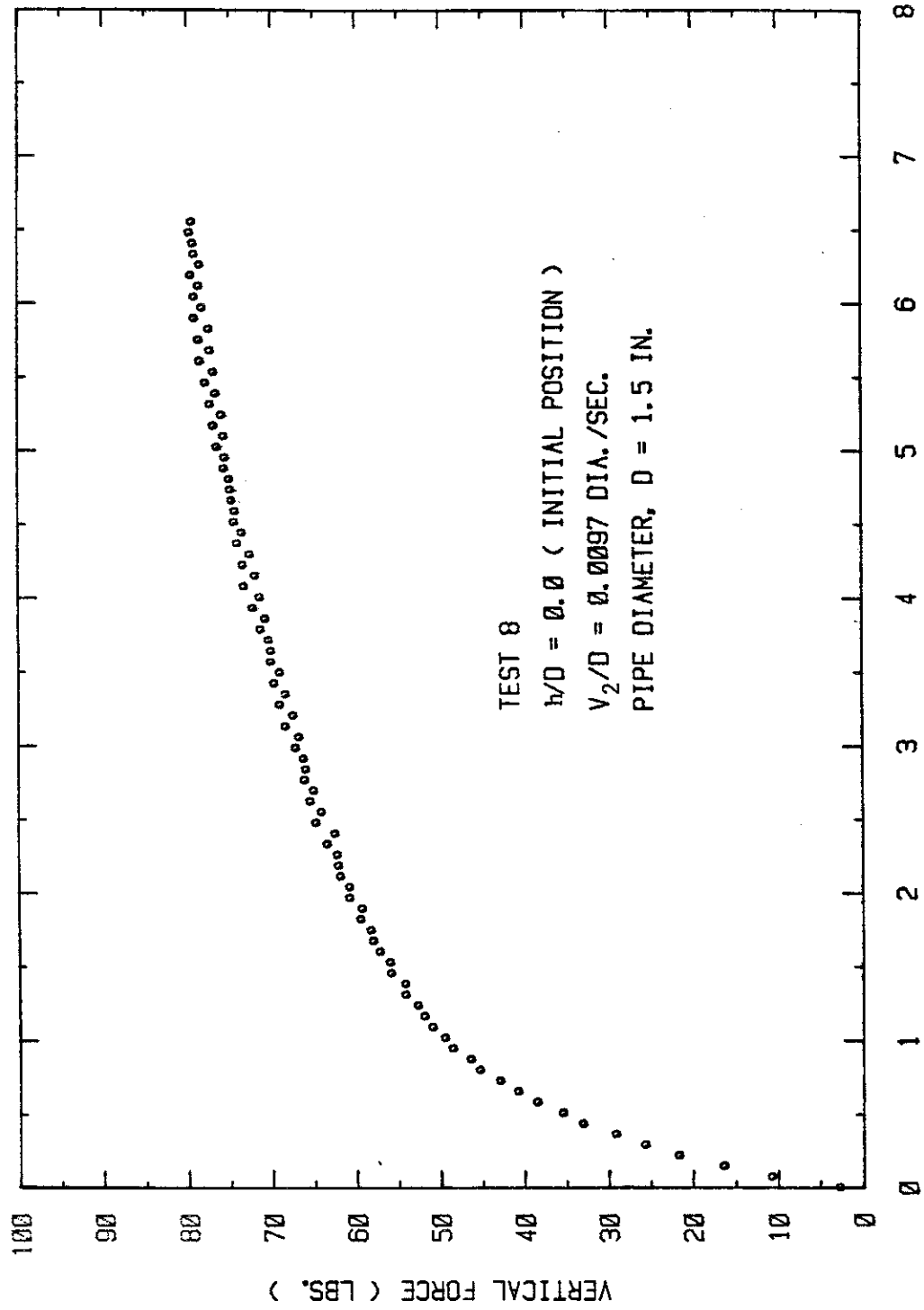

FIG. 3.65 - Vertical Force for h/D of 0.0. Pushed-Down Vertical Test.

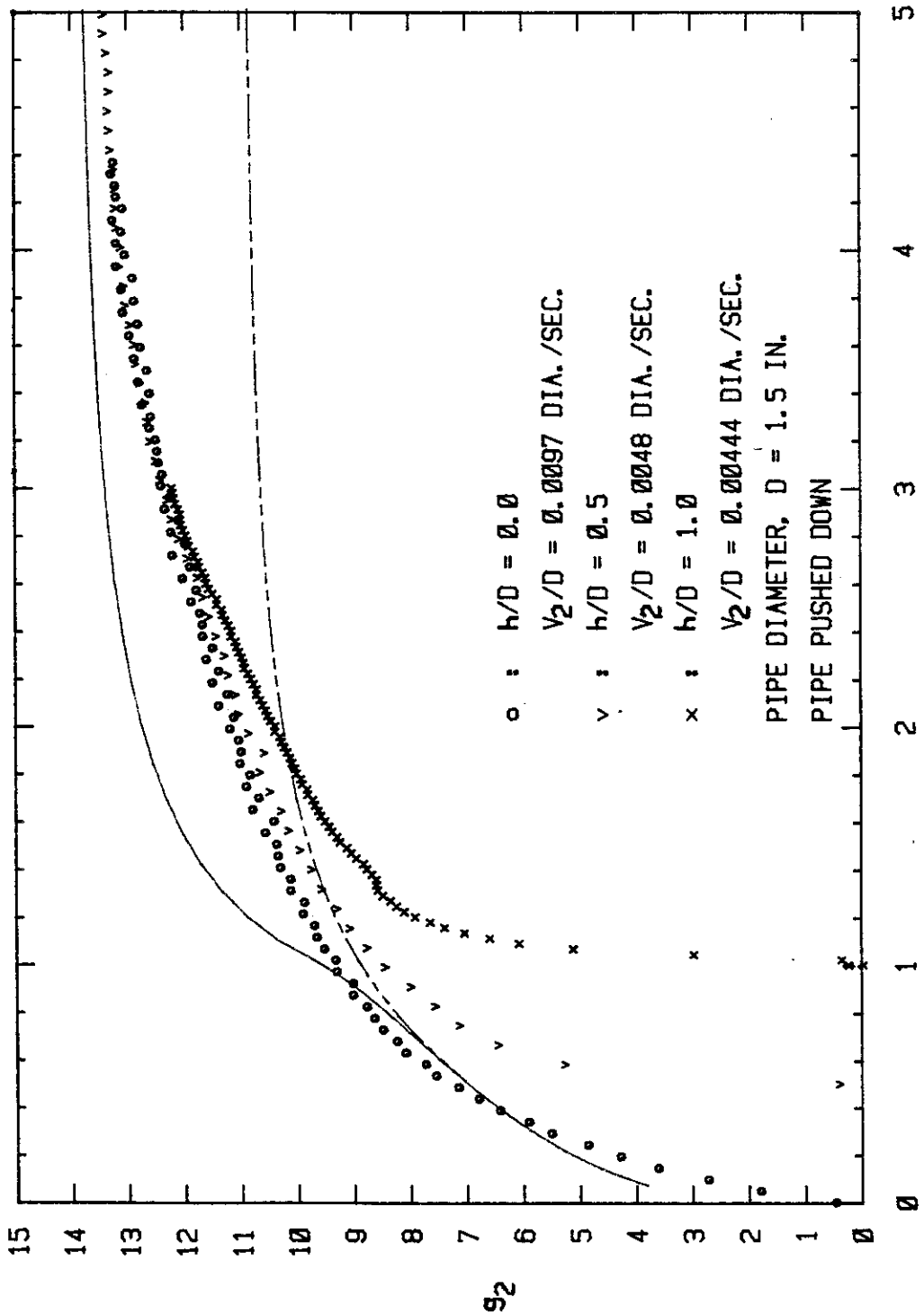

FIG. 3.66a - Vertical Force Coefficient for Pushed-Down Vertical Tests. Arithmetic Scale.

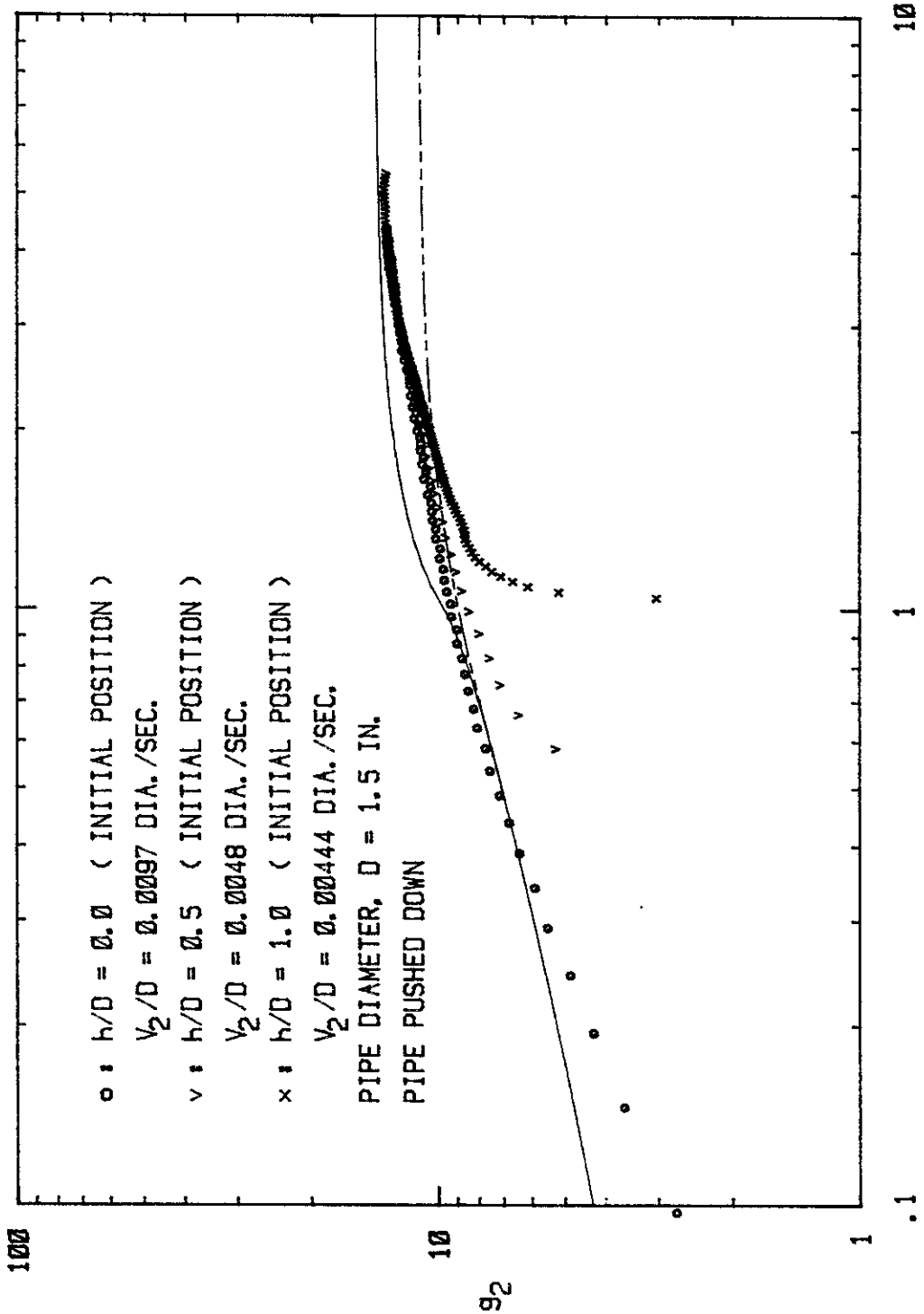

FIG. 3.66b - Vertical Force Coefficient for Pushed-Down Vertical Tests. Logarithmic Scale.

increased as the pipe plunged deeper into the mud. Since there is not a single maximum drag factor for these tests, as in the horizontal drag tests, the results are displayed in Fig. 3.67 as a combined plot of all horizontal force coefficients versus recess depth, h/D. The horizontal force coefficient is seen to increase as recess depth increases following a fairly smooth curve except for the individual peaks. All these tests started with different initial recess depths, but the general pattern is apparently what would exist if the pipe were started at h/D = 0, and continued to travel in one continuous movement to an h/D of approximately 4. The maximum value of the horizontal force coefficient was approximately 12 at h/D near 4, but the trend shows it would increase somewhat for greater recess depths.

The general pattern of vertical drag forces varied depending on the initial recess depth. For initial recess depth, h/D, less than 1, no distinct breakaway force was obtained; the forces reached a peak and gradually decreased. When the initial recess depths, h/D, were equal to or greater than 1.0, distinct breakaway forces occurred at small displacements. Figure 3.68 compares these two patterns for h/D of 0.25 and 1.0. It should be noted that for shallow initial recess depths, the forces remained positive (buoyant), but they gradually decreased as the sediment began to accumulate over the pipe. For deeper initial recess depths, such as h/D = 1.0, the weight of overlying sediment exceeded the buoyant force at relatively small displacements and the vertical drag force became negative, whereas with the deepest burial depth (h/D = 3), the vertical drag force remained nearly zero.

Vertical force coefficients versus recess depth for six different tests are combined and plotted in Fig. 3.69. A similar plot using the

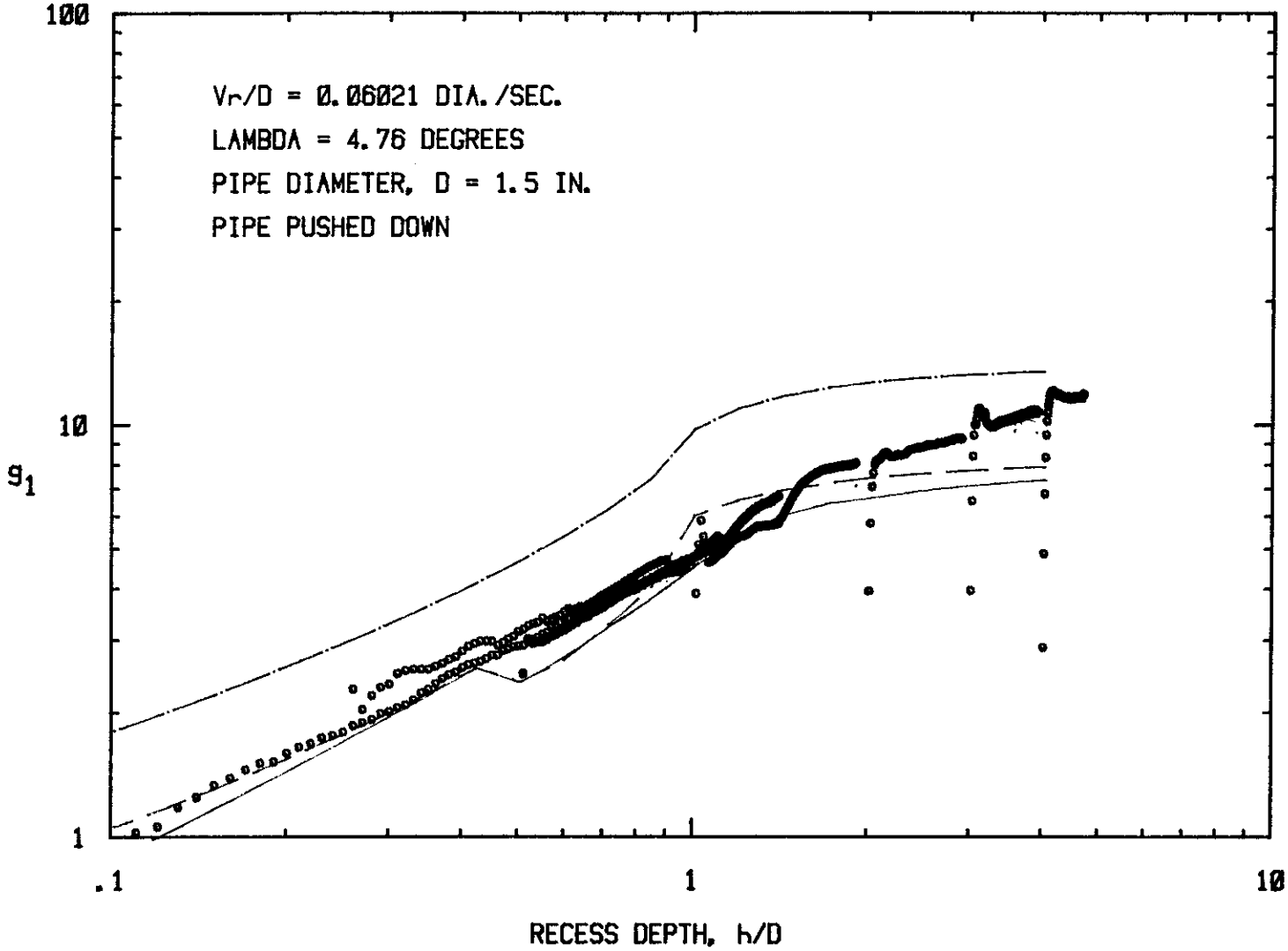

FIG. 3.67 - Horizontal Force Coefficient Curves for Shallow Angle (4.76°) Pushed-Down Angle Tests. Logarithmic Scale.

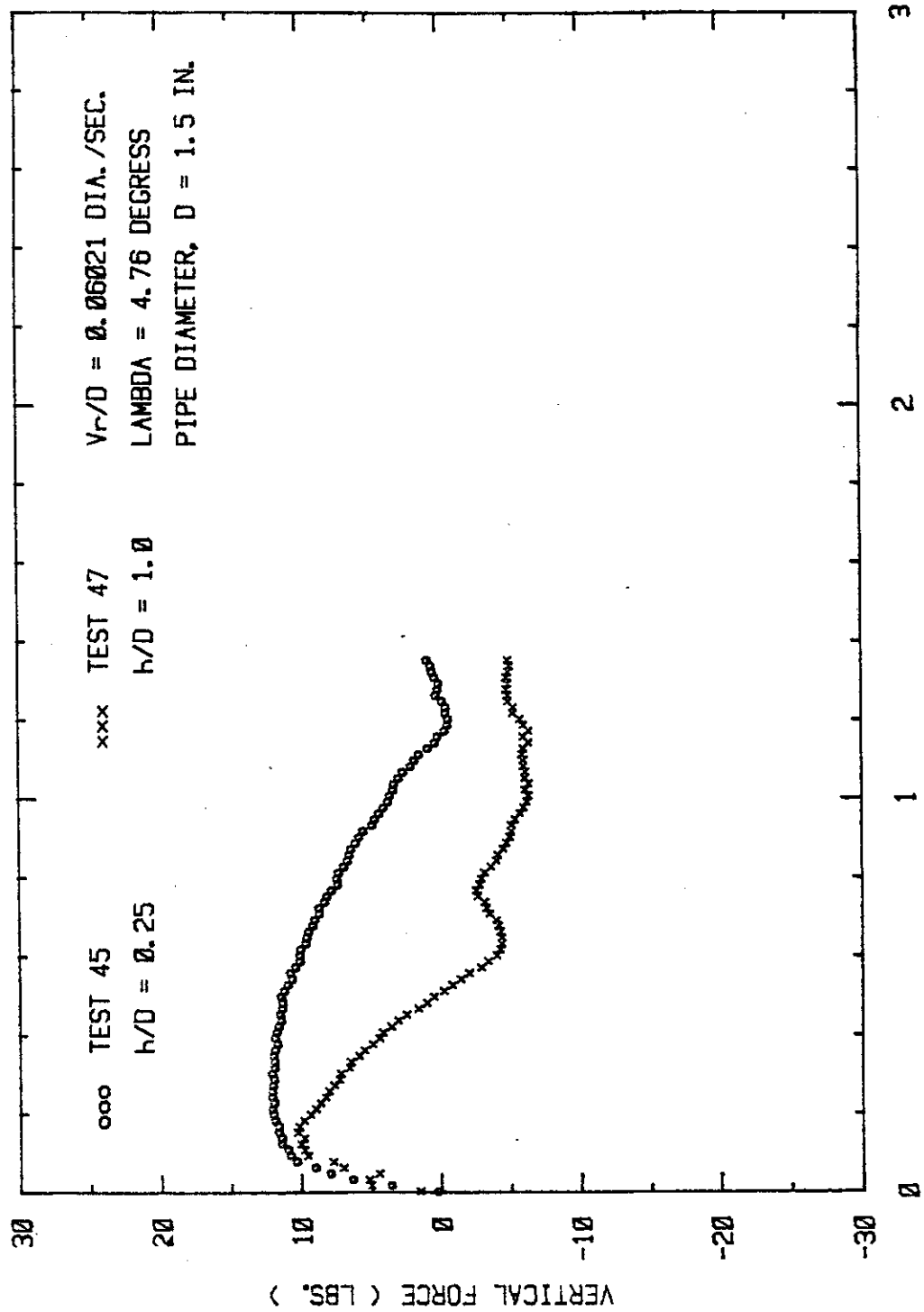

FIG. 3.68 - Comparison of Vertical Forces for h/D of 0.25 and 1.0. Shallow Angle (4.76°) Pushed-Down Angle Tests.

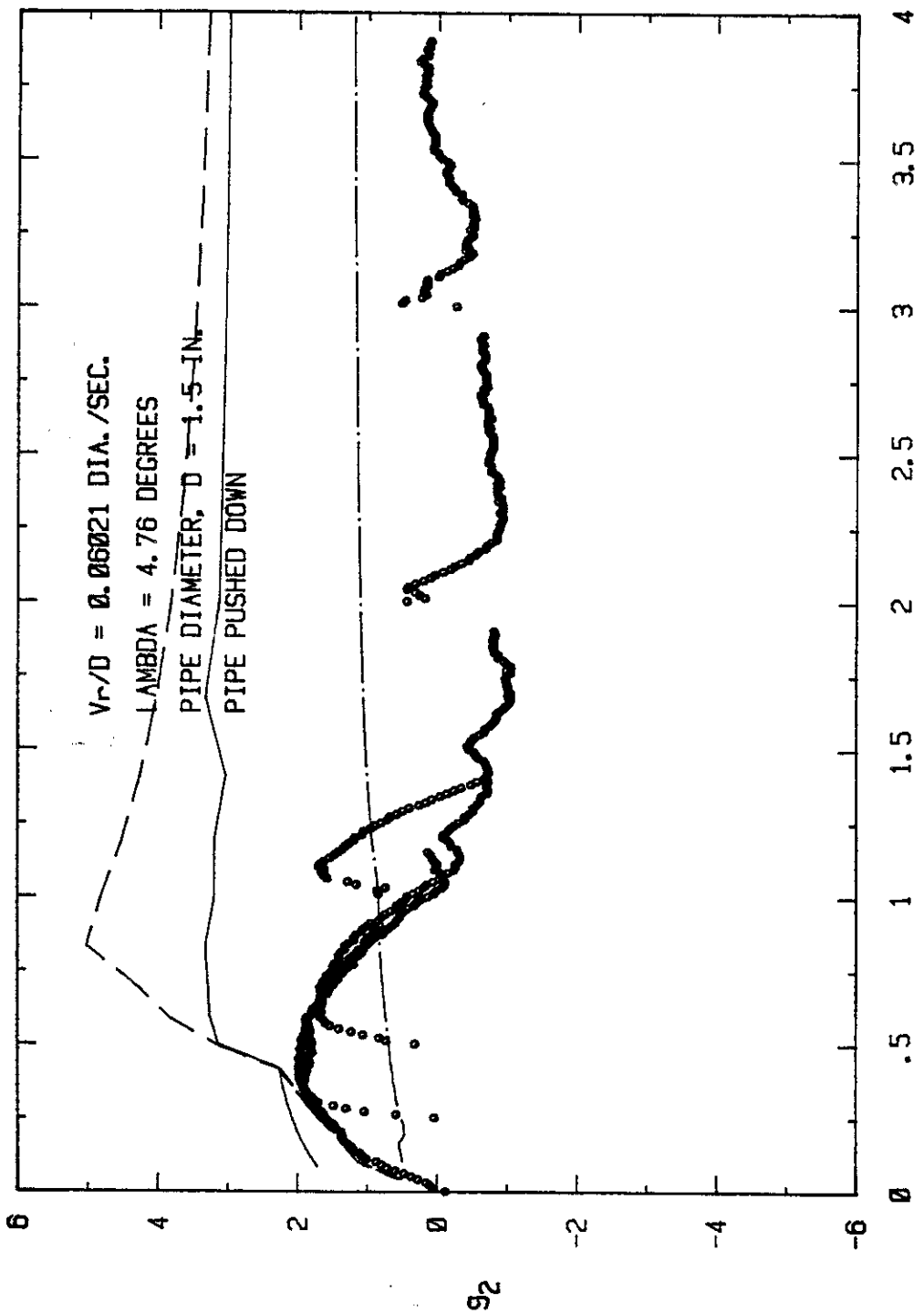

FIG. 3.69 - Combined Plot of Vertical Force Coefficient Versus Recess Depth for Six Different Shallow Angle (4.76°) Pushed-Down Angle Tests.

correction for theortical combined buoyant and vertical mud force (from Fig. 3.50) is shown in Fig. 3.70. Both figures show the same general trend. The force coefficients are positive for h/D < 1, but they become negative (except for the initial peaks) for h/D between 1 and 3. When h/D exceeds 3, the vertical force coefficients approach zero, or become slightly positive. This trend is in general agreement with the horizontal drag test results (Fig. 3.57).

For the steep angle (43.17°), five tests were performed. Four were identical tests with initial h/D of 0, and the other had an initial h/D of 0.25. The four tests with initial h/D of 0 showed very similar results when plotted in terms of horizontal force coefficient versus h/D (Fig. 3.71), although one test had a slightly higher force coefficient. The curve for h/D = 0.25 is not shown in Fig. 3.71 as the test was terminated early, but it blended smoothly into the other curves as the value of h/D increased. Comparison of the curves in Fig. 3.71 with the upper envelope of curves obtained for the shallow angle pushed-down tests in Fig. 3.67 shows that the maximum horizontal force coefficient versus recess depth for the two test types are nearly identical, which indicates that the force coefficient is primarily a function of recess depth and is independent of the path taken by the pipe to get to the recess depth.

The horizontal force coefficients from both pushed-down angle tests are only a few percent lower (depending on the recess depth) than those obtained from the horizontal drag tests (Figs. 3.54 and 3.55). However, the force coefficients for the latter tests were based on peak or U/D = 3 values as opposed to the envelope of values used for the angle tests.

Vertical force coefficients for the steep pushed-down angle tests

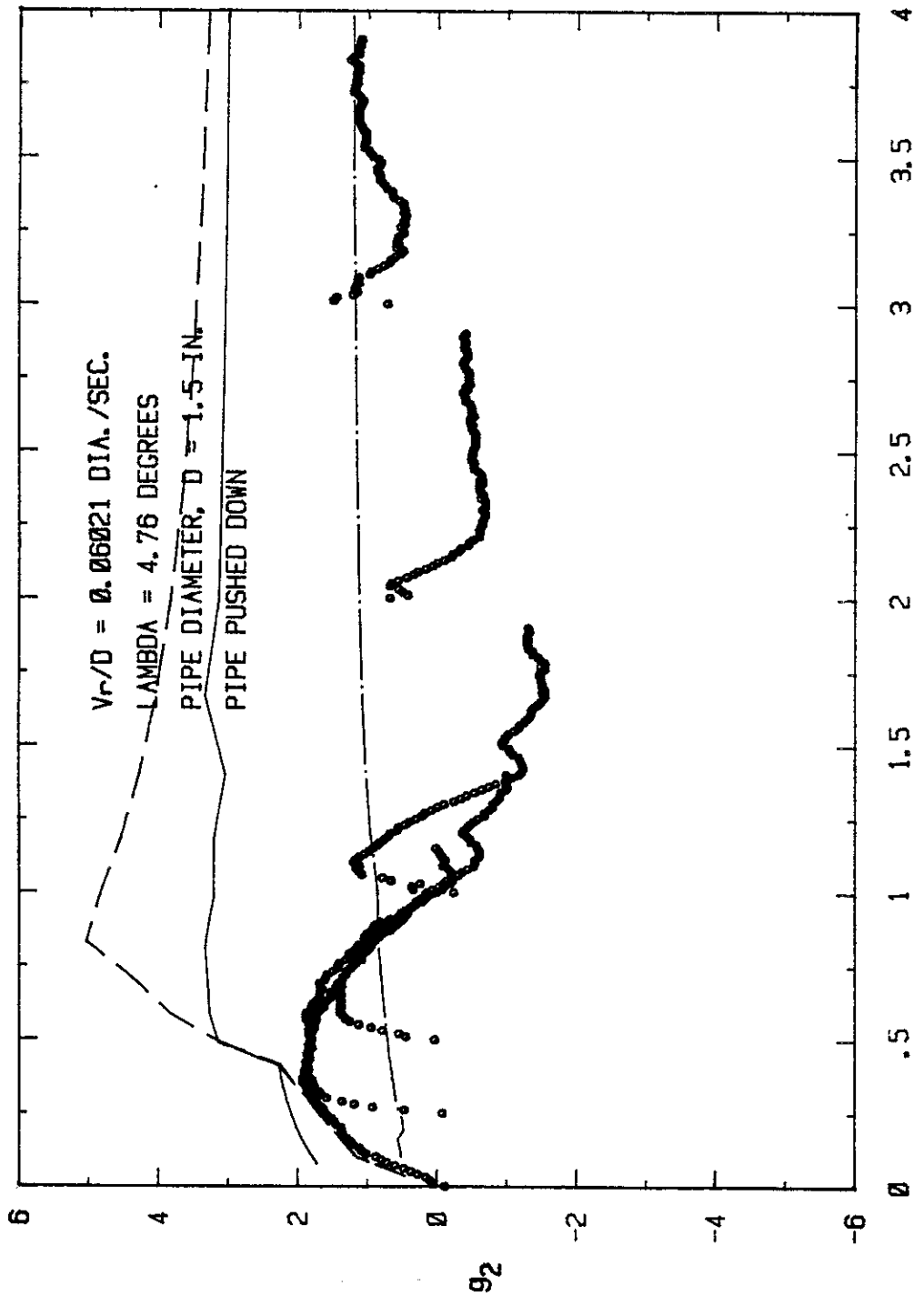

FIG. 3.70 - Combined Plot of Vertical Force Coefficient with Theoretical Combined Buoyant and Vertical Mud Force Correction for Six Different Shallow Angle (4.76°) Pushed-Down Angle Tests.

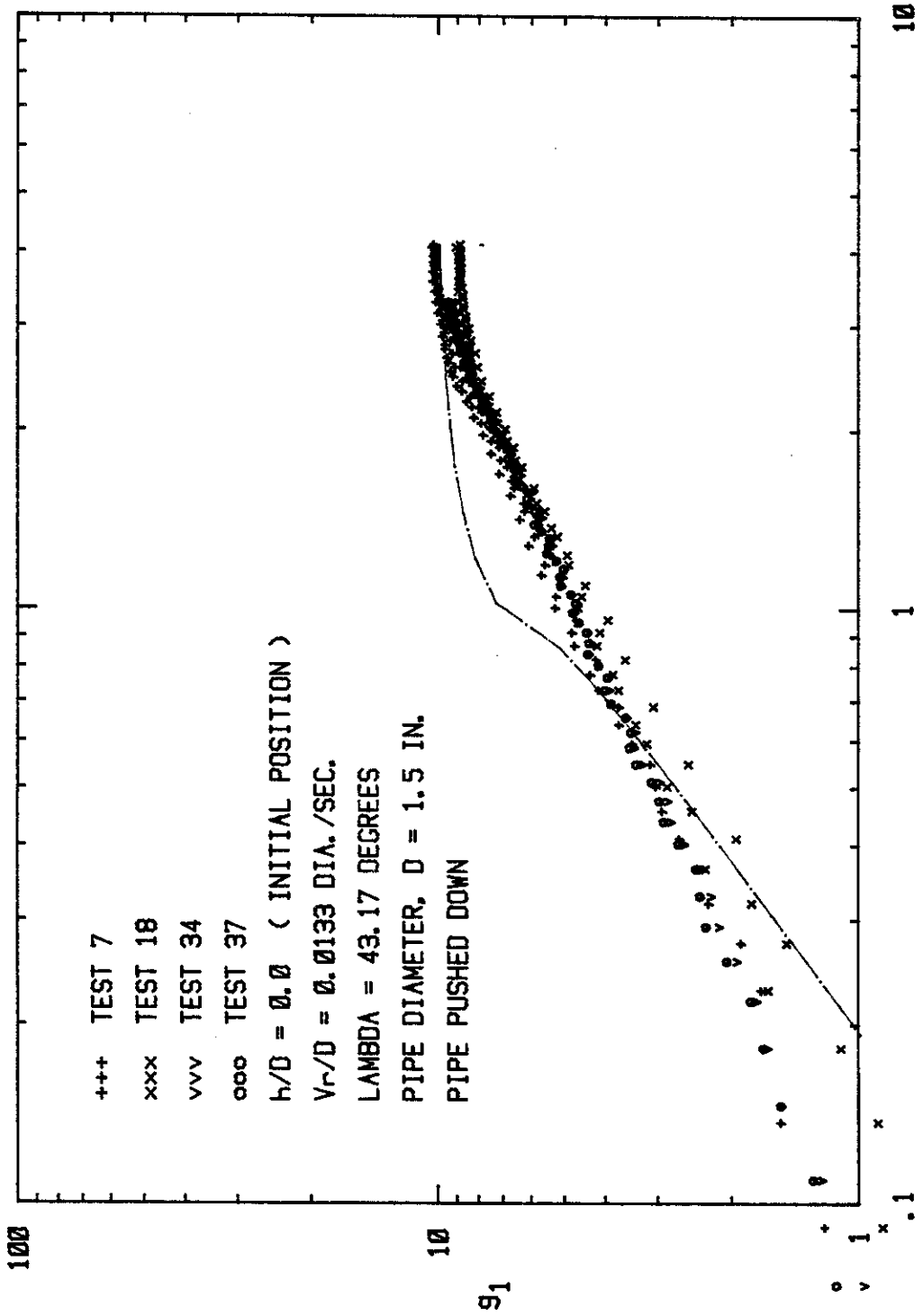

FIG. 3.71 - Combined Plot of Horizontal Force Coefficients Versus Recess Depth for Steep Angle (43.17°) Pushed-Down Angle Tests. Logarithmic Scale.

are plotted in Fig. 3.72. These force coefficients initially increased very rapidly, then leveled off and experienced a slight dip in values at an h/D of approximately 2.25-2.50. The dip was caused by the weight of sediment exerted on top of the pipe when the sediment suddenly collapsed into the void created by the pipe as it moved downward. The initial vertical force coefficients were significantly higher than the horizontal force coefficients, but once the sediment collapse occurred, the vertical force coefficients closely matched the horizontal ones, as might be expected for a pipe moving downward at nearly 45°.

4. Pulled-Up Vertical Tests (1.5 in. O.D Pipe).

A series of three tests were performed at initial h/D values of 0.25, 0.5 and 1.0 in which the pipe was pulled up vertically. Only vertical forces were examined since the horizontal forces and torques remained at zero. The vertical forces increased very quickly as the pipe was pulled from the sediment, reached a peak at very small displacements, and rapidly decreased as the pipe approached the surface. Results are plotted in Fig. 3.73 in terms of vertical force coefficients versus h/D. In contrast to the previous drag curves, these curves start at the initial recess depth and move to the left as the test progresses.

5. Pulled-Up Angle Tests (1.5 in. O.D. Pipe).

These were companion tests to the pushed-down angle tests. The pipes were buried at various values of h/D and then pulled out of the sediment at a shallow angle (4.95°) and at a steep angle (43.17°).

The shallow angle tests were conducted at initial h/D values of 0.25, 0.5, 2.0 and 4.0. All tests exhibited peak or breakaway horizontal forces. For the two shallow depths of burial (h/D = 0.25 and 0.50), this occurred at very small displacements. Breakaway forces for

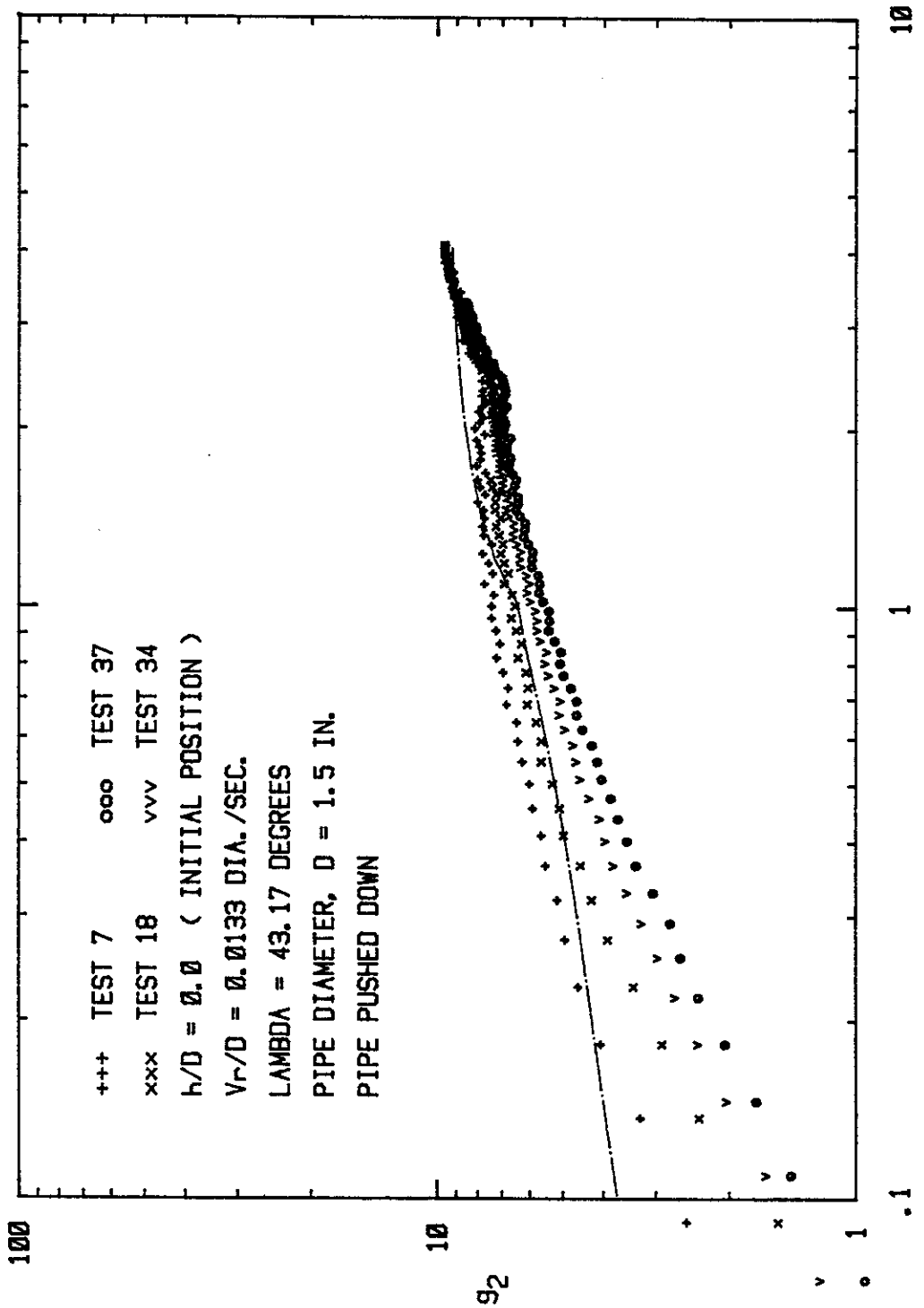

FIG. 3.72 - Combined Plot of Vertical Force Coefficients Versus Recess Depth for Steep Angle (43.17°) Pushed-Down Angle Tests. Logarithmic Scale.

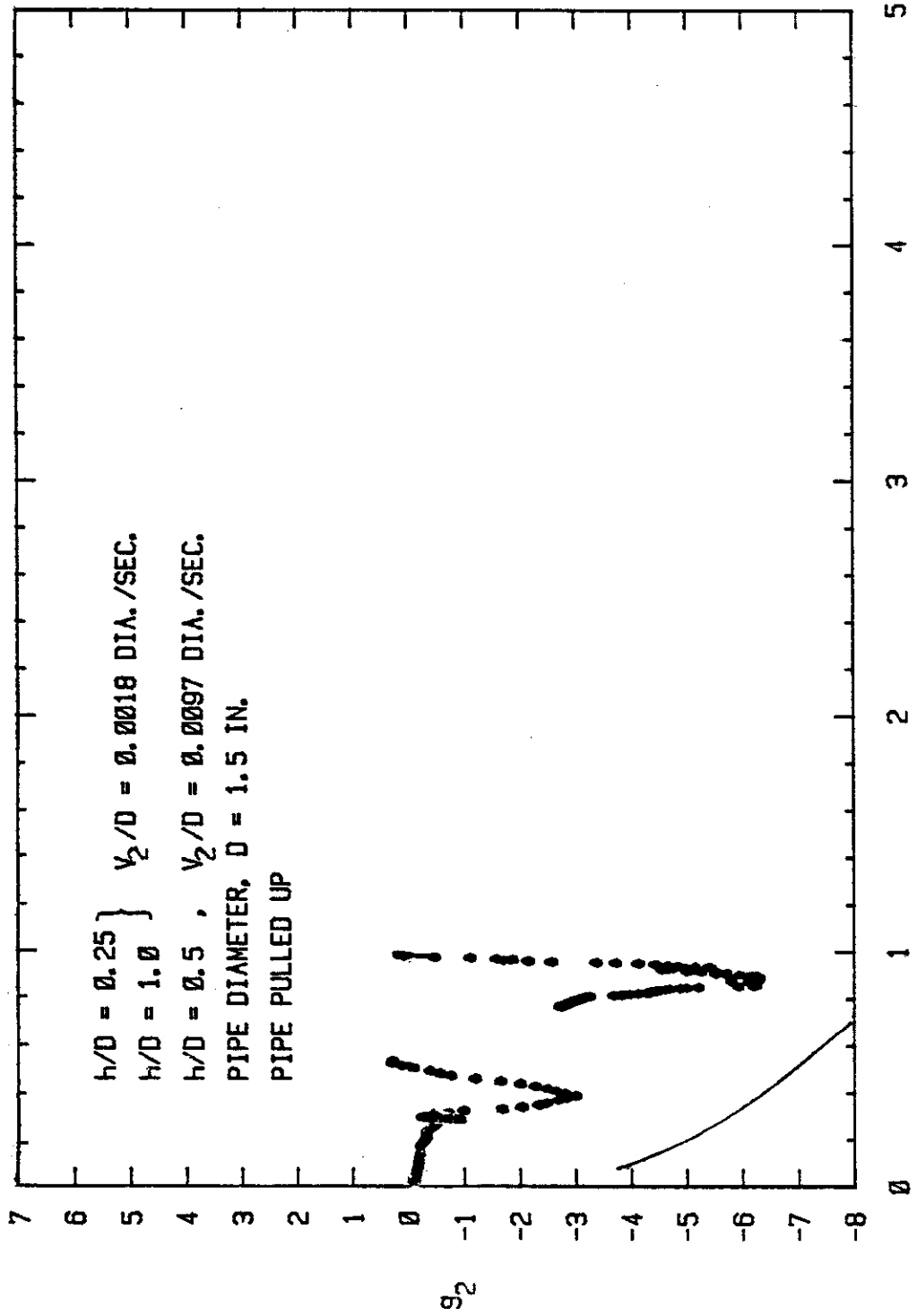

FIG. 3.73 - Combined Plot of Vertical Force Coefficients Versus Recess Depth for Vertical (90°) Pulled-Up Angle Tests.

the deeper burial depths occurred at somewhat larger displacements. Results of the tests are expressed in Fig. 3.74 as horizontal force coefficient versus h/D. These curves have somewhat unusual shapes owing to the sediment pileup as the pipe movement increased. Even though the pipe was attempting to move out of the sediment, the sediment was piling up in front of the pipe and offering additional drag resistance. This explains why the curves for h/D of 0.25 and 0.5 show an initial peak, a decrease and a subsequent increase to a second peak. It also explains why the forces do not go to zero even though the recess depth reaches zero.

A comparison of the horizontal force coefficients for these tests with those obtained for the horizontal drag test shows that the force coefficients for the pull-up tests are larger for h/D of 0.25 and 0.5 and are approximately the same for h/D of 2 and 4.

No vertical drag forces or force coefficients are presented for the shallow angle pull-up tests since the vertical force transducers were found to be malfunctioning.

The results from the pull-up tests conducted at a steep angle were quite different from those conducted at a shallow angle. Peak horizontal forces were obtained for the shallow depths of burial, but at larger displacements than for the shallow angle pull-up tests and sharp peaks were not observed at all for the deeper burial depths. These results are presented in Fig. 3.75 in terms of horizontal force coefficient versus h/D. All horizontal force coefficients are significantly smaller than those obtained for the shallow angle pull-up tests, and they are also smaller than those obtained for the horizontal drag tests as shown in Fig. 3.54.

Vertical force coefficients for the pull-up steep angle tests are

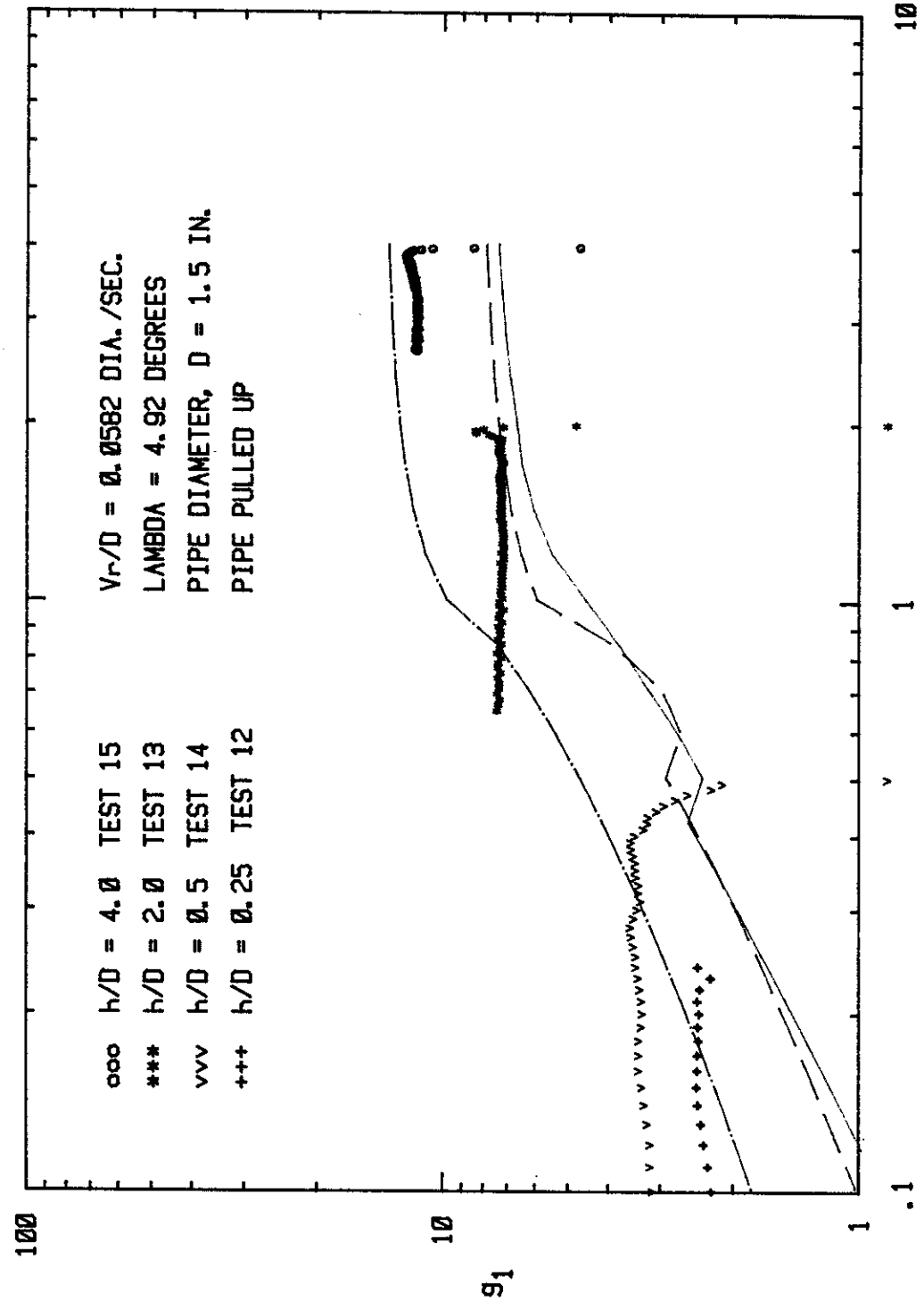

FIG. 3.74 - Combined Plot of Horizontal Force Coefficients Versus Recess Depth for Shallow Angle (4.92°) Pulled-Up Angle Tests. Logarithmic Scale.

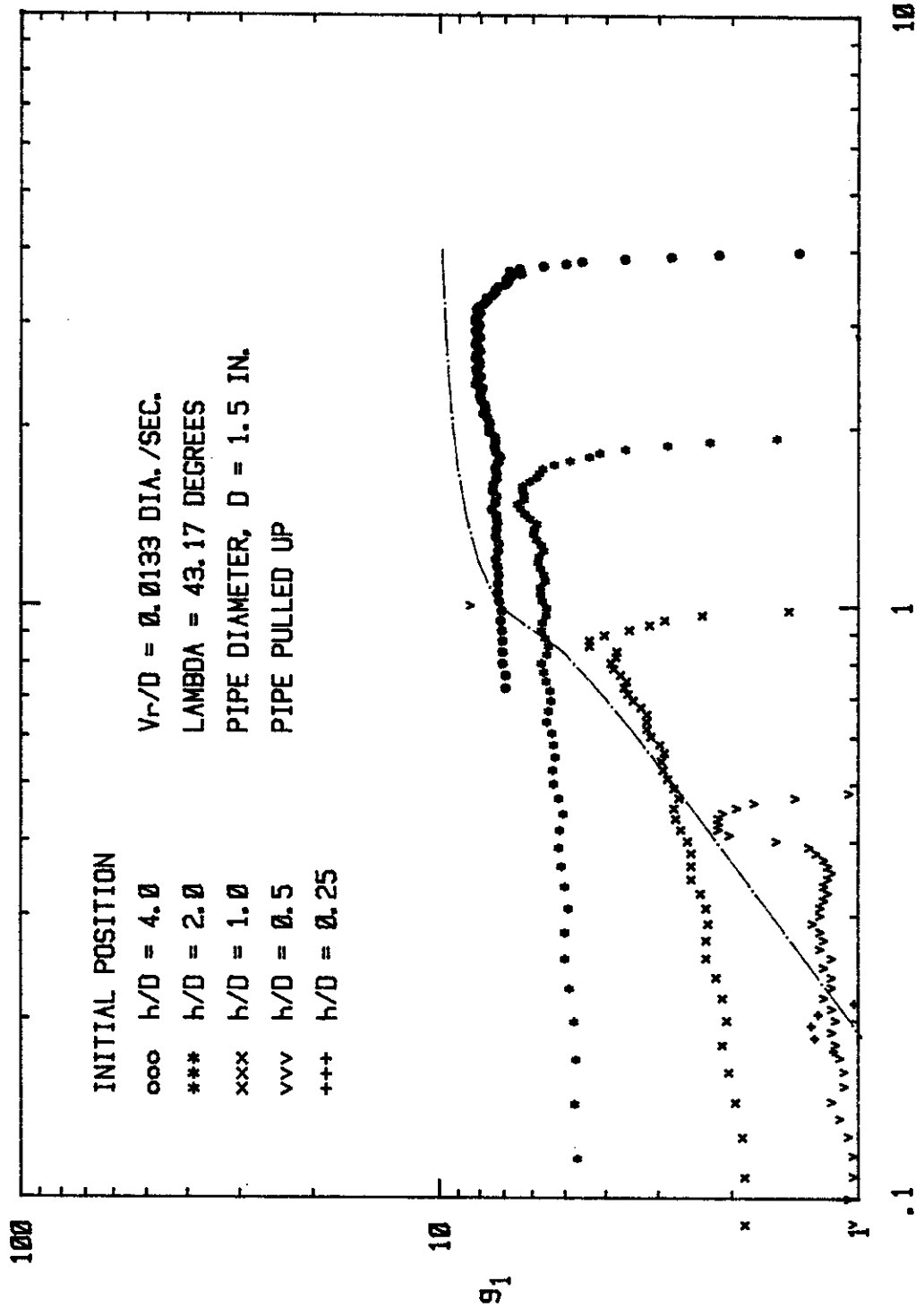

FIG. 3.75 - Combined Plot of Horizontal Force Coefficients Versus Recess Depth for Steep Angle (43.17°) Pulled-Up Angle Test. Logarithmic Scale.

shown in Fig. 3.76. All of these tests exhibited a distinct peak as the pipes were pulled from the sediment. The force coefficients do not approach zero as the pipe approaches the surface owing to pile up of sediment over the pipe. The same data, after being corrected for the initial vertical forces using Fig. 3.50, are shown in Fig. 3.77.

6. Horizontal Drag Tests with 1.5 in. O.D. Freely Rotating Pipe. These tests were performed on 1.5 in. pipe to determine whether the drag forces would be affected by free rotation of the pipe. Initial recess depths, h/D, of 0.25, 0.5, 1.0, 2.0 and 4.0 were utilized with replicate tests at h/D of 1.0 and 4.0.

Horizontal drag force curves are similar to those obtained for the fixed end or nonrotating pipes. The major difference occurred at the initiation of movement where the breakaway force was slightly smaller for the freely rotating pipes. The horizontal force coefficient is plotted versus h/D in Fig. 3.78 for the failure points, and in Fig. 3.79 for U/D = 3 points. These results are nearly identical to those shown in the companion curve (Figs. 3.54 and 3.55) for the fixed end tests.

The same observations held for the vertical forces. Curves of vertical force versus displacement are similar to those obtained for the nonrotating pipe. When the results are plotted as vertical force coefficient versus h/D (Fig. 3.80) and compared to Fig. 3.57 some minor differences are noted. At h/D = 0.25, the vertical force coefficient for the freely rotating pipe was slightly higher. It was slightly smaller for h/D of 0.5, 1.0 and 2.0, but the results overall are probably within the error band of the data for the two types of tests.

Thus, the test results indicate that pipe rotation has a relatively minor effect on horizontal and vertical drag forces.

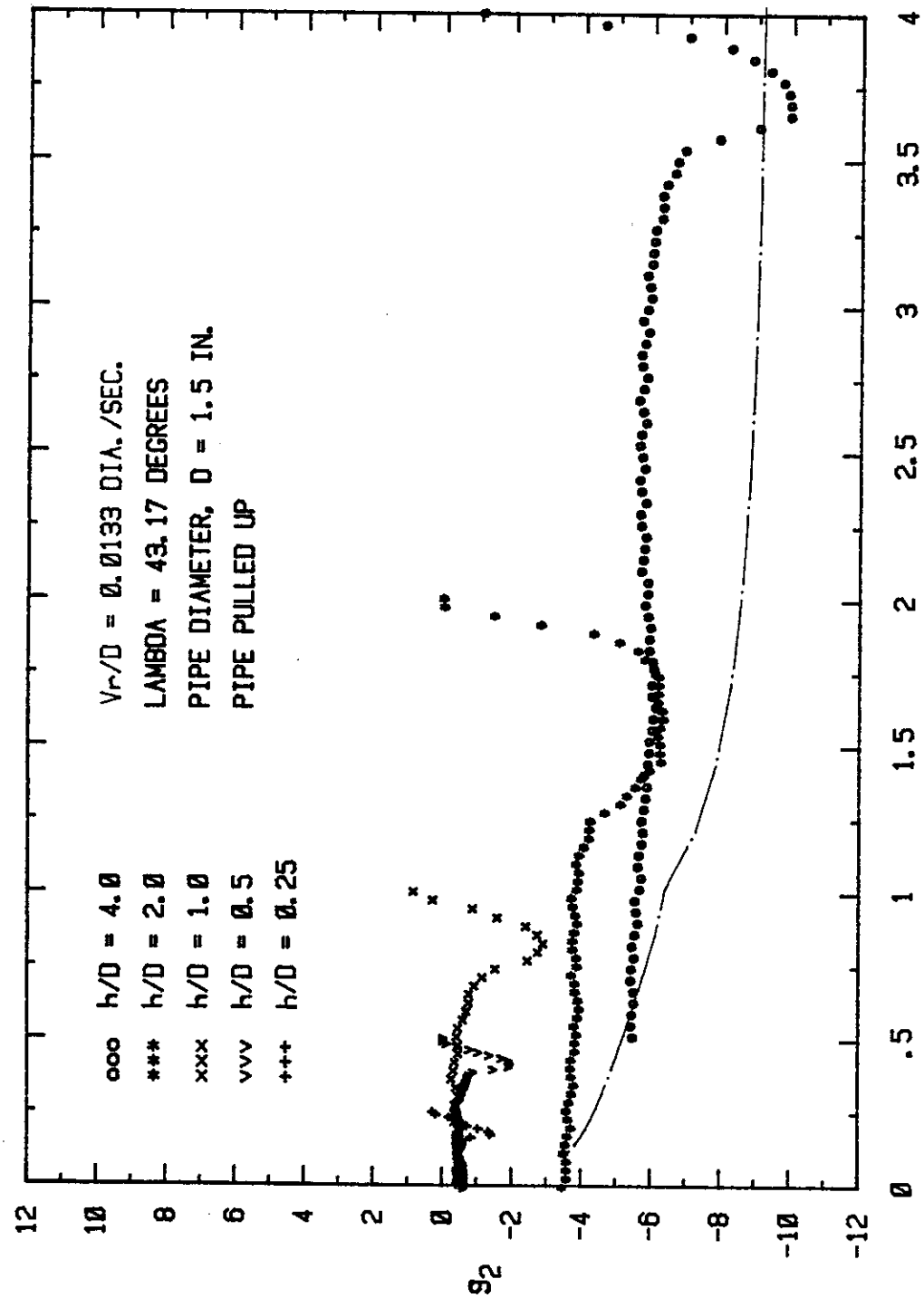

FIG. 3.76 - Combined Plot of Vertical Force Coefficients Versus Recess Depth for Steep Angle (43.17°) Pulled-Up Angle Tests.

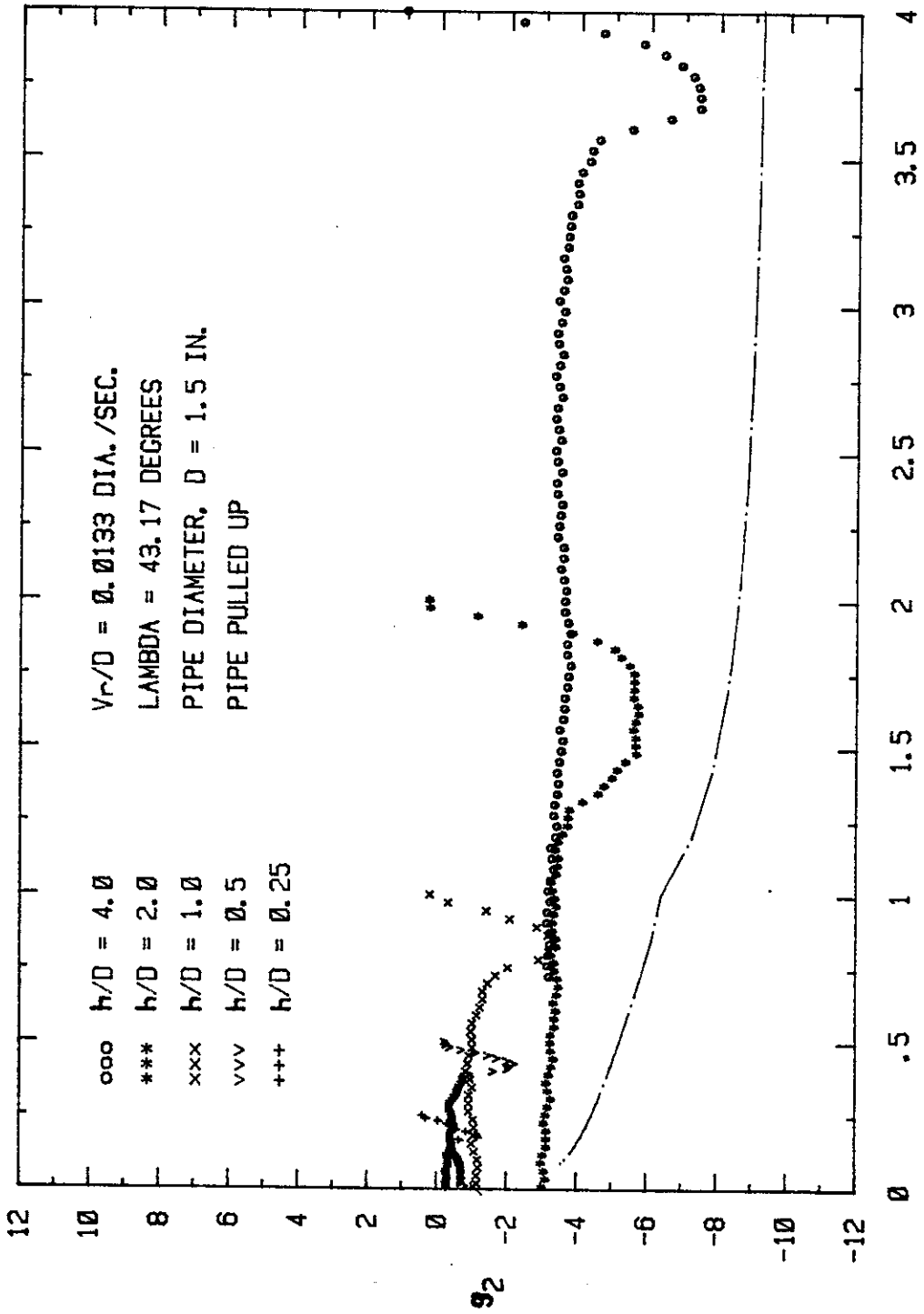

FIG. 3.77 - Combined Plot of Vertical Force Coefficients with Theoretical Combined Buoyant and Vertical Mud Force Correction for Steep Angle (43.17°) Pulled-Up Angle Tests.

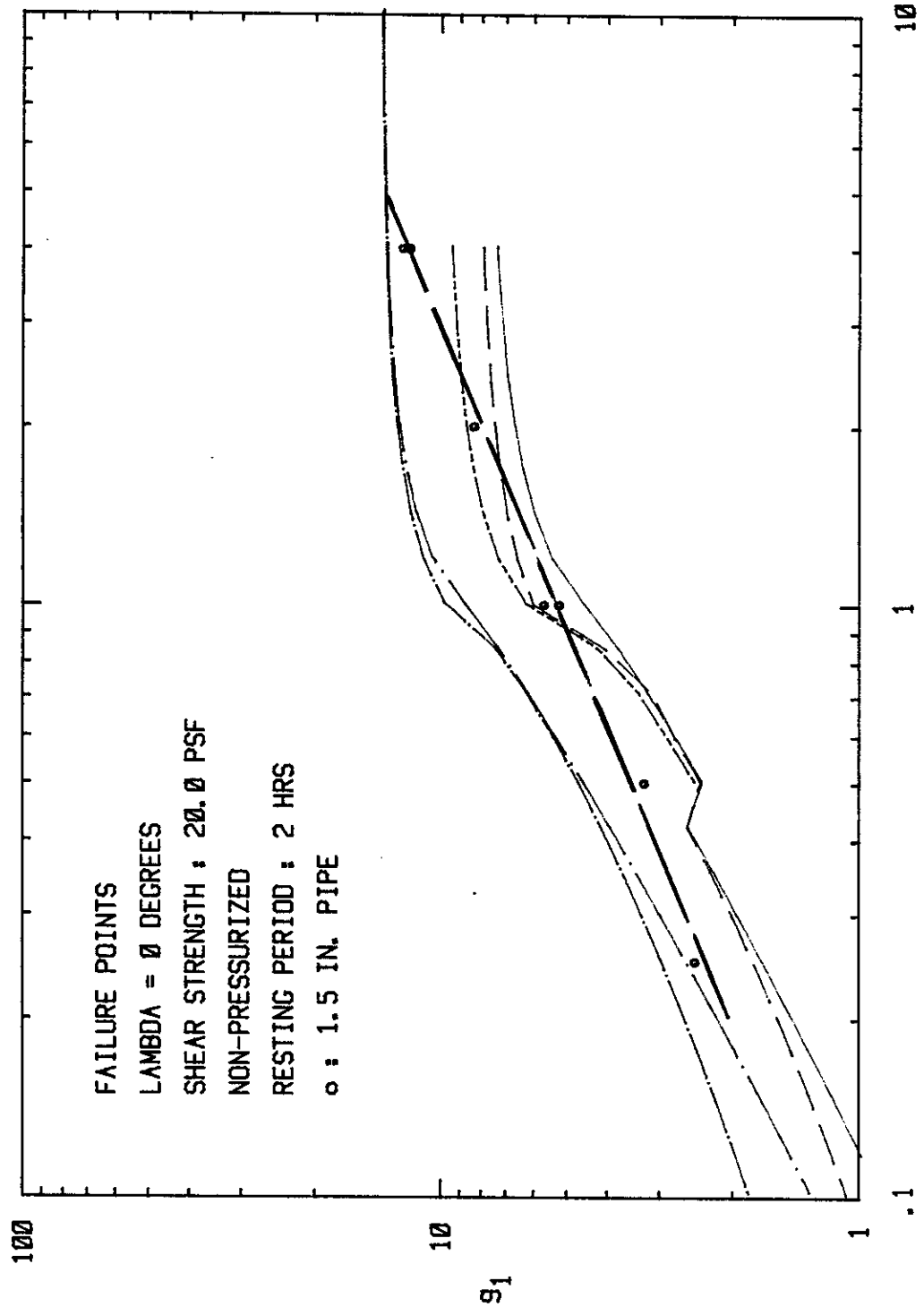

FIG. 3.78 - Horizontal Force Coefficients at Failure Points Versus Recess Depths for Freely Rotated Horizontal Drag Tests. Logarithmic Scale.

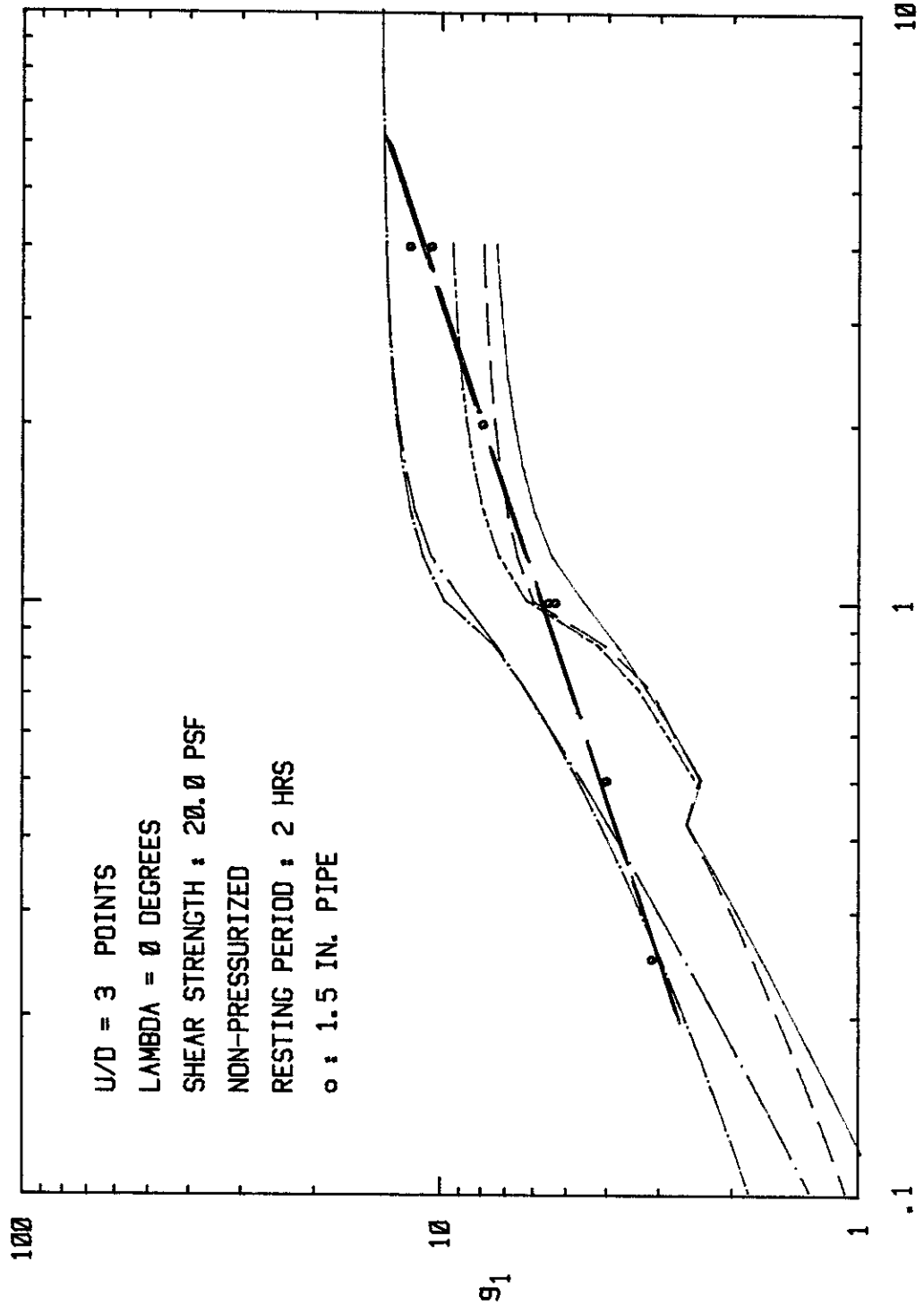

FIG. 3.79 - Horizontal Force Coefficients at U/D = 3 Points Versus Recess Depths for Freely Rotated Horizontal Drag Tests. Logarithmic Scale.

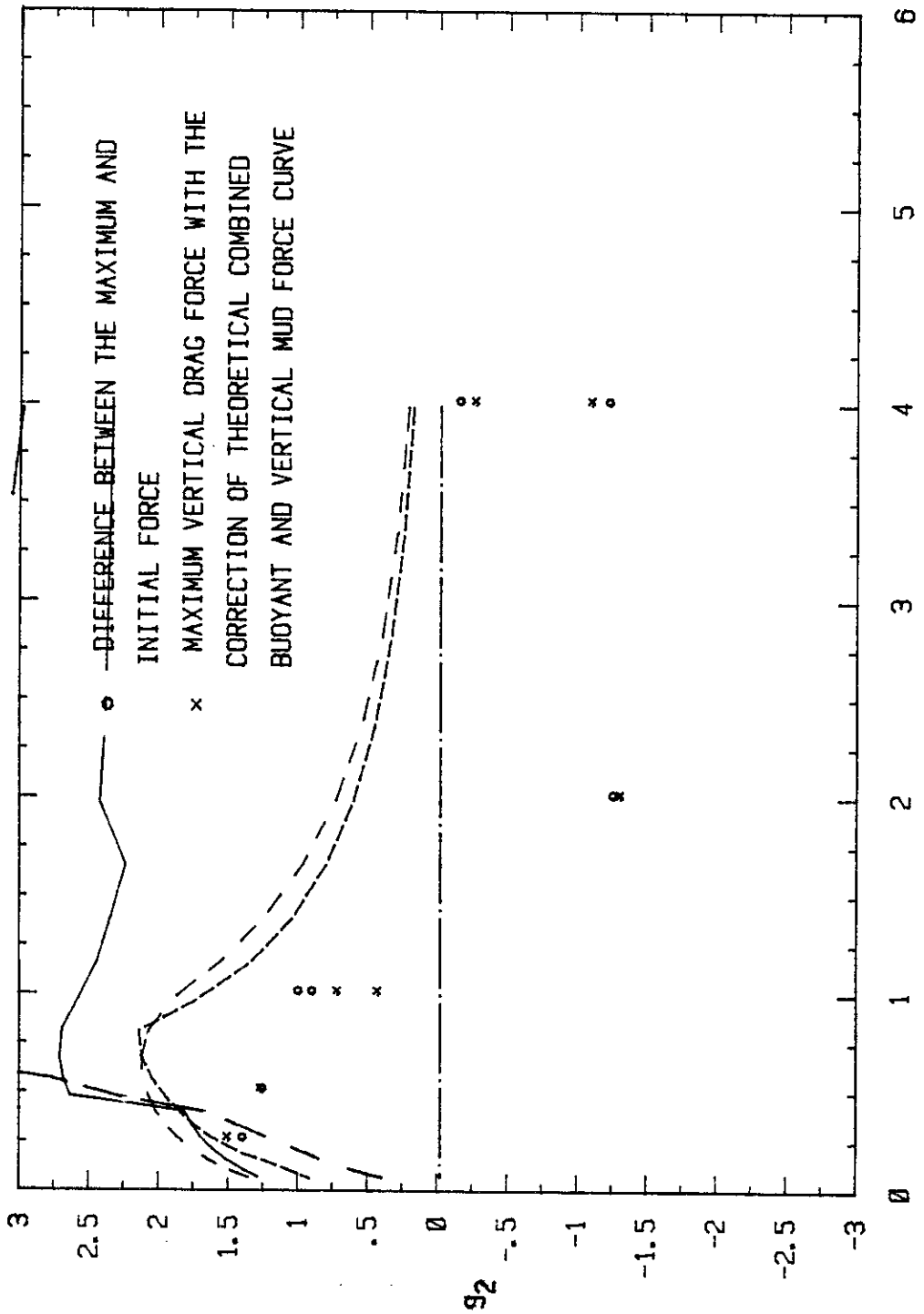

FIG. 3.80 - Vertical Force Coefficients Versus Recess Depths for Freely Rotated Horizontal Drag Tests.

7. Horizontal Drag Tests with 6 in. O.D. Pipe.

In this series of tests, a nonrotating 6 in. diameter pipe with a 12 in. long active or instrumented test section was used. These tests were performed during the latter stages of the program, and there was some deterioration of the instrumentation, which was manifested primarily in the form of electronic signal "drift". Drift during the actual pipe movement was insignificant and had no influence on the horizontal or vertical drag forces. However, during the rest period between packing the pipe in the sediment and performing the drag test, the drift was large enough to render the initial or at-rest vertical forces questionable. Since these forces influence the calculation of the vertical force coefficients, these factors are also questionable; however, the horizontal force coefficients are not affected.

In general, during the early portion of the test, the trend of the horizontal force coefficient versus displacement curves for the 6 in. pipe was similar to the trend observed for the 1.5 in pipe (Fig. 3.81). There was an initial peak or breakaway force in the early stages of pipe displacement, followed by a decrease in force, and then an increase as the pipe displacement increased and the sediment started piling up over the pipe. The horizontal force coefficients for the two pipe sizes, shown on Fig. 3.82, are nearly identical at the failure points. However, at $U/D = 3$, g_1 is higher for the 6 in. pipe (Fig. 3.83).

Vertical force versus displacement curves for the two pipe sizes differed in shape (Fig. 3.84), including a significant difference between the initial vertical forces, due in part to the electronic drift described earlier. Because of the drift, the correction to the initial vertical forces (from Fig. 3.50) was inappropriate, and the vertical force coefficients were calculated only by using the difference in the

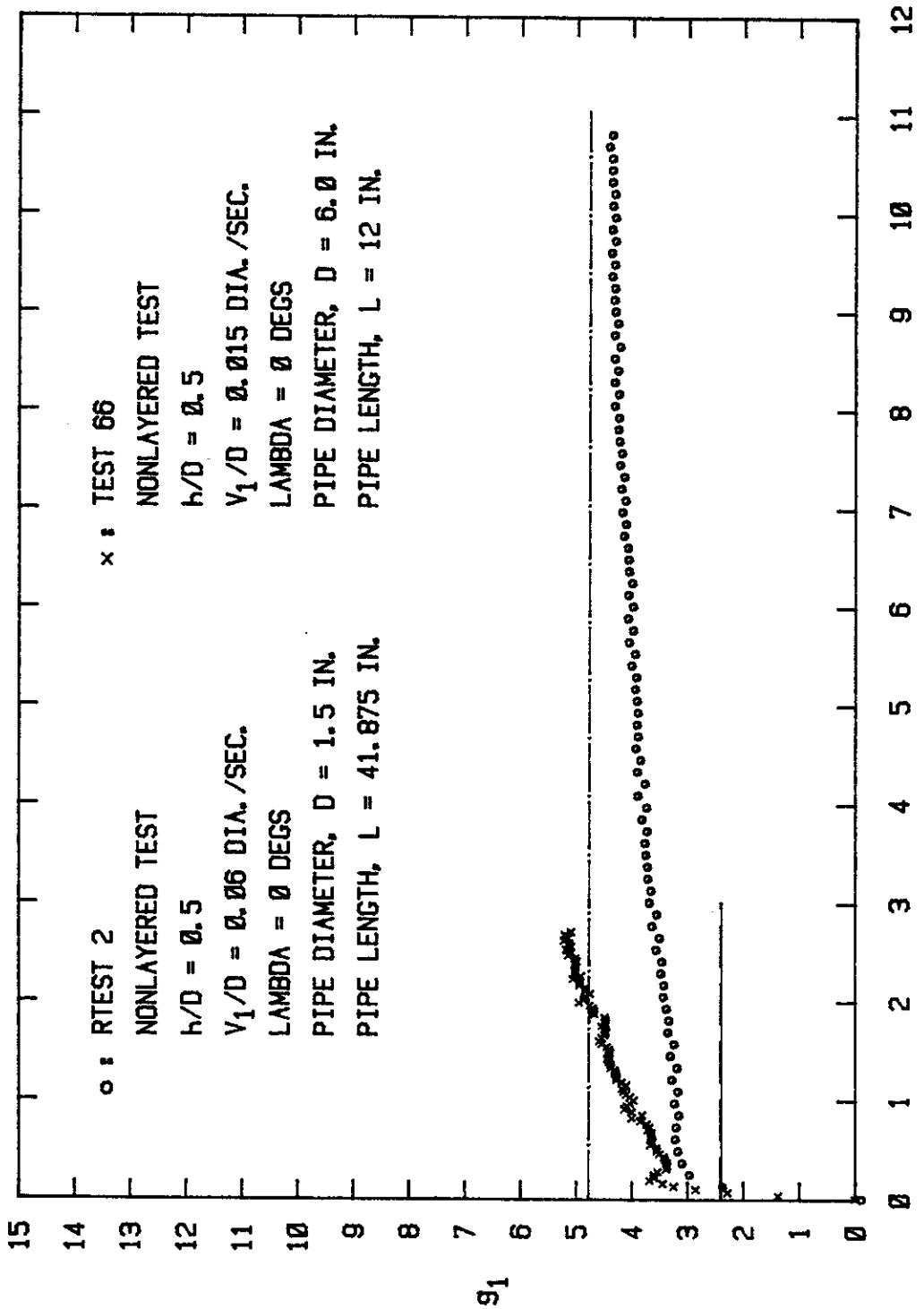

FIG. 3.81 - Comparison of Horizontal Force Coefficients Versus Displacement Curve for 1.5 in. and 6.0 in. Diameter Pipes for h/D = 0.5.

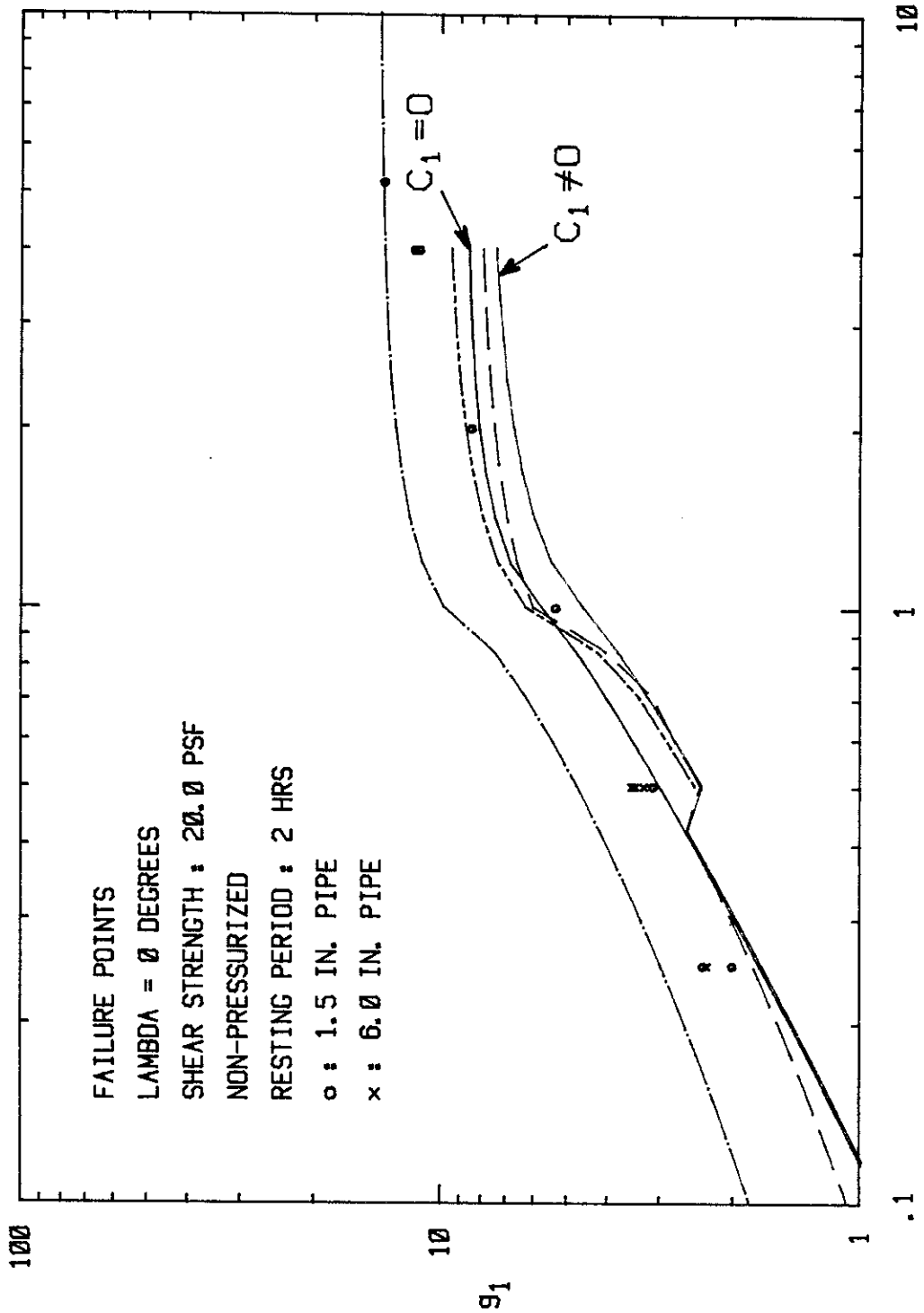

FIG. 3.82a - Comparison of Horizontal Force Coefficients at Failure Points for 1.5 in. and 6.0 in. Pipe. Fixed-Ends Horizontal Drag Tests. Logarithmic Scale.

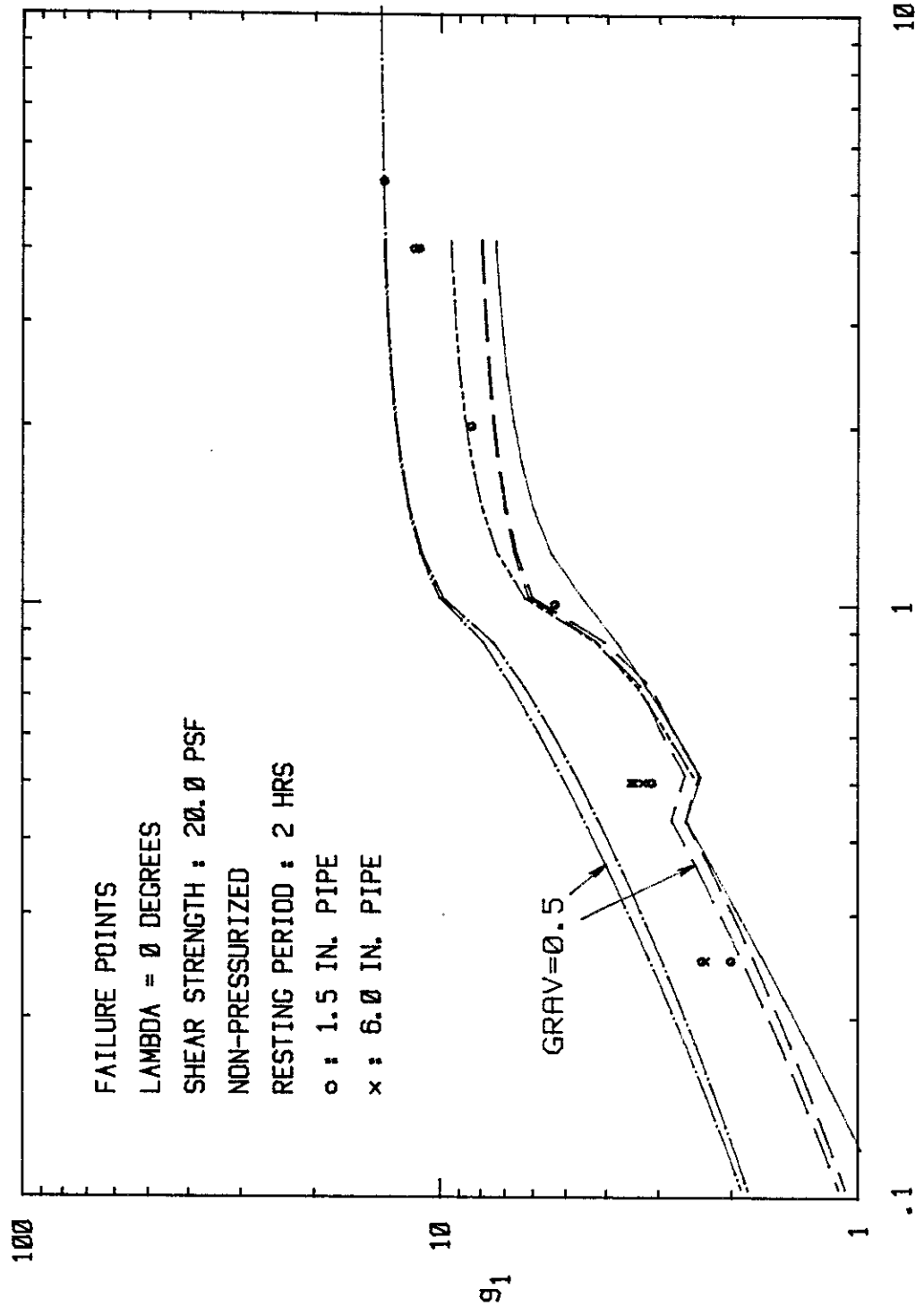

FIG. 3.82b - Comparison of Horizontal Force Coefficients at Failure Points for 1.5 in. and 6.0 in. Pipe. Fixed-Ends Horizontal Drag Tests. Logarithmic Scale. (Same experimental data as in FIG. 3.82a)

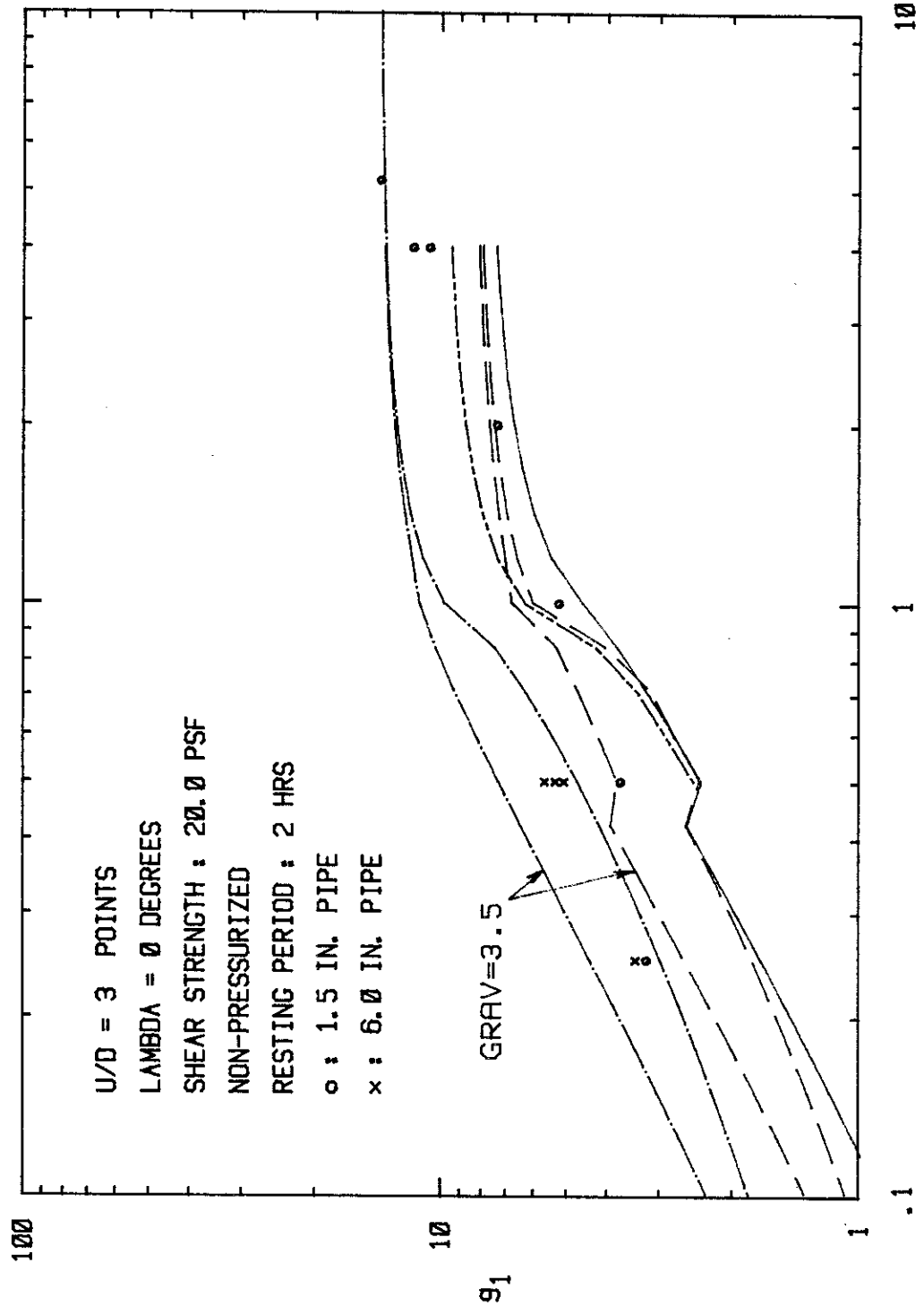

FIG. 3.83 - Comparison of Horizontal Force Coefficients at U/D = 3 Points for 1.5 in. and 6.0 in. Pipe for Fixed-Ends Horizontal Drag Tests. Logarithmic Scale.

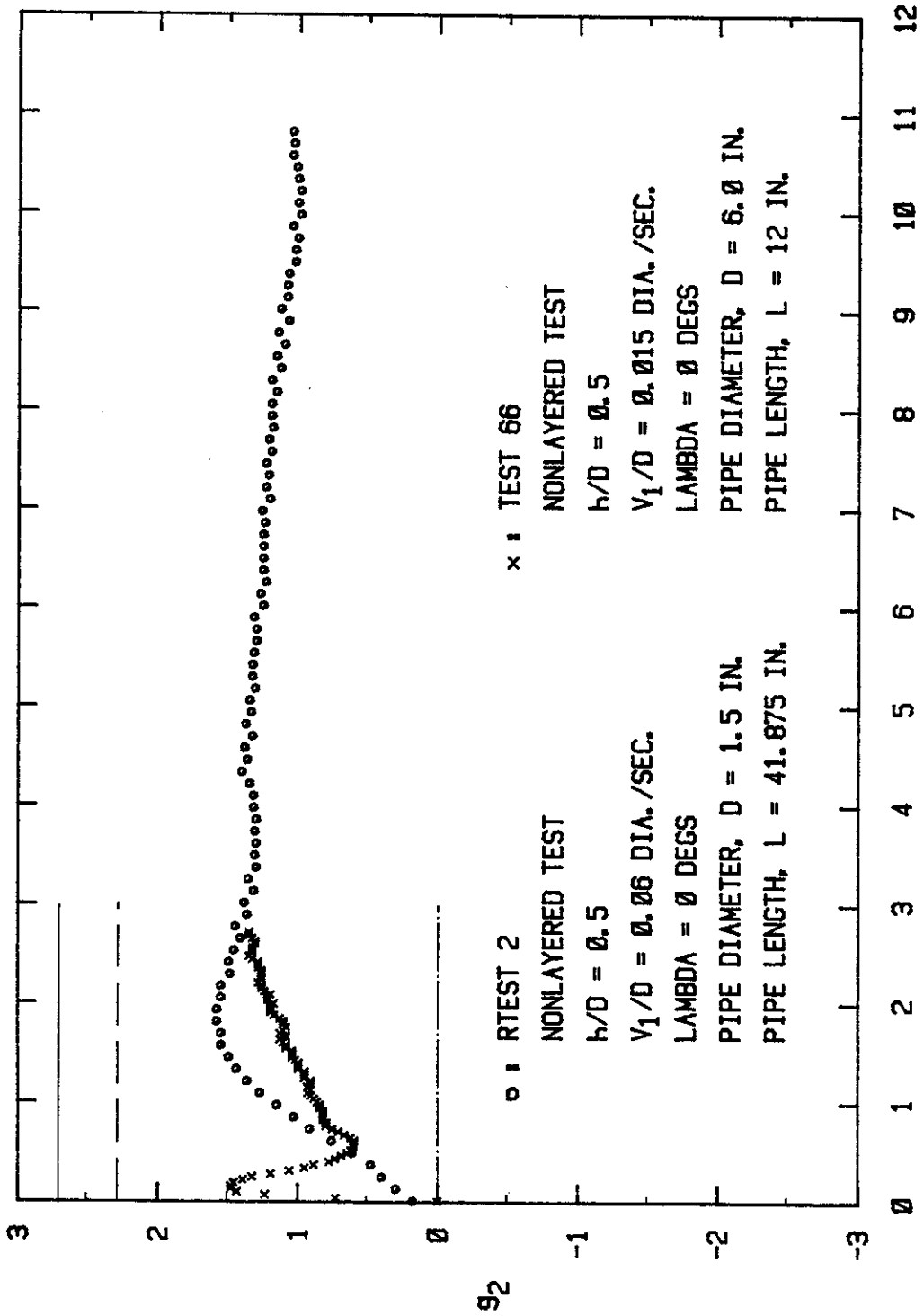

FIG. 3.84 - Comparison of Vertical Force Coefficients Versus Displacement Curves for 1.5 in. and 6.0 in. Diameter Pipe for h/D = 0.5.

initial and peak forces. With this approach, the vertical force coefficients for the 6 in. pipe appear to be slightly higher than for the 1.5 in. pipe (Fig. 3.85).

8. Fixed-Ends Horizontal Layered Drag Tests (6.0 in. O.D. Pipe). The sediment used in these tests consisted of two layers with softer material (smaller undrained shear strength) on the top. Force coefficients were calculated utilizing weighted average shear strengths based on the initial depth of immersion of the pipe in each layer. These results, shown in Table 3.2, may be misleading since the influence of the sediment extends to a depth greater than the base of the pipe. Nevertheless, this approach provides an intuitive way of analyzing drag factors in sediment with varying shear strengths.

It is also appropriate to analyze the actual force-displacement curves to view differences between the layered and homogeneous sediment drag forces. The horizontal force-displacement curves for the two layered tests with h/D = 0.5 are compared with a similar test in a nonlayered sediment in Fig. 3.86. Tests 67 and 68 were similar with the softer layer, which was 3 in. thick, extending from the surface to the bottom of the pipe, but the soft layer in Test 67 had an undrained strength of 12.9 psf, whereas for Test 68 it was 9.5 psf. The layered tests do not have a pronounced force peak as observed in the companion nonlayered test (Test 66). The increase in force with continued displacement is smaller in the layered soil than in the nonlayered soil, but the lower overall strength in the layered soil may be responsible for these smaller forces.

Figure 3.87 compares the results of a layered soil test with h/D = 1 to a similar nonlayered test on 1.5 in. diameter pipe. The

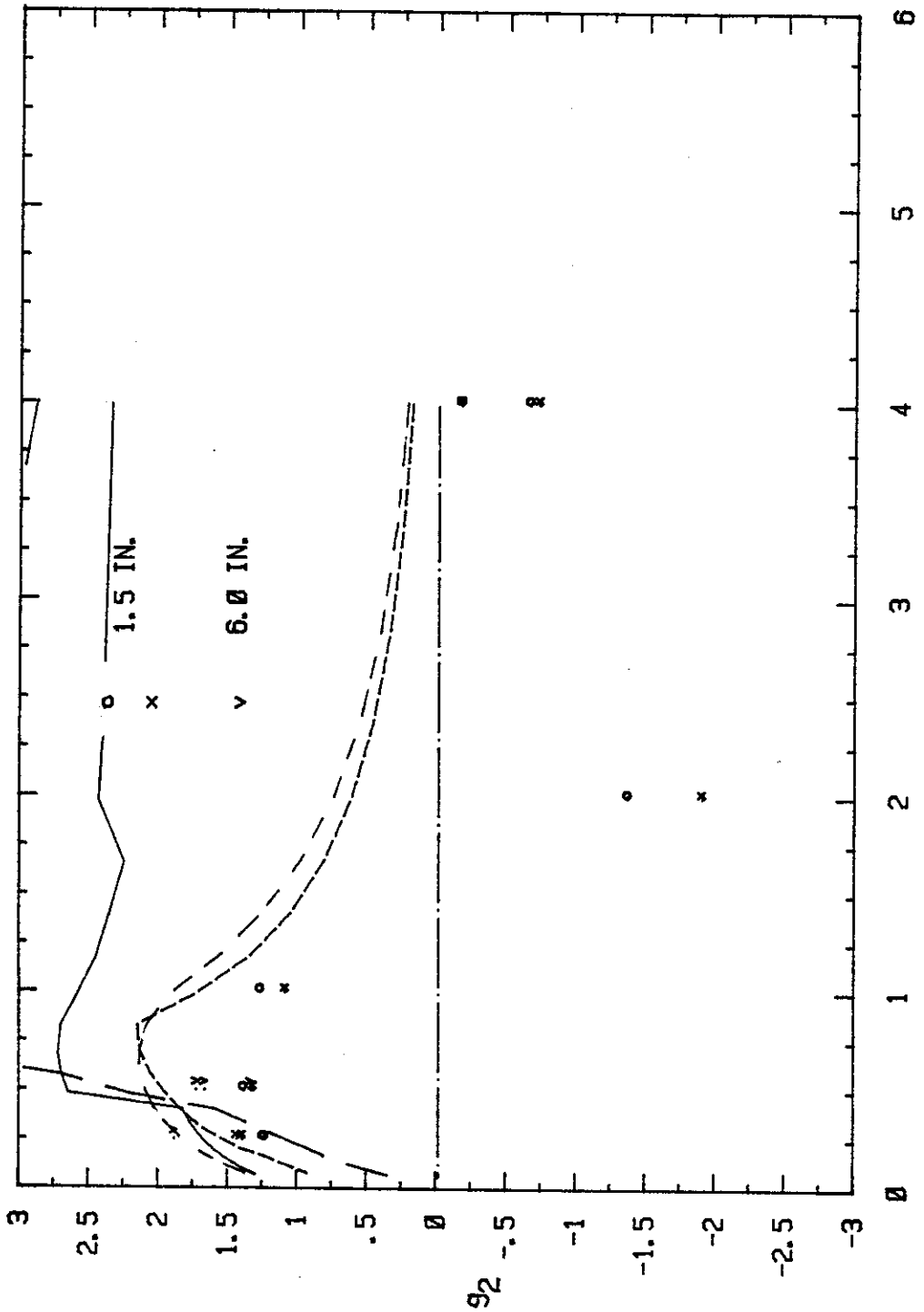

FIG. 3.85 - Comparison of Vertical Force Coefficients for 1.5 in. and 6.0 in. Pipes. Fixed-Ends Horizontal Drag Tests.

Table 3.2 - Comparison of Test Results for Layered and Nonlayered Sediments - Horizontal Drag Test

Test Description	Layered Sediments 3 in. Softer Sediment Overlying Stronger Sediment		Nonlayered Sediment		Layered Sediments 4.5 in. Softer Sediment Overlying Stronger Sediment	Nonlayered Sediment
Test Number	67	68	64	66	69	RTEST3
Recess Depth, h/D	0.5	0.5	0.5	0.5	1.0	1.0
Pipe Diameter, D (in.)	6.0	6.0	6.0	6.0	6.0	1.5
Use of Weighted Shear Strength Extending to Bottom of Pipe						
Undrained Shear Strength Used in Calculations, C_{u_o} (psf)	12.9	9.5	20.0	20.0	12.13	23.0
Horizontal Force Coefficient g_1	4.27	5.08	3.42	3.34	6.55	5.26
Vertical Force Coefficient g_2	1.85	2.61	1.72	1.66	2.72	1.26
Use of Weighted Shear Strength Extending 3 in. Below Pipe						
Undrained Shear Strength Used in Calculations, C_{u_o} (psf)	16.45	14.75	20.0	20.0	14.75	23.0
Horizontal Force Coefficient, g_1	3.35	3.3	3.42	3.34	5.40	5.26
Vertical Force Coefficient, g_2	1.45	1.7	1.72	1.50	2.23	1.26

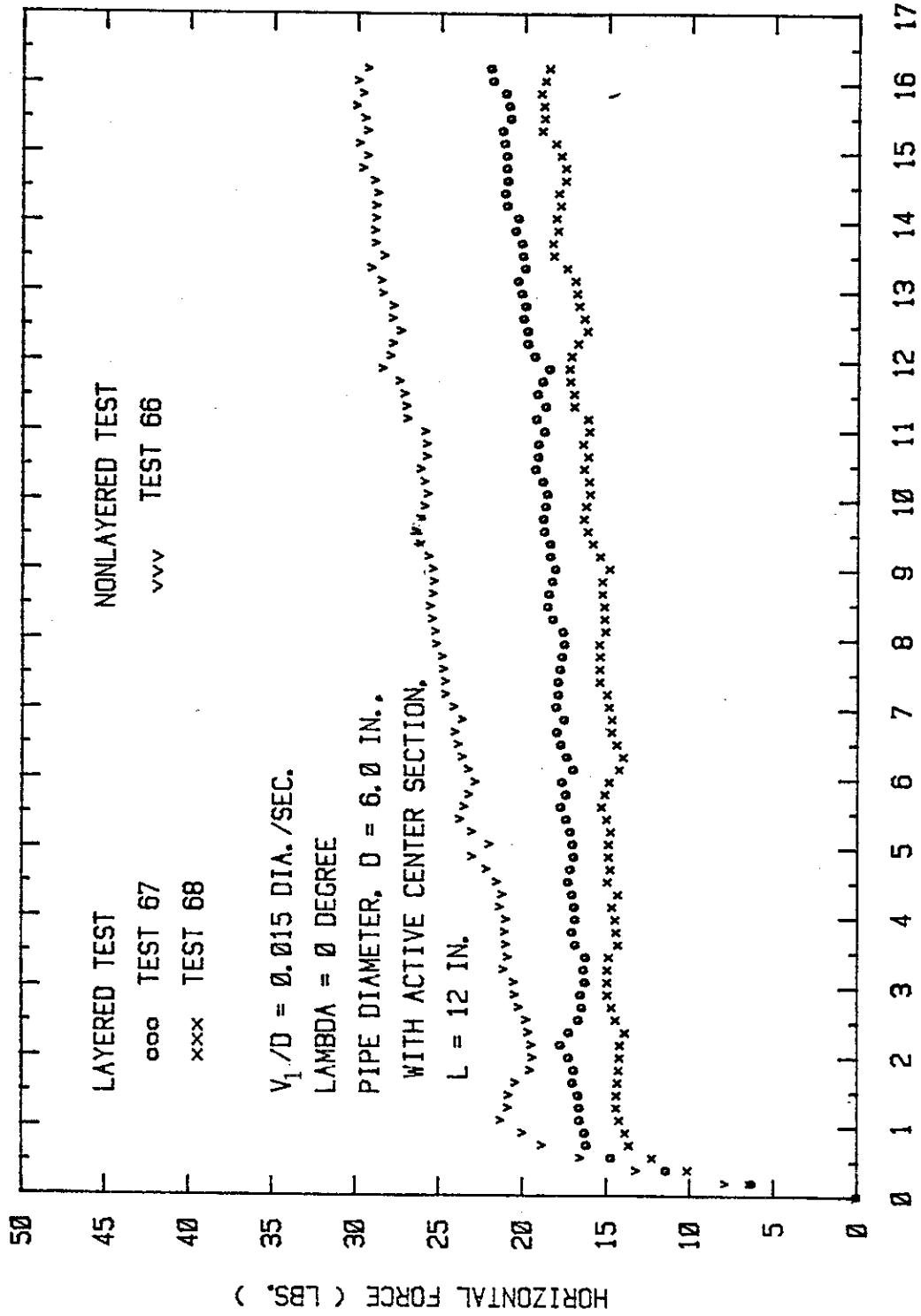

FIG. 3.86 - Comparison of Horizontal Force Versus Displacement Curves for h/D = 0.5 for Layered and Nonlayered Tests

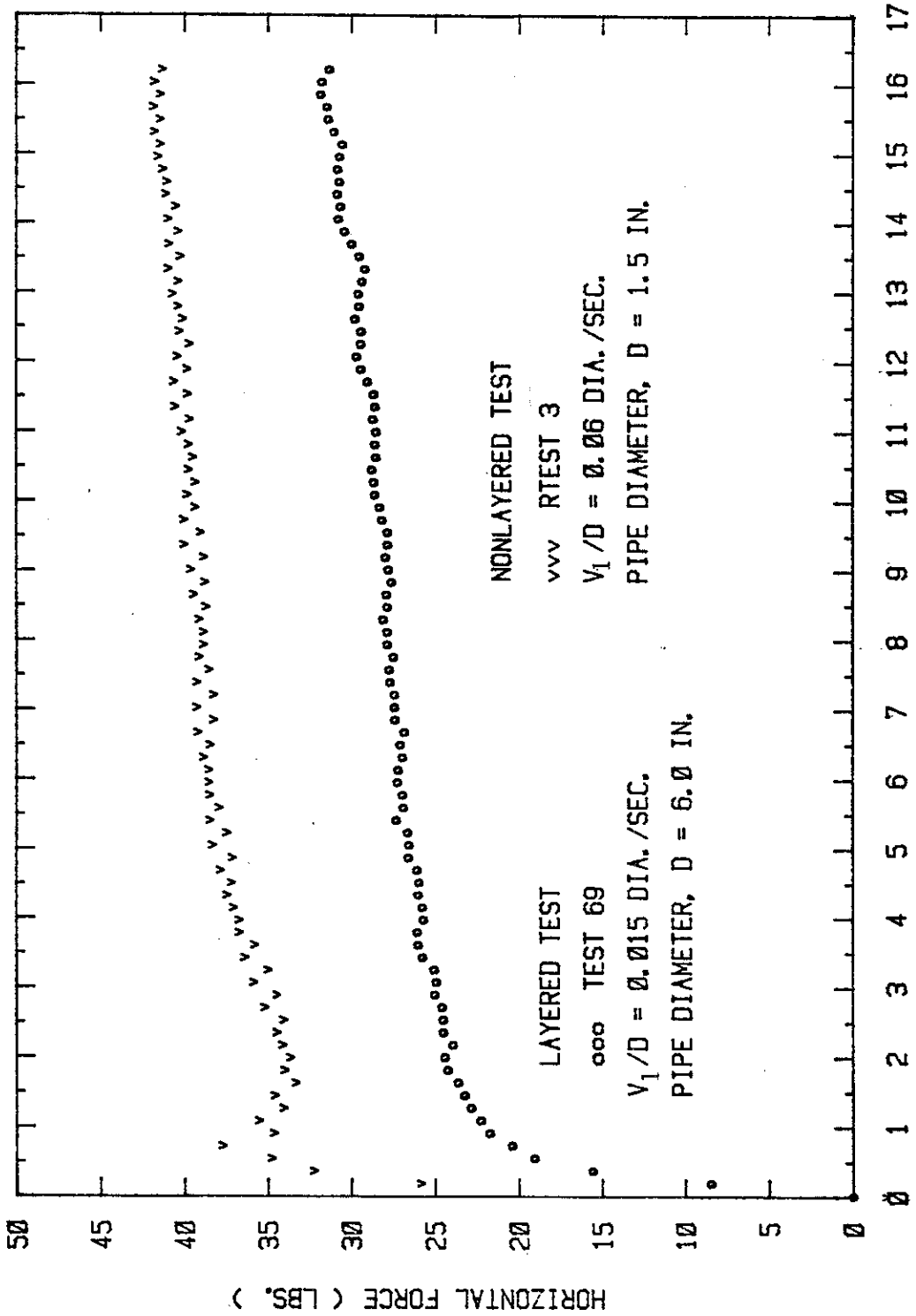

FIG. 3.87 - Comparison of Horizontal Force Versus Displacement Curves for h/D = 1.0 for Layered and Nonlayered Tests.

layered soil was 4.5 in. of very soft (9.5 psf) shear strength soil overlying 20 psf shear strength material. Except for the force peak exhibited at small displacement for the nonlayered soil, there is little difference in the general shape of these two curves.

The vertical force-displacement curves at h/D = 0.5 for layered and nonlayered soils are similar except the nonlayered soil exhibited a pronounced peak before the vertical force started rising as displacement increased (Fig. 3.88). However, there was a completely different pattern for the h/D = 1 tests (Fig. 3.89): the nonlayered vertical force decreased nearly to zero with large displacements, whereas the vertical force in the layered soil continuously increased. This is not unexpected since the stronger lower layer of soil will continuously push upward on the pipe.

Table 3.2 shows that both horizontal and vertical force coefficients are higher for the layered tests when the drag factors are based on a weighted average shear strength extended to the base of the pipe. This implies that the pipe stresses extend into the underlying stronger material and that the underlying, high strength layer has a greater effect on the drag force than was considered in the calculations. If the computations are based on a weighted average shear strength with the sediment assumed to be contributing to drag resistance to a depth of one radius (3 in.) below the pipe, essentially the same drag factors are obtained as for the nonlayered case. This latter approach was used for Figs. 3.90-3.92, which are plots of g_1 versus U/D, and for Figs. 3.93-3.95, which are plots of g_2 versus U/D. The failure points selected from these plots are also shown in Table 3.2.

3.4.2 Test Results in Intermediate Drag Box

Again, several types of tests were performed in this drag box.

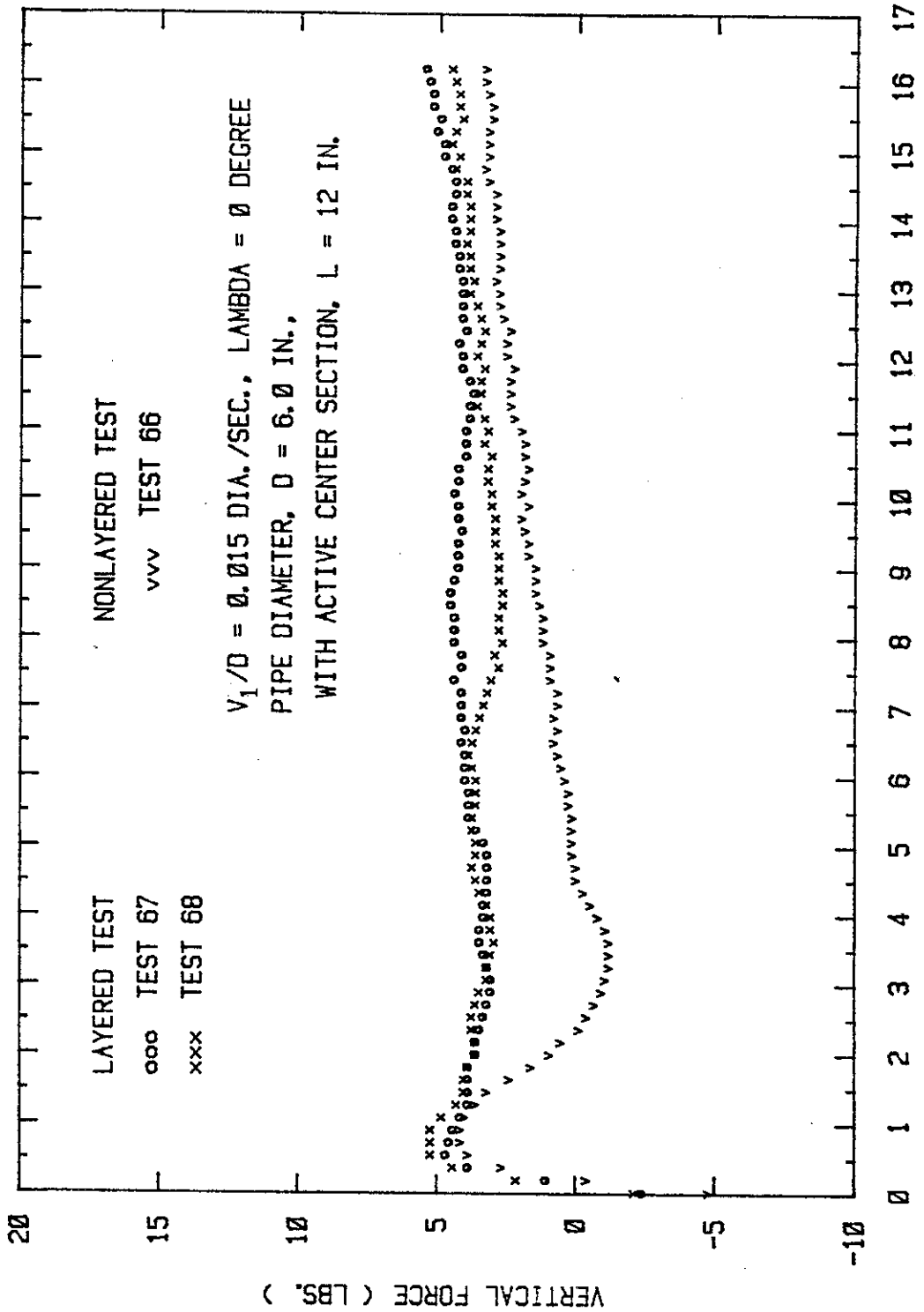

FIG. 3.88 - Comparison of Vertical Force Versus Displacement Curves for h/D = 0.5 for Layered and Nonlayered Tests.

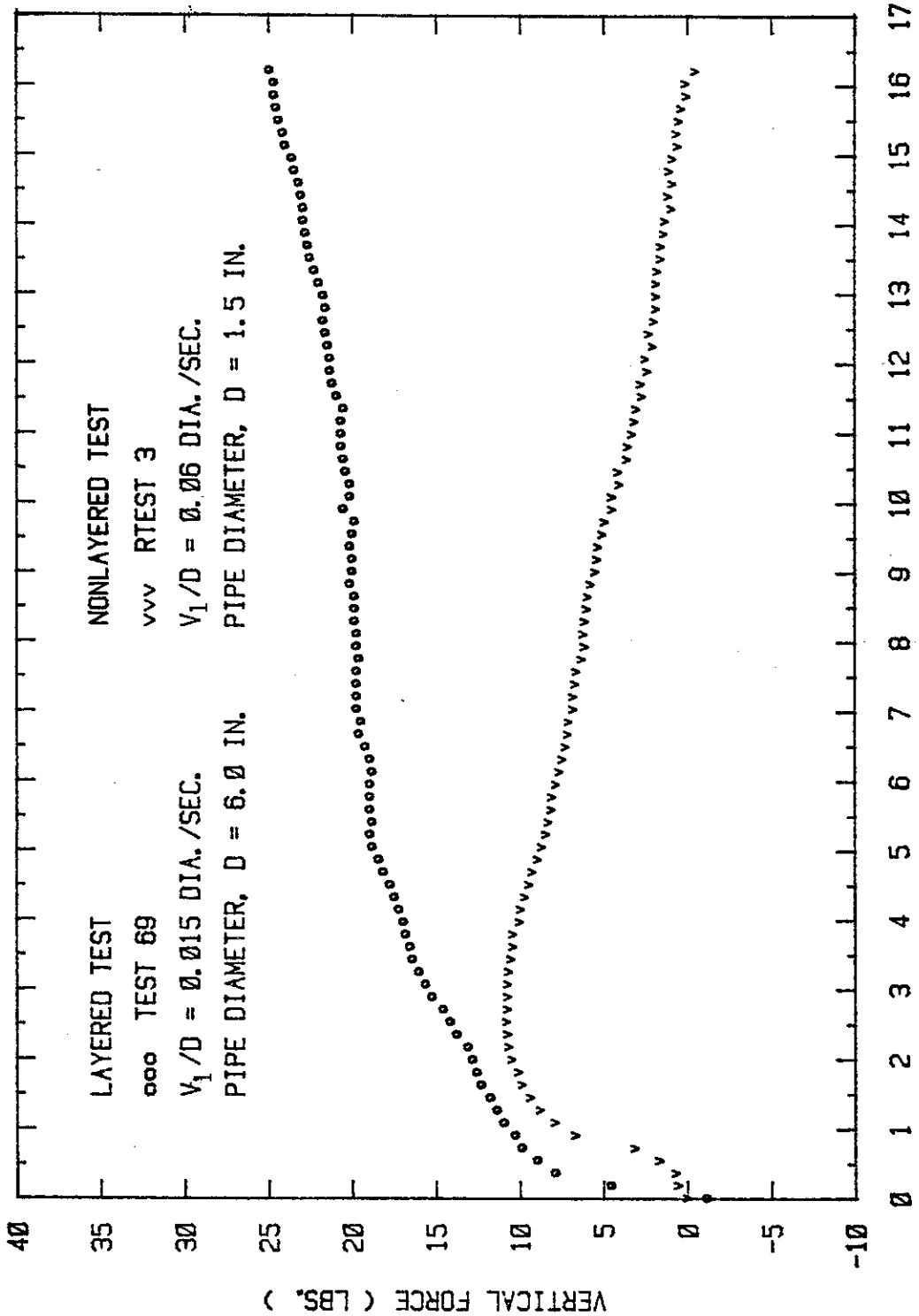

FIG. 3.89 - Comparison of Vertical Force Versus Displacement Curves for h/D = 1.0 for Layered and Nonlayered Tests.

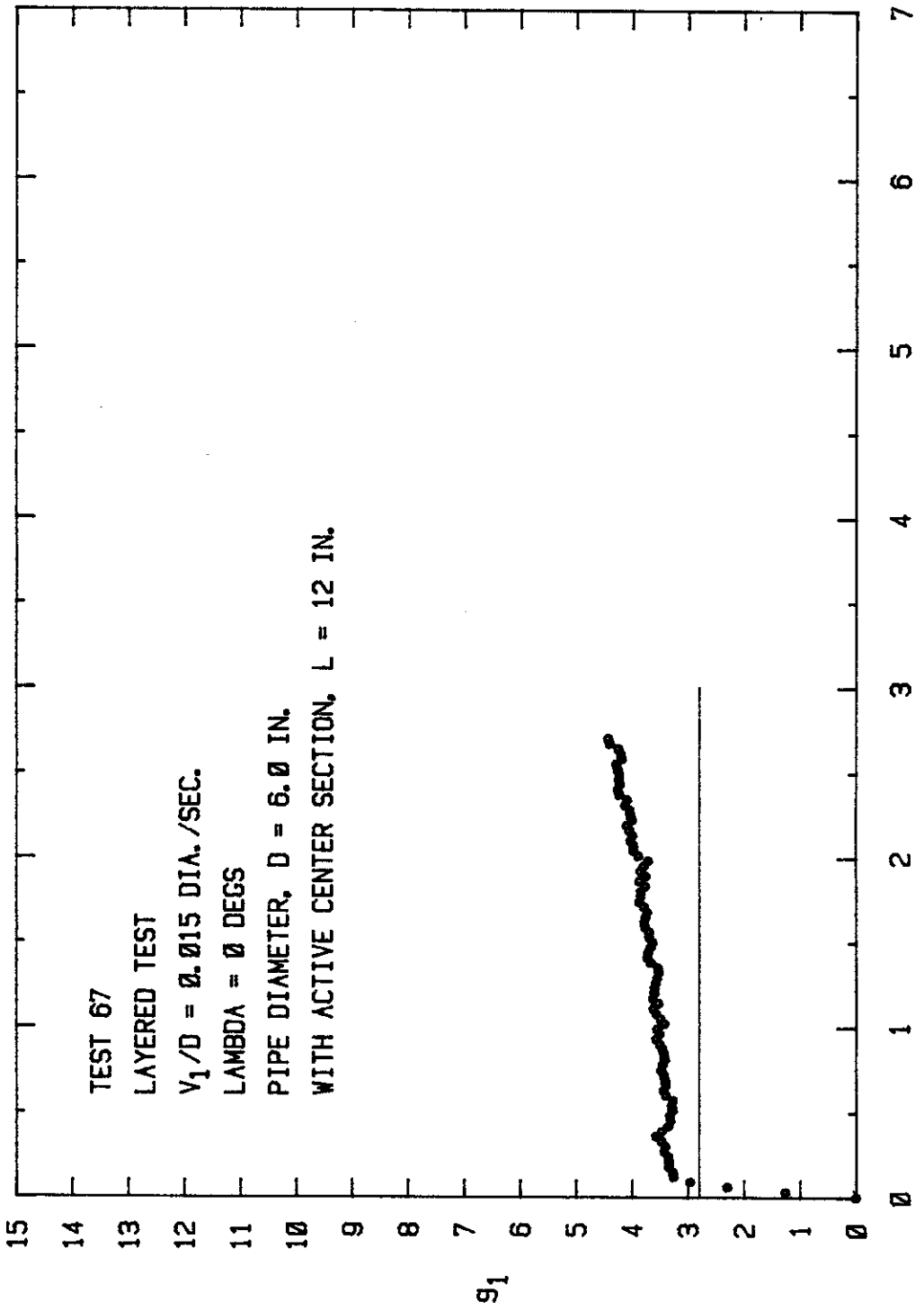

FIG. 3.90 - Horizontal Force Coefficient Versus Displacement Curve Based on Weighted Average Shear Strength for h/D = 0.5 Layered Test.

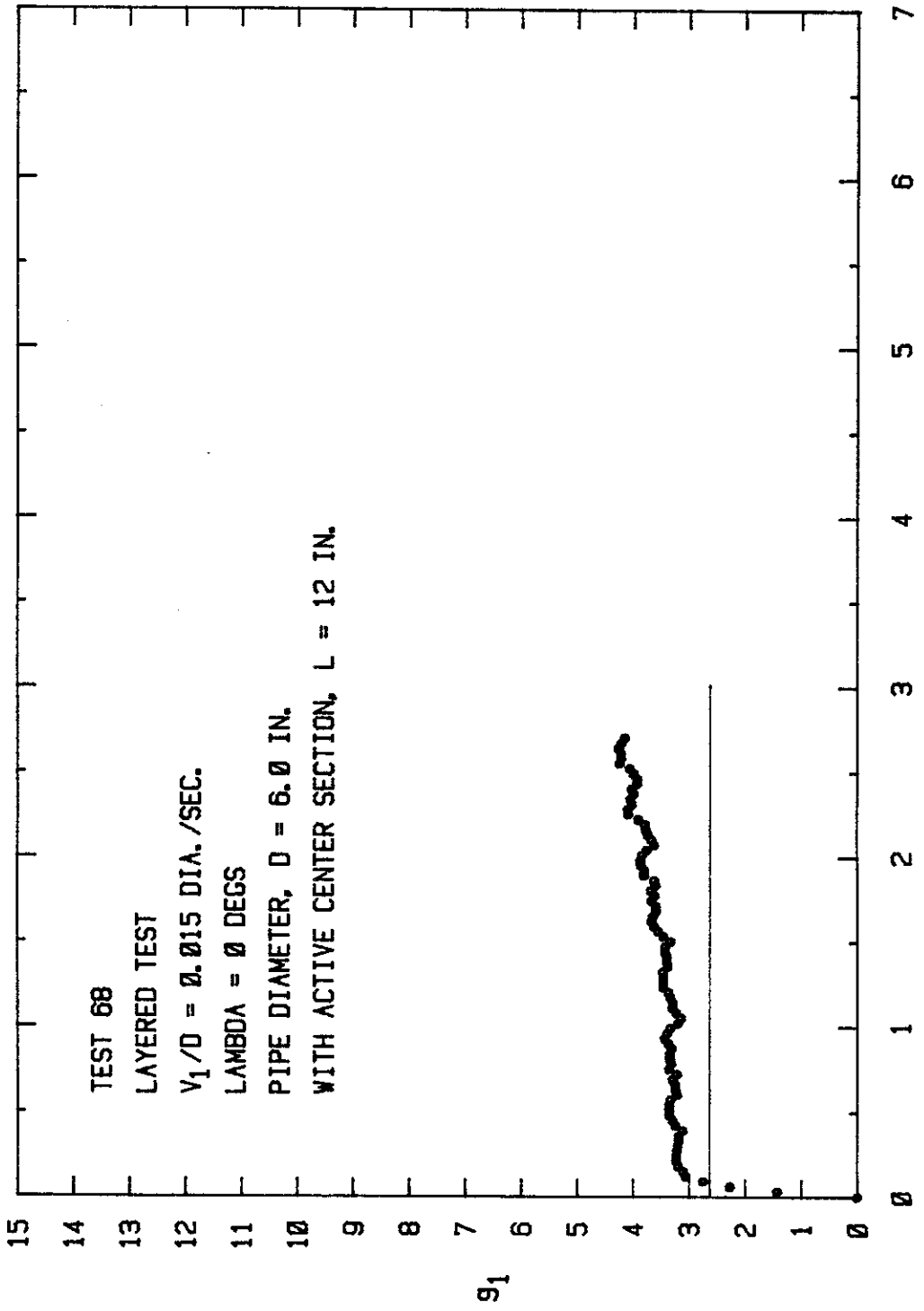

FIG. 3.91 - Horizontal Force Coefficient Versus Displacement Curve Based on Weighted Average Shear Strength for h/D = 0.5 Layered Test.

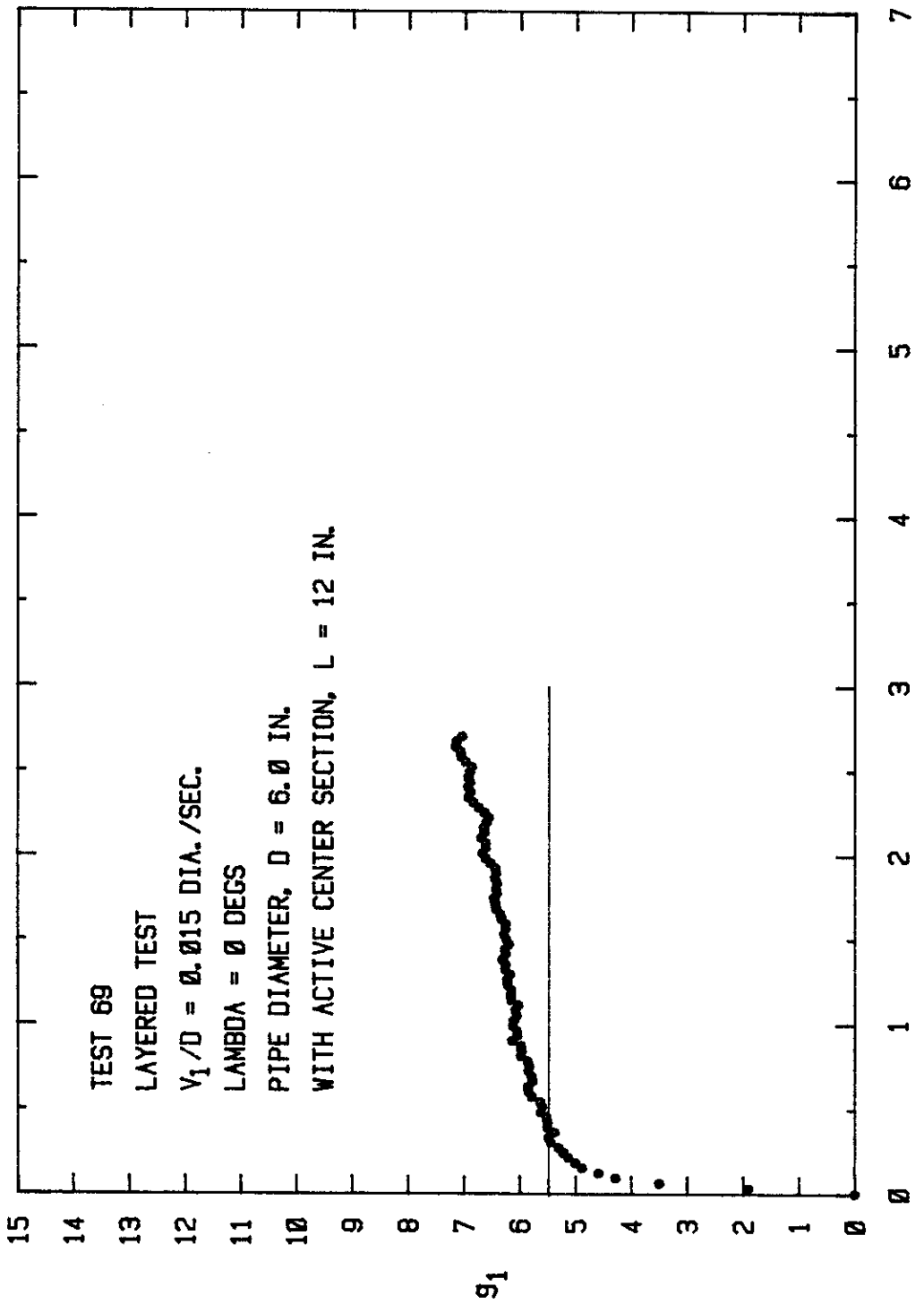

FIG. 3.92 - Horizontal Force Coefficient Versus Displacement Curve Based on Weighted Average Shear Strength for h/D = 1.0 Layered Test.

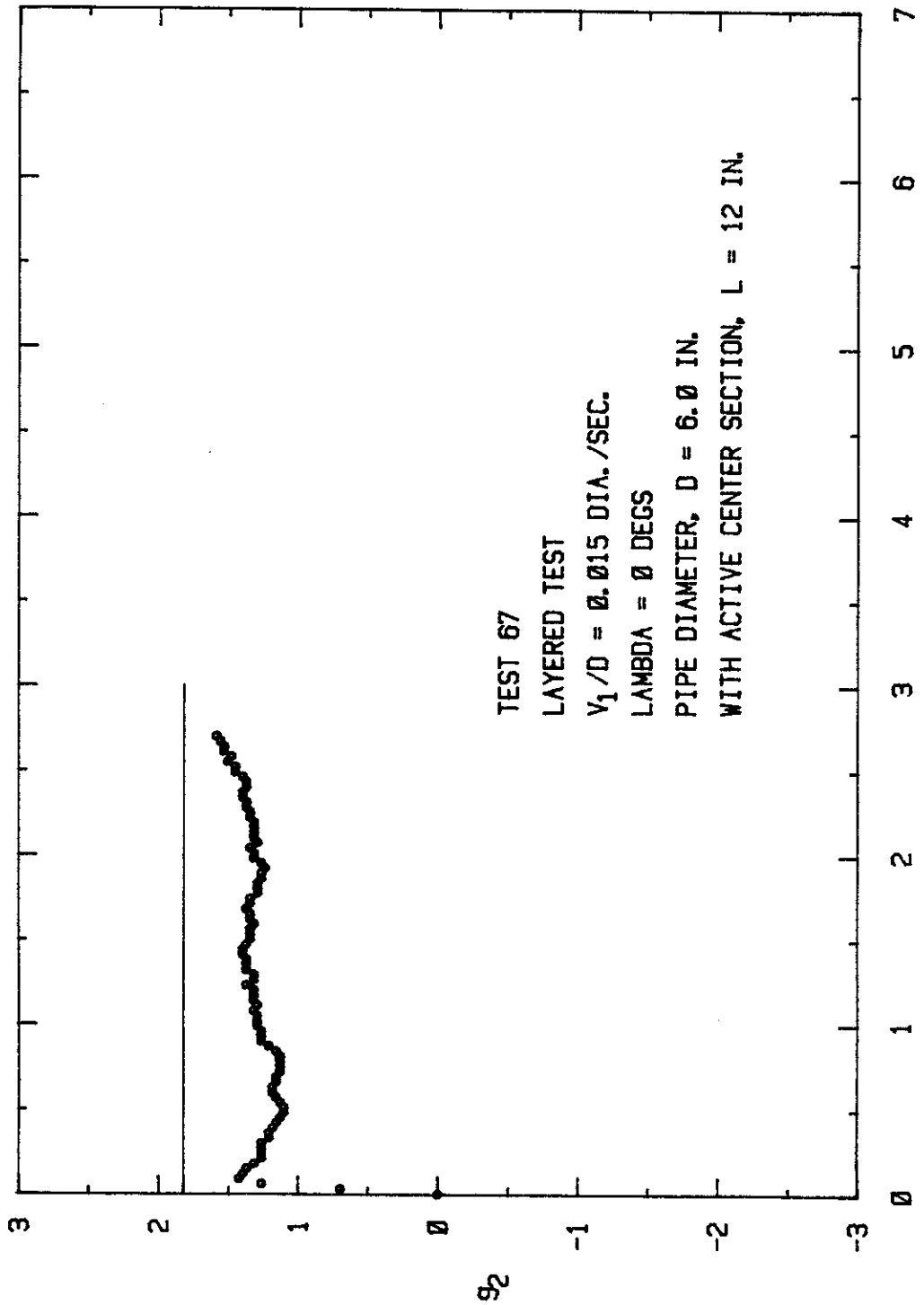

FIG. 3.93 - Vertical Force Coefficient Versus Displacement Curve Based on Weighted Average Shear Strength for h/D = 0.5 Layered Test.

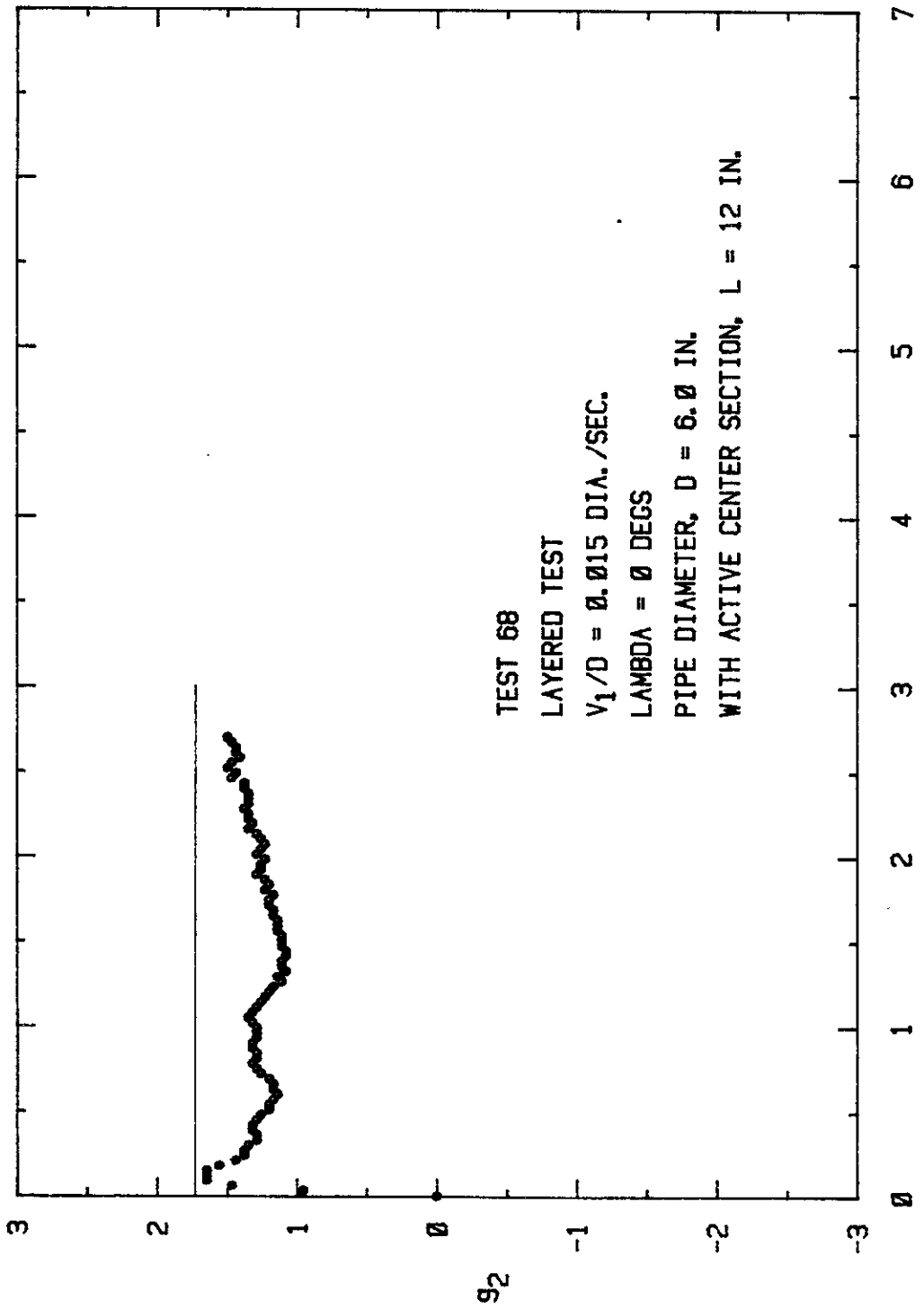

FIG. 3.94 - Vertical Force Coefficient Versus Displacement Curve Based on Weighted Average Shear Strength for h/D = 0.5 Layered Test.

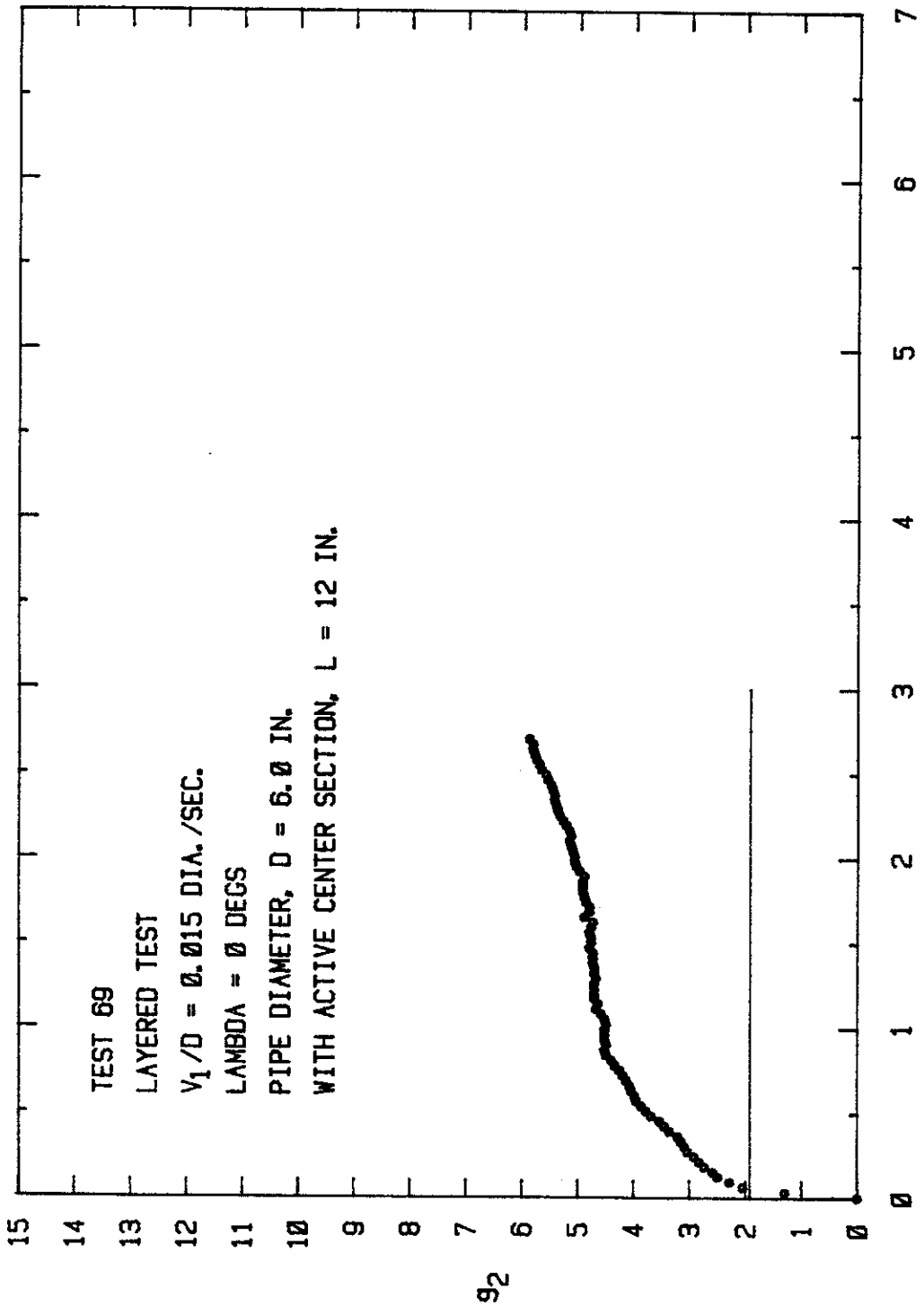

FIG. 3.95 - Vertical Force Coefficient Versus Displacement Curve Based on Weighted Average Shear Strength for h/D = 1.0 Layered Test.

Each type of test is discussed individually below.

1. Rate Effects on Drag Factors: These tests were conducted to determine whether there was a velocity dependence on the drag force. In the first series of tests, six different rates (V_1/D) were used on deeply buried ($h/D = 9$) pipe with the pipe oriented normal to flow ($\alpha = 90^\circ$). The sediment, which had an undrained shear strength of 55 psf, was pressurized to 21 psi.

Results are shown in Fig. 3.96 in terms of an uncorrected drag factor, K, versus normalized velocity, V/D, plotted on a log-log scale. The drag factor, K, uses the total force exerted on both the stub and the pipe for reasons which will become apparent later, and it is not normalized with respect to velocity, since it is velocity effects which are being investigated. Two distinct linear portions of the data are shown in Fig. 3.96. For $V/D > 0.005$, K is a function of $(V/D)^{0.1}$, where the exponent, 0.1, is essentially the same as the strain rate exponent, n, of the sediment. This trend had been observed repeatedly, and it came as no surprise. The horizontal portion of the curve for $V/D < 0.005$ was unexpected, but may be at least qualitatively explained by the sediment properties. In all of these tests, 21 hrs. elapsed between the time the sediment was packed around the pipe and the test was performed to allow thixotropic strength gain in the sediment. There will undoubtedly be additional strength gain after 21 hrs, but at a decreasing rate, and for pipe drag tests which take only a few minutes to a few hours, the strength for the duration of the test can be considered constant. However, for the tests with small values of V/D, some strength gain will probably occur as the test is performed (the slowest test in this series took over 3 days to complete), and this will

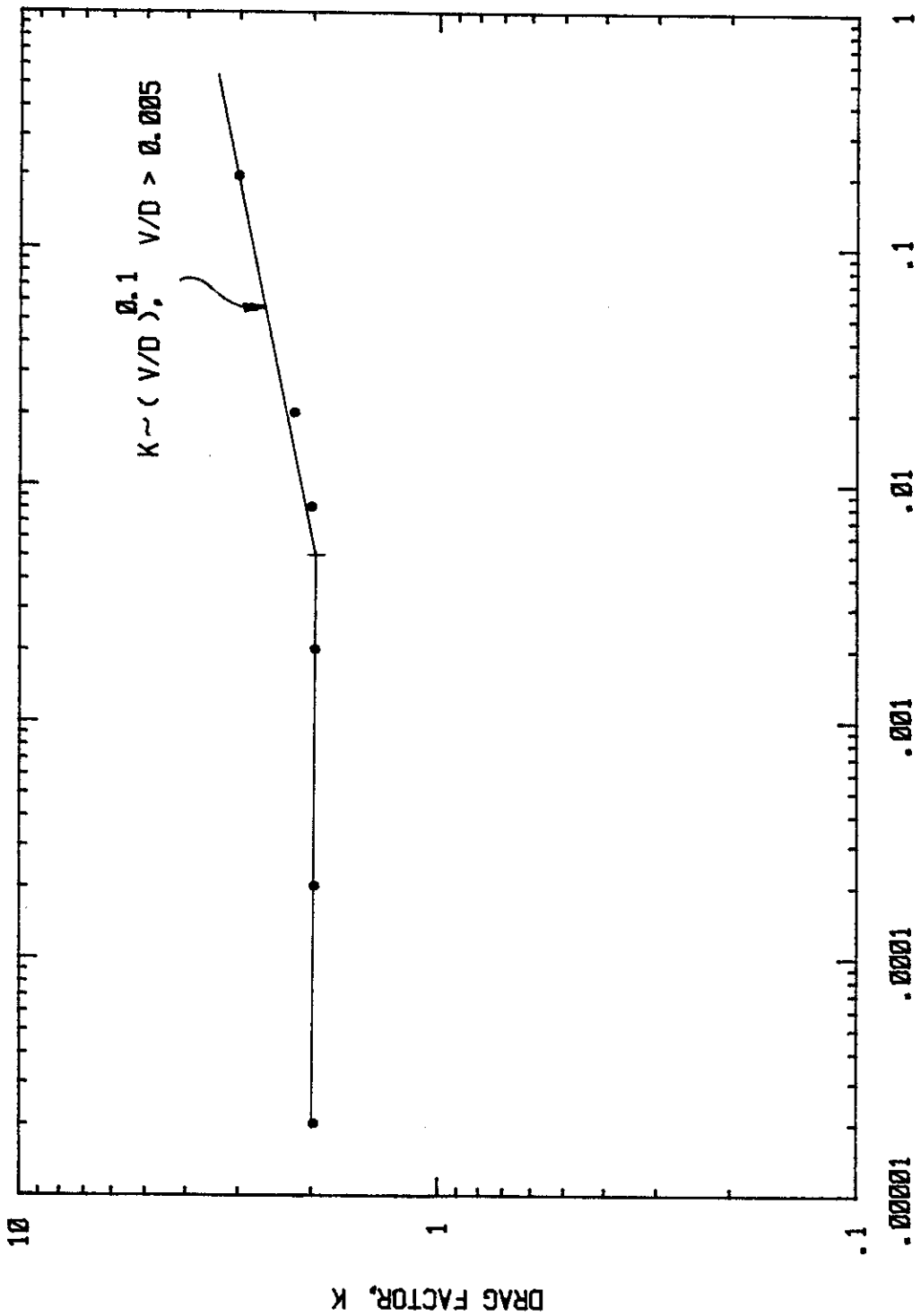

FIG. 3.96 - Velocity Dependence of Drag Factor for Flow Normal to Deeply Buried Pipes.

cause an increase in the drag force. Another possibility is the slow dissipation of excess pore pressure away from the zone stressed by the pipe (consolidation), which will also cause an increase in the shear strength of the sediment. Investigation of these factors is beyond the scope of this research, but the subjects should be studied to obtain a more complete picture of the phenomena involved.

The effect of the stub in pipe drag tests performed in the intermediate drag box was usually considered by performing separate tests to determine the drag force on the stub only; this force was subtracted from the total recorded force to determine the force on the pipe. In the test series reported above, this was not done since it was realized that the stress concentrations around the end of the stub might create unusual effects, particularly in the very slow tests, which would be misleading. This explains the use of the total drag force for both pipe and stub.

The second series of rate effect tests were more standard drag tests performed at two burial depths, $h/D = 0.25$ and 2, with pipes oriented at various angles, α, and at two velocities, V_1/D = 0.08 dia/sec and 0.0008 dia/sec. The results for g_1 are shown in Fig. 3.97, and Fig. 3.98 shows similar results for g_3, the axial force coefficient. For the shallow burial depth, there seems to be no significant difference between the fast and slow speed results for either g_1 or g_3, but for the burial depth of $h/D = 2$, the slower speed produces a trend of values somewhat smaller than the fast speed for flow angles greater than 45°, and the g_3 values are all somewhat higher than those for the fast speed. However, the differences between the fast and slow speed results do not exceed 10%, and most differences are smaller.

It appears that for velocities smaller than V/D of 0.005, the

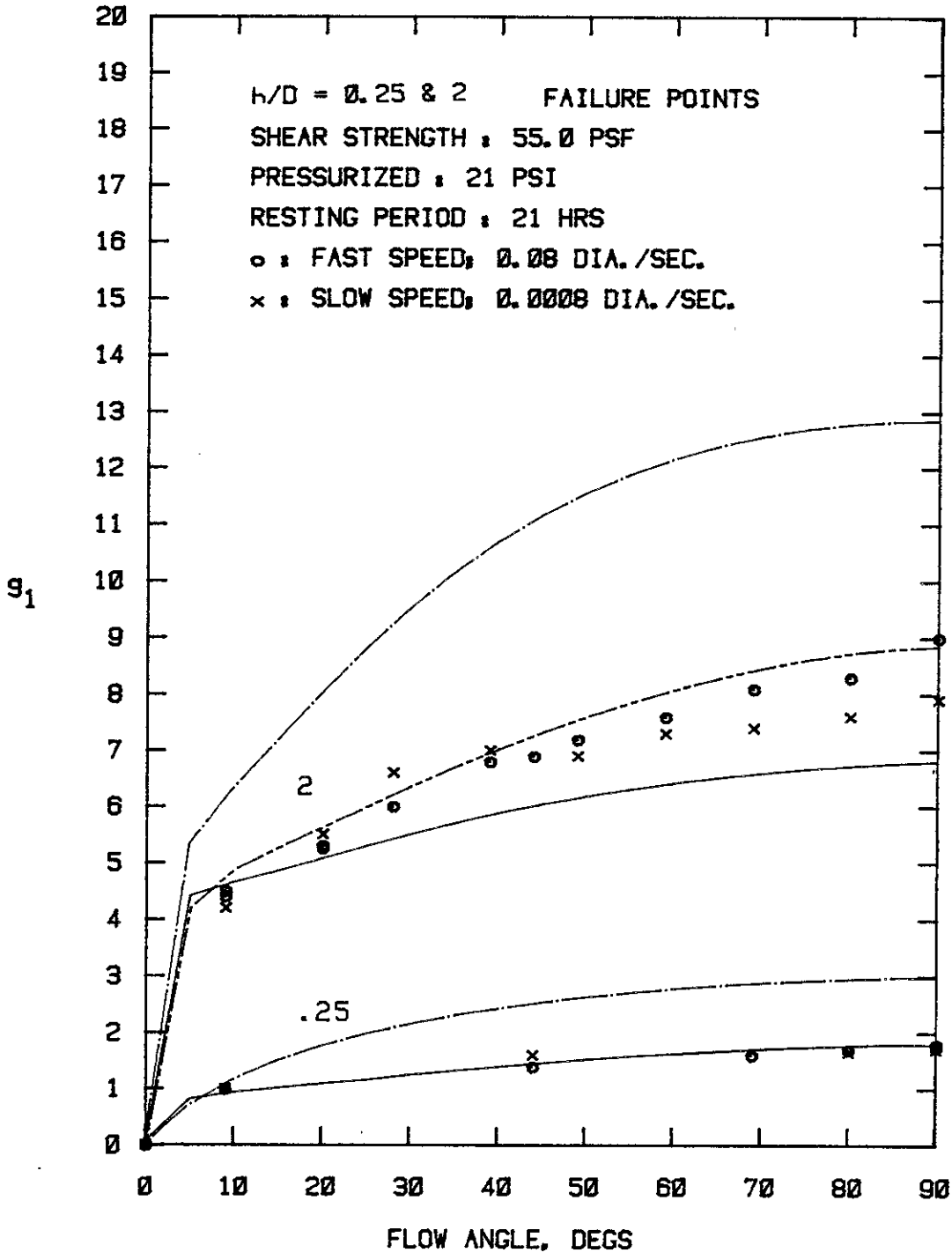

FIG. 3.97 - Comparison of Normal Force Coefficients Versus Flow Angle at Fast and Slow Speed for h/D = 0.25 and 2.

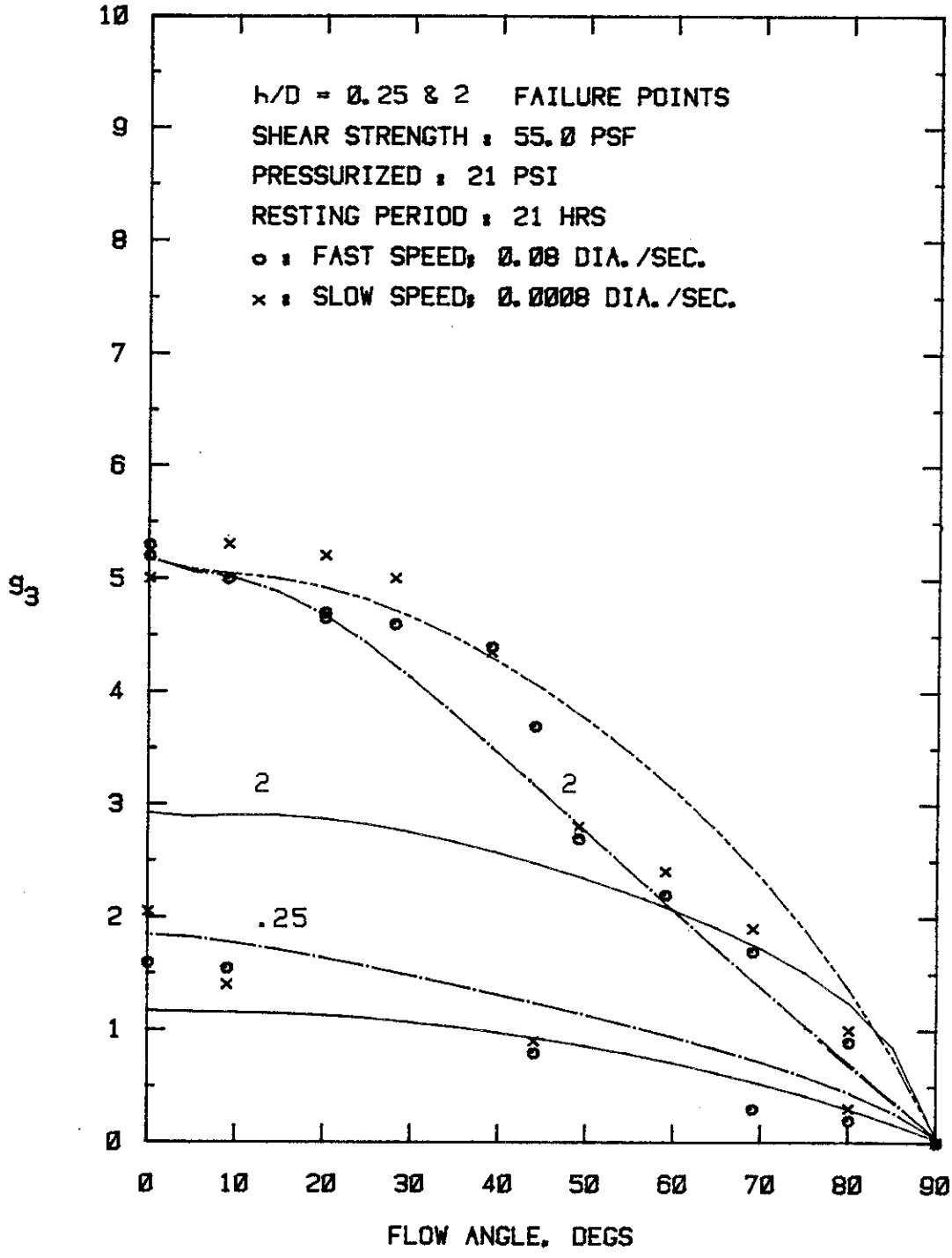

FIG. 3.98 - Comprison of Axial Force Coefficients Versus Flow Angle at Fast and Slow Speed for h/D = 0.25 and 2.

strain rate dependence of the sediment is influenced by other factors, perhaps those mentioned earlier, and that these factors may alter the force coefficients and drag forces. However, within the range of pipe velocities which have been tested, the effects are small.

2. Pipe Angle Tests (0.75 in. diameter pipe): These tests were performed to determine the effect of pipe flow angle, α, and burial depth, on the normal and axial drag forces for horizontally moving pipe. Undrained shear strength was nominally 55 psf, the pipe travelled at a velocity of 0.08 dia/sec, and the system was pressurized to 21 psi. A limited number of tests were performed at a velocity of 0.0008 dia/sec. In these tests, a distinct peak or breakaway value of force was usually discernible, and the results are expressed in terms of this value - termed the failure point.

The combined results of all tests performed at the fast speed are plotted in Fig. 3.99 for g_1 and Fig. 3.100 for g_3. Note that for the shallow depths of burial (h/D = 0.25 and 0.50), not all angles were tested. Similar results are given in Figs. 3.101 and 3.102 for the slow speed tests. This extensive series of tests show very good agreement between replicate tests. Also, there is wide separation of the results for the different burial depths for the normal force coefficients, g_1, but this is not the case for the axial force coefficients, g_3, which are, of course, numerically smaller. The g_3 results for h/D of 2 and 9 are almost identical, which indicates that for axial movement, the pipe can be considered as infinitely deep for h/D roughly greater than 2.

The results indicate that there is little difference in the force coefficients for the two pipe velocities, a result which was anticipated from the previous rate effect tests.

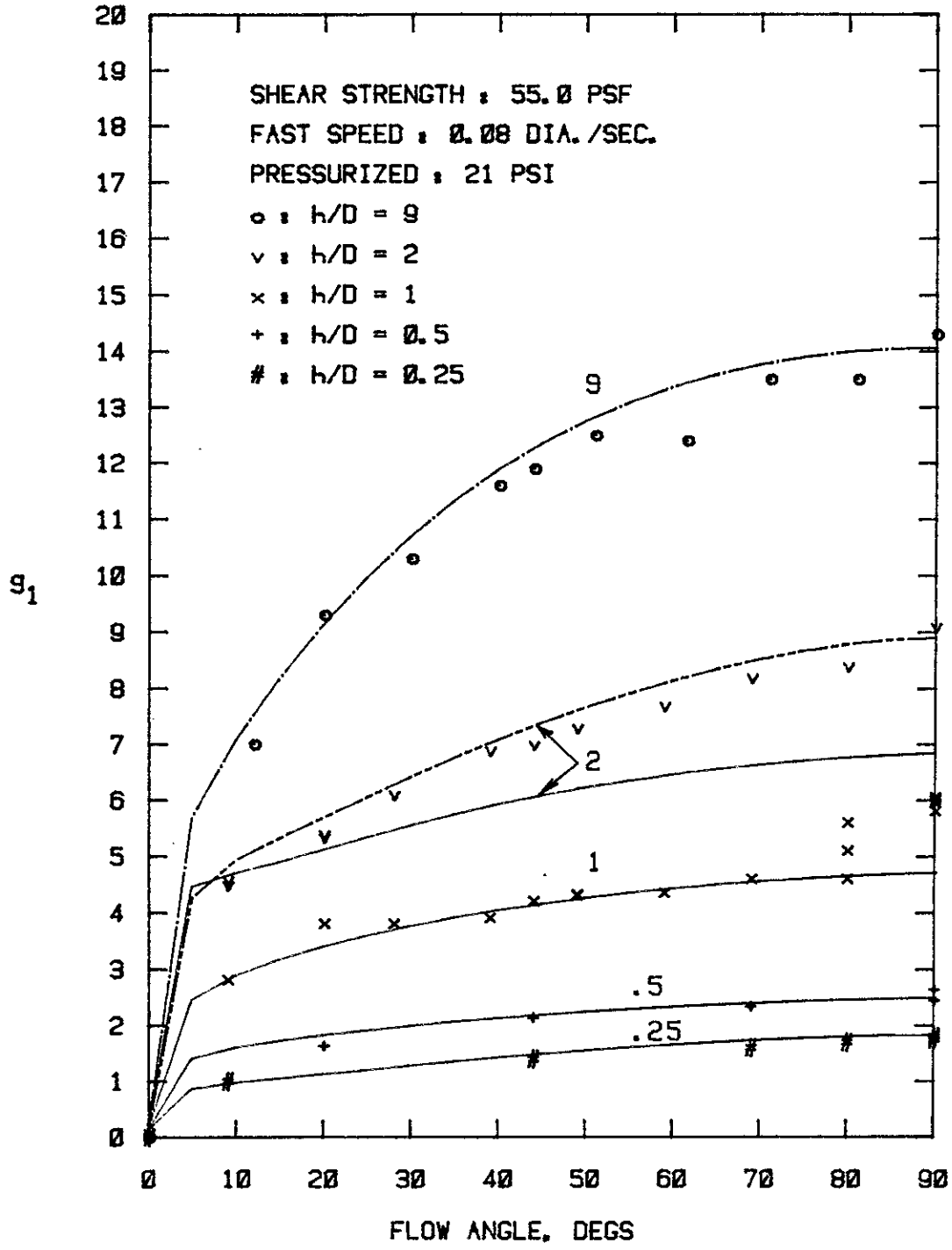

FIG. 3.99 - Normal Force Coefficients at Failure Points Versus Flow Angle at Fast Speed for h/D = 0.25 to 9.

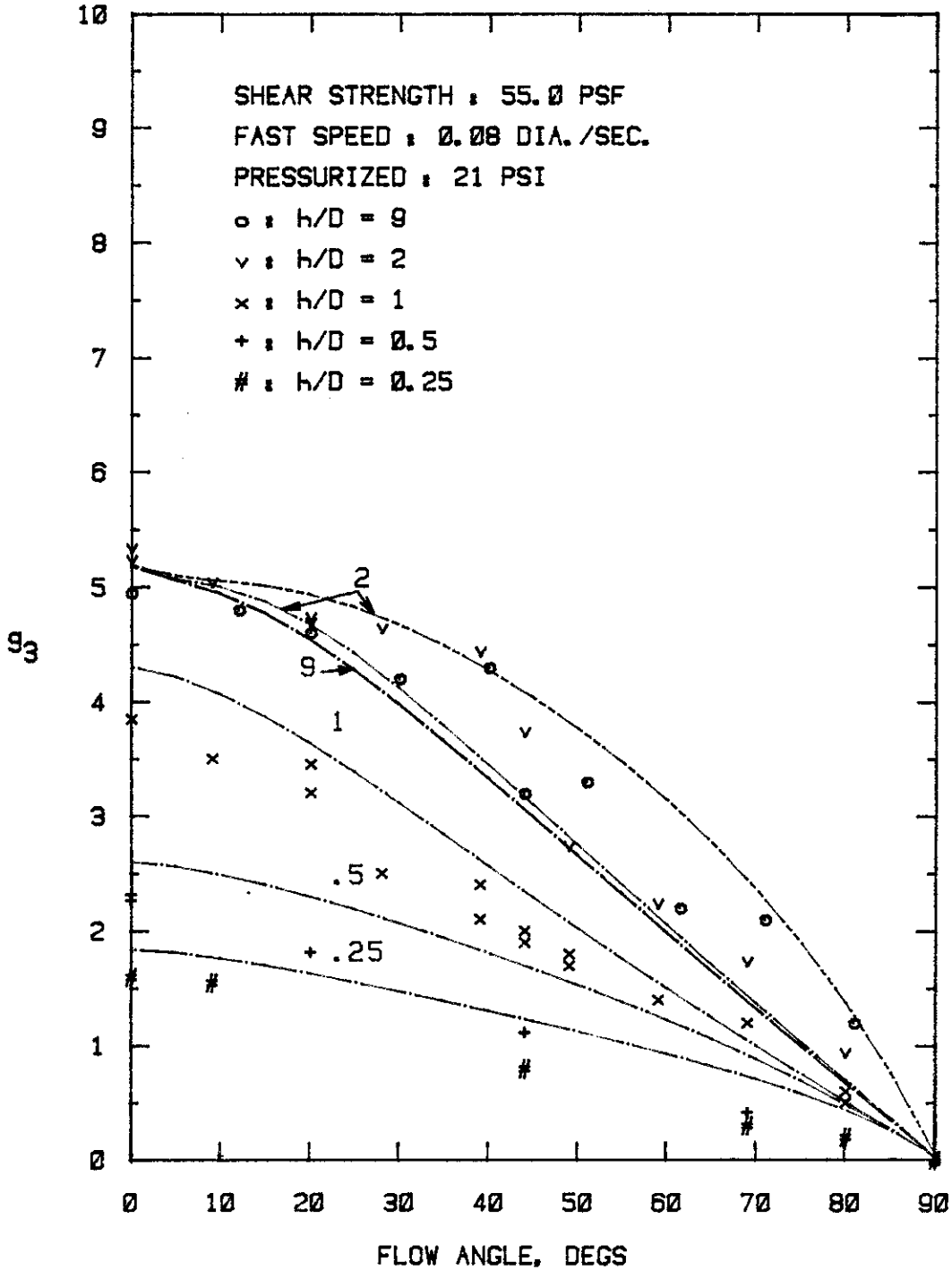

FIG. 3.100 - Axial Force Coefficients at Failure Points Versus Flow Angle at Fast Speed for h/D = 0.25 to 9.

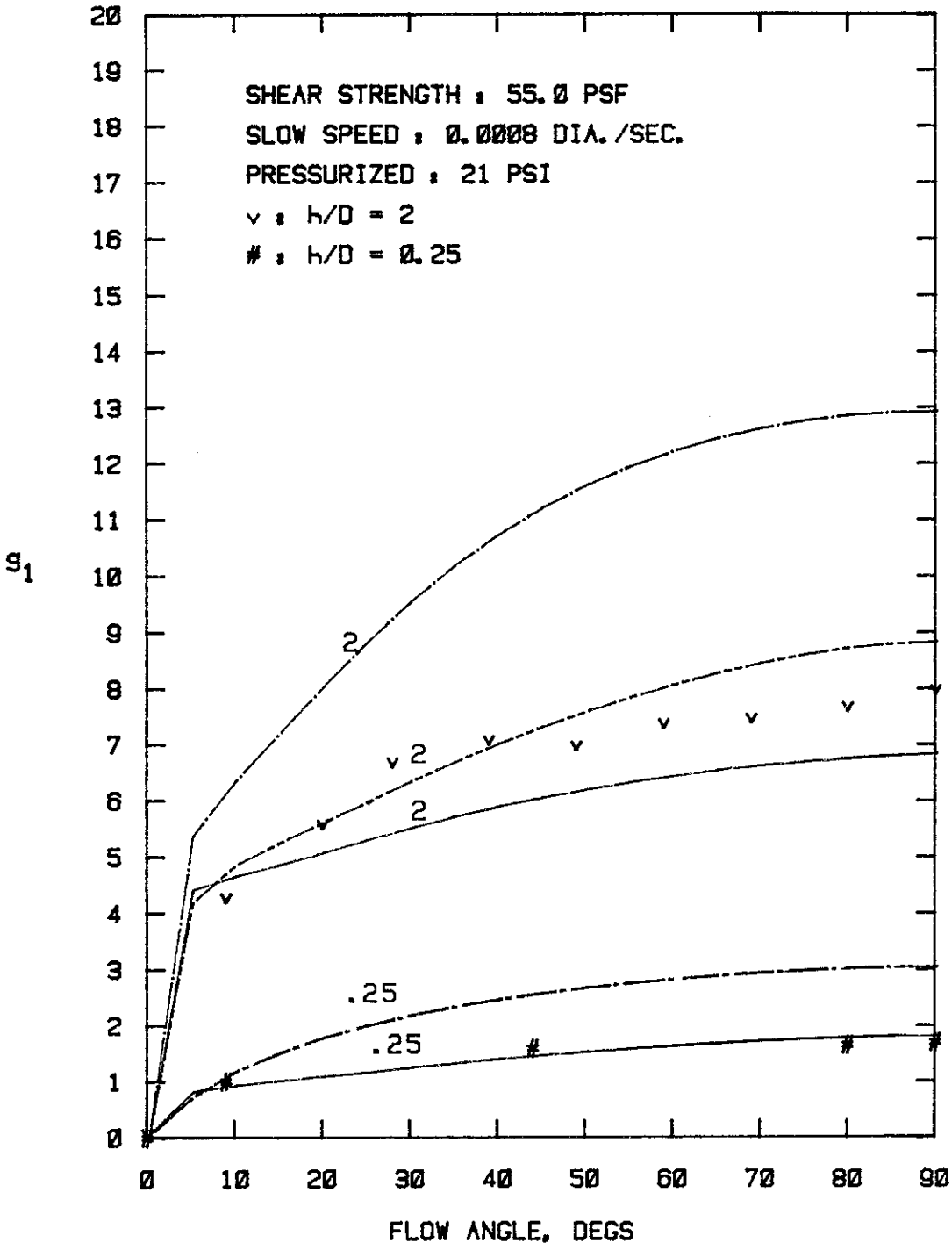

FIG. 3.101 - Normal Force Coefficients at Failure Points Versus Flow Angle at Slow Speed for h/D = 0.25 and 2.

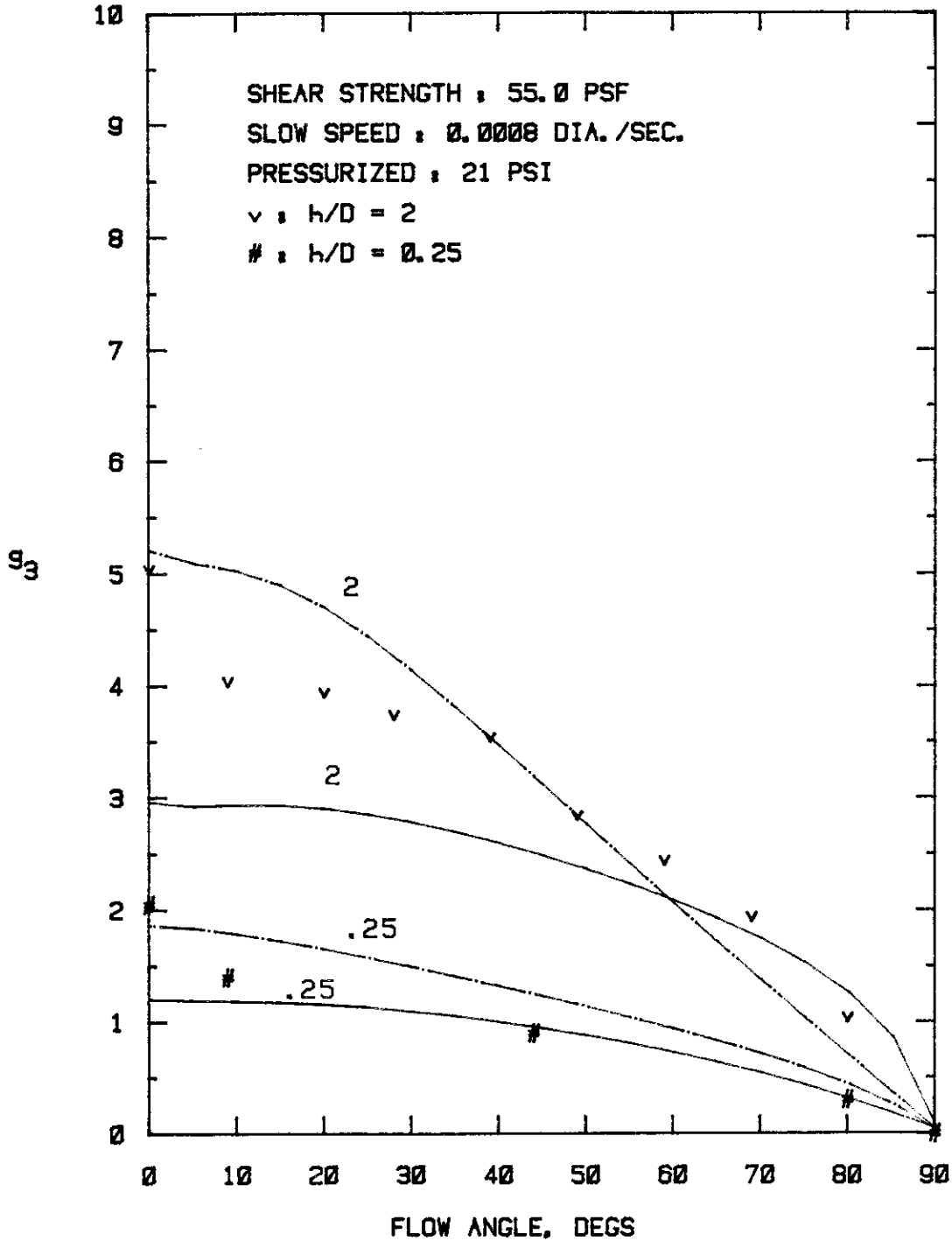

FIG. 3.102 - Axial Force Coefficients at Failure Points Versus Flow Angle at Slow Speed for h/D = 0.25 and 2.

An alternative approach to portraying these results would be plots of g versus h/D for different values of flow angle. Figures 3.103-3.106 are plots of this type for g_1 at flow angles of 90°, 70°, 45° and 20°. Similar plots for g_3 are presented in Figs. 3.107-3.110.

3. Effects of Pressure on Drag Characteristics: This test series examined whether total pressure, within the range of 0 to 30 psi, had an effect on the drag factors. The tests were conducted for a range of recess depths, at a single angle of flow, $\alpha = 90°$ (pipe oriented normal to flow), at fast and slow pipe velocities. The results are difficult to interpret, especially for the normal force coefficients, g_1, which showed several different patterns of behavior depending on the pressure magnitude, recess depth and pipe velocity.

In many cases, particularly for the pressurized tests on partially buried pipes, there was no distinct peak or failure values, whereas companion nonpressurized tests exhibited peaks. It appeared that the effect of pressure was to suppress the cracking of the sediment that results in the breakaway forces. The approach taken herein where there was not a distinct peak was to utilize the point of inflection in the early part of the curve where the drag factor started leveling off after the initial rapid rise, the point previously termed the "failure point". In most cases, at a value of U/D of 3, the curve had reached a maximum, and this also represented a point to be analyzed. Figure 3.111 is a plot of the failure g_1 points, whereas Fig. 3.112 presents g_1 at U/D of 3. Figure 3.111 (failure points) shows that for g_1, the pressurized results are highest for $h/D \geq 2$ but lower than the nonpressurized for $h/D \leq 1$. For the U/D of 3 points (Fig. 3.112), the pressurized results are somewhat higher overall except at h/D = 1 where the pressurized results for the fast speed are smaller than for the nonpressurized case.

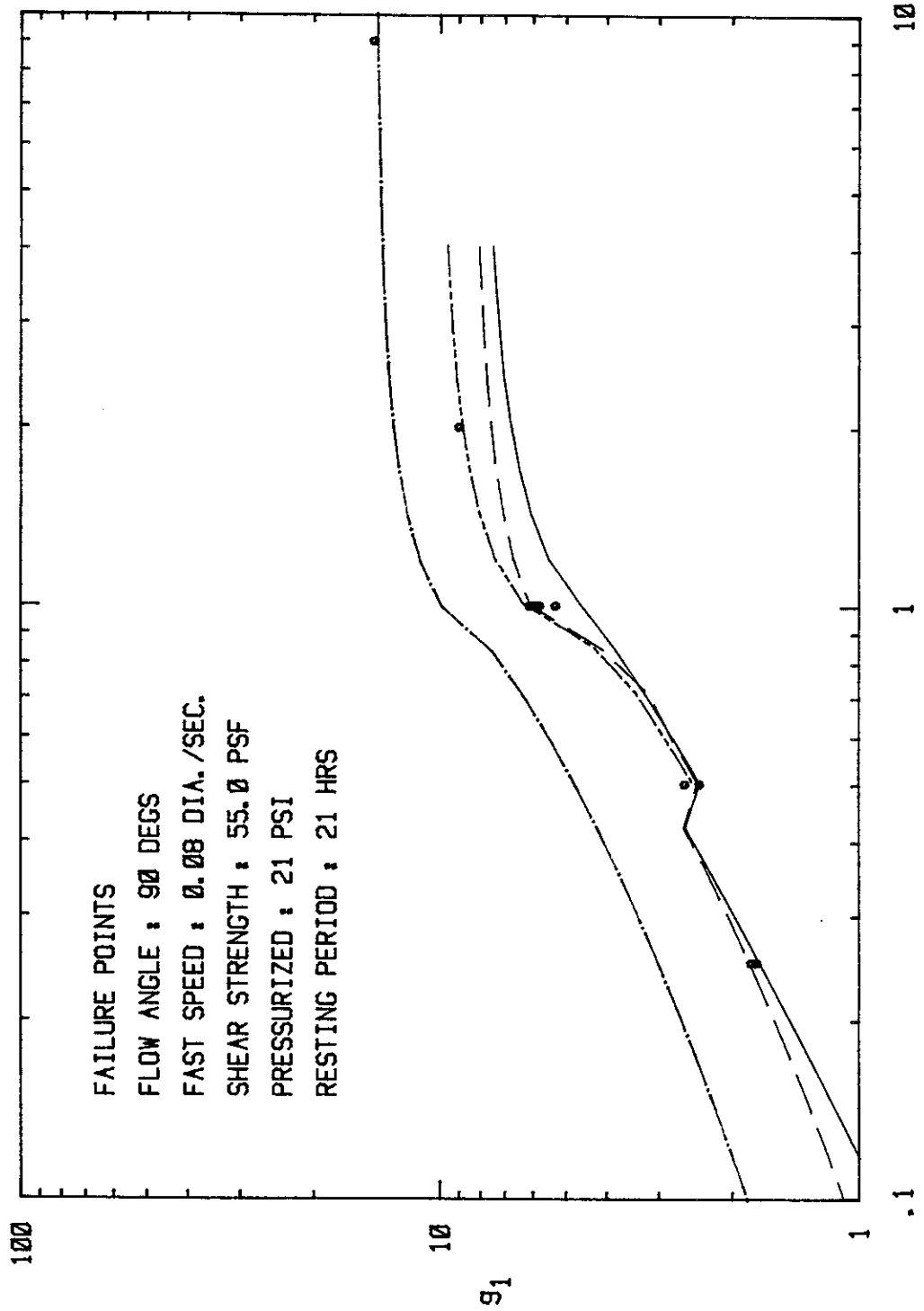

FIG. 3.103 - Normal Force Coefficients at Failure Points Versus Recess Depth for 90° Flow Angle. Logarithmic Scale.

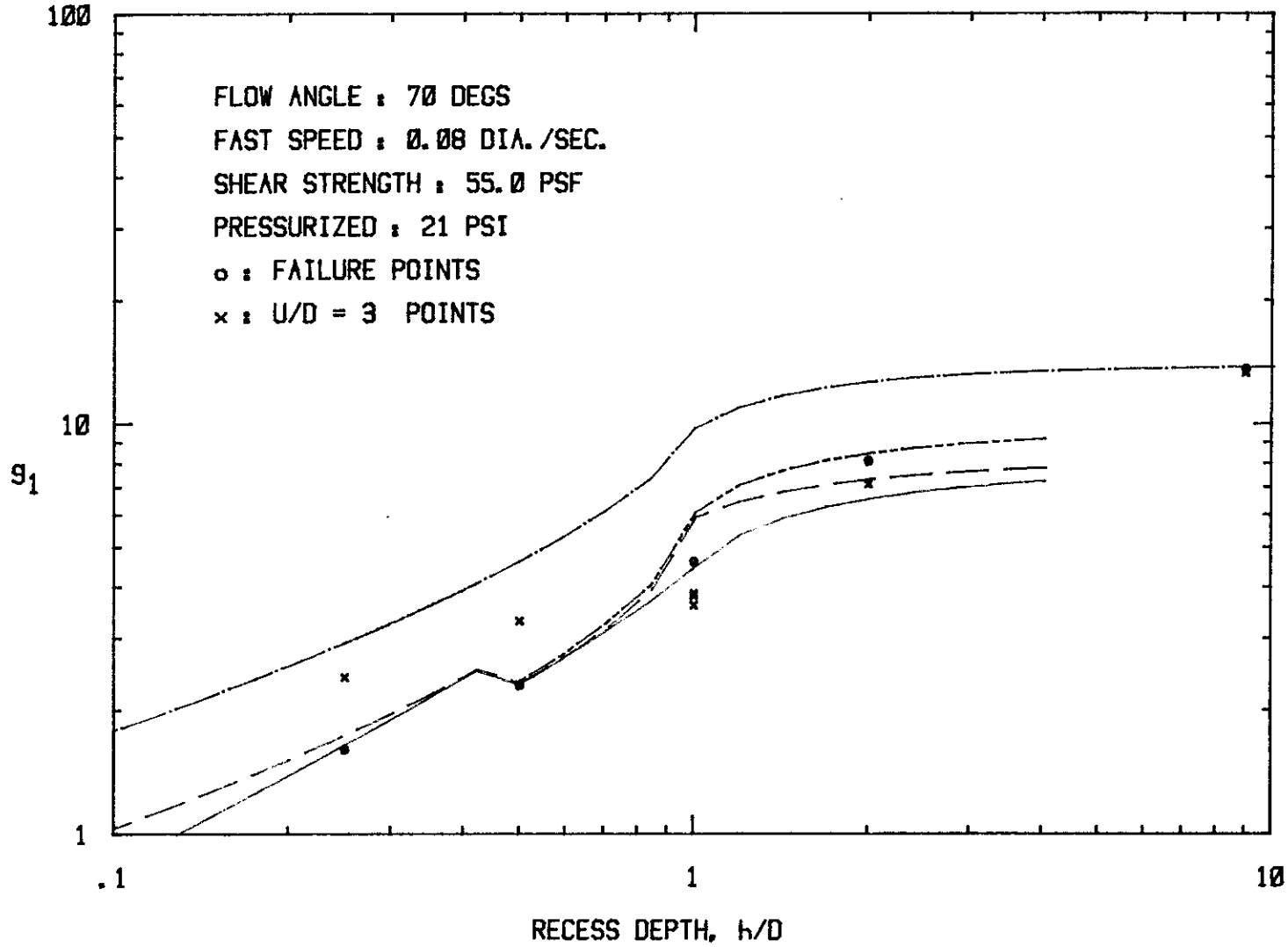

FIG. 3.104 - Normal Force Coefficients Versus Recess Depth for 70° Flow Angle. Logarithmic Scale.

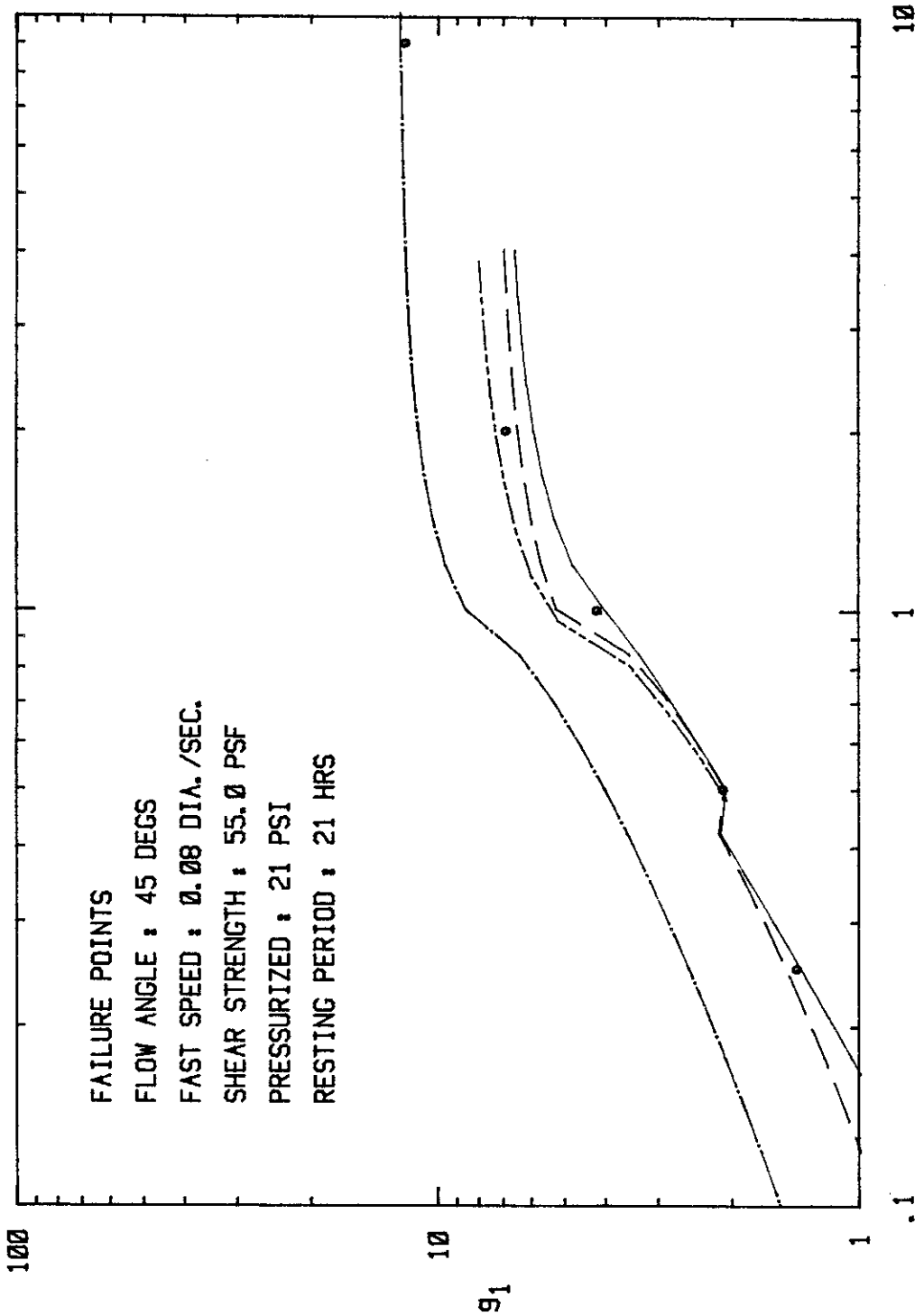

FIG. 3.105 - Normal Force Coefficients at Failure Points Versus Recess Depth for 45° Flow Angle. Logarithmic Scale.

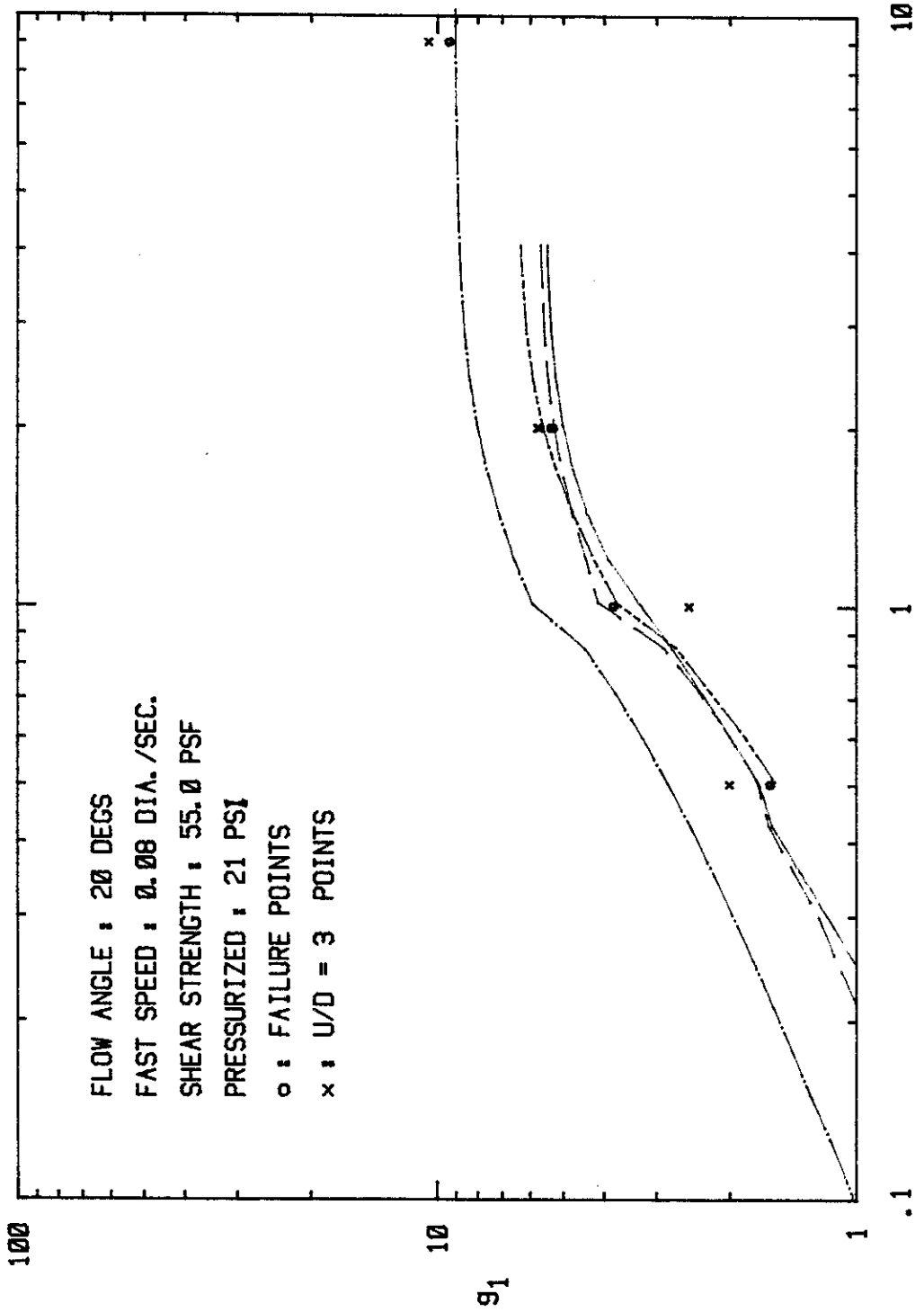

FIG. 3.106 - Normal Force Coefficients Versus Recess Depth for 20° Flow Angle. Logarithmic Scale.

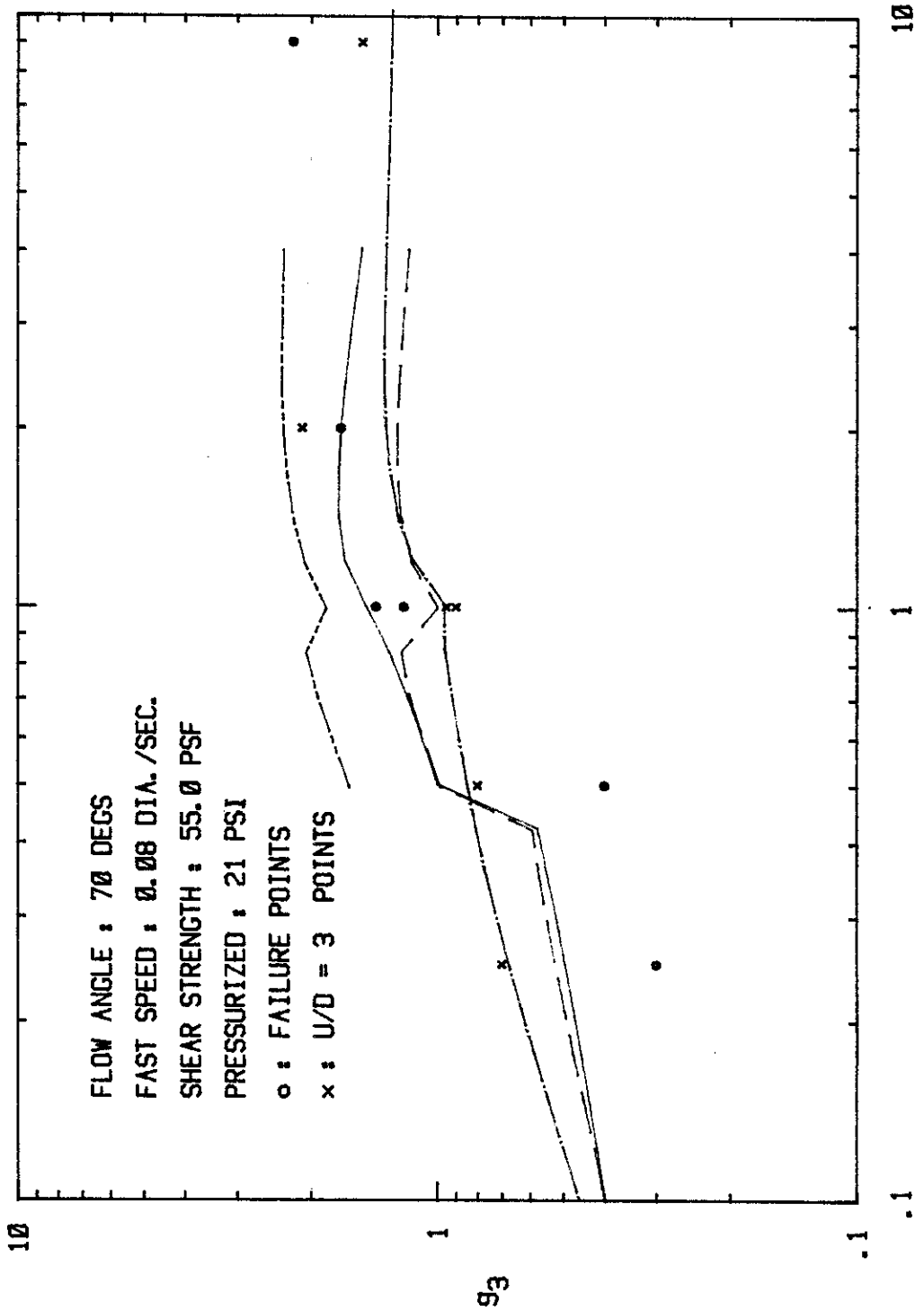

FIG. 3.107 – Axial Force Coefficients Versus Recess Depth for 70° Flow Angle. Logarithmic Scale.

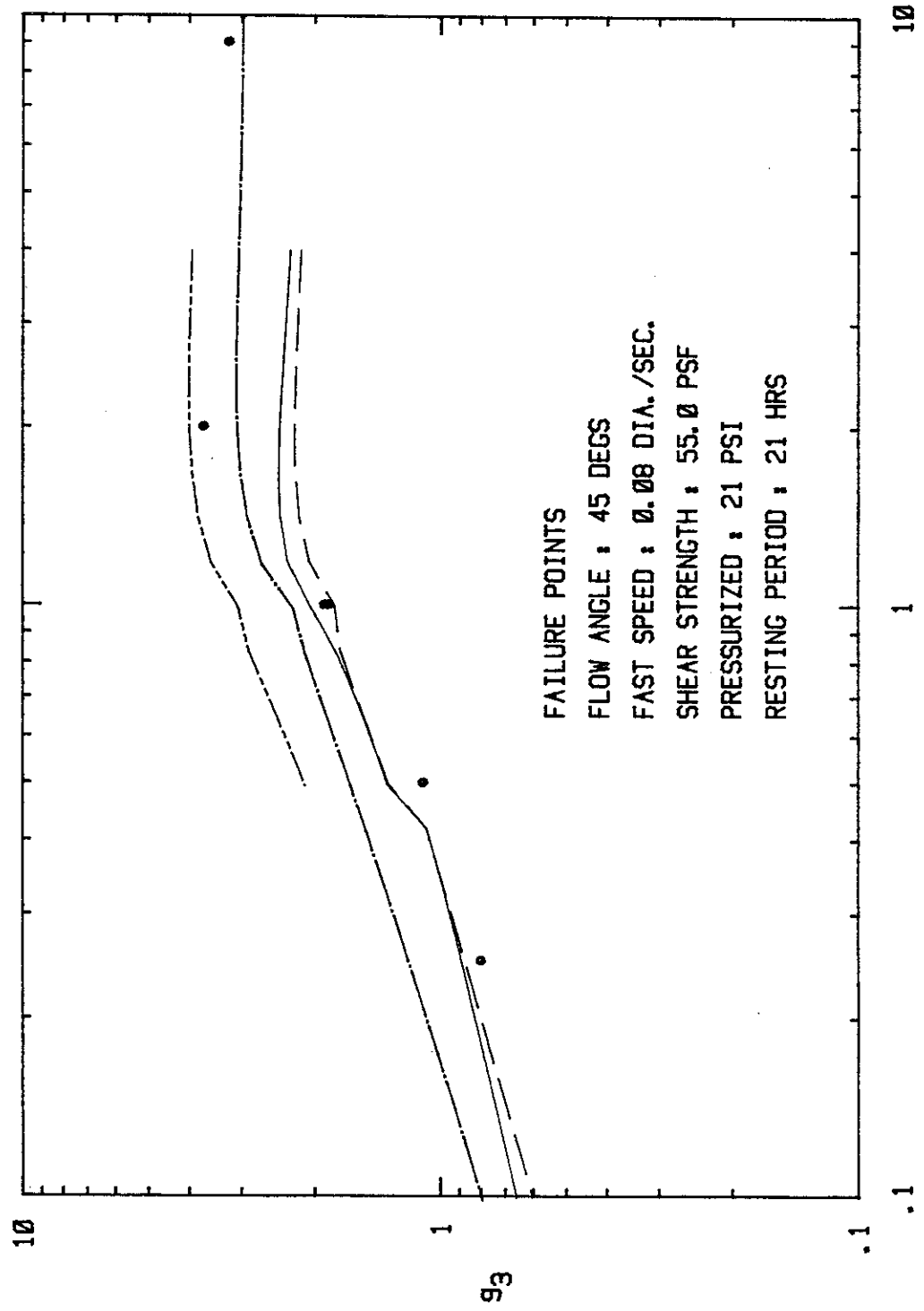

FIG. 3.108 - Axial Force Coefficients at Failure Points Versus Recess Depth for 45° Flow Angle. Logarithmic Scale.

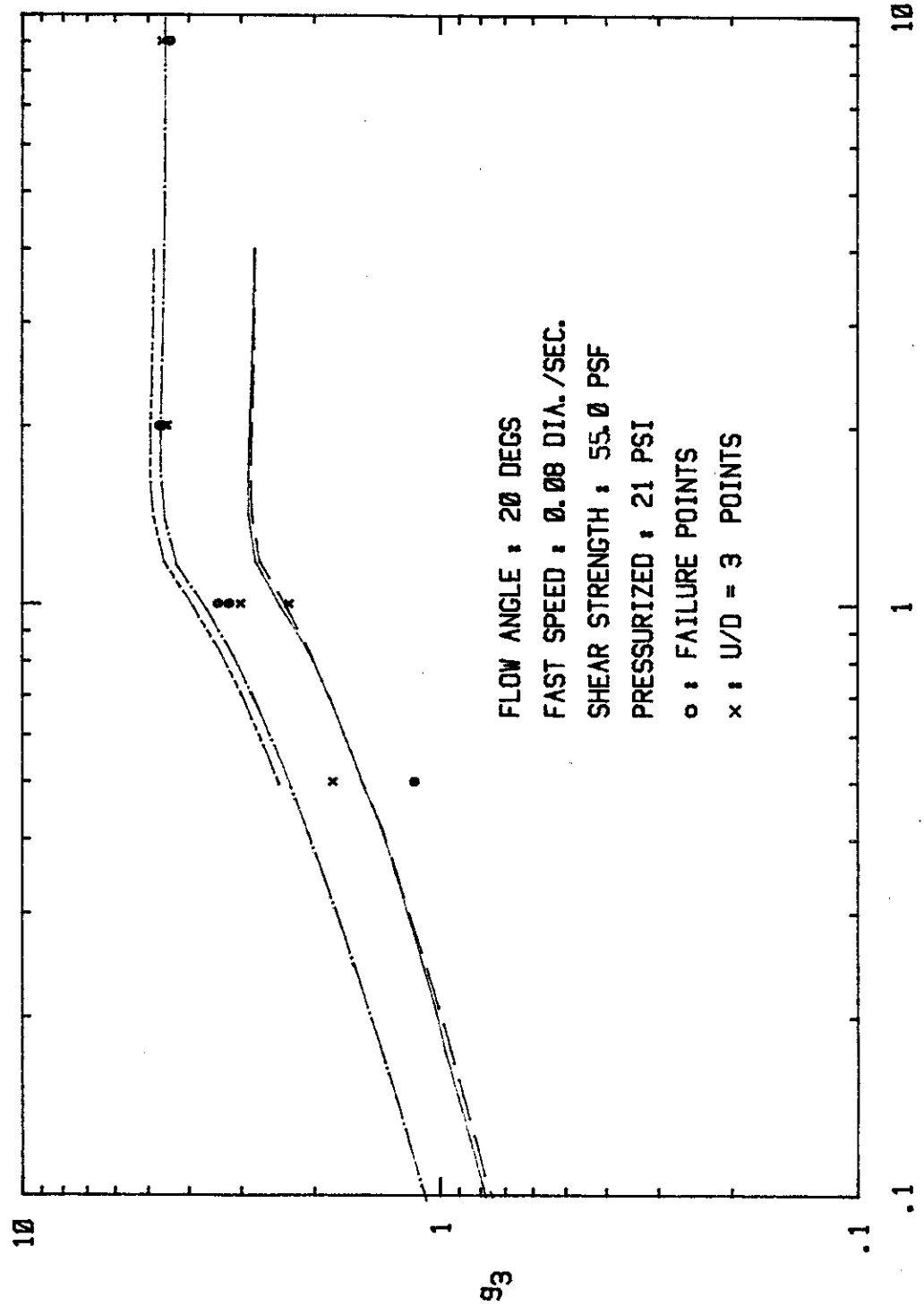

FIG. 3.109 - Axial Force Coefficients Versus Recess Depth for 20° Flow Angle. Logarithmic Scale.

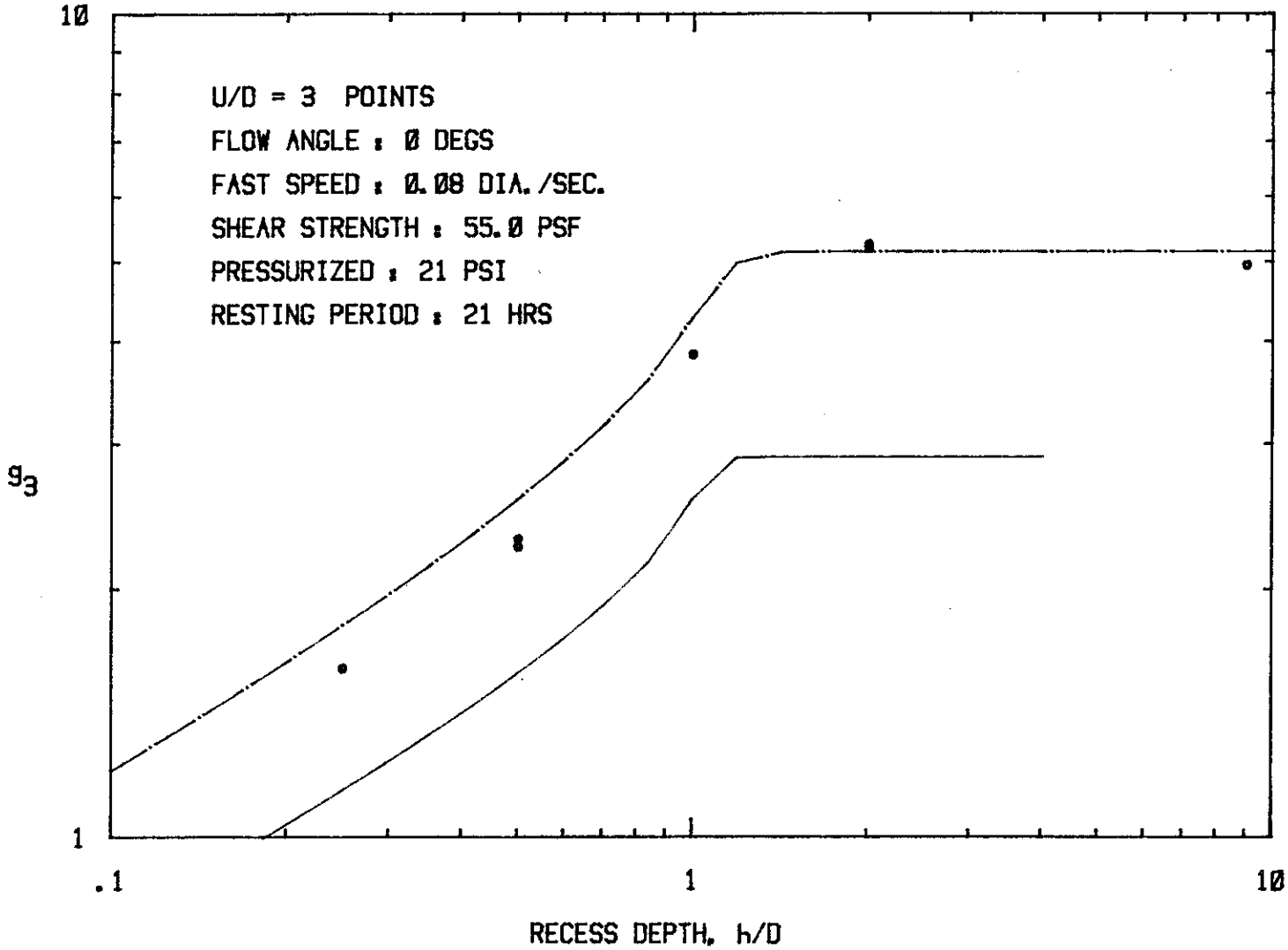

FIG. 3.110 - Axial Force Coefficients at U/D = 3 Points Versus Recess Depth for 0° Flow Angle. Logarithmic Scale.

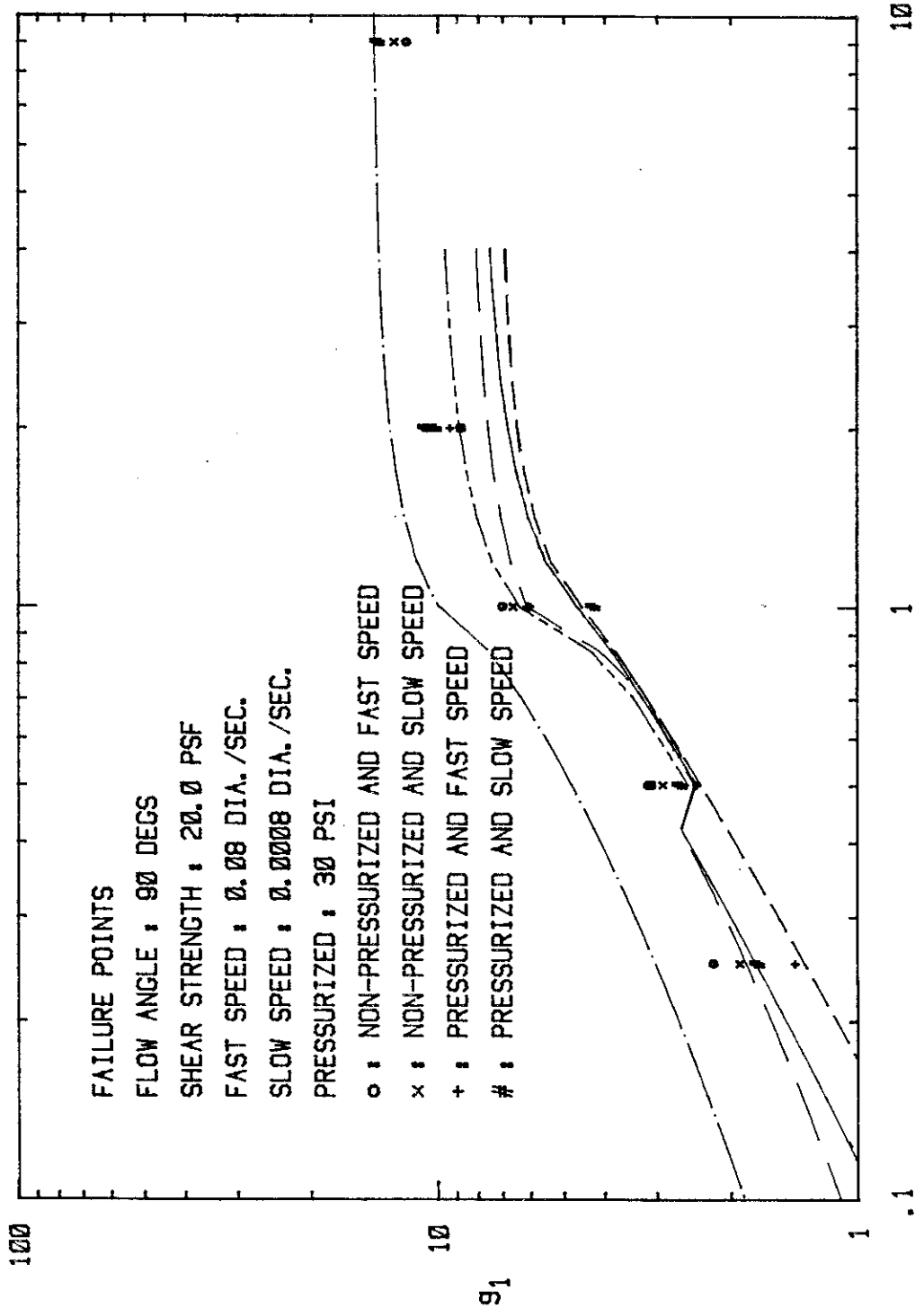

FIG. 3.111 - Normal Force Coefficients at Failure Points Versus Recess Depth for Speed and Pressure Effects. Logarithmic Scale.

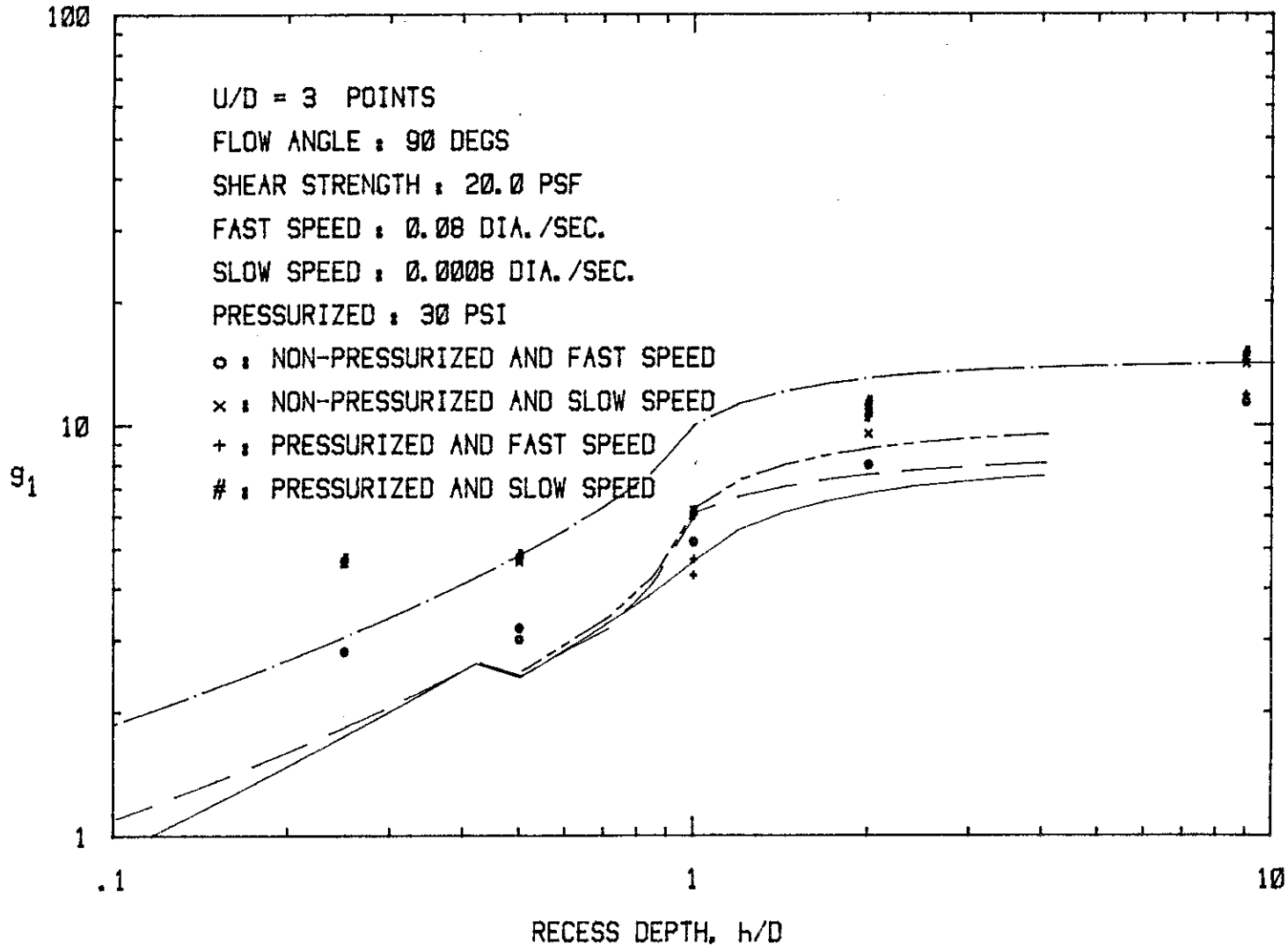

FIG. 3.112 - Normal Force Coefficients at U/D = 3 Points Versus Recess Depth for Speed and Pressure Effects. Logarithmic Scale.

The results for the axial force coefficient, g_3 (Fig. 3.113), are presented only for U/D = 3 points, which are essentially the same as the failure point. The pressurized fast speed tests produced somewhat lower values of g_3, but variations for the remaining tests are probably within the range of experimental error. Probably the most striking aspect is that g_3 does not change with recess depths, h/D, greater than 2, a result confirmed in other tests.

Some additional studies conducted in the intermediate box can also be used to illustrate pressure effects, but perhaps not as clearly as the previous results. Figures 3.114 and 3.115 show the results from a series of tests in which sediment with a shear strength of 55 psf was pressurized to 21 psi and another in which a shear strength of 20 psf and pressure of 30 psi was utilized. All tests were performed with the pipe normal to the direction of flow. When the force coefficient at the failure point is considered (Fig. 3.114), there is little discernable difference between the two cases. For U/D = 3 (Fig. 3.115), the only major difference occurred at h/D of 9, where the high shear strength-lower pressure combination produced a significantly higher value of g_1 than did the case of low strength-high pressure.

Another test series involved tests with recess depth, h/D = 1, at pressures of 21 and 30 psi, and for different angles of flow, α. A full range of angles, α, was used for the pressure of 21 psi, but only intermediate angles were used for the 30 psi case. The results for g_1 (Fig. 3.116) and g_3 (Fig. 3.117) show no distinct differences between the two different pressures.

In general terms the test results show that pressure:

(a) suppresses the cracking characteristics of the sediment,

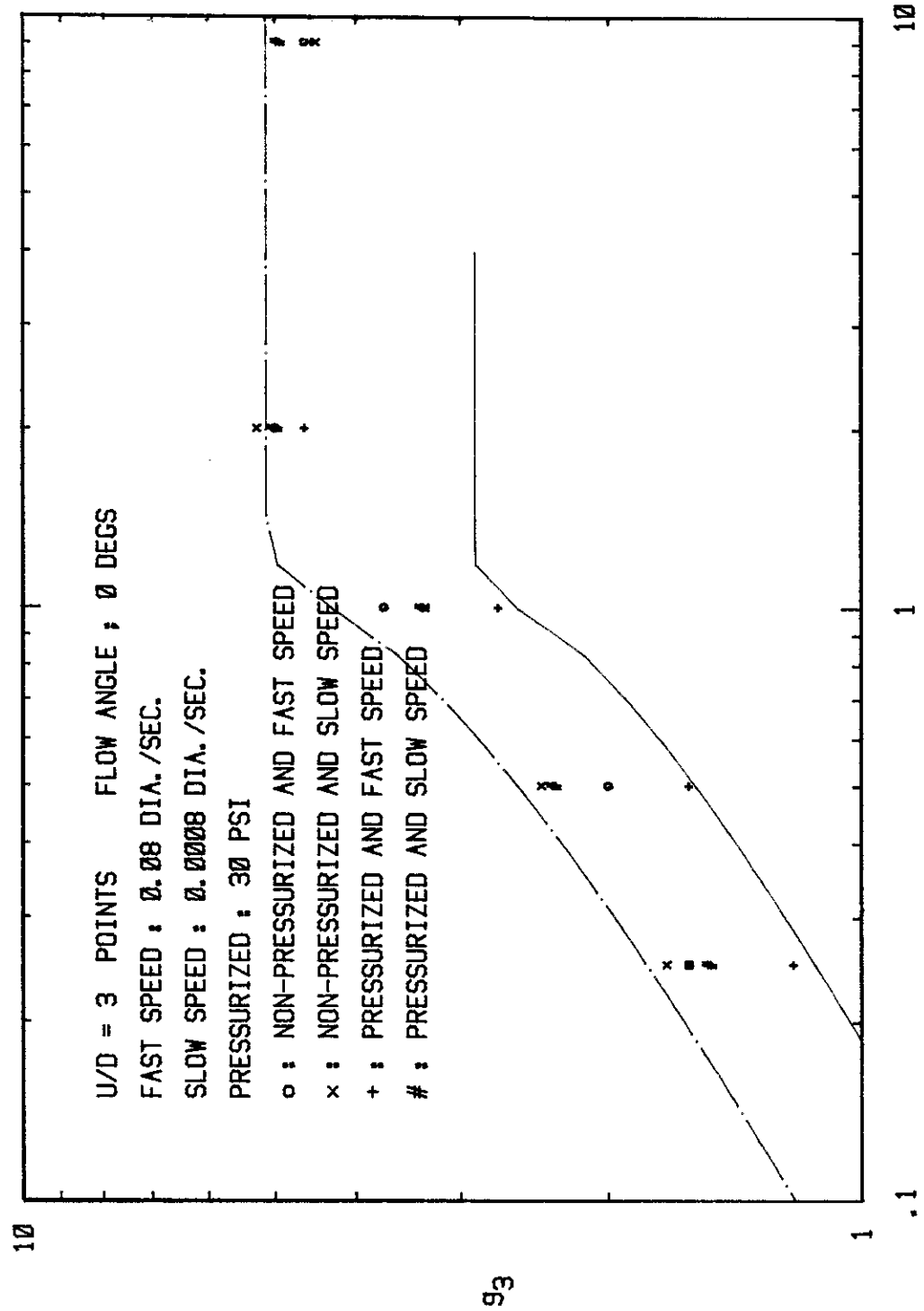

FIG. 3.113 - Axial Force Coefficients at U/D = 3 Points Versus Recess Depth for Speed and Pressure Effects. Logarithmic Scale.

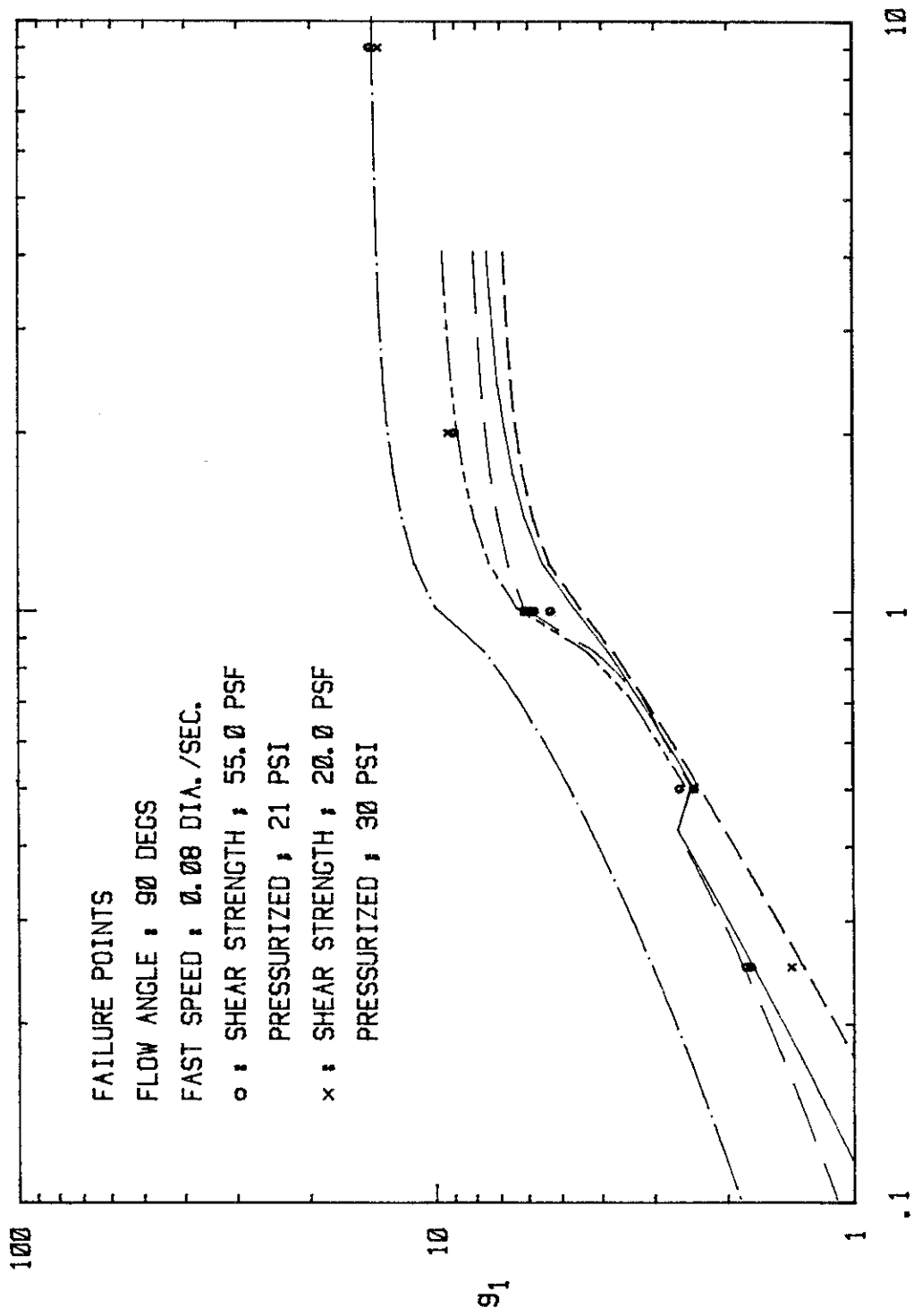

FIG. 3.114 - Normal Force Coefficients at Failure Points Versus Recess Depth for Shear Strength and Pressure Effects. Logarithmic Scale.

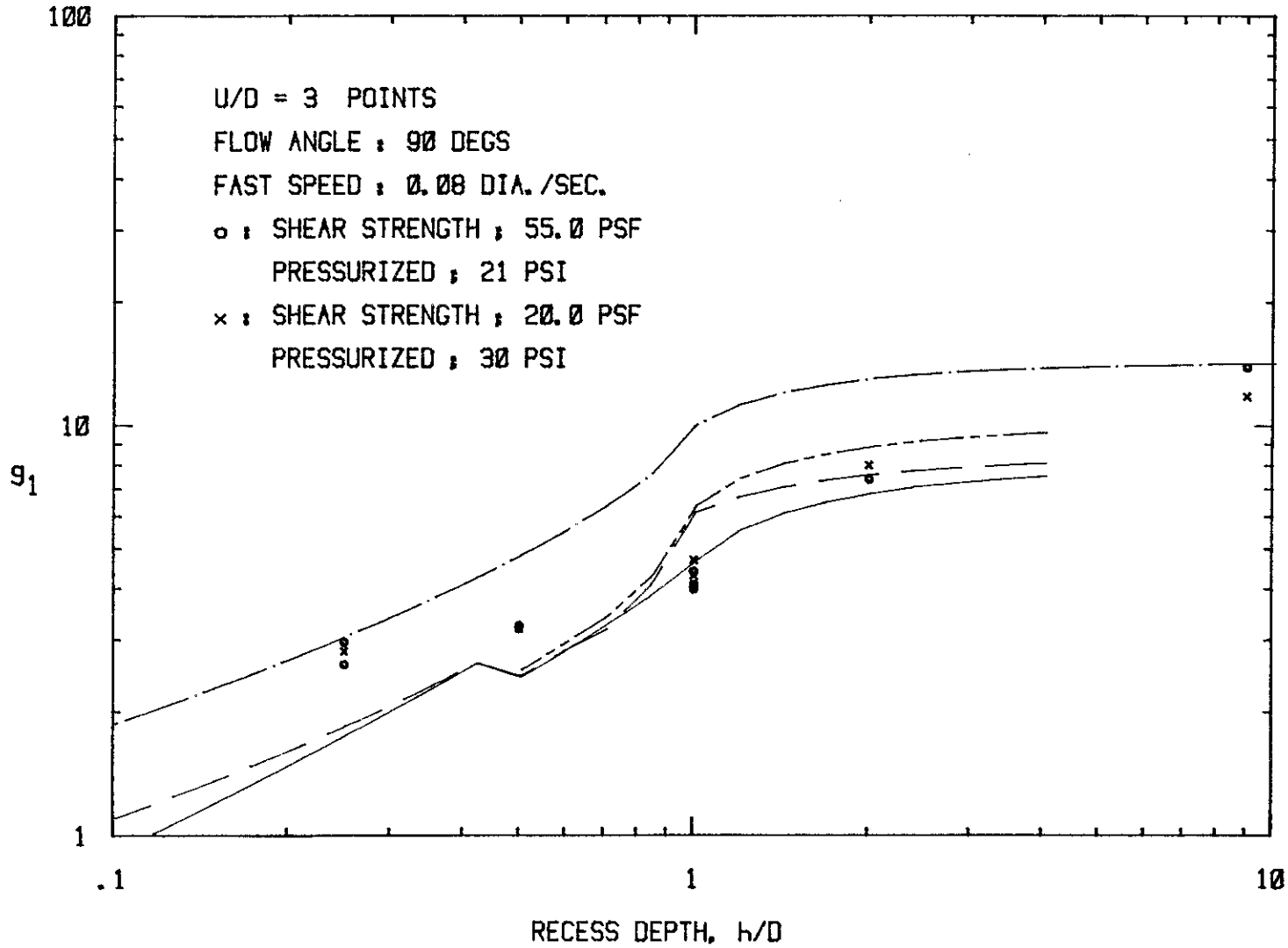

FIG. 3.115 - Normal Force Coefficients at U/D = 3 Points Versus Recess Depth for Shear Strength and Pressure Effects. Logarithmic Scale.

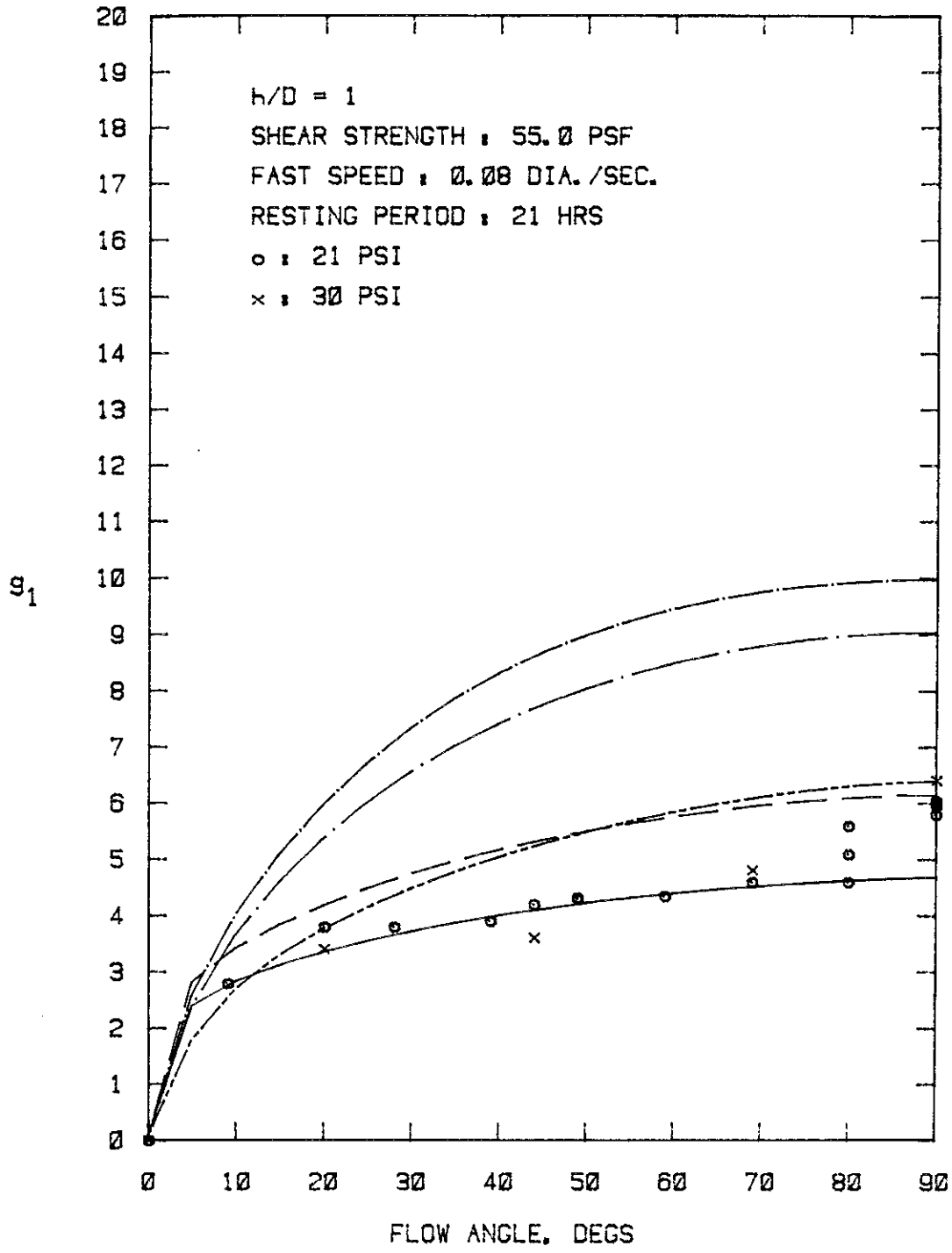

FIG. 3.116 - Normal Force Coefficients Versus Flow Angle for h/D = 1 at Two Pressures.

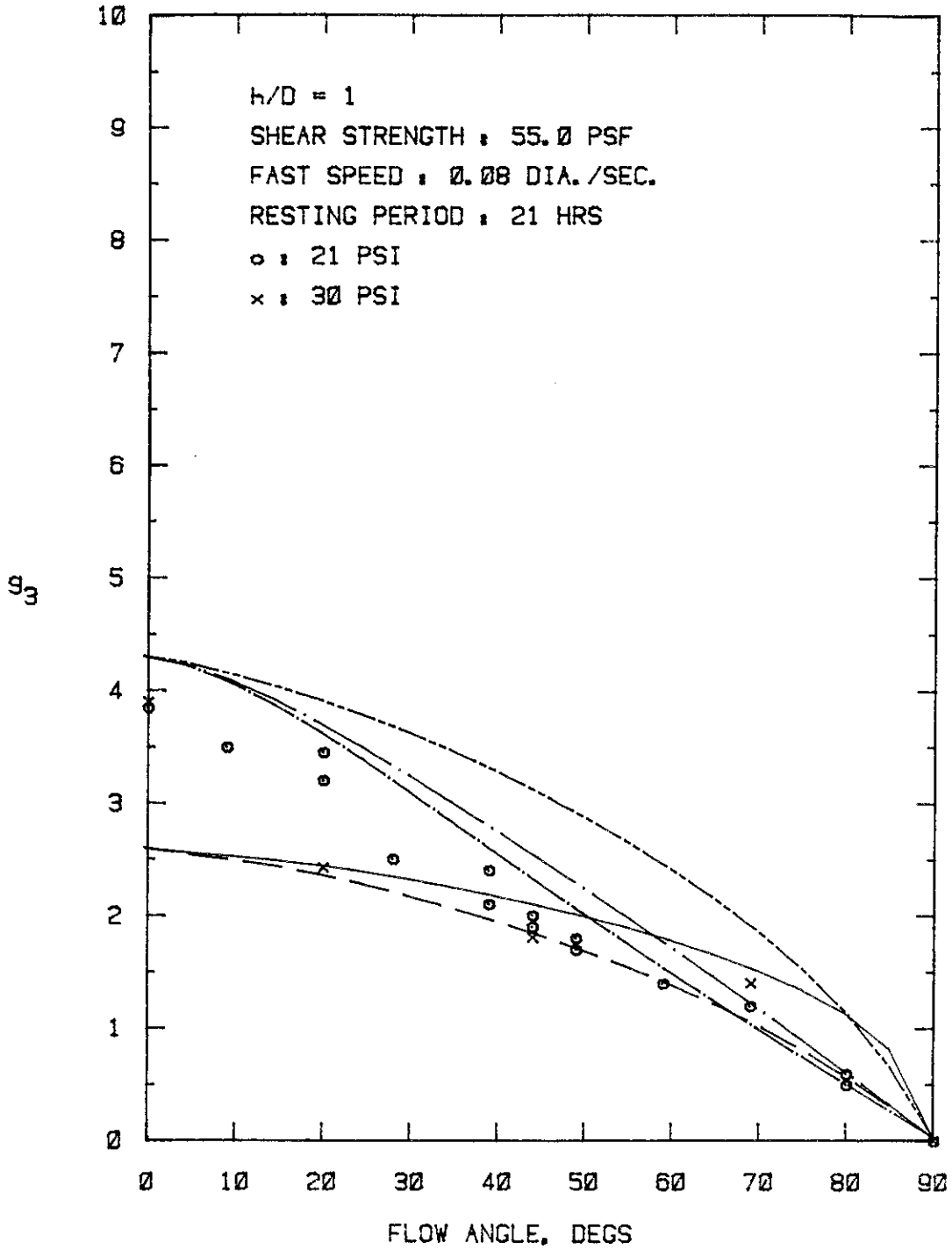

FIG. 3.117 - Axial Force Coefficients Versus Flow Angle for h/D = 1 at Two Pressures.

(b) changes the shape of the drag force-displacement curves as a result of the change in cracking characteristics, and

(c) slightly increases the normal force coefficient, g_1, but has little effect on the axial force coefficient, g_3.

4. End Effect Study: The dimensions of this size drag box limited the length of model pipe which could be used without inducing effects from the edge of the box. At the same time, it was desired to use a pipe large enough to produce high drag forces to increase resolution and accuracy of results. Somewhat arbitrarily, a pipe size of 0.75 in. diameter and 12 in. long (L/D = 16) was selected for the initial studies. Subsequently, a series of tests was performed in which the L/D ratio was changed by using different pipe diameters, while maintaining the same pipe length (12 in.). Pipes of 3/8, 3/4 and 1-1/2 in. diameter were used to produce L/D ratios of 32, 16, and 8. This required some modification of the pipe mounter which held the pipes to the stub. All tests were performed with 21 psi pressure and sediment shear strength of 55 psf.

The results of the tests are shown in Figs. 3.118 and 3.119 for g_1 and g_3, respectively. Differences between g_1 for the various L/D ratios are relatively small (Fig. 3.118), but it can be observed that the 1-1/2 in. diameter pipe gives slightly higher values than the 3/4- and 3/8-in. diameter pipes. One complicating factor is that the dimensions of the box limited the vertical placement of the pipes resulting in h/D ratios of 4.23, 9 and 18 for the 1-1/2, 3/4 and 3/8 in. pipes, respectively. This means that the 1-1/2 in. pipe was probably influenced somewhat by surface effects, i.e. it could not be considered as being buried infinitely deep. However, if this were a dominating effect, g_1 for the 1-1/2 in. pipe should be smaller, not larger, than the results from the

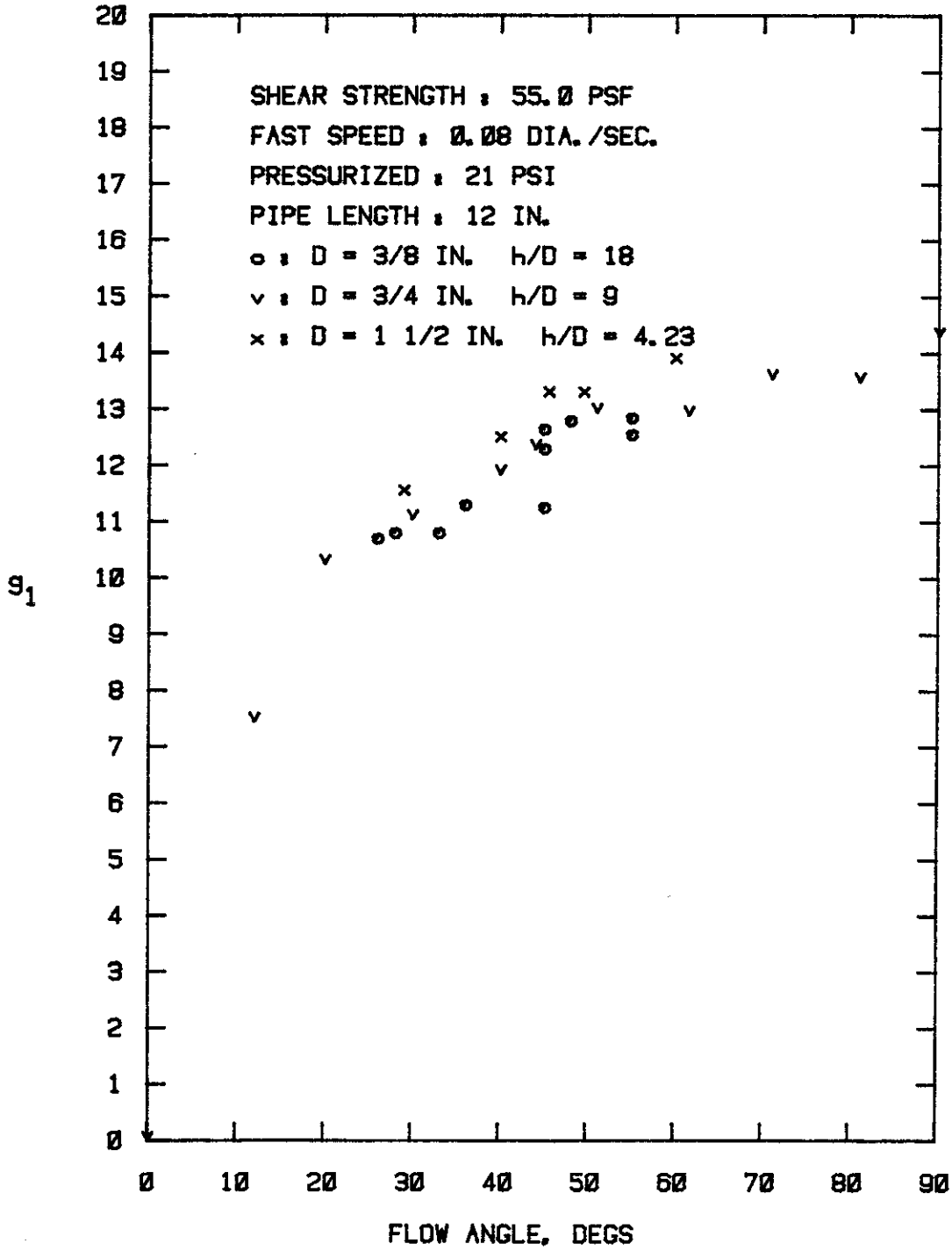

FIG. 3.118 - Normal Force Coefficients Versus Flow Angle at U/D = 3 Points for Three Different Pipe Diameters.

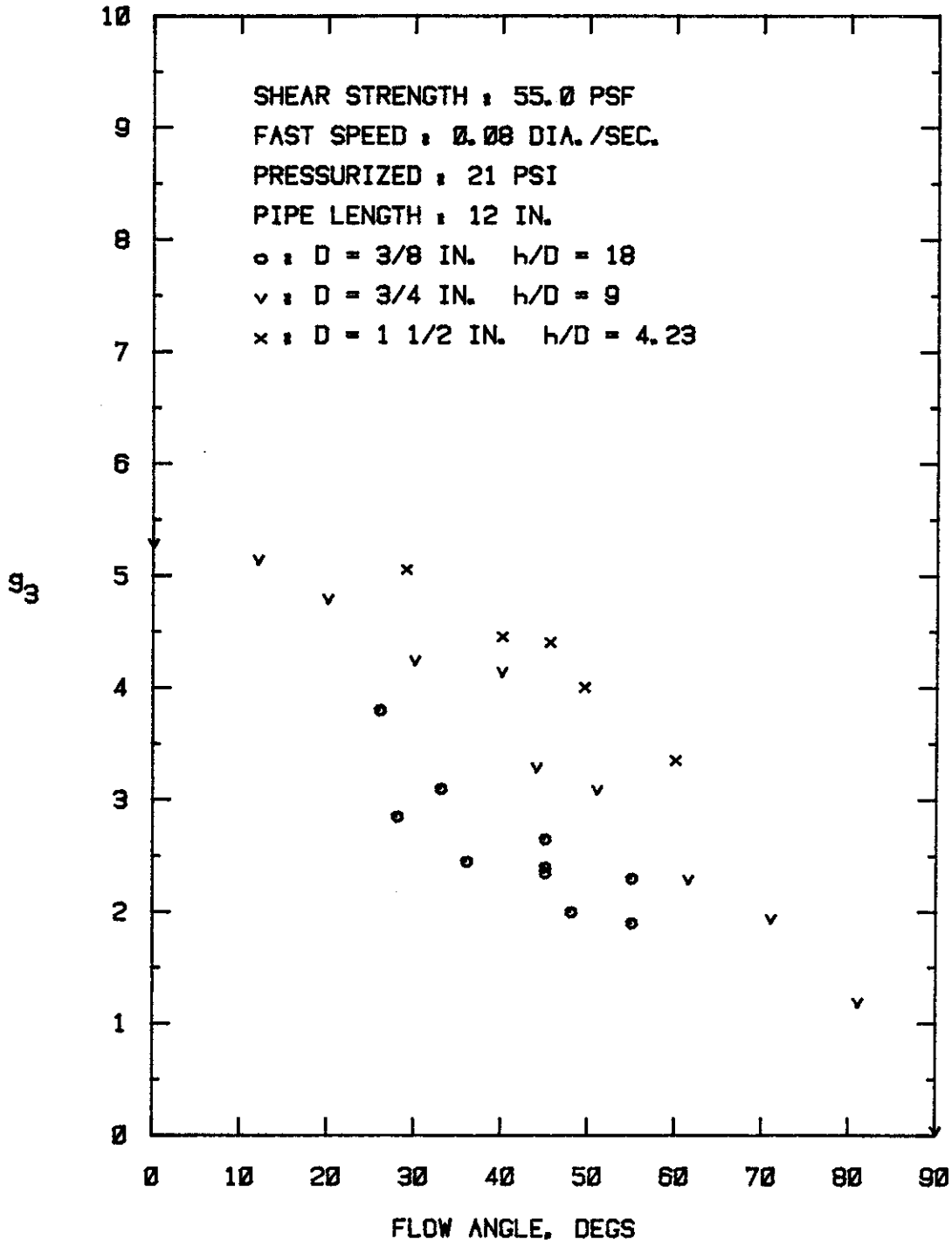

FIG. 3.119 - Axial Force Coefficients Versus Flow Angle at U/D = 3 Points for Three Different Pipe Diameters.

other two pipes.

The results for g_3 (Fig. 3.119) show a distinct spread for the 3 pipe diameters with the 1-1/2 in. pipe again showing the highest values and the 3/8 in. pipe the lowest values.

The above force coefficients were calculated using Eq. (4.116) in which the frontal area was obtained using the projected length of the pipe; the exposed ends were not considered. By adding the exposed ends to the pipe frontal area the drag factors would be reduced - a step in the right direction. However, there is at present no adequate theoretical approach for considering the characteristics of the complicated flow field around the pipe ends, and it is necessary to use empirical approaches. Three such approaches were tried. In the first method, the frontal area of the pipe was increased by the additional area at the leading edge of the pipe ($\frac{\pi D^2}{4} \cos \alpha$), and in the second method this area was multiplied by two to consider a suction force on the trailing edge of the pipe. For the third method, the measured force coefficient was modified by subtracting the theoretical force coefficient for that angle multiplied by the projected end area.

The most successful approach was the use of the second method for g_1, and the third method for g_3. As shown in Fig. 3.120, the second method reduced the spread of values for g_1, but it also lowered all g_1 values slightly. The third method (Fig. 3.121) also reduced the spread of values for g_3, but the results for the 3/8 in. pipe are still lower than those obtained for the other two diameters. This difference may possibly be attributed to the effect of the stub, which does create some disturbance of the sediment flow field. Such disturbance would have a larger effect on the small diameter pipe than on the larger ones.

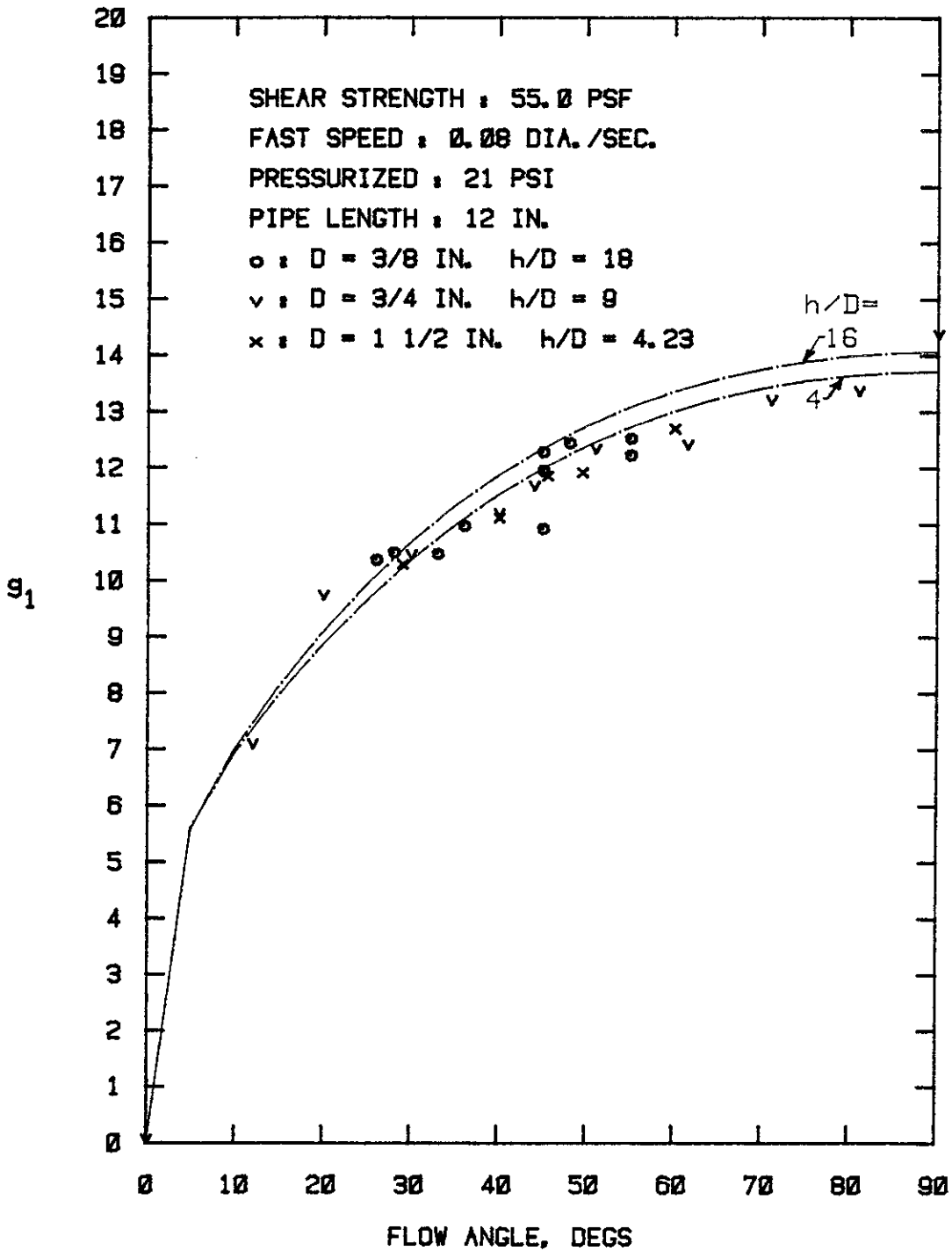

FIG. 3.120 - Normal Force Coefficients Versus Flow Angle at U/D = 3 Points for Three Different Pipe Diameters After Correction by Method 2.

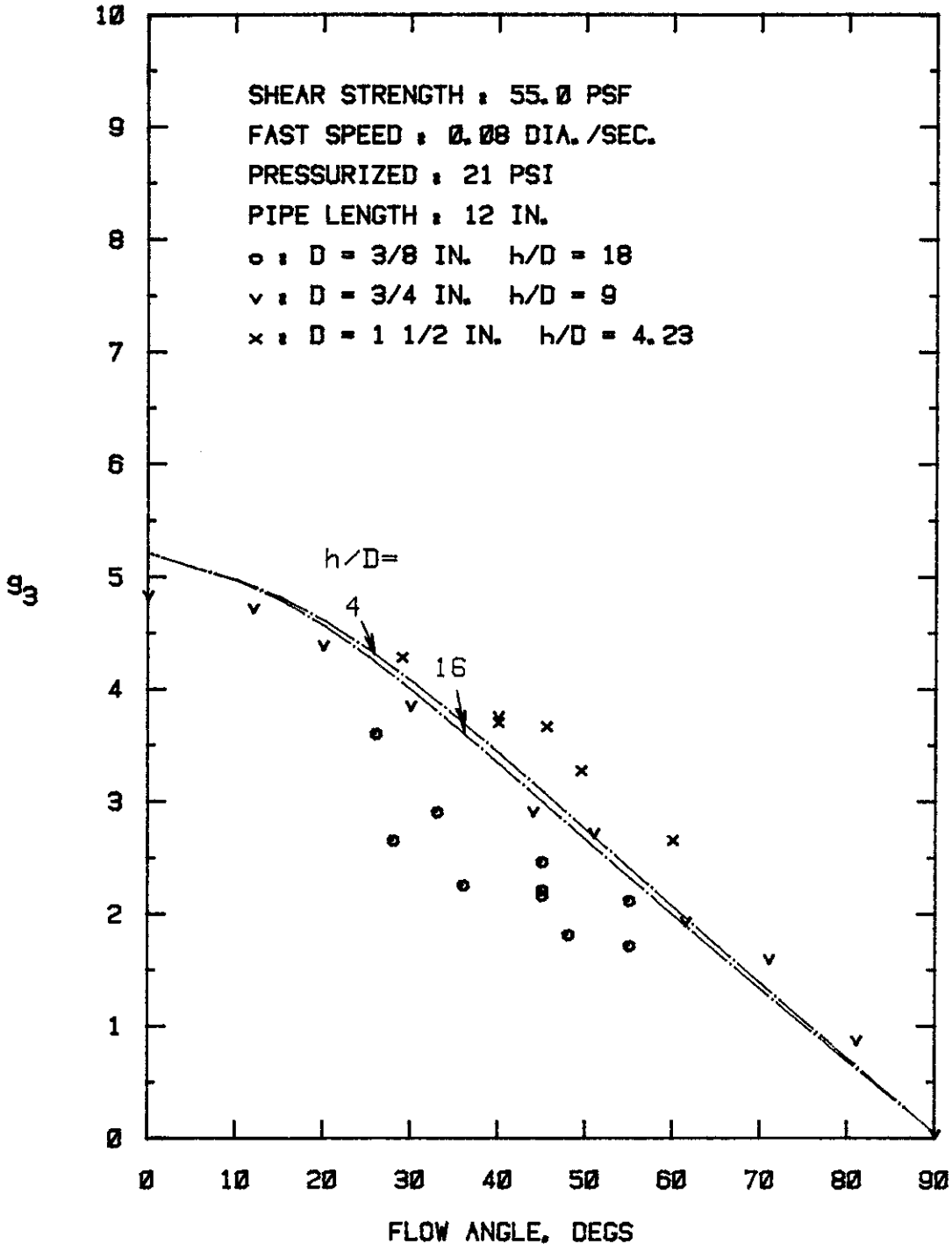

FIG. 3.121 - Axial Force Coefficients Versus Flow Angle at U/D = 3 Points for Three Different Pipe Diameters After Correction by Method 3.

In the previous discussions relating to the intermediate box, the end effect corrections have not been made.

3.4.3 Tests in Small Drag Box

1. Angle Tests: This series of tests was performed to verify the relationship between force coefficients and flow angle, α, that had been previously developed in the intermediate drag box. All tests were performed at total pressures of 30 psi. The rest time for these tests was only 2 hrs., and the pipe was allowed to freely rotate. Only three angles, $\alpha = 90°$, 45°, and 0°, were deemed necessary for verification purposes.

Test results are expressed in terms of g_1 and g_3 versus flow angle in Figs. 3.122 and 3.123, respectively. In nearly every test conducted in this series, a distinct failure or peak point resulted, and the data shown in Figures 3.122 and 3.123 used these failure points. Several replicate tests were performed, and as seen from the curves, there was excellent agreement between replications.

The results have also been replotted in terms of g-values versus recess depth, h/D, for the separate flow angles. Figures 3.124 and 3.125 present the g_1-values for flow angles of 90° and 45°, respectively, whereas Figs. 3.126 and 3.127 present the g_3-values for 0° and 45°.

2. Effect of Shear Strength/Pressure: These tests were conducted to determine the effect of shear strength changes of the sediment on the force coefficients and on the shape of the drag force curves under conditions of constant total pressure (21 psi). The pipe was clamped to prevent rotation, the rest period was 21 hrs., and the flow angle was 90°. The two shear strengths investigated were nominally 20 psf and 42.5 psf.

The shape of the curves for the horizontal force coefficient, g_1,

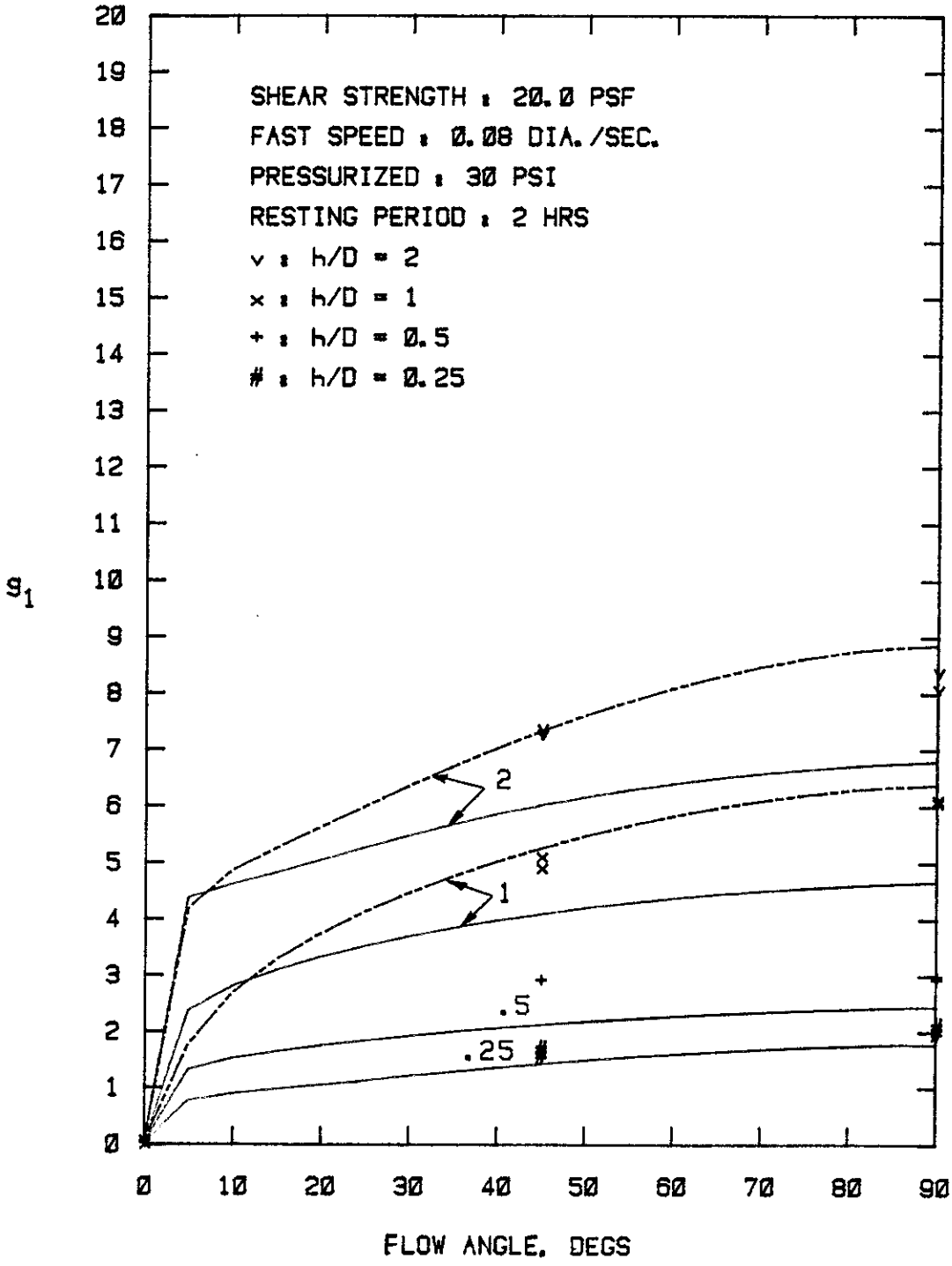

FIG. 3.122 - Normal Force Coefficients at Failure Points Versus Flow Angle for h/D = 0.25, 0.5, 1 and 2.

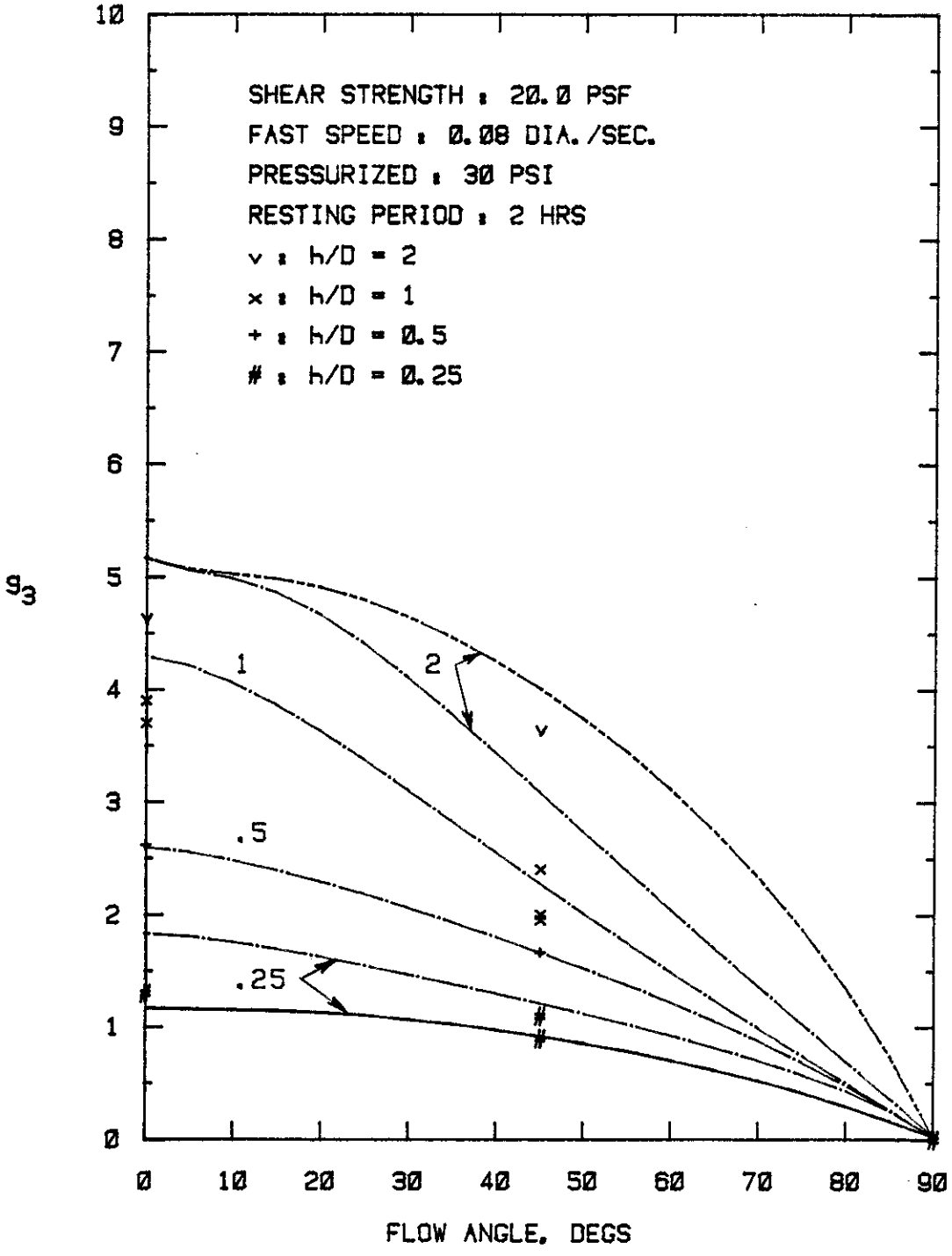

FIG. 3.123 - Axial Force Coefficients at Failure Points Versus Flow Angle for h/D = 0.25, 0.5, 1 and 2.

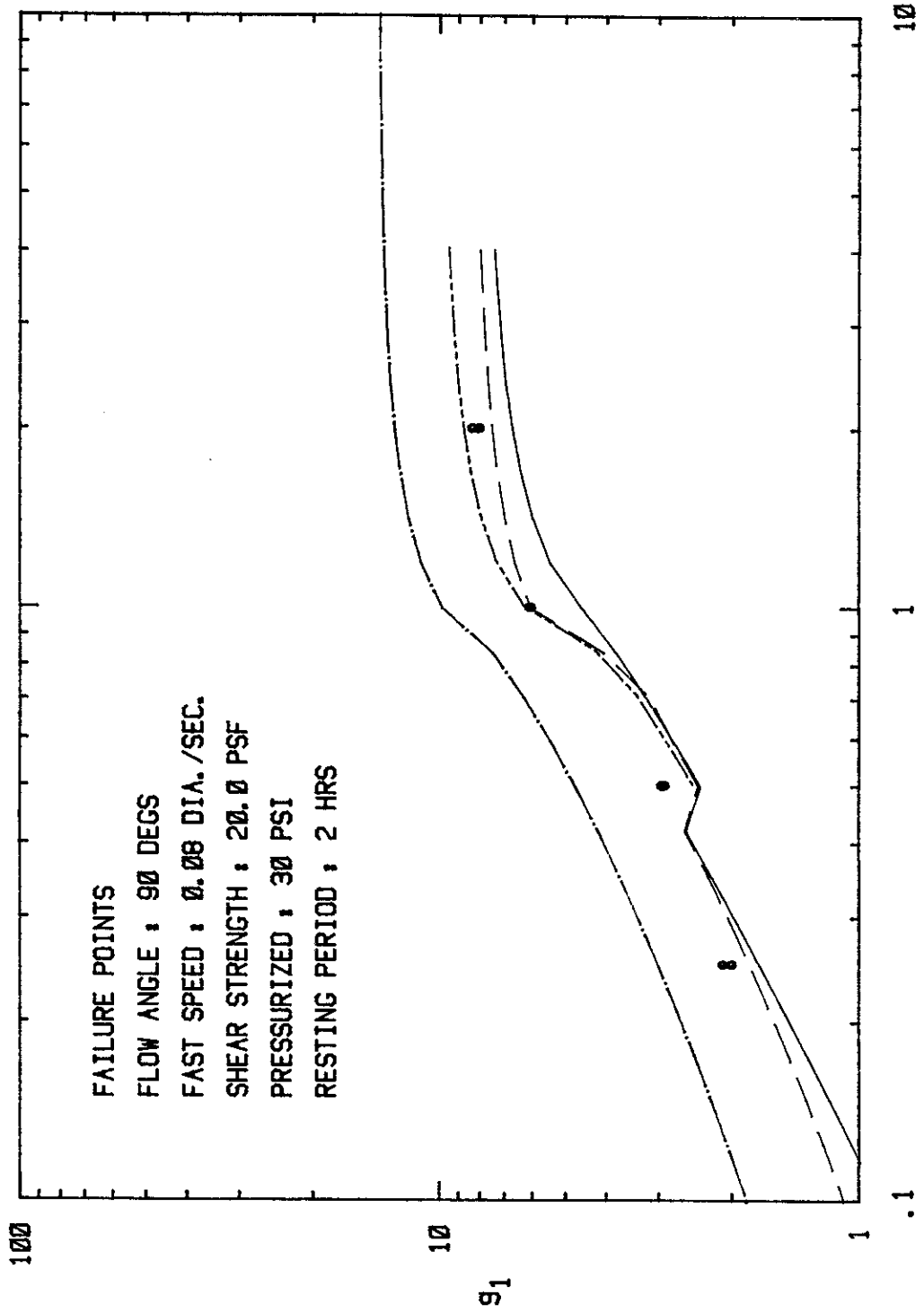

FIG. 3.124 - Normal Force Coefficients Versus Recess Depth for 90° Flow Angle. Logarithmic Scale.

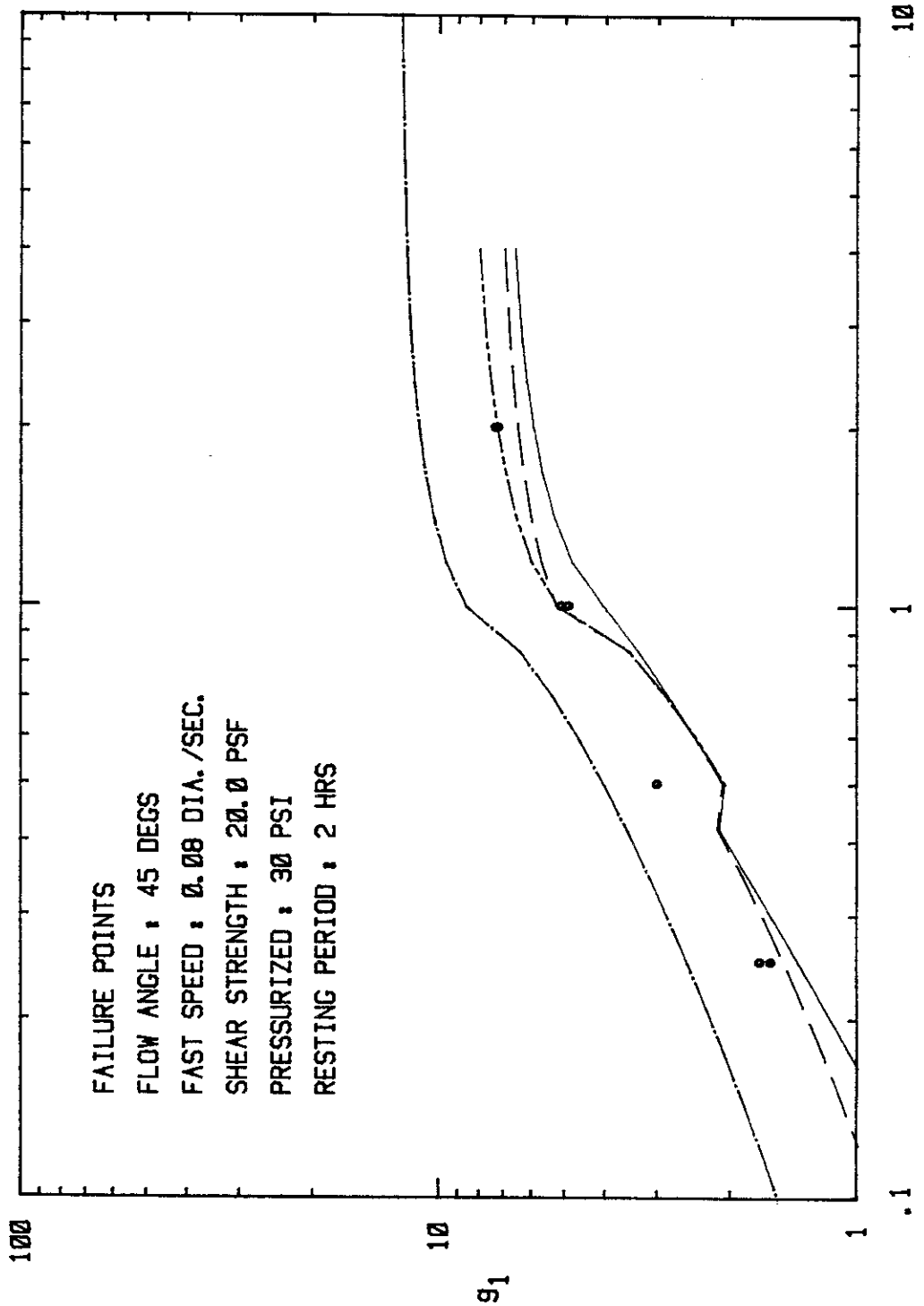

FIG. 3.125 - Normal Force Coefficients Versus Recess Depth for 45° Flow Angle. Logarithmic Scale.

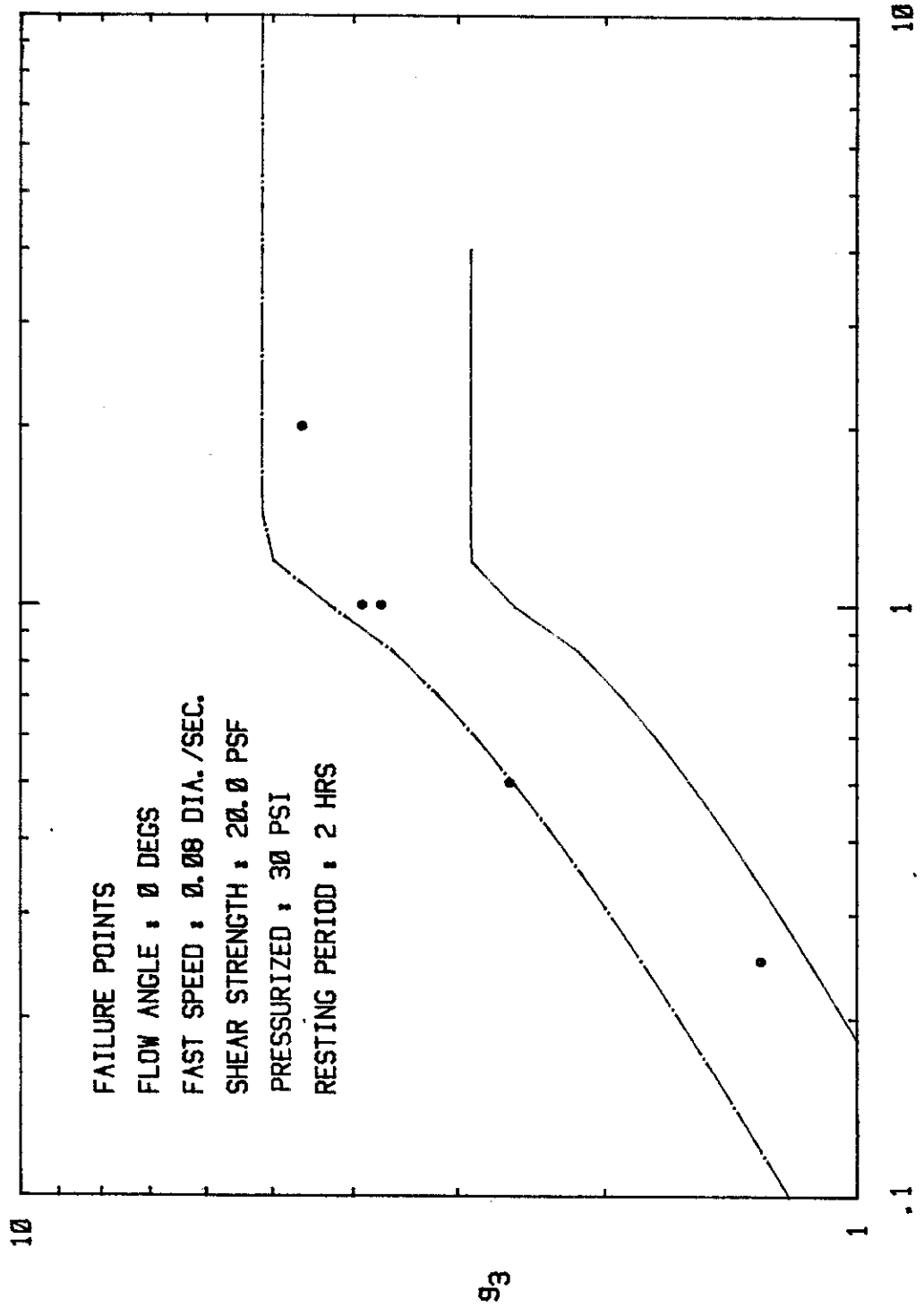

FIG. 3.126 - Axial Force Coefficients Versus Recess Depth for 0° Flow Angle. Logarithmic Scale.

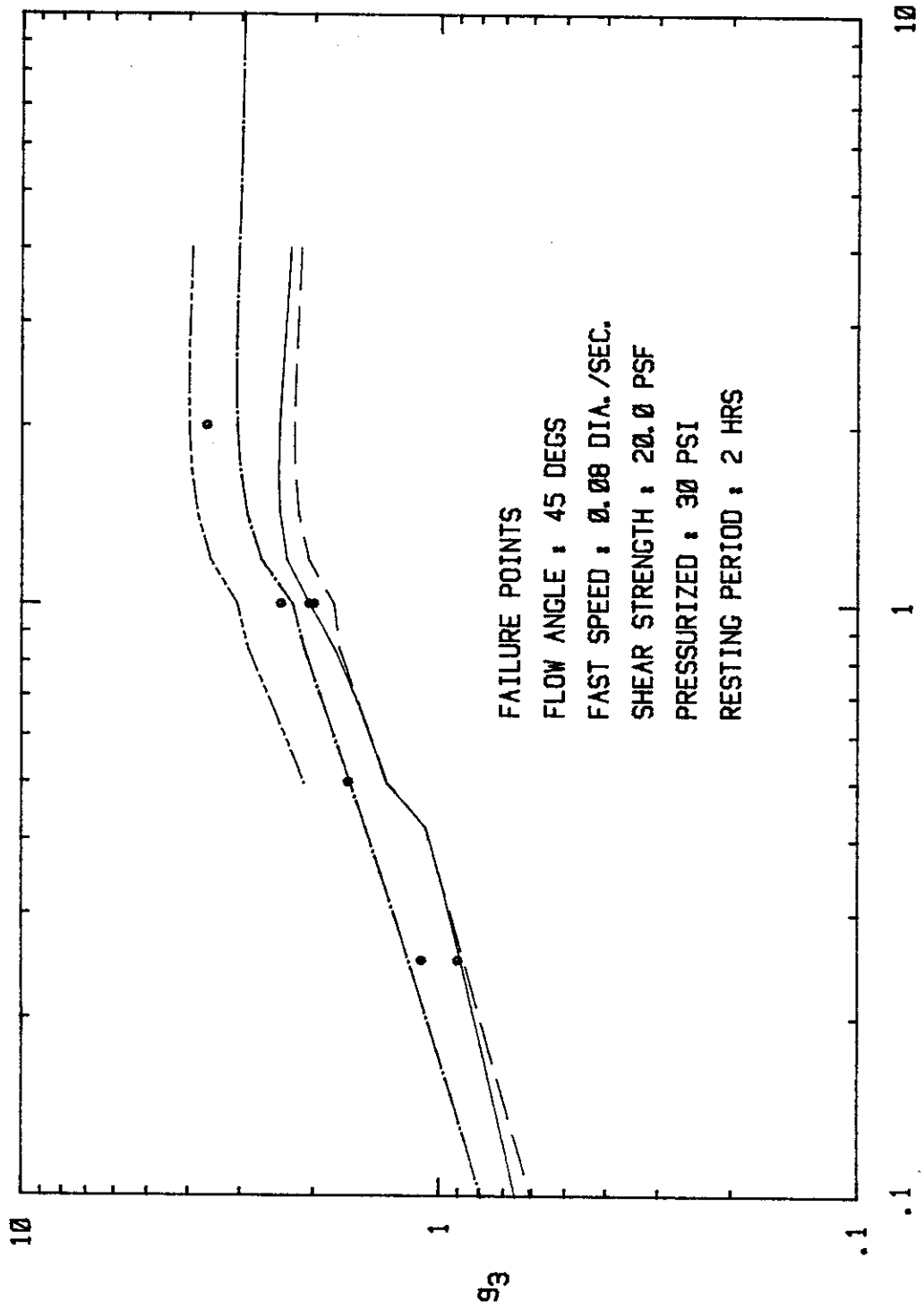

FIG. 3.127 – Axial Force Coefficients Versus Recess Depth for 45° Flow Angle. Logarithmic Scale.

versus normalized displacement, U/D, was found to be affected by the shear strength of the sediment. The most striking changes occurred at recess depths, h/D, of 1 and 2. Figure 3.128 shows results for shear strength of 42.5 psf and h/D of 2. A very sharp initial peak occurred. With a shear strength of 20 psf, the same peak value of g_1 was obtained, but the dropoff was more gradual (Fig. 3.129). For partially buried pipes, h/D of 0.25 and 0.5, the early portions of the curves were similar for the two shear strengths, but at large displacements, the value of g_1 continued to slightly increase for the higher shear strength, whereas it remained constant for the lower shear strength.

The results from all tests are presented in Fig. 3.130 for the peak or failure point. This figure shows no significant difference in the value of g_1 for the different shear strengths except at h/D = 1 where the lower shear strength produced a higher g_1. For larger displacements, U/D = 3, there is little difference between the two shear strengths, although the lower strength seems to produce slightly lower values of g_1 (see Fig. 3.131).

3. Effects of Pipe Surface Roughness: These tests were conducted on pipes with smooth, standard and rough surfaces to determine whether surface roughness influenced the horizontal force coefficient. All tests were conducted under conditions of no pressure after a 2 hr. rest period.

In one series of tests, the pipes were allowed to freely rotate. All of these tests exhibited a discernible peak force at small displacements. For h/D = 0.5, the standard pipe had a g_1 of 3.4, the polished pipe had 3.60, and the rough pipe had 3.70. For h/D = 1, both the standard and rough pipes had a g_1 of 5.9 (smooth pipe not tested at

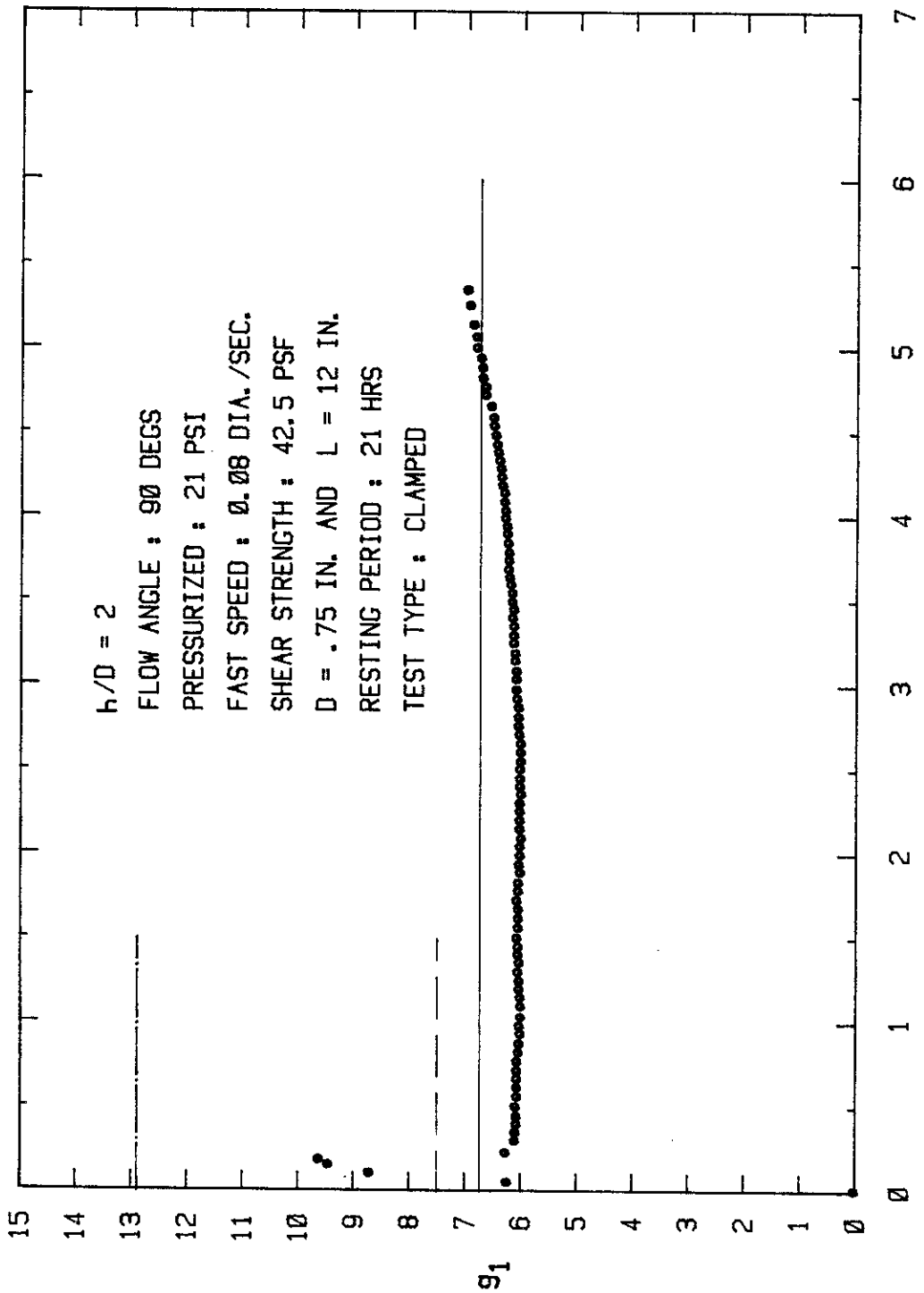

FIG. 3.128 - Normal Force Coefficients Versus Displacement for Shear Strength of 42.5 psf and h/D = 2.

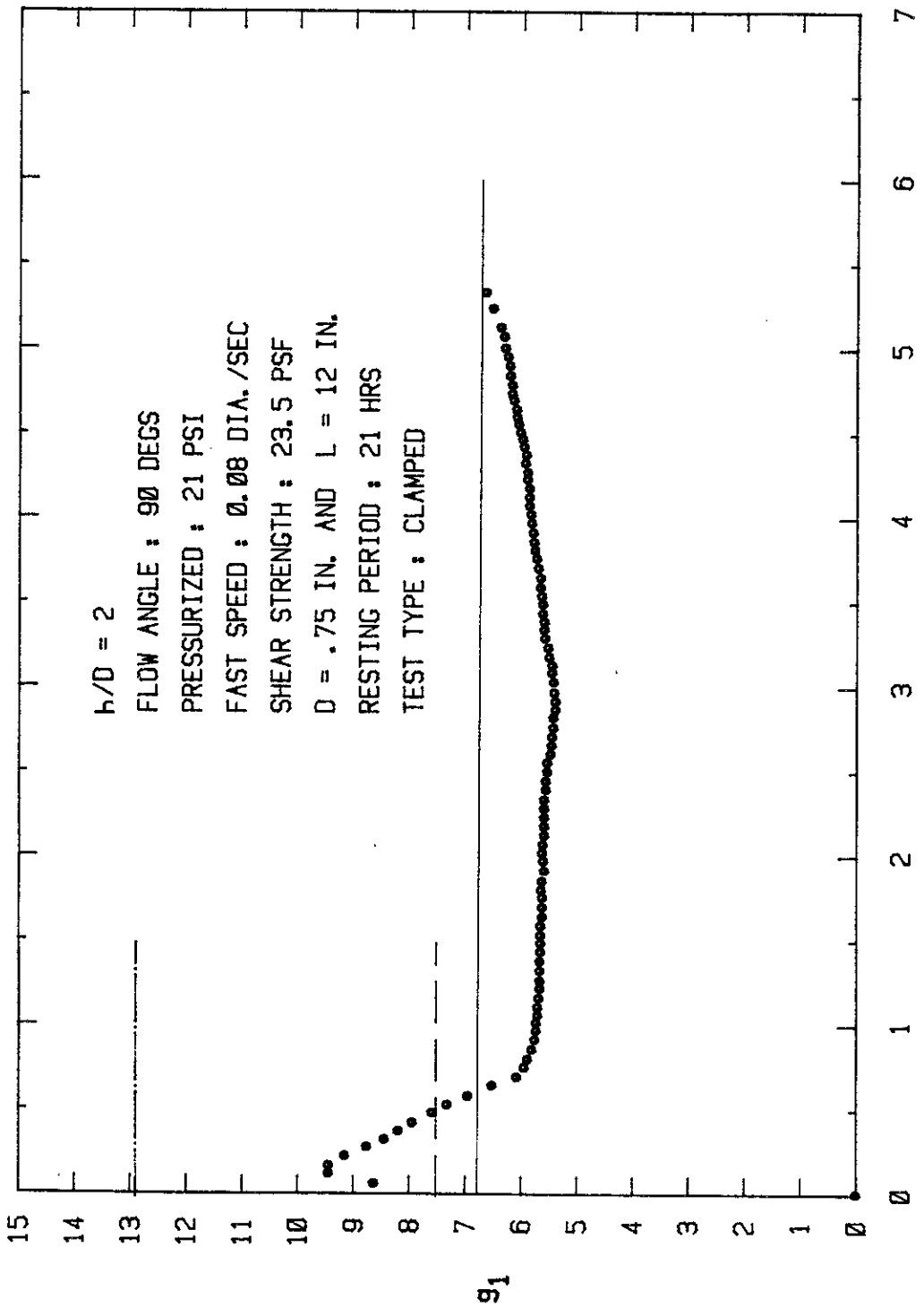

FIG. 3.129 - Normal Force Coefficient Versus Displacement for Shear Strength of 20 psf and h/D = 2.

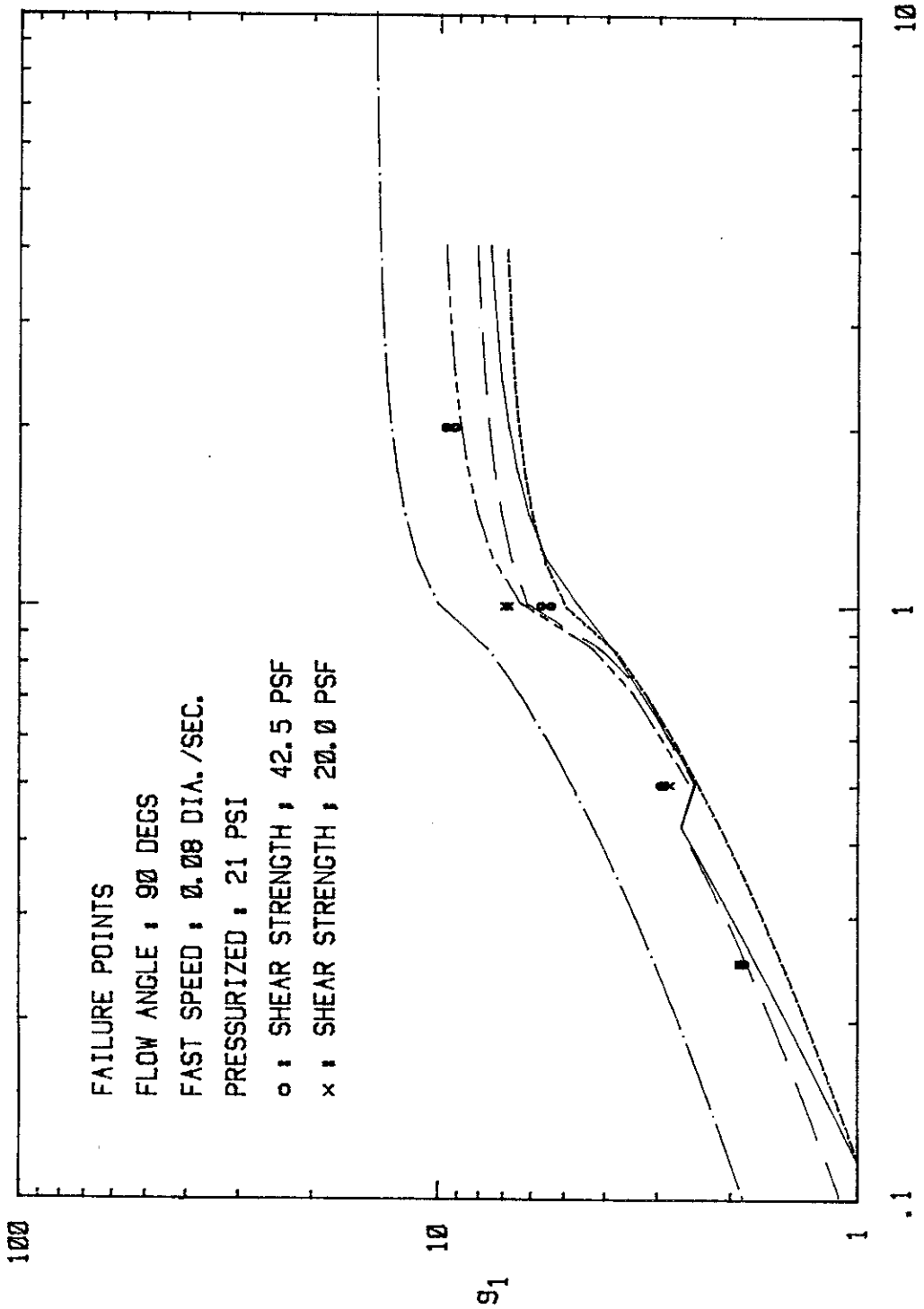

FIG. 3.130 – Normal Force Coefficient Versus Recess Depth at Failure Points for Shear Strengths of 20 and 42.5 psf. Logarithmic Scale.

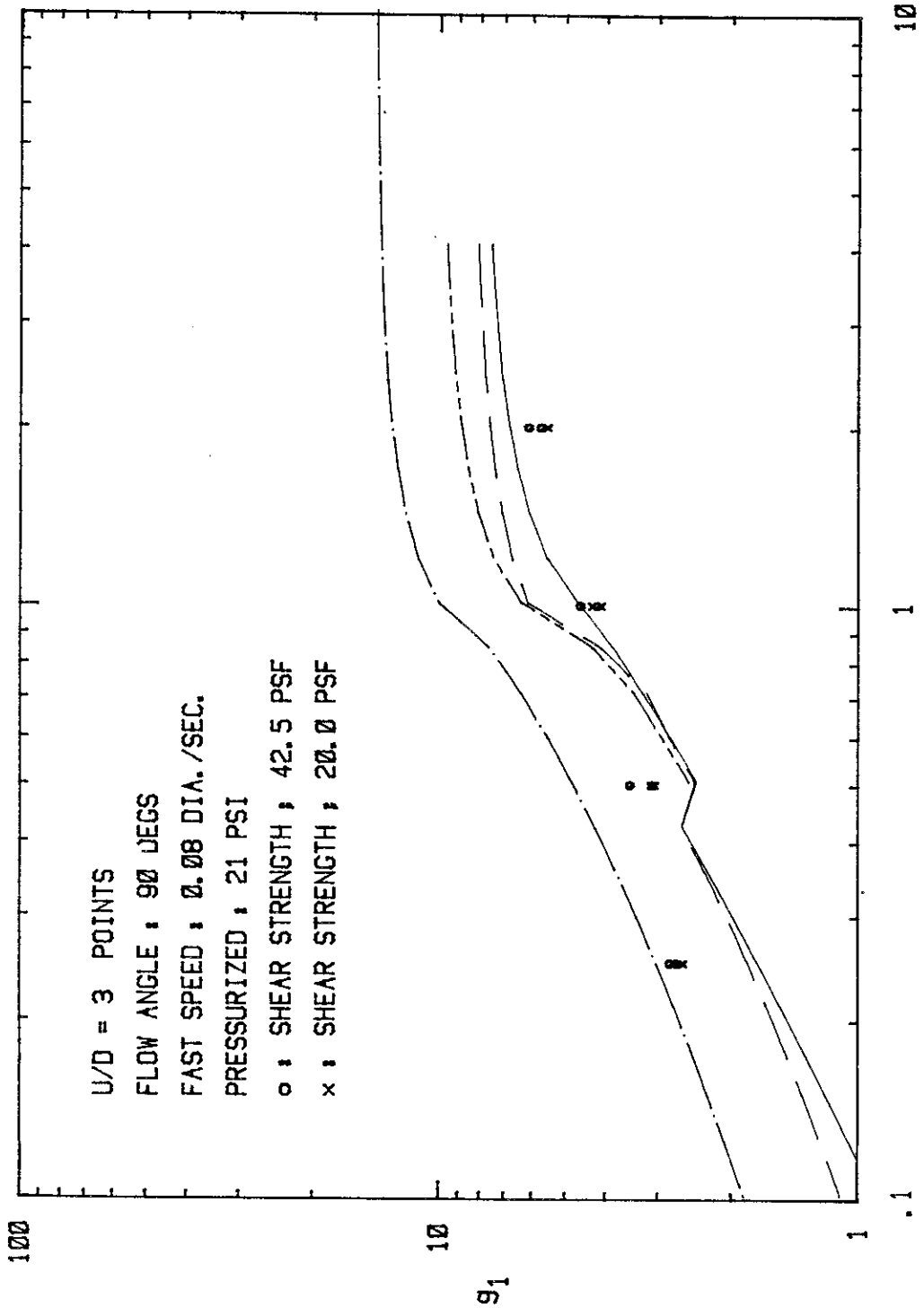

FIG. 3.131 - Normal Force Coefficients Versus Recess Depth at U/D = 3 Points for Shear Strength of 20 and 42.5 psf. Logarithmic Scale.

this recess depth). At large displacements (U/D = 3), the values of g_1 for the standard, polished and rough pipes were 3.5, 3.4 and 3.55, respectively for h/D = 0.5, and for h/D = 1, g_1 was 3.7 for the standard pipe and 3.4 for the rough pipe. Thus, the differences in g_1 between the various pipes are certainly minor.

A few tests were performed at h/D = 0.5 with the pipes clamped against rotation. At the failure points, the polished pipe had a g_1 of 4.1 whereas the rough pipe had a value of 4.7. At U/D = 3, the polished and rough pipe had g_1 values of 3.4 and 3.7, respectively; these are approximately the same as observed at U/D = 3 for the free rotation case. There were no tests performed with the standard pipe, but based on similar tests in the other boxes, a g_1 of 3.3 is appropriate.

These tests indicate that for the free rotation condition pipe roughness has no significant effect, but for the clamped or nonrotating case, the surface roughness may have an effect on the initial drag forces. At large displacements, drag forces will be the same for all pipes, regardless of surface roughness.

Test results are presented in Figs. 3.132 and 3.133 for the failure point and U/D = 3 cases, respectively.

4. Sediment Surface Elevations During Drag Tests: Several tests were performed in which the height of sediment above and around the pipe was measured as the pipe travelled through the sediment. The results were utilized for verification of the theory.

Measurements made during one test with a clamped pipe at a recess depth, h/D of 1, are shown in Fig. 3.134. The results are expressed in terms of height of sediment accumulating above the original sediment surface ($-U_2$) divided by the pipe diameter. Two measurements were made: one was the sediment height directly above the center of the pipe and

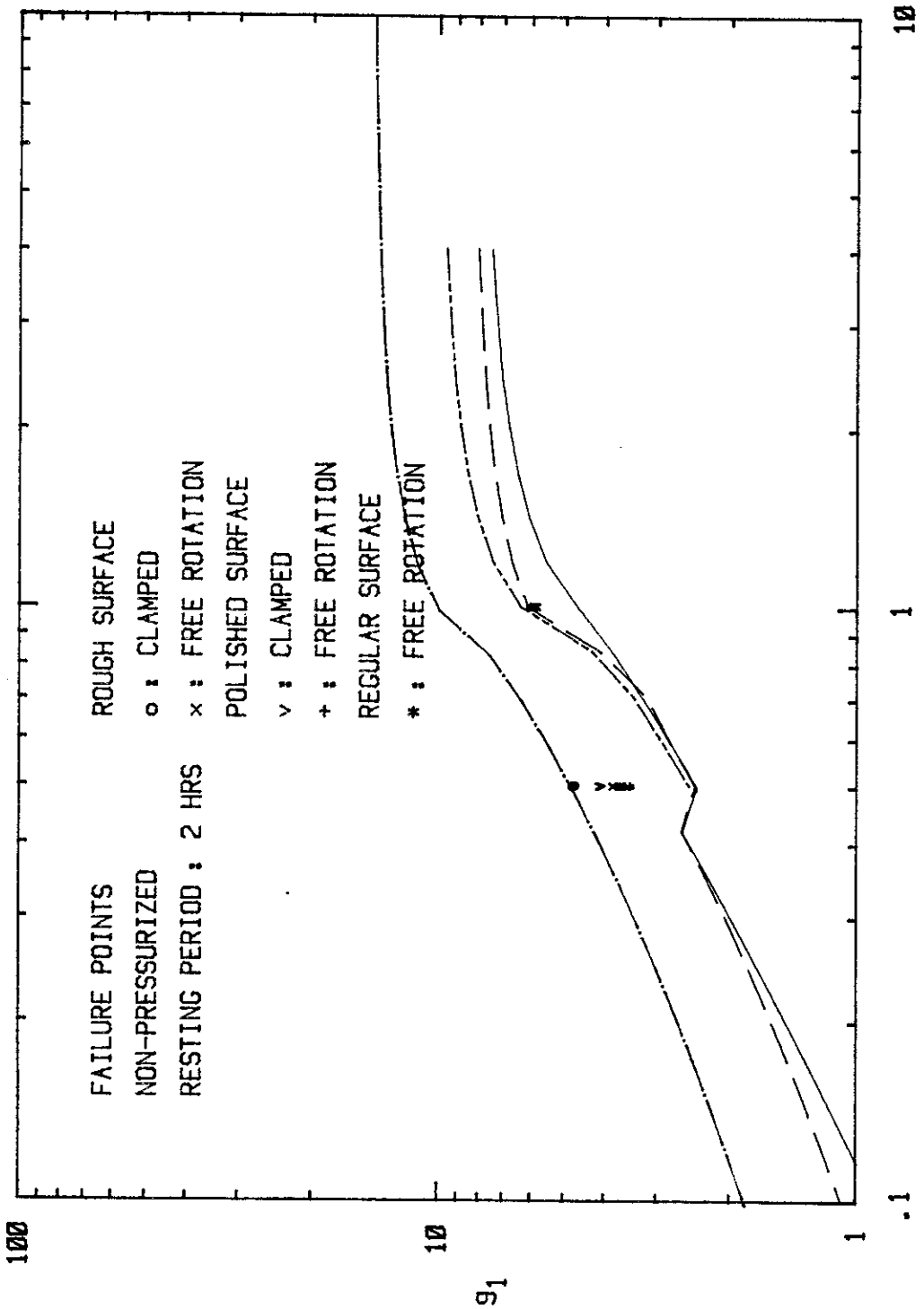

FIG. 3.132 - Comparison of Normal Force Coefficients Versus Recess Depths at Failure Points for Pipes of Different Roughness. Logarithmic Scale.

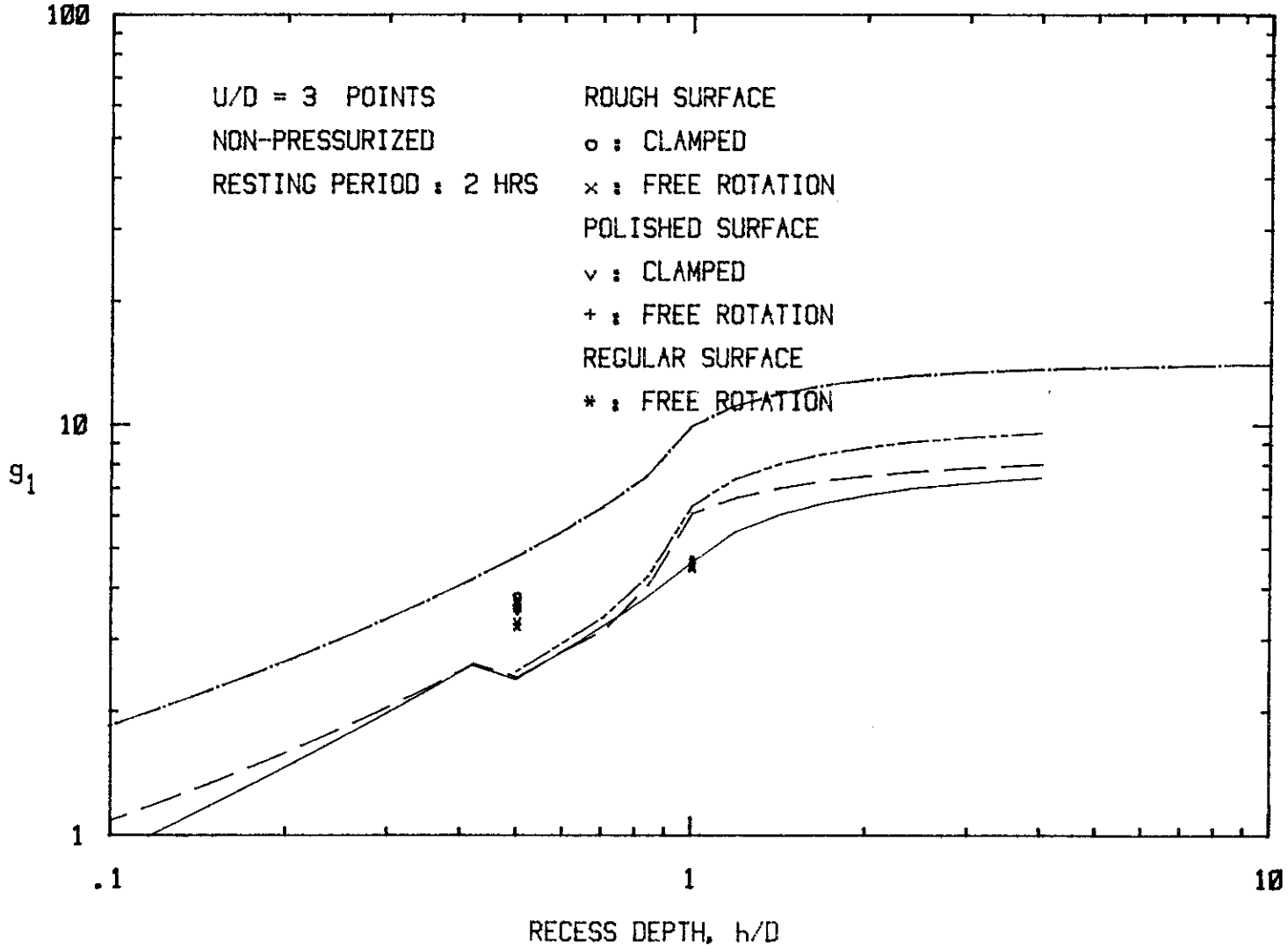

FIG. 3.133 - Comparison of Normal Force Coefficients Versus Recess Depths at U/D = 3 Points for Pipes of Different Roughness. Logarithmic Scale.

the other was the maximum height of sediment, which was usually between the center and leading edge of the pipe. The results show that the sediment started slowly accumulating over the top of the pipe as horizontal movement was initiated. Then, with continued movement, the sediment started rolling over the pipe and falling into the hollow behind the trailing edge of the pipe. At large displacements, U/D approximately 12, the rate at which the sediment accumulated behind the pipe became constant, and the sediment surface at the leading edge of the pipe was level with the sediment accumulation over the top of the pipe. At this point the thickness of sediment over the pipe was twice the pipe diameter ($U_2/D = 2$).

The force coefficients are directly affected by the sediment accumulation over the pipe, although not in a step-wise fashion as might be indicated by Fig. 3.134. It was observed that the force coefficients tended to become constant at U/D of approximately 12.

Another observation made in these tests was that freely floating pipes tended to maintain their initial vertical position as the sediment moved past them. If the pipe started to rise, the accumulation of sediment over the pipe pushed it down to the original depth. If the pipe started to sink the sediment accumulation decreased and the pipe rose to the original depth.

3.5 Summary of Test Results

The drag boxes developed for this research proved to be effective in determining horizontal and vertical forces exerted by soft sediment on moving pipes. Pipes ranging from 3/8- to 6-in. in diameter were tested in sediments having undrained shear strengths of 9.5- to 55-psf.

1. The horizontal force coefficient, g_1, for nonrotating pipes

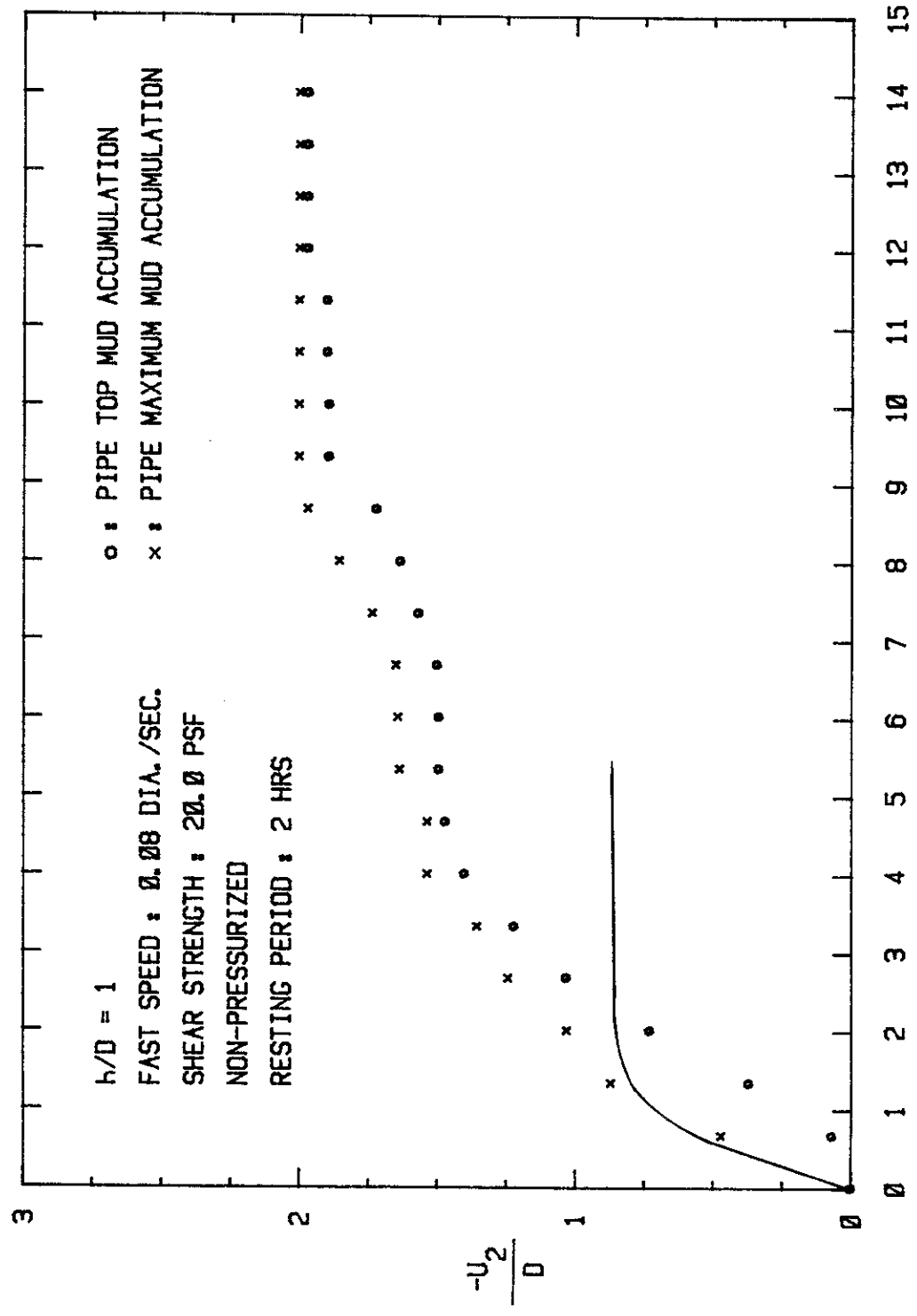

FIG. 3.134 - Sediment Accumulation Over Pipe Expressed as Normalized Vertical Displacement Versus Horizontal Displacement.

oriented normal to the direction of flow, was found to vary from approximately 2.0 for h/D = 0.25 to 14.3 for h/D = 9. The results indicate that surface effects disappear at h/D of 6 to 7, and that pipes buried greater than this depth can be considered infinitely deep with respect to normal flow. For purely axial flow the horizontal force coefficient, g_3, ranged from 1.6 for h/D = 0.25 to 5.3 for h/D = 2; it remained constant for burial depths greater than h/D of 2.

2. The initial vertical forces - those forces which resulted from pipe burial and which were measured before the drag test began - were upward (buoyant) for pipes with $h/D \leq 1$. For pipes buried deeper than this, the initial forces were downward, indicating that the overlying sediment was pushing down on the pipe rather than behaving in a fluid-like fashion.

3. For nonrotating pipes, there was a complex relationship between the vertical force coefficient, g_2, and the pipe recess depth which was further complicated by the magnitude of the initial vertical forces as mentioned above. The value of g_2 was a maximum of approximately 1.5 at h/D = 0.25, decreased to -1.25 at h/D = 2, then increased to approximately -0.7 at h/D = 4. The trend of the data is that g_2 will approach zero with greater depth of burial, as might be expected.

4. Test results indicate very little difference in force coefficients for freely rotating and nonrotating pipes; in fact, there was no perceptible difference in g_1, the horizontal force coefficient. Vertical force coefficients seemed to be slightly smaller for freely rotating pipes when $h/D \leq 2$ (slightly larger at h/D = 0.25), but the results are probably within the error band of the data for the two types of tests.

5. Horizontal force coefficients for the 6 in. diameter pipe compared very well with those obtained for the 1.5 in. diameter pipe at the failure point. The vertical force coefficients seemed to be somewhat higher for the 6 in. diameter pipe, although there is some doubt about the accuracy of the values for the 6 in. diameter pipe owing to instrumentation problems. At large displacements, the force coefficients are higher for the 6 in. diameter pipe. The results seem to indicate that gravity and buoyancy effects are significant, i.e. the weight of the sediment retards cracking and affects far-field mud behavior.

6. For tests is which pipes were pushed straight down in the sediment, a vertical force coefficient, g_2, of 13.4 was obtained; however, extrapolation of the data indicated that g_2 would have reached approximately 14 if the pipe could have been pushed deeper. This compares favorably with the horizontal force coefficient, g_1, of 14.3 that was obtained for deeply buried pipes.

7. Deeply buried pipes pulled up at a shallow angle (approximately 5°) produced the same peak horizontal force coefficents, g_1, as obtained from horizontal drag tests at corresponding depths of burial. However, deeply buried pipes pulled up at a steep angle (approximately 45°) gave lower values of g_1 than horizontal drag tests at the same burial depths.

8. When pipes were pushed into the sediment at an angle of approximately 45°, the horizontal and vertical force coefficients were essentially equal once the pipes were deep enough ($h/D > 3$) to overcome the effects of surface cracking.

9. Results obtained from tests where the pipe was recessed in layered sediment whose shear strength increased with depth, showed that the force coefficients, g_1 and g_2, were essentially the same as obtained

for the nonlayered case provided that an appropriate weighted average shear strength was used. The method of weighting the strength assumed that the sediment contributed to drag resistance to a depth of one radius below the pipe.

10. The soft marine sediment used in this research is a strain-rate dependent material which means that the drag forces on pipes should be dependent on the velocity of sediment movement. For pipe velocities $\geq$ 0.005 dia/sec the rate dependence seems to be adequately considered in the normalized force coefficients by inclusion of the term $(V/D)^n$. At slower velocities, the rate effects do not appear to be adequately considered, although the differences are small, say 10% or less. The rate effects at the very slow velocities may in reality be due to changes in the strength of the sediment as a result of either thixotropy or consolidation around the pipe. These effects will need to be handled by other methods separate from the development of generalized force coefficients.

11. The effect of total pressure on the drag characteristics was somewhat ambiguous. However, it appears that an increase in pressure will suppress the far-field cracking characteristics of the sediment but it may increase pipe-sediment separation , it will change the shape of the drag force-displacement curves as a result of the change in cracking and separation characteristics, and it will have a greater effect on the normal force coefficient, g_1, than on the axial force coefficient, g_3. The effect of pressure on the vertical force coefficient, g_2, was not investigated.

12. Surface roughness of the pipe has negligible effect on the drag force if the pipe is freely rotated. For clamped pipes which are very

rough, the horizontal drag force at failure is higher than observed for a pipe with standard surface finish, and is close to that predicted when there is no separation of mud from the pipe. At large displacements, all pipes have the same drag force regardless of surface roughness.

13. Freely floating pipes have no tendency to undergo a permanent change in elevation as sediment flows horizontally past them. Rather, they tend to remain at their initial depth of burial. Direct observations indicate that if the pipe tends to rise, the weight of mud above the pipe increases and thus counters the lift force. Just the opposite is observed if the pipe begins to sink. This conclusion is based on small diameter pipes with horizontal movement limited by the test device, and it is therefore not known if it applies to actual pipelines at the seabottom.

4.0 THEORY

The basic equations needed to predict forces between sediment and pipes are developed here. The field equations and boundary conditions are discussed in Sections 4.1 and 4.2. Included in Section 4.1 are certain constitutive equations which are more general than those used later to make predictions; on the basis of this discussion, it is suggested that the pipe-soil interaction analysis could be extended to a broader class of problems than treated in detail in this report.

Different methods of solving the equations were considered, including the finite element method. The latter method was tried for deeply and partially buried pipes, but without success. It was not possible to achieve convergence, apparently because of the near-incompressibility of the sediment. The highly nonlinear behavior of this material compounded the difficulties. Subsequently, the classical Ritz method [9] was successfully employed. Its development and use are discussed in Sections 4.4-4.6, following the derivation in Section 4.3 of the underlying variational principle. The theory goes beyond standard treatments because of the need to include nonlinear effects of gravity on the instantaneous states of stress and deformation.

The basic simplifying feature of the Ritz method is that in many problems it permits the use of realistic analytical expressions for displacements with only a few free constants. These constants are then found by imposing a stationary condition on a certain energy functional. For the pipe problem, an important feature is that it is realistic to use soil displacements which obey a power law in distance from the centerline of the pipe. Besides the simplicity inherent in a power law, this form happens to be exact for some special cases. The exponent is one of the free parameters which is derived by the Ritz method.

4.1 Field Equations

The three-dimensional equations of motion for either soil or water in a state of initial stress have been derived by Biot [10] (Eq. 2.9, p. 264). Using his notation, they are

$$\frac{\partial s_{ij}}{\partial x_j} + \rho \Delta X_i - \rho \omega_{ik} X_k(x_\ell) - \rho e X_i(x_\ell) + S_{kj} \frac{\partial \omega_{ik}}{\partial x_j}$$

$$+ S_{ik} \frac{\partial \omega_{ik}}{\partial x_j} - e_{jk} \frac{\partial S_{ik}}{\partial x_j} = \rho \frac{\partial^2 u_i}{\partial t^2} \qquad (4.1)$$

where i, j, k, ℓ = 1, 2, 3 and the usual summation convention is followed for terms with repeated indices. An orthogonal set of Cartesian axes (x_i) is used, which are position coordinates for material particles in their initial position. Figure 4.1 shows x_1 and x_2 for the system of interest; the x_3-axis is perpendicular (and into) the plane of the page. Also,

t = time

ρ = initial density

u_i = displacement component in direction of x_i as measured relative to initial location of particles (cf. Figure 4.2).

The quantities e_{ij} and ω_{ij} are the strains and rotations, respectively,

$$e_{ij} \equiv \frac{1}{2}(\partial u_i/\partial x_j + \partial u_j/\partial x_i) \qquad (4.2)$$

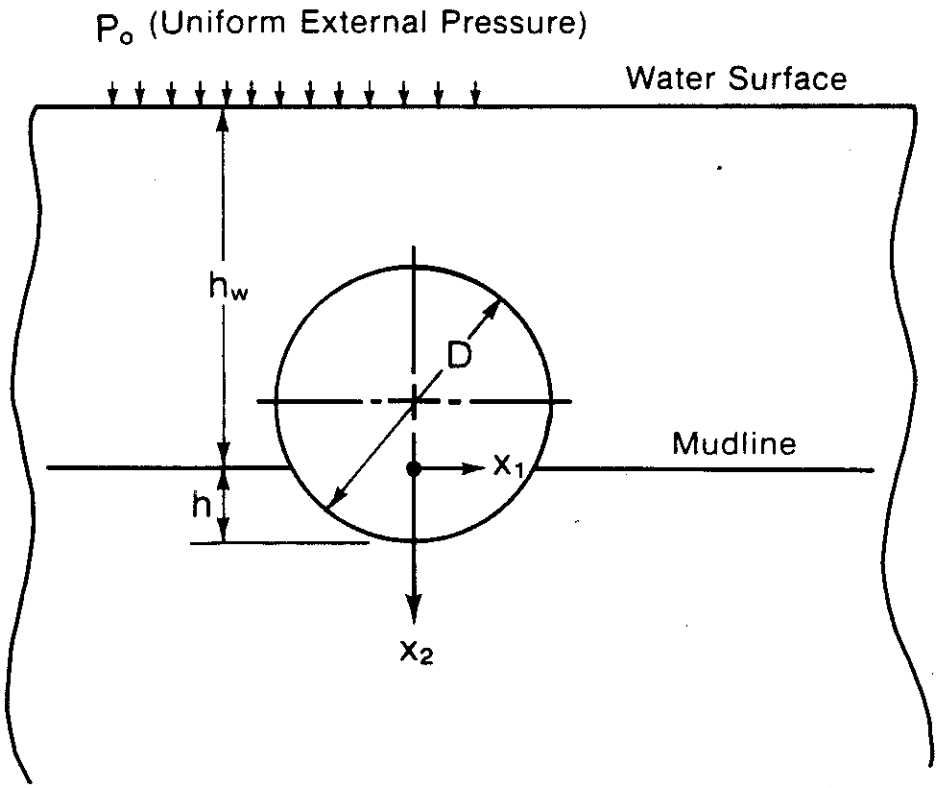

Figure 4.1 Initial Geometry of Pipe-Mud-Water System

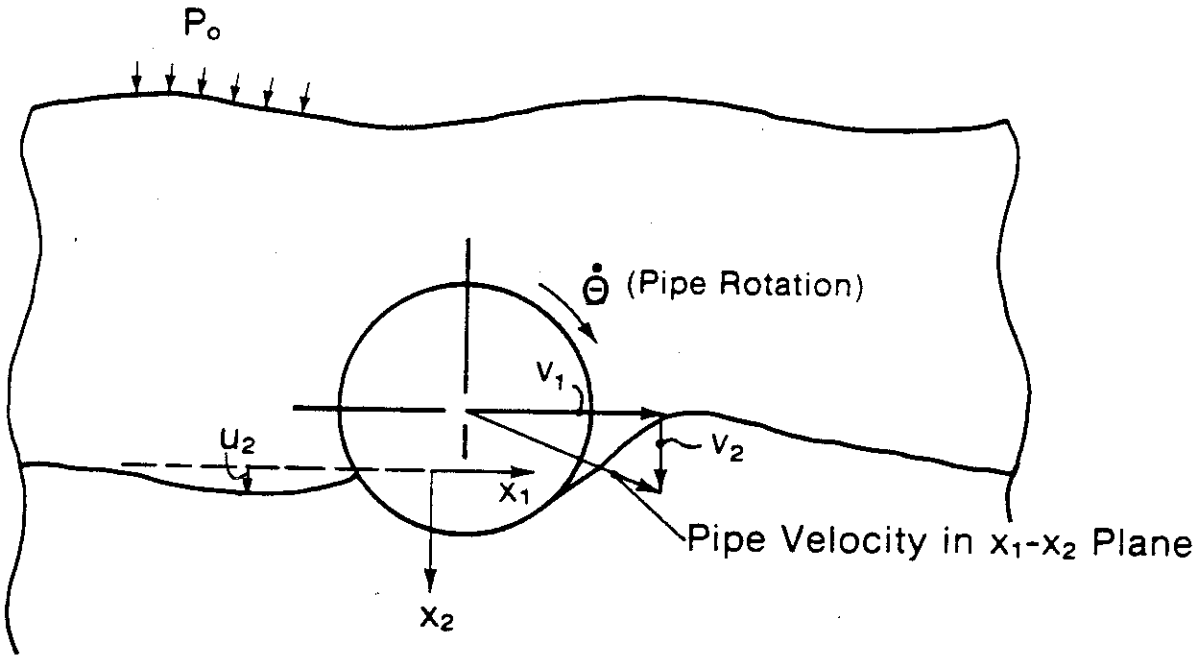

Figure 4.2 Deformed Geometry and Notation for Pipe Motion

$$\omega_{ij} \equiv \frac{1}{2}(\partial u_i/\partial x_j - \partial u_j/\partial x_i) \tag{4.3}$$

and e is the dilatation or volume strain,

$$e \equiv e_{ii} = e_{11} + e_{22} + e_{33} \tag{4.4}$$

Additionally, S_{ij} are the initial stresses, while s_{ij} are the stresses due to pipe movement (and other disturbances to the initial state) referred to a locally translated and rotated set of axes; these stresses in the $x_1 - x_2$ plane are shown in Figure 4.3. The axes $\bar{x}_1 - \bar{x}_2$ translate and rotate with each material element through the displacements u_i and angles ω_{ij}, respectively. Both sets of stresses S_{ij} and s_{ij} are symmetric; i.e. $S_{ij} = S_{ji}$ and $s_{ij} = s_{ji}$.

Body forces (per unit mass) in the initial state and their changes due to deformation are denoted by $X_k(x_\ell)$ and ΔX_i, respectively. In the problem of interest, the only body force is due to gravity: $X_1 = X_3 = \Delta X_1 = \Delta X_2 = \Delta X_3 = 0$ and $\rho X_2 = \gamma$, where γ is the unit weight.

The initial stresses satisfy the equilibrium equations

$$\partial S_{ij}/\partial x_j + \rho X_i(x_\ell) = 0 \tag{4.5}$$

and for a body force due only to gravity,

$$\partial S_{ij}/\partial x_j = 0 \quad \text{for} \quad i = 1, 3 \tag{4.6}$$

and

$$\partial S_{2j}/\partial x_j + \gamma = 0 \tag{4.7}$$

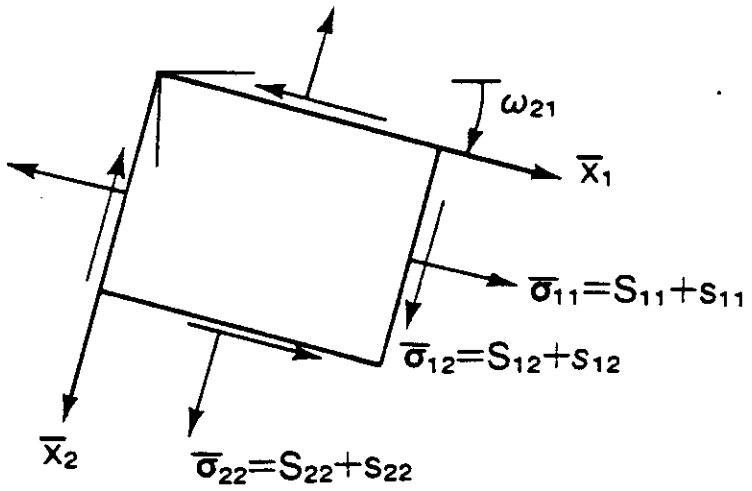

Figure 4.3 Representation of the Initial Stresses S_{11}, S_{22}, S_{12} and the Incremental Stresses s_{11}, s_{22}, s_{12} Referred to Rotated Axes $\bar{x}_1$ - $\bar{x}_2$

It is now assumed that each material element has the initial stress state,

$$S_{11} = S_{22} = S_{33} \equiv -p\ ,\ S_{12} = S_{23} = S_{13} = 0 \tag{4.8}$$

From Eqs. (4.6) and (4.7) we find p is independent of x_1 and x_3 and

$$dp/dx_2 = \gamma \tag{4.9}$$

where $\gamma = \gamma(x_2)$, allowing for a unit weight variation with depth. Equation (4.1) simplifies considerably when Eqs. (4.8) and (4.9) are introduced. In expanded notation, one finds

$$\frac{\partial}{\partial x_1}(s_{11} + \gamma u_2) + \frac{\partial s_{12}}{\partial x_2} + \frac{\partial s_{13}}{\partial x_3} = \rho \frac{\partial^2 u_1}{\partial t^2} \tag{4.10}$$

$$\frac{\partial s_{12}}{\partial x_1} + \frac{\partial}{\partial x_2}(s_{22} + \gamma u_2) + \frac{\partial s_{23}}{\partial x_3} = \rho \frac{\partial^2 u_2}{\partial t^2} + \gamma e \tag{4.11}$$

$$\frac{\partial s_{13}}{\partial x_1} + \frac{\partial s_{23}}{\partial x_2} + \frac{\partial}{\partial x_3}(s_{33} + \gamma u_2) = \rho \frac{\partial^2 u_3}{\partial t^2} \tag{4.12}$$

Constitutive equations for the water and soil may be expressed in terms of the incremental stresses s_{ij} and strains e_{ij}. Because the s_{ij} are referred to axes that rotate and translate with each material element, rigid body motion appropriately has no effect on the stress-strain equations when these mechanical variables are used.

The water is assumed to be inviscid and incompressible; thus,

$$s_{ij} = -\delta_{ij}\, p_w \tag{4.13a}$$

$$e = 0 \tag{4.13b}$$

where p_w is the incremental pressure in the water and δ_{ij} is the Kronecker delta,

$$\delta_{ij} \equiv \begin{cases} 0, & i \neq j \\ 1, & i = j \end{cases} \tag{4.14}$$

The equations of motion, Eqs. (4.10) - (4.12), reduce to

$$-\frac{\partial p_w^*}{\partial x_i} = \frac{\gamma_w}{g}\frac{\partial^2 u_i}{\partial t^2} \tag{4.15}$$

where, by definition,

$$p_w^* \equiv p_w - \gamma_w u_2 \tag{4.16}$$

Also, γ_w is the unit weight of the water and g is the acceleration due to gravity. The quantity p_w^* is the incremental pressure at a fixed vertical position x_2, whereas p_w is the incremental pressure acting on a given water element.

The deformation and failure behavior of submarine sediment is very complex, and cannot be realistically modeled using classical equations of elasticity or plasticity. Viscoelastic effects as well as changes in the soil fabric (or "microstructure") must be considered if the maximum soil resistance and pipe-soil forces subsequent to soil failure (or "breakaway") are to be predicted. A realistic constitutive theory that accounts for such effects was recently developed by the author [11]; it contains, as special cases, the linear viscoelastic and nonlinear viscous equations used in Phase I [1], as well a pre- and post-failure

behavior reported by Schapery and Riggins [5]. Under the assumption that the incremental dilatation e is very small compared to the shearing strains, the equations for an "incompressible" material may be used. Specialization of the theory in [11, Eq. 154] to this case of zero volume change yields the incremental deviatoric stresses

$$\sigma_{ij} = \psi \frac{\partial W}{\partial e^{o}_{ij}} \tag{4.17}$$

where

$$\sigma_{ij} \equiv s_{ij} - (1/3)s\delta_{ij} \tag{4.18}$$

and

$$s \equiv s_{ii} = s_{11} + s_{22} + s_{33} \tag{4.19}$$

is the incremental dilatational stress. Also, e^{o}_{ij} are called <u>pseudo strains</u>, as defined by

$$e^{o}_{ij} \equiv \frac{1}{E_R}\int_o^t E(t-\tau)\frac{\partial e_{ij}}{\partial \tau}\,d\tau \tag{4.20}$$

in which $E(t-\tau)$ is the linear viscoelastic relaxation modulus at time $t-\tau$, and the e_{ij} are the actual incremental strains, Eq. (4.2); the term E_R is an arbitrarily selected constant having the dimensions of modulus. The factor ψ reflects changes in the soil's fabric, and is a function of the <u>damage parameter</u> S_D,

$$S_D \equiv \int_o^t F_D(W)\,dt \tag{4.21}$$

where F_D is a function of the function $W = W(e^{o}_{ij})$ appearing in Eq. (4.17). This latter function is the strain energy density for the

special case of a linear or nonlinear elastic material ($E(t - \tau) \equiv E_R$) without damage ($\psi = 1$); in general, however, W is not strain energy, and therefore we shall call it psuedo strain energy.

Besides containing elastic behavior, linear and nonlinear viscous behavior is represented by Eq. (4.17) if we use the special case

$$E(t - \tau) = t_c E_R \delta(t - \tau) \tag{4.22}$$

where $\delta(t - \tau)$ is the Dirac delta function of the argument $t - \tau$ and t_c is a time constant. The pseudo strain becomes the strain rate times t_c,

$$e^o_{ij} = \frac{\partial e_{ij}}{\partial t} t_c \tag{4.23}$$

Guided by the theory in [11] and experimental studies of submarine sediment conducted at Texas A&M University over several years [e.g., 1-5], we shall propose certain special representations of W, E, ψ, and F_D, all in the form of power laws. It is currently believed they are good (tentative) representations of sub-bottom mud and are adequate for the purpose of the pipeline project. For the relaxation modulus we may use

$$E(t) = (t/t_c)^{-m} E_R \tag{4.24}$$

As before, t_c is a positive constant with the dimension of time. The exponent m is a positive dimensionless constant; for many viscoelastic materials, $0 < m < 1/2$.

The pseudo strains, Eq. (4.20), become

$$e^o_{ij} = t_c^m \int_o^t (t - \tau)^{-m} \frac{\partial e_{ij}}{\partial \tau} d\tau \tag{4.25}$$

The function F_D represents the driving force for defect growth, and is assumed to obey the power law,

$$F_D = (W/G_R)^k \tag{4.26}$$

where k is a positive, dimensionless constant; typically, for many materials, $k >> 1$ [11]. The quantity G_R is a constant with dimensions of modulus, and therefore F_D is dimensionless because W has these dimensions. The function $\psi = \psi(S_D)$ is also dimensionless, and a tentative form, which exhibits explicitly the time constant t_d, is

$$\psi = \frac{1}{[1 + (S_D/t_d)^r]^n} \tag{4.27}$$

where r and n are positive, dimensionless constants. For $r = 1$, ψ corresponds to a theoretical damage model [11, Eq. (137)].

The pseudo strain energy density is assumed to be a power law in the pseudo strains. For a function of several quantities (i.e. e^o_{ij}) this power law behavior is expressed by the mathematical statement that it is a "homogeneous function" of a given degree. We first introduce the dimensionless pseudo strain energy density,

$$W_R \equiv W/G_R \tag{4.28}$$

and then specify W_R to be homogeneous of degree $N + 1$,

$$W_R(\lambda e^o_{ij}) = |\lambda|^{1+N} W_R(e^o_{ij}) \tag{4.29}$$

where $|\ |$ denotes absolute value and λ is a scalar factor. Various types of predictions are made in [11] using the power law behavior expressed by Eq. (4.29).

For simple shear in terms of a shear strain e^o_{12}, Eq. (4.29)

predicts that $\partial W/\partial e^o_{12}$ is proportional to $|e^o_{12}|^N \text{sgn}(e^o_{12})$, where sgn is equal to (+1) or (-1), depending on the sign of its argument, e^o_{12}. Thus, apart from the factor ψ in Eq. (4.17), σ_{12} is proportional to $|e^o_{12}|^N \text{sgn}(e^o_{12})$. The exponent N is seen to provide a measure of nonlinear behavior for constant "damage", ψ = constant; the tangent modulus, $d\sigma_{12}/de^o_{12}$, decreases with increasing strain when $0 < N < 1$ and increases with strain when $N > 1$.

Equation (4.29) may be used for physically nonhomogeneous and anisotropic soils. As we shall presently demonstrate Eq. (4.17), together with Eqs. (4.28) and (4.29), contain the special case of a power law nonlinear, viscous, isotropic soil model used in Phase I [1, Eq. (3.1)]. Specifically, consider the power law,

$$W_R = W_R(e^o_{ij}) = \frac{1}{1+N}(e^o_e)^{1+N} \tag{4.30}$$

where e^o_e is an invariant which we shall call "pseudo effective shear strain", and is defined by the non-negative expression,

$$e^o_e \equiv (2e^o_{ij}e^o_{ij})^{1/2} \tag{4.31}$$

Observe that

$$(2\lambda e^o_{ij}\lambda e^o_{ij})^{1/2} = |\lambda|(2e^o_{ij}e^o_{ij})^{1/2} \tag{4.32}$$

and therefore Eq. (4.30) yields

$$W_R(\lambda e^o_{ij}) = \frac{1}{1+N}|\lambda|^{1+N}(e^o_e)^{1+N}$$

$$= |\lambda|^{1+N} W_R(e^o_{ij}) \tag{4.33}$$

which is in accordance with Eq. (4.29). Moreover,

$$\partial W_R/\partial e^o_{ij} = 2(e^o_e)^{N-1}e^o_{ij} \tag{4.34}$$

and thus

$$\sigma_{ij} = 2\psi G_R (e_e^o)^{N-1} e_{ij}^o \tag{4.35}$$

It should be noted that the differentiation indicated in Eqs. (4.17) and (4.34) has been made with all nine strains considered as independent variables; for example, e_{12}^o and e_{21}^o were treated as independent quantities. This rule stems from the virtual work principle used in deriving Eq. (4.17).

Let us now invert Eq. (4.35) so as to express strain in terms of stress. Multiply each side by itself for each i and j, sum over i and j, and then introduce the "effective shear stress", defined as

$$\tau_e \equiv (\tfrac{1}{2}\sigma_{ij}\sigma_{ij})^{1/2} \tag{4.36}$$

A simple power law relationship results,

$$\tau_e = \psi G_R (e_e^o)^N \tag{4.37}$$

or equivalently,

$$e_e^o = (\tau_e/\psi G_R)^{1/N} \tag{4.38}$$

Substituting Eq. (4.38) in (4.35) we find

$$e_{ij}^o = \frac{1}{2\tau_e}(\tau_e/\psi G_R)^{1/N}\sigma_{ij} \tag{4.39}$$

For the case of simple shearing, in which the only non-zero stress is σ_{12}, Eq. (4.36) yields $\tau_e = |\sigma_{12}|$, and from Eq. (4.39),

$$2e_{12}^o = |\sigma_{12}/\psi G_R|^{1/N} \mathrm{sgn}(\sigma_{12}) \tag{4.40}$$

which is the only non-zero strain.

The effective shear stress, Eq. (4.36), can be written in the form

$$\tau_e = [\tfrac{1}{6}(\sigma_{11} - \sigma_{22})^2 + \tfrac{1}{6}(\sigma_{22} - \sigma_{33})^2 + \tfrac{1}{6}(\sigma_{33} - \sigma_{11})^2 + \sigma_{12}^2 + \sigma_{13}^2 + \sigma_{23}^2]^{1/2} \tag{4.41}$$

after using the fact that σ_{ij} are deviatoric stresses, Eq. (4.18), and therefore $\sigma_{ii} = 0$. In [10, Eq. 3.3), this shear stress is written in terms of total stresses (denoted here by s_{ij}); but it is identical to Eq. (4.41) because τ_e depends on only the normal stress differences and shear stresses.

Use of Eq. (4.23) in (4.39) yields the constitutive equation for a power law viscous material with damage,

$$\partial e_{ij}/\partial t = \frac{1}{2\tau_e t_c}(\tau_e/\psi G_R)^{1/N}\sigma_{ij} \tag{4.42}$$

The constitutive relation in [1, Eq. 3.1] is recovered by using $\psi = 1$ and making the substitutions $G_R \to C$ and $N \to 1/q$.

Finally, we shall comment on certain generalizations in concluding this discussion of constitutive equations. First, observe that the initial stress, designated in Eq. (4.8) as -p, in principle may have an effect on all of the relationships and material parameters (e.g., N and t_c) discussed above. However, existing data on submarine sediment [e.g. 1-3] indicate a negligible pressure dependence on deformation response if the pressure is at least high enough to prevent the development and growth of cracks and other voids.

Constitutive equations similar to Eq. (4.17), but more general, are available. For example, one generalization is [11, Eq. 88],

$$\sigma_{ij} = \sum_{\alpha} \psi_\alpha \partial W_\alpha/\partial e_{ij}^{\circ} \tag{4.43}$$

where each ψ_α and W_α is a damage-dependent coefficient and energy density respectively, corresponding to different effects of changes in the soil's fabric. Residual stresses may be included through the use of a term in W_α which is linear in e_{ij}.

Development and verification of relatively general constitutive equations for soil is outside the scope of this project. Consequently, we shall base all of our detailed analysis of soil-pipe interactions on Eq. (4.35), using a constant damage factor ψ which is absorbed into G_R.

4.2 Surface and Interface Equations for the Soil and Water

The boundary conditions needed to solve the problems in Section 4.4 are given here.

Figure 4.1 depicts a general initial state, in which the mud is subjected to the weight of the water and to an externally applied pressure P_o. On the water surface the incremental water pressure p_w vanishes. Therefore, from Eq. (4.16),

$$p_w^* = -\gamma_w u_2 \quad \text{at} \quad x_2 = -h_w \tag{4.44}$$

At the mud-water interface, the normal displacements for the soil and water are equal,

$$(u_2)_{soil} = (u_2)_{water} \quad \text{at} \quad x_2 = 0 \tag{4.45}$$

Also, the negative of the water pressure p_w is equal to the soil normal stress s_{22},

$$s_{22} = -p_w = -(p_w^* + \gamma_w u_2) \quad \text{at} \quad x_2 = 0 \tag{4.46}$$

where Eq. (4.16) has been used; the negative sign arises because the convention for stresses in solids is followed here, in which normal

stresses are negative when compressive and positive when tensile. The soil shear stress is zero at the interface because the water is inviscid,

$$s_{12} = 0 \quad \text{at} \quad x_2 = 0 \tag{4.47}$$

We shall assume the soil is deep enough to model it as being infinitely deep. Thus, all incremental soil displacements and stresses vanish as $x_2 \to \infty$. In the absence of water, Eq. (4.46) reduces to $s_{22} = 0$.

It is to be noted that by using incremental stresses, s_{ij}, which are referred to current areas and to coordinate axes which translate and rotate with each material element, the boundary and interface conditions are especially simple [cf. 10, p. 226]. This selection also aids the writing of the constitutive equations as the effect of rigid body rotations is automatically excluded. The specific conditions which pertain to the interface for the pipe and soil and the pipe and water will be treated in Section 4.3.

Before turning to an explicit prediction of pipe-soil interactions, observe Eqs. (4.10)-(4.12) without dilatation ($e = 0$) become identical to those for soil without initial stress when expressed in terms of the stresses s^*_{ij},

$$s^*_{ij} \equiv s_{ij} + \gamma_s u_2 \quad \text{for} \quad i = j \tag{4.48a}$$

and

$$s^*_{ij} = s_{ij} \quad \text{for } i \neq j \tag{4.48b}$$

where γ_s is the unit weight of the soil. The starred stresses act at a given depth x_2, rather than on a given material element. In view of interface Eq. (4.46), we obtain

$$s^*_{22} = -p^*_w + \Delta\gamma u_2 \quad \text{at} \quad x_2 = 0 \tag{4.49}$$

where $\Delta\gamma$ is the submerged unit weight of the soil at the mudline,

$$\Delta\gamma \equiv \gamma_s - \gamma_w \tag{4.50}$$

Without water, $s_{22} = 0$ at $x_2 = 0$; therefore

$$s^*_{22} = \gamma_s u_2 \quad \text{at} \quad x_2 = 0 \tag{4.51}$$

4.3 Variational Principle for Prediction of Reactions

4.3.1 Development of the Variational Principle: In this section we develop the variational principle that is used in Section 4.4 to predict the pipe forces and moment by an approximate method of analysis. Effects of inertia and dilatation are neglected; i.e. all of the terms on the right-hand side of Eqs. (4.10)-(4.12) are dropped. First write the equations of equilibrium for the soil in compact form,

$$\partial s^*_{ij}/\partial x_j = 0 \tag{4.52}$$

where, by definition,

$$s^*_{ij} \equiv s_{ij} + \gamma_s u_2 \delta_{ij} \tag{4.53}$$

which conforms to Eq. (4.48), but the Kronecker delta, Eq. (4.14), is now used.

The variational principle will be expressed using pseudo displacements, u^o_i,

$$u^o_i \equiv \frac{1}{E_R}\int_o^t E(t-\tau)\frac{\partial u_i}{\partial \tau}\, d\tau \tag{4.54}$$

From Eqs. (4.2) and (4.54),

$$\frac{1}{2}(\partial u_i^o/\partial x_j + \partial u_j^o/\partial x_i) = \frac{1}{E_R}\int_o^t E(t-\tau)\frac{\partial e_{ij}}{\partial \tau}\,d\tau \qquad (4.55)$$

The right-hand side is identical to that in Eq. (4.20), and thus

$$e_{ij}^o = \frac{1}{2}(\partial u_i^o/\partial x_j + \partial u_j^o/\partial x_i) \qquad (4.56)$$

which shows that the pseudo strain-displacement relations are identical in form to those for the physical quantities, Eq. (4.2). If we use a constant modulus E_R for $E(t-\tau)$, Eq. (4.56) reduces to Eq. (4.2). If, as another special case, we use Eq. (4.22) for $E(t-\tau)$ and $t_c = 1$, the pseudo strains become strain rates and the pseudo displacements become velocities. Hence, Eq. (4.56) is simply an equation for the physical strain rates,

$$\dot{e}_{ij} = \frac{1}{2}(\partial \dot{u}_i/\partial x_j + \partial \dot{u}_j/\partial x_i) \qquad (4.57)$$

where ($\dot{}$) denotes differentiation with respect to time. As mentioned earlier, all of the theoretical development and approximate analyses will be done using these pseudo quantities. This type of formulation is useful for our studies of mud because its behavior ranges from nearly elastic to viscous as the amount of deformation increases.

Next, multiply Eq. (4.52) by small virtual (or real) changes in pseudo displacements, δu_i^o, and integrate over the entire volume of soil, V_s,

$$\int_{V_s}(\partial s_{ij}^*/\partial x_j)\,\delta u_i^o\,dV = 0 \qquad (4.58)$$

According to the divergence theorem [9],

$$\int_{V_s} \partial(s^*_{ij}\delta u^o_i)/\partial x_j \, dV = \int_{S_s} s^*_{ij} n_j \delta u^o_i \, dS \tag{4.59}$$

where S_s is the bounding surface of the soil. The quantity n_j represents the vector components of the outward-pointing unit normal to this surface. Carrying out the differentiation shown in Eq. (4.59) and then using Eqs. (4.56) and (4.58) and the fact that $s^*_{ij} = s^*_{ji}$ (which follows directly from Eq. (4.53) and symmetry of the incremental stresses, $s_{ij} = s_{ji}$ [10]), we obtain,

$$\int_{S_s} T^*_i \delta u^o_i \, dS = \int_{V_s} s^*_{ij} \delta e^o_{ij} \, dV \tag{4.60}$$

where, by definition,

$$T^*_i \equiv s^*_{ij} n_j \tag{4.61}$$

(Equation (4.60) can be reduced to the familiar principle of virtual work by setting $E(t - \tau) = E_R$ and neglecting $\gamma_s u_2$; if $\gamma_s u_2 = 0$, then $s^*_{ij} = s_{ij}$ and T^*_i become the components of force per unit area acting along S_s.) It is helpful to express Eq. (4.60) in terms of the deviatoric stresses σ_{ij}, as defined in Eq. (4.18). From the latter relation and Eq. (4.53),

$$s^*_{ij} = \sigma_{ij} + \frac{1}{3} s^* \delta_{ij} \tag{4.62}$$

where

$$s^* \equiv s + 3\gamma_s u_2 \tag{4.63}$$

Substitute Eq. (4.62) into (4.60) and use the incompressibility condition, $e^o_{ii} = 0$, to obtain

$$\int_{S_s} T^*_i \delta u^o_i \, dS = \int_{V_s} \sigma_{ij} \delta e^o_{ij} \, dV \tag{4.64}$$

If the deviatoric stresses σ_{ij} can be derived from a potential $W_p = W_p(e^o_{ij})$ (e.g., strain-energy density in the case of elastic media),

$$\sigma_{ij} = \partial W_p / \partial e^o_{ij} \tag{4.65}$$

then Eq. (4.64) may be written as

$$\int_{S_s} T^*_i \delta u^o_i \, dS = \delta \int_{V_s} W_p \, dV \tag{4.66}$$

For constant damage, ψ, Eq. (4.17) yields $W_p = \psi W$. Depending on the material's behavior, it may be possible to construct a potential W_p even with changing damage [12] but we will not consider this generalization here. (It should also be added that in placing δ outside of the integral, we have, in effect, assumed V_s does not vary with δu^o_i; e.g. internal mud cracks and geometry of any soil-pipe separation surfaces are fixed when calculating the changes due to δu^o_i.) It will be helpful to divide S_s into three parts: (i) the soil-pipe interface, S_{sp}; (ii) the initially horizontal mudline S_{sm} (which may or may not be subjected to gas or water pressure); and (iii) remaining surface, S_{ss}, such as a non-horizontal surface of separation between the pipe and soil, if any. The surface integrals corresponding to S_{sp} and S_{sm} will be evaluated next. The remaining surface integral depends on the geometry of S_{ss} for each specific problem; but this integral is believed to be relatively small compared to the integral over S_{sm} and it will be omitted in the subsequent analyses.

The virtual displacements along the soil-pipe interface are assumed to be those for rigid-body virtual motion of the pipe itself. Referring to Figure 4.4, a material point at the initial location (a,θ), where a is the pipe radius, undergoes virtual displacements

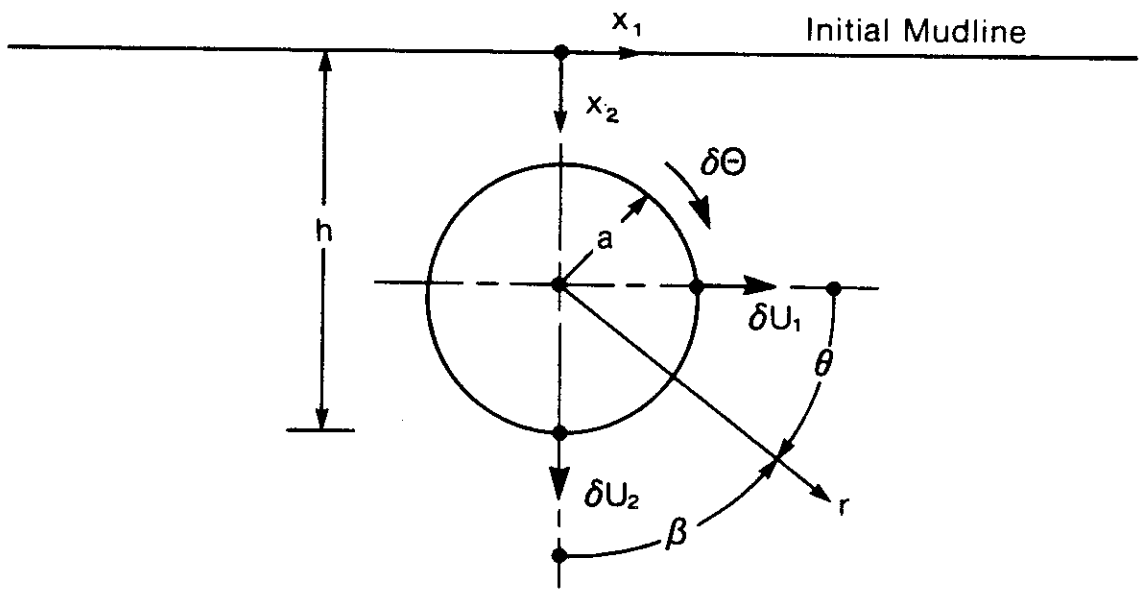

Figure 4.4 Polar Coordinate System and Virtual Displacement Notation

$$\delta u_1 = \delta U_1 - a \sin \theta \, \delta\theta \tag{4.67a}$$

$$\delta u_2 = \delta U_2 + a \cos \theta \, \delta\theta \tag{4.67b}$$

$$\delta u_3 = \delta U_3 \tag{4.67c}$$

when the pipe is subjected to virtual translations δU_i (i = 1,2,3) and rotation $\delta\theta$. Inasmuch as θ refers to the initial orientation, it is independent of time. Thus, when we operate on Eq. (4.67) with the convolution integral, the virtual pseudo displacements are easily found to be

$$\delta u_1^o = \delta U_1^o - a \sin \theta \, \delta\theta^o \tag{4.68a}$$

$$\delta u_2^o = \delta U_2^o + a \cos \theta \, \delta\theta^o \tag{4.68b}$$

$$\delta u_3^o = \delta U_3^o \tag{4.68c}$$

The surface integral over S_{sp} becomes

$$\int_{S_{sp}} T_i^* \delta u_i^o dS = F_i^* \delta U_i^o + M^* \delta\theta^o \tag{4.69}$$

where

$$F_i^* \equiv \int_{S_{sp}} T_i^* dS \tag{4.70}$$

$$M^* \equiv a \int_{S_{sp}} (T_2^* \cos \theta - T_1^* \sin \theta) dS \tag{4.71}$$

If the effect of gravity on the soil is neglected, i.e. if $\gamma_s u_2$ in Eq. (4.53) is neglected, then from Eq. (4.61),

$$T_i^* = s_{ij} n_j \ , \tag{4.72}$$

which are the components of force per unit area acting along the pipe (due to changes from the initial state). In this case, F_i^* and M^* are the resultant forces and moment, respectively, acting between the pipe and soil. The relationship of total forces F_i and moment M due to both water and soil to the quantities in Eqs. (4.70) and (4.71) will be developed following the derivation of an explicit formula for the integral along the initially horizontal mudline surface S_{sm}.

For the mudline, $n_1 = n_3 = 0$ and $n_2 = -1$, and the shearing stresses s_{12} and s_{32} are negligible. Thus, using Eqs. (4.49), (4.53) and (4.61),

$$T_1^* = s_{12}^* n_2 = -s_{12} = 0 \tag{4.73a}$$

$$T_2^* = s_{22}^* n_2 = -\Delta\gamma u_2 \tag{4.73b}$$

$$T_3^* = s_{32}^* n_2 = -s_{32} = 0 \tag{4.73c}$$

The pressure due to water inertia, p_w^*, has been neglected in Eq. (4.73b) on the basis of the analysis in Appendix 2. Consequently,

$$\int_{S_{sm}} T_i^* \delta u_i^o \, dS = -\Delta\gamma \int_{S_{sm}} u_2 \delta u_2^o \, dS \tag{4.74}$$

For an elastic soil, $u_2^o = u_2$. For viscous soil, $u_2^o = t_c \dot{u}_2$, and if the velocity $\dot{u}_2$ is constant in time, $u_2 = (t/t_c)u_2^o$. For the case in which the soil is viscoelastic and both E(t) and u_2 obey power laws in time with constant exponents, we find from Eq. (4.54) that $u_2 = fu_2^o$, where $f = f(t/t_c)$ is a dimensionless power law. In all of these special cases, the surface integral, Eq. (4.74) may be written in the form,

$$\int_{S_{sm}} T_i^* \delta u_i^o \, dS = -\frac{1}{2}\Delta\gamma f \, \delta \int_{S_{sm}} (u_2^o)^2 \, dS \tag{4.75}$$

The left-hand side of Eq. (4.66) consists of the sum of Eqs. (4.69) and (4.75) (or, if desired, the more general version, Eq. (4.74)). Hence, Eq. (4.66) becomes

$$F_i^* \delta U_i^o + M^* \delta \theta^o = \delta W_T \tag{4.76}$$

where

$$W_T \equiv \int_{V_s} W_p dV + \frac{1}{2} \Delta\gamma f \int_{S_{sm}} (u_2^o)^2 dS \tag{4.77}$$

If the soil were elastic, the first integral would be the strain energy of the soil and the second integral the strain energy of linear elastic springs (f=1, "spring" constant=$\Delta\gamma$) distributed along the mudline. For viscous and viscoelastic soil, these integrals are not strain energy, but they are analogous to strain energy. We shall use the term "pseudo strain energy" in referring to them, and W_T will be called "total psuedo strain energy" or, more briefly, "total energy".

4.3.2 Resultant Force and Moment Equations: The total energy W_T is a function of pipe movement, U_i^o and θ^o. Thus,

$$\delta W_T = \frac{\partial W_T}{\partial U_i^o} \delta U_i^o + \frac{\partial W_T}{\partial \theta^o} \delta \theta^o \tag{4.78}$$

Inasmuch as the virtual changes are independent of one another, each coefficient in Eq. (4.78) must equal the respective coefficient in Eq. (4.76); i.e.

$$F_i^* = \partial W_T / \partial U_i^o \ , \qquad M^* = \partial W_T / \partial \theta^o \tag{4.79}$$

The physical resultants, F_i and M, may be found from these expressions

and the boundary traction equations developed by Biot [10, Eq. 7.54 p. 53]

$$f_i = (S_{ij} + s_{ij} + S_{kj}\omega_{ik} + S_{ij}e - S_{ik}e_{jk})n_j \tag{4.80}$$

where the notation corresponds to that used previously in Eq. (4.1). These tractions, which are forces per unit initial area, reduce considerably after taking into account the special initial stress state, Eq. (4.8), and the incompressibility condition $e = 0$; one finds

$$f_i = (-p\delta_{ij} + p\frac{\partial u_j}{\partial x_i} + s_{ij})n_j \tag{4.81}$$

This expression applies to the soil-pipe, water-pipe, and air-pipe interfaces. It is also applicable to the water-soil interface.

Let us now write Eq. (4.81) in terms of expressions for s_{ij}. For the water, Eqs. (4.13) and (4.16) may be used (in which we neglect the pressure p_w^* due to inertia of the water) to find

$$s_{ij} = -\delta_{ij}\gamma_w u_2 \tag{4.82}$$

Thus, for the water-pipe interface,

$$f_i = [-\delta_{ij}(p+\gamma_w u_2) + p\frac{\partial u_j}{\partial x_i}]n_j \tag{4.83}$$

For the soil-pipe interface we replace s_{ij} in Eq. (4.81) in favor of s_{ij}^*, Eq. (4.53), and also use Eq. (4.61); thus,

$$f_i = T_i^* + [-\delta_{ij}(p+\gamma_s u_2) + p\frac{\partial u_j}{\partial x_i}]n_j \tag{4.84}$$

Observe that Eq. (4.83) is the same as Eq. (4.84) except $T_i^* = 0$ and γ_w appears in place of γ_s. We shall use this similarity together with the fact that $n_3 = 0$ (because the pipe axis is parallel to x_3) and write the tractions in explicit form,

$$f_1 = T_1^* + [-(p+\gamma u_2) + p\frac{\partial u_1}{\partial x_1}]n_1 + p\frac{\partial u_2}{\partial x_1}n_2 \tag{4.85a}$$

$$f_2 = T_2^* + p\frac{\partial u_1}{\partial x_2}n_1 + [-(p+\gamma u_2) + p\frac{\partial u_2}{\partial x_2}]n_2 \tag{4.85b}$$

$$f_3 = T_3^* \tag{4.85c}$$

It should be noted that the terms $\partial u_1/\partial x_3$ and $\partial u_2/\partial x_3$ may be in Eq. (4.84) for f_3; however, these terms vanish as we assume all displacements are independent of x_3. Additionally, the unit weight is shown without a subscript since Eq. (4.85) will be used for both water-pipe and soil-pipe interfaces. In general, $\gamma = \gamma(x_2)$, where the initial pressure gradient is given by Eq. (4.9). Also, recall that $T_i^* = 0$ along the water-pipe interface.

Pipe force and moment resultants are

$$F_i = \int_{S_p} f_i dS, \quad M = a\int_{S_p} (f_2 \cos\theta - f_1 \sin\theta)dS \tag{4.86}$$

where integration is extended over the entire pipe surface r = a. The coordinate system in Figure 4.4 is used. For a pipe of length L,

$$n_1 dS = -Ldx_2, \quad n_2 dS = Ldx_1 \tag{4.87}$$

Clockwise integration around the pipe will be used in subsequent work,

corresponding to positive θ in Figure 4.4; for this direction Eq. (4.87) provides the correct signs for the components of the unit normal n_i (which points outward from the soil).

The elemental forces $f_i dS$ needed in Eq. (4.86) may be found from Eqs. (4.85) and (4.87) and then reduced to the simple expressions

$$f_1 dS = T_1^* dS + Lp(y_2)dy_2 \tag{4.88a}$$

$$f_2 dS = T_2^* dS - Lp(y_2)dy_1 \tag{4.88b}$$

$$f_3 dS = T_3^* dS \tag{4.88c}$$

The quantities y_1 and y_2 define the <u>current</u> Cartesian coordinates of a material point which was initially at x_1, x_2; namely,

$$y_1 = x_1 + u_1(x_1, x_2), \quad y_2 = x_2 + u_2(x_1, x_2) \tag{4.89}$$

The pressure $p = p(y_2)$ is the pressure in the soil or water at the current material location of a boundary point, y_2, due <u>only</u> to gravity; viz.,

$$dp(y_2)/dy_2 = \gamma(y_2) \tag{4.90}$$

or, equivalently,

$$p(y_2) = \int \gamma(y_2)dy_2 + \text{constant} \tag{4.91}$$

That Eq. (4.88) is equivalent to Eq. (4.85) (after multiplying the latter by dS) can be shown through using Eq. (4.89) to compute dy_1 and dy_2 and then drawing upon Eq. (4.87) and the condition of incompressibility,

$$e = \partial u_1/\partial x_1 + \partial u_2/\partial x_2 = 0 \tag{4.92}$$

We have set $\partial u_3/\partial x_3 = 0$ in the expression for e since all displacements are independent of x_3. Besides these considerations in establishing equivalence, one has to neglect the second order terms $u_2 \partial u_i/\partial x_j$ and recognize that

$$p(y_2) = p(x_2) + \gamma u_2 \tag{4.93}$$

where $p(x_2)$ is the pressure appearing in Eq. (4.85). Biot's incremental deformation theory is valid up to only first order terms in displacement, and therefore the second order terms should be dropped for consistency. If the unit weights of the soil and water are constant, Eq. (4.93) is exact; in the context of a first order theory, it is valid for unit weights which vary continuously with depth.

Although we are not considering the soil-water interface in the present discussion, it is of interest to note that Eq. (4.88) does apply to the mudline. Indeed by equating $f_2 dS$ in Eq. (4.88b) for the soil to the negative of $f_2 dS$ for the water, Eq. (4.49) (with $p_w^* = 0$) is recovered.

Let us now substitute Eq. (4.88) into Eq. (4.86), and then use Eqs. (4.70), (4.71), and (4.79). There results, finally,

$$F_1 = \partial W_T/\partial U_1^o \ , \quad F_2 = \partial W_T/\partial U_2^o + F_B$$

$$F_3 = \partial W_T/\partial U_3^o \ , \quad M = \partial W_T/\partial \theta^o \tag{4.94}$$

where

$$F_B \equiv L \int_{A_p} \gamma(y_2) dA \tag{4.95}$$

and A_p is the pipe's cross-sectional area. The quantity F_B is the familiar buoyant force of Archimedes' principle, which acts upward on a

body in a liquid; here, it is equal to the weight of soil and water displaced by the pipe at its current location. Thus, the direct effect of the unit weight is the same as for a liquid. However, it should be recalled that there is an indirect effect as well since W_T depends on unit weight, Eq. (4.77). There is no contribution to the moment M from the pressure terms in Eq. (4.88) as they combine to produce a resultant force which is perpendicular to the pipe surface. These results do not account for variation of the geostatic pressure p in the horizontal direction, and therefore the effect of this pressure is not fully accounted for when the soil separates from the pipe. On page xviii an approximate method is used with separation, and this analysis leads to a direct effect of unit weight on horizontal force.

The right-hand side of the relations in Eq. (4.94) represents the resistance of the soil-water system to pipe translation and rotation. The left-hand side consists of the "externally applied" forces and moment. For an actual pipeline, these latter quantities are the pipe weight (as part of F_2) and the net shearing and torsional reactions between the pipe of differential length dL and sections of the pipeline on either side of this short segment. In the laboratory tests, the pipe has a finite length L, and the loading consists of its weight and the forces and torque applied through an external mechanism.

The foregoing development considers water to be above the soil. In the laboratory tests water was not used, although in many tests the air above the soil was pressurized. The theory for the soil-water system is equally valid for a soil-air system if we use $\gamma_w \simeq 0$, where γ_w is now the unit weight of air. Confining air pressure may influence the amount of cracking in the soil and soil-pipe separation. However, since the soil is assumed to be incompressible, the air pressure can have no

effect on the pipe forces and moment for a given state of cracking and separation if the same pressure acts on all surfaces (including crack faces).

4.4 Prediction of Pipe Loading

4.4.1 Dimensionless Form of the Reaction Equations: A general dimensional analysis was given in Section 2, and several generic dimensionless ratios were defined. Here, we shall introduce dimensionless ratios using parameters relevent to the particular theory and results covered in Section 4.3 for the geometry in Figure 4.4. Reaction Eqs. (4.94) will then be written employing dimensionless variables.

Using $(\hat{})$ to denote dimensionless variables, the forces and the moment (or torque) are,

$$\hat{F}_i \equiv F_i/(LDG_R) \ , \quad \hat{F}_B \equiv F_B/(LDG_R) \ , \quad \hat{M} \equiv M/(LD^2G_R) \tag{4.96}$$

Recall that G_R is a constant, with dimensions of modulus, which was introduced in Section 3.1. Local and pipe pseudo displacements and the gravity parameter (cf. Eq. (4.77)) are, respectively,

$$\hat{u}_i^o \equiv u_i^o/D \ , \quad \hat{U}_i^o \equiv U_i^o/D \ , \quad \hat{\gamma} \equiv \Delta\gamma fD/G_R \tag{4.97}$$

The total pseudo strain energy W_T, Eq. (4.77), will be written in terms of the polar and rectangular Cartesion coordinate systems in Figure 4.4. In developing detailed formulas for the prediction of W_T, it is helpful to use coordinates which are nondimensionlized with respect to pipe radius, a, instead of diameter,

$$\hat{x} \equiv x_i/a \ , \quad \hat{r} \equiv r/a \tag{4.98}$$

so that the pipe surface is defined by $\hat{r} = 1$. Also let

$$\hat{W}_T \equiv W_T/(La^2G_R) \ , \qquad \hat{W}_p \equiv W_p/(La^2G_R) \tag{4.99}$$

Using these dimensionless variables, the reactions, Eqs. (4.94), become

$$\hat{F}_1 = \frac{1}{4}\partial\hat{W}_T/\partial\hat{U}_1^o \ , \qquad \hat{F}_2 = \frac{1}{4}\partial\hat{W}_T/\partial\hat{U}_2^o + \hat{F}_B$$

$$\hat{F}_3 = \frac{1}{4}\partial\hat{W}_T/\partial\hat{U}_3^o \ , \qquad \hat{M} = \frac{1}{4}\partial\hat{W}_T/\partial\,\Theta^o \tag{4.100}$$

where the factor of 1/4 arises from the use of radius a in Eq. (4.98) and diameter D in Eq. (4.96).

4.4.2 Total Energy Representation Including Effects of Separation: The primary quantity needed to predict pipe loading is the total energy $\hat{W}_T$. Here we shall express this quantity in a more explicit form than in Eq. (4.77) using dimensionless variables and realistic cases of separation of mud from the pipe. Figure 4.5 illustrates the various cases which are studied later in detail. No separation is denoted by Sep = 0, which may exist with sufficiently high air or water pressure; the mud flows around the pipe and fills in any gap that would tend to form. The case Sep = 1 approximates the situation observed in the laboratory, except for deeply buried pipes, after a large amount of horizontal movement normal to the pipe axis, x_3; a horizontal shelf behind and close to the bottom of the pipe forms even under the highest air pressures (30 psig) studied experimentally. When downward vertical motion of the pipe is imposed in the laboratory tests, and the bottom of the pipe is initially at or close to the mudline, vertical walls form above the pipe, as shown for Sep = 2; as the pipe continues downward the walls slowly move inward, filling the cavity, and finally resulting in the same force as predicted for Sep = 0. The case Sep = 3 appears to

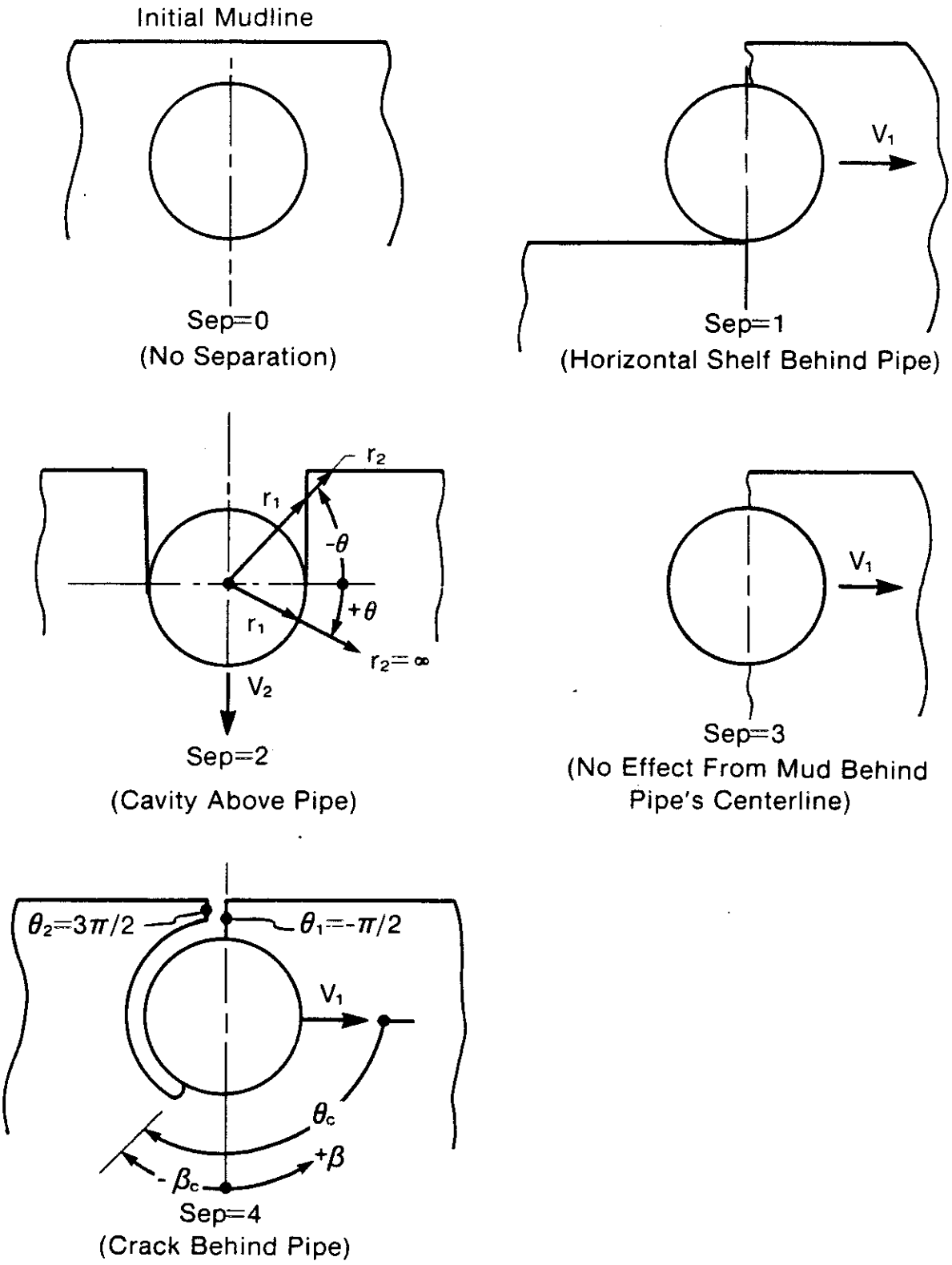

Figure 4.5 Idealized Types of Separation of Mud from the Pipe

approximate behavior in a few test cases involving horizontal movement; separation behind the pipe develops, and the crack associated with this separation continues on downward through the mud under the pipe. The theory for Sep = 3 is an idealization of this situation, in which all of the mud behind the vertical plane passing through the pipe's centerline is excluded in the calculation of $\hat{W}_T$. Finally, Sep = 4 represents the initial stage of the development of Sep = 1. The separation exists in the form of a crack which extends along the back surface of the pipe to a depth defined by the angle β_c; fracture mechanics theory is used to predict β_c. When $h/D > 1$, the crack extends from the mudline down to the pipe, directly over the center of the pipe. Other cases of separation may exist, depending on the relative movement between pipe and soil; but calculations are made for only those depicted in Figure 4.5.

The dimensionless total energy is obtained by rewriting Eq. (4.77) in terms of the coordinates in Figure 4.4, for which

$$dV = Lrdrd\theta \ , \qquad dS = Ldx_1 \tag{4.101}$$

and then introducing the dimensionless variables in Eqs. (4.96)-(4.99). We find

$$\hat{W}_T = \hat{W}_v + \hat{W}_s \tag{4.102}$$

where, by definition,

$$\hat{W}_v \equiv \int_{\theta_1}^{\theta_2}\int_{\hat{r}_1}^{\hat{r}_2} \hat{W}_p \hat{r} d\hat{r} d\theta \ , \quad \hat{W}_s \equiv \hat{\gamma}\left[\int_{-\infty}^{\hat{x}_a} (\hat{u}_2^o)^2 d\hat{x}_1 + \int_{\hat{x}_b}^{\infty} (\hat{u}_2^o)^2 d\hat{x}_1\right] \tag{4.103}$$

The integration with respect to $\hat{r}$ extends from $\hat{r}_1$ to $\hat{r}_2$; these radii may vary with θ, as illustrated in Figure 4.5. For the particular displacement representations $\hat{u}_i = \hat{u}_i(\hat{r},\theta)$ that are used, it is best to perform the integration with respect to $\hat{r}$ before θ. The angles θ_1 and

θ_2 define the total range of integration over θ, although the complexity of the geometry is such that subdivisions are needed in the actual calculation of the energy.

We shall specialize $\hat{W}_T$ even further by using the power law form of pseudo strain energy density, Eq. (4.30). Equation (4.103) for $\hat{W}_v$ becomes

$$\hat{W}_v = \int_{\theta_1}^{\theta_2} \int_{\hat{r}_1}^{\hat{r}_2} \frac{F}{1+N} (e_e^o)^{1+N} \hat{r} d\hat{r} d\theta \tag{4.104}$$

Variation of the soil properties with location is characterized by the dependence of F and N on the coordinates (r,θ). For homogeneous soil, N is constant and F = 1.

4.4.3 Representation of Movement Between Pipe and Soil: As stated previously, for purposes of analysis we suppose the soil is motionless at points far away from the pipe. The instantaneous components of the pipe displacements (referred to the pipe centerline) are shown in Fig. 4.6a. The resultant displacement is U_R, and the components U_i are related to U_R through the (time-dependent) displacement angle α_d and penetration angle λ_d,

$$\begin{aligned} U_1 &= \sin \alpha_d \cos \lambda_d U_R \\ U_2 &= \sin \lambda_d U_R \\ U_3 &= \cos \alpha_d \cos \lambda_d U_R \end{aligned} \tag{4.105}$$

Operating on these displacements and pipe rotation θ with the convolution integral in Eq. (4.54), and dividing displacements by diameter D, yields

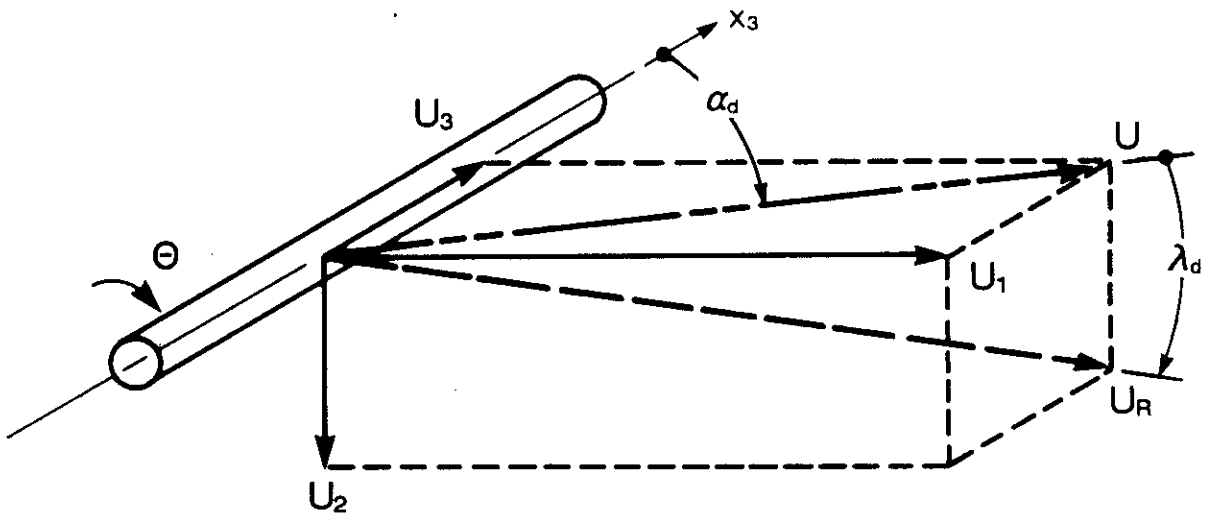

(a) Displacements

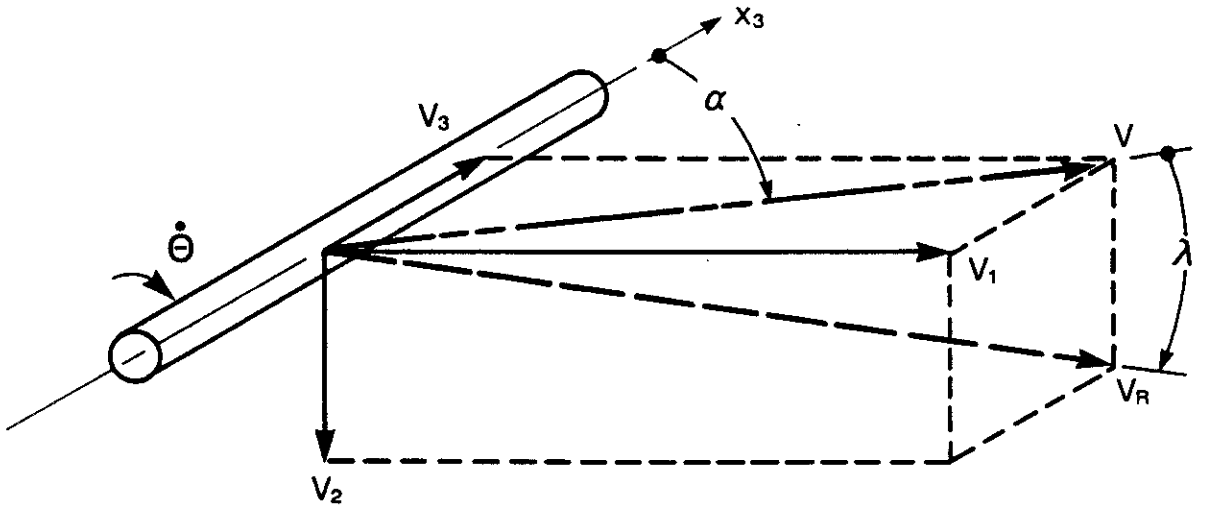

(b) Velocities

Figure 4.6 Notation Used for Three Dimensional Movement of the Pipe Relative to the Free-Field Mud

$$\hat{U}_i^o = \frac{1}{E_R}\int_o^t E(t-\tau)\frac{d\hat{U}_i}{d\tau}d\tau \ , \qquad \theta^o = \frac{1}{E_R}\int_o^t E(t-\tau)\frac{d\theta}{d\tau}d\tau \tag{4.106}$$

where $\hat{U}_i \equiv U_i/D$ are dimensionless displacements. The dimensionless pseudo variables $\hat{U}_i^o$ and θ^o are the particular kinematic quantities needed to predict the pipe reactions, Eq. (4.100).

For a viscoelastic soil it is necessary to consider the entire displacement history to evaluate the convolution integrals. In all subsequent discussions we shall consider only the special cases of elastic behavior and viscous behavior. For an elastic soil,

$$\hat{U}_i^o = \hat{U}_i \ , \qquad \theta^o = \theta \tag{4.107}$$

and from Eq. (4.105),

$$\begin{aligned} \hat{U}_1^o &= \sin\alpha_d \ \cos\lambda_d \hat{U}_R \\ \hat{U}_2^o &= \sin\lambda_d \hat{U}_R \\ \hat{U}_3^o &= \cos\alpha_d \ \cos\lambda_d \hat{U}_R \end{aligned} \tag{4.108}$$

where $\hat{U}_R \equiv U_R/D$.

For a viscous soil,

$$\hat{U}_i^o = t_c d\hat{U}_i/dt, \qquad \theta^o = t_c d\theta/dt \tag{4.109}$$

where t_c is a previously introduced constant with dimensions of time. In this case, the pseudo displacements are proportional to the instantaneous velocity components, and therefore the dimensionless variables may be written in the form

$$\begin{aligned} \hat{U}_1^o &= \sin\alpha \cos\lambda \hat{V}_R \\ \hat{U}_2^o &= \sin\lambda \hat{V}_R \end{aligned} \tag{4.110}$$

$$\hat{U}_3^o = \cos\alpha \cos\lambda \hat{V}_R \qquad (4.110)\ (\text{cont.})$$

where

$$\hat{V}_R = t_c V_R / D \qquad (4.111)$$

and V_R is the resultant velocity (cf. Fig. 4.6b). In Eq. (4.110) we are using α and λ to define the orientation of the instantaneous resultant velocity vector relative to the x_i coordinates. Of course, if the orientation is constant in time, $\alpha = \alpha_d$ and $\lambda = \lambda_d$. For a viscous body, the pseudo rotation is proportional to the rotation rate

$$\theta^o = t_c \dot{\theta} \qquad (4.112)$$

4.4.4 Generalized Force Coefficients for Viscous Soil Model: In the post-failed state, the soil behaves approximately as a viscous body. In this report comparisons between theoretical and experimental values of force will use the viscous theory. In order to make these comparisons conveniently and to present theoretical predictions in a form that is useful for pipeline design analysis it is helpful to introduce and use so-called "generalized force coefficients". These coefficients will be defined in a manner which makes them independent of the soil strength and the amplitude of the resultant velocity vector for power-law nonlinear soils.

As the first step in developing the force coefficients it is necessary to define soil strength, which we do here in terms of a standard rotating vane test. From Appendix 3, the shear stress at the surface of a circular vane is (cf. Eq. (A.27))

$$\tau_V = G_R(\gamma_V^o) N \qquad (4.113)$$

where

$$\gamma_v^o = |2\theta_v^o/N| \tag{4.114}$$

is the corresponding pseudo shear strain and θ_v^o is the vane pseudo rotation. For a viscous soil $\theta_v^o = t_c \dot{\theta}_v$, where $\dot{\theta}_v$ is the vane rotation rate. The "strength" is customarily denoted by C, with or without a subscript, and taken as the shear stress τ_v for a standard vane rotation rate $\dot{\theta}_{vo}$. Let C_o denote this strength, and therefore

$$C_o = G_R|2t_c \dot{\theta}_{vo}/N|^N \tag{4.115}$$

Generalized force coefficients g_i corresponding to the four reactions in Eq. (4.94), less the buoyancy force F_B, are now defined,

$$g_1 \equiv F_1/k \ , \quad g_2 \equiv (F_2 - F_B)/k$$

$$g_3 \equiv F_3/k \ , \quad g_4 \equiv M/(kD) \tag{4.116}$$

where

$$k \equiv LDC_o(V_R/D)^N \tag{4.117}$$

These coefficients may be expressed in terms of the dimensionless derivatives in Eq. (4.100) by using Eq. (4.115) and the definitions in Eq. (4.96); there results,

$$g_i = f_g^{-1} \hat{V}_R^{-N} \partial \hat{W}_T/\partial \hat{U}_i^o \ , \quad (i=1,2,3)$$

$$g_4 = f_g^{-1} \hat{V}_R^{-N} \partial \hat{W}_T/\partial \Theta^o \tag{4.118}$$

where

$$f_g \equiv 4|2\dot{\theta}_{vo}/N|^N \tag{4.119}$$

and $\hat{V}_R$ is defined in Eq. (4.111).

It is important to observe that Eq. (4.116) may be used to obtain g_i from experimental data on forces and moment. The factor k can be calculated from a soil strength measurement along with other test-related information. The intrinsic material constants t_c and G_R do not appear explicitly in these formulas or in those used to predict g_i from theory, Eq. (4.118). Moreover, as work in Section 4.5 shows, a numerical value for t_c is not needed even though t_c appears in the relation between $\hat{V}_R$ and pipe speed V_R, Eq. (4.111).

Equation (4.118) may be simplified by absorbing the factor $\hat{V}_R^N$ into the energy derivatives. When the gravity-related factor $\hat{\gamma}$, Eq. (4.97), can be neglected and $\theta^o/\hat{V}_R$ is constant, all g_i are independent of $\hat{V}_R$. This behavior may be proved for the exact solution to the pipe-soil boundary value problem. It also holds true for all approximate solutions g_i derived in this report. Proof of this latter case is given in Section 4.4.6 as part of the development of the approximate solutions. The effect of $\hat{V}_R$ on g_i when $\hat{\gamma}$ is not neglected is also discussed.

4.4.5 Derivation of Approximate Solutions: Prediction of pipe reactions due to the soil loading, Eq. (4.100), and the associated generalized force coefficients, Eq. (4.118), requires the determination of total energy $\hat{W}_T$. Approximate formulas for this energy are developed here by using the Ritz method of approximate analysis [9]. In the context of the present formulation this method consists of first selecting a set of continuous pseudo displacement functions u_i^o for the soil which (i) satisfy the displacement boundary conditions and incompressibility condition, (ii) are physically reasonable, and (iii) contain one or more initially unspecified or "free" constants. (The

displacement boundary conditions are simply those conditions which make the soil displacement at the soil-pipe interface equal to the pipe surface displacement where separation or slipping does not occur.) The second step in the Ritz method consists of evaluating the free constants from Eq. (4.76); i.e., this equation is required to hold for virtual changes in displacement as calculated from infinitesimal changes in the free constants. Knowing the constants,we then find energy $\hat{W}_T$ and its derivatives with respect to pipe pseudo displacement and rotation.

The pseudo displacements to be used for all reaction calculations are expressed most conveniently in cylindrical coordinates, Fig. 4.4, and are assumed in dimensionless form as

$$\hat{u}_r^o = \left[\hat{U}_1^o \cos\theta + \hat{U}_2^o \sin\theta + c_1(\theta-\theta_c)^q H(\theta-\theta_c)\right]\hat{r}^{-p} \tag{4.120}$$

$$\hat{u}_\theta^o = (p-1)\left[\hat{U}_1^o \sin\theta - \hat{U}_2^o \cos\theta + \frac{c_2}{p-1} + \frac{c_1}{(q+1)}(\theta-\theta_c)^{(q+1)} H(\theta-\theta_c)\right]\hat{r}^{-p} \tag{4.121}$$

$$\hat{u}_z^o = \hat{U}_3^o \hat{r}^{-p} \tag{4.122}$$

where c_1, c_2, p, and q are the "free" constants, and θ_c is the angle at which the soil separates from the pipe (cf. Fig. 4.5); this angle for the Sep = 4 case will be found using concepts from fracture mechanics. The constant c_2 defines rotation of the soil, while c_1 and q are used with separation in the Sep = 1 and Sep =4 cases. Also,

$$H(\theta-\theta_c) \equiv \begin{cases} 0, & \theta < \theta_c \\ 1, & \theta > \theta_c \end{cases} \tag{4.123}$$

is the unit step function. In keeping with earlier definitions, Eqs. (4.97) and (4.98), the dimensional radial, tangential, and axial pseudo displacements are, respectively,

$$u_r^o = D\hat{u}_r^o \ , \quad u_\theta^o = D\hat{u}_\theta^o \ , \quad u_z^o = D\hat{u}_z^o \tag{4.124}$$

and the radial and axial coordinates are, respectively,

$$r = a\hat{r} \ , \qquad z = a\hat{z} \tag{4.125}$$

Observe that if $p > 0$ these displacements vanish as $\hat{r} \to \infty$, as required.

The radial displacement, Eq. (4.120), is constructed so that it is equal to the radial component of pipe pseudo displacement for $\hat{r} = 1$ and $\theta < \theta_c$. Similarly, the axial displacement, Eq. (4.122), satisfies the axial displacement condition at the soil boundary, $\hat{r} = 1$. However, Eq. (4.121) does not satisfy the boundary condition of no-slip,

$$\hat{u}_\theta^o = \hat{U}_\theta^o \quad \text{for} \quad \hat{r} = 1 \quad \text{and} \quad \theta < \theta_c \tag{4.126}$$

where

$$\hat{U}_\theta^o = -\hat{U}_1^o \sin\theta + \hat{U}_2^o \cos\theta + \Theta/2 \tag{4.127}$$

is the tangential component of pseudo pipe displacement. The no-slip condition could be met by adding another term to Eq. (4.121) (such as a term that is proportional to an exponential in $\hat{r}$ with an exponent different from p) but this complicates the integration which is needed to evaluate $\hat{W}_T$. For the current choice of displacements, in which each is proportional to $\hat{r}^{-p}$, integration with respect to $\hat{r}$ can be made analytically; all other displacements we have tried, which satisfy the incompressibility condition, lead to numerical integration in both θ and $\hat{r}$. For this reason, as well as the likelihood of increased difficulties with convergence of the numerical solution method used to derive the free constants, we shall not attempt to satisfy the no-slip condition exactly. Instead, a Lagrange multiplier [13] will be employed to

approximate it. First, however, use Eqs. (4.120)-(4.122) to find e_e^o.

The strain-displacement equations in cylindrical coordinates are [9],

$$e_r = \frac{\partial u_r}{\partial r}, \quad e_\theta = \frac{u_r}{r} + \frac{1}{r}\frac{\partial u_\theta}{\partial \theta}, \quad e_z = \frac{\partial u_z}{\partial z},$$

$$2e_{r\theta} = \frac{1}{r}\frac{\partial u_r}{\partial \theta} + \frac{\partial u_\theta}{\partial r} - \frac{u_\theta}{r}, \quad 2e_{rz} = \frac{\partial u_r}{\partial z} + \frac{\partial u_z}{\partial r},$$

$$2e_{z\theta} = \frac{\partial u_\theta}{\partial z} + \frac{1}{r}\frac{\partial u_z}{\partial \theta} \tag{4.128}$$

Pseudo strain-displacement equations follow by operating on these with the convolution integral, Eq. (4.20). With this step and the introduction of the dimensionless variables in Eqs. (4.124) and (4.125) we obtain

$$e_r^o = 2\frac{\partial \hat{u}_r^o}{\partial \hat{r}}, \quad e_\theta^o = 2\frac{\hat{u}_r^o}{\hat{r}} + \frac{2}{\hat{r}}\frac{\partial \hat{u}_\theta^o}{\partial \theta}, \quad e_z^o = 2\frac{\partial \hat{u}_z^o}{\partial \hat{z}},$$

$$e_{r\theta}^o = \frac{1}{\hat{r}}\frac{\partial \hat{u}_r^o}{\partial \theta} + \frac{\partial \hat{u}_\theta^o}{\partial \hat{r}} - \frac{\hat{u}_\theta^o}{\hat{r}}, \quad e_{rz}^o = \frac{\partial \hat{u}_r^o}{\partial \hat{z}} + \frac{\partial \hat{u}_z^o}{\partial \hat{r}},$$

$$e_{z\theta}^o = \frac{\partial \hat{u}_\theta^o}{\partial \hat{z}} + \frac{1}{\hat{r}}\frac{\partial \hat{u}_z^o}{\partial \theta} \tag{4.129}$$

These expressions are needed to derive the pseudo effective shear strain e_e^o, Eq. (4.31), which in turn is needed to evaluate the pseudo strain energy in Eq. (4.104).

In terms of pseudo strains and cylindrical coordinates, the incompressibility condition is

$$e_r^o + e_\theta^o + e_z^o = 0 \tag{4.130}$$

which one can verify for the displacements in Eqs. (4.120)-(4.122). Observe that since none of these displacements depend on z, and $\hat{u}_z^o$ is

independent of θ,

$$e_z^o = e_{z\theta}^o = 0 \tag{4.131}$$

This result, together with $e_r^o = -e_\theta^o$, which follows from Eqs. (4.130) and (4.131), enables us to write e_e^o, Eq. (4.31), in the form

$$e_e^o = 2[(e_r^o)^2 + (e_{r\theta}^o)^2 + (e_{rz}^o)^2]^{1/2} \tag{4.132}$$

where each normal and shear strain component e_{ij} in Eq. (4.31) has been replaced by each normal and shear strain in the cylindrical coordinate system; e.g., $e_{11} = e_r$, $e_{13} = e_{rz}$. This association is permissible since both coordinate systems are orthogonal. From Eqs. (4.120)-(4.122), (4.129), and (4.132) we obtain, finally,

$$e_e^o = 2pB_e^{1/2}\, \hat{r}^{-(p+1)} \tag{4.133}$$

where

$$\begin{aligned} B_e = {} & 4[\hat{U}_1^o \cos\theta + \hat{U}_2^o \sin\theta + c_1(\theta-\theta_c)^q H(\theta-\theta_c)]^2 \\ & + [p(\hat{U}_2^o \cos\theta - \hat{U}_1^o \sin\theta) - \frac{p+1}{p} c_2 + \frac{qc_1}{p}(\theta-\theta_c)^{(q-1)} H(\theta-\theta_c) \\ & - \frac{(p^2-1)c_1}{p(q+1)}(\theta-\theta_c)^{(q+1)} H(\theta-\theta_c)]^2 + (\hat{U}_3^o)^2 \end{aligned} \tag{4.134}$$

The energy W_T is a function of the pipe movement and free parameters (c_1, c_2, p, q) appearing in Eqs. (4.120)-(4.122). If the pipe displacements and rotation are specified quantities (or treated as such) so that $\delta U_i^o = \delta\theta^o = 0$, then Eq. (4.76) reduces to the "stationary" condition, $\delta W_T = 0$; i.e.,

$$\delta W_T = \frac{\partial W_T}{\partial c_1}\delta c_1 + \frac{\partial W_T}{\partial c_2}\delta c_2 + \frac{\partial W_T}{\partial p}\delta p + \frac{\partial W_T}{\partial q}\delta q = 0 \qquad (4.135)$$

For arbitrary variations of the free parameters, Eq. (4.135) cannot be satisfied unless each derivative vanishes. This requirement yields four equations for the four parameters. However, there is a problem with this formulation because the no-slip condition, Eq. (4.126), is not met by the assumed set of displacements. The difficulty will be resolved by use of a Lagrange multiplier (as mentioned previously) which leads to a modification of Eq. (4.135).

According to the Lagrange multiplier method [13] one adds a term to the energy which includes the no-slip constraint. We shall write the modified energy in the form

$$W_L = W_T - \int_{S_{ns}} (u_\theta^o - U_\theta^o)\, s_p \, dS \qquad (4.136)$$

where S_{ns} is the portion of the pipe surface where the no-slip condition is required and s_p is the Lagrange multiplier; the negative sign outside the integral is used for convenience of interpretation. The energy W_L replaces W_T in the stationary condition $\delta W_T = 0$, and therefore

$$0 = \delta W_L = \delta W_T - \int_{S_{ns}} \delta u_\theta^o \, s_p \, dS - \int_{S_{ns}} (u_\theta^o - U_\theta^o)\, \delta s_p \, dS = 0 \qquad (4.137)$$

The pseudo tangential pipe displacement, $U_\theta^o = a\theta^o$, is not varied since 0^o is considered to be specified. If δs_p is varied arbitrarily at each point (a, θ, z) of the pipe surface, the coefficient $(u_\theta^o - U_\theta^o)$ is required to vanish, thus producing the no-slip condition. Further, if the variation δu_θ^o in the first integral and in W_T is not restricted, the remaining portion of Eq. (4.137),

$$0 = \delta W_T - \int_{S_{ns}} \delta u_\theta^o \, s_p \, dS \tag{4.138}$$

is found to yield the exact set of equilibrium equations and boundary conditions if the Lagrange multiplier s_p is interpreted as the shear traction (force/area) acting along the pipe-soil interface; this traction is positive if it acts in the direction of positive θ (clockwise) on the soil. This process of deriving the governing equations consists essentially of working backwards through the steps that originally lead to Eq. (4.76), but now using $\delta U_i^o = \delta\Theta^o = 0$. The soil displacements one considers in this derivation have to be continuous, include the exact solution, and be such that u_θ^o can be varied arbitrarily at the pipe, r = a. Although the assumed displacements in Eqs. (4.120)-(4.122) do not contain the exact set as a special case, the above discussion is helpful because it provides us with a physical interpretation for the Lagrange multiplier s_p.

Just as for displacements, we shall use an approximate representation of s_p. Inasmuch as this quantity is the interfacial shear traction produced by the pipe on the mud, it will be assumed to be proportional to the soil strength at a constant pseudo strain, in which the coefficient of proportionality, denoted by c_3, is treated as a "free" constant. (The traction itself is found to be a function of pseudo pipe displacement through the predicted value of c_3.) Thus write

$$s_p = c_3 f_p \tag{4.139}$$

where $f_p = f_p(\theta)$ varies as the soil strength distribution varies around the pipe, such as found from the standard rotating vane test at a fixed pseudo rotation, Appendix 3; for homogeneous mud around the pipe use

$f_p = 1$. Since the displacements, Eqs. (4.120)-(4.122), do not depend directly on c_3, and the variation in s_p is $\delta s_p = \delta c_3 f_p$, Eq. (4.137) implies

$$\int_{S_{ns}} (u_\theta^o - U_\theta^o) f_p dS = 0 \tag{4.140}$$

Note that $dS = La d\theta$. Also, we shall impose the no-slip condition over the portion of the pipe where the mud does not separate from it, $\theta_1 \leq \theta < \theta_c$; see, for example, the angles shown in Fig. 4.5. Divide Eq. (4.140) by LaD and then introduce Eqs. (4.121) at $\hat{r} = 1$ and (4.127) to obtain a dimensionless relationship,

$$\int_{\theta_1}^{\theta_c} [p\hat{U}_1^o \sin\theta - p\hat{U}_2^o \cos\theta + c_2 - \theta/2] f_p \, d\theta = 0 \tag{4.141}$$

Observe that according to Eq. (4.140) the Lagrange multiplier method leads to the simple condition that the soil's weighted average tangential pseudo displacement at r = a must equal a weighted average of tangential pseudo pipe displacement.

Equation (4.138) provides four additional equations when arbitrary variations of c_1, c_2, p, and q are introduced. These four constants plus the fifth one, c_3, are then to be found by solving simultaneously all five equations in terms of the inputs U_1^o and θ^o.

This process involving five equations yields results which can be shown to be identical to those found by a simpler process with only three equations. The three equations are derived next.

We began by rewriting Eq. (4.141) to obtain c_2 explicitly in terms of only one of the free constants, p; the constants q and c_1 do not enter because $\theta_1 \leq \theta < \theta_c$. The result is

$$c_2 = \frac{\theta^o}{2} + p\int_{\theta_1}^{\theta_c}(-\hat{U}^o \sin\theta + \hat{U}^o \cos\theta) f_p \, d\theta \Big/ \int_{\theta_1}^{\theta_c} f_p \, d\theta \qquad (4.142)$$

If the soil around the pipe is homogeneous we obtain simply,

$$c_2 = \frac{\theta^o}{2} + \frac{p}{\theta_c - \theta_1}\left[\hat{U}_1^o(\cos\theta_c - \cos\theta_1) + \hat{U}_2^o(\sin\theta_c - \sin\theta_1)\right] \qquad (4.143)$$

In all subsequent steps for which θ^o is given, c_2 is no longer treated as a free constant. Instead, the only free constants are p, q, and c_1, and the equations for them are obtained from the stationary requirement, $\delta W_T = 0$. Thus, in terms of the dimensionless energy $\hat{W}_T$, Eq. (4.99),

$$\delta\hat{W}_T/\partial p = \delta\hat{W}_T/\partial q = \partial\hat{W}_T/\partial c_1 = 0 \qquad (4.144)$$

When there is no separation between the soil and pipe (Sep = 0 and $\theta_c = \theta_2$), we set $c_1 = 0$ and note that p is the only remaining free constant. Hence, p is derived from

$$d\hat{W}_T/dp = 0 \qquad (4.145)$$

According to our earlier discussion, the pipe movement, as expressed now by $\hat{U}_1^o$, $\hat{U}_2^o$, $\hat{U}_3^o$, and θ^o, is not varied when the derivatives in Eqs. (4.144) and (4.145) are evaluated.

After the constants are found by solving Eqs. (4.144) or (4.145), they are substituted into $\hat{W}_T$ so that the dimensionless pipe reactions,

Eq. (4.100), or generalized force coefficients, Eq. (4.118), may be calculated. The constants depend on $\hat{U}_i^o$ and θ^o, and it would appear necessary to account for this dependence when differentiating $\hat{W}_T$. Specifically, on the basis of Eqs. (4.102)-(4.104), (4.120)-(4.122), and (4.143),

$$\hat{W}_T = \hat{W}_T(\hat{U}_i^o,\ \theta^o,\ p,\ q,\ c_1) \tag{4.146}$$

Note that $\hat{u}_2^o$ in Eq. (4.103) is related directly to the pseudo displacements $\hat{u}_r^o$ and $\hat{u}_\theta^o$ since

$$\hat{u}_2^o = \hat{u}_r^o \sin\theta + \hat{u}_\theta^o \cos\theta \tag{4.147}$$

Inasmuch as p, q, and c_1 depend on $\hat{U}_i^o$ and θ^o, we may write, for example,

$$\frac{\partial \hat{W}_T}{\partial \hat{U}_1^o} = \frac{\partial \hat{W}_T}{\partial \hat{U}_1^o} + \frac{\partial \hat{W}_T}{\partial p}\frac{\partial p}{\partial \hat{U}_1^o} + \frac{\partial \hat{W}_T}{\partial q}\frac{\partial q}{\partial \hat{U}_1^o} + \frac{\partial \hat{W}_T}{\partial c_1}\frac{\partial c_1}{\partial \hat{U}_1^o} \tag{4.148}$$

where the derivative $\partial \hat{W}_T / \partial \hat{U}_1^o$ on the right side of Eq. (4.148) is evaluated holding p, q, and c_1 as well as $\hat{U}_2^o$, $\hat{U}_3^o$, and θ^o constant. The constants satisfy Eq. (4.144) and consequently there is no contribution from the last three terms in Eq. (4.148). It is concluded that p, q, and c_1 do not have to be varied when calculating the derivatives in Eq. (4.100) or (4.118).

The pipe reactions may be found as functions of pipe motion, $\hat{U}_i^o$ and θ^o, over any given range of values. With these numerical results and an interpolation procedure one could find components of the motion if the reactions instead are given. Numerical results for the case of zero moment will be examined in some detail later in this report, and therefore it will be helpful to incorporate the condition $\hat{M} = 0$ directly into the evaluation of the free constants instead of using a post-

analysis interpolation method. For this case

$$\partial \hat{W}_T / \partial \theta^o = 0 \tag{4.149}$$

Observe that $\hat{W}_T$ depends on θ^o only through c_2, Eq. (4.143). Hence,

$$\frac{\partial \hat{W}_T}{\partial \theta^o} = \frac{\partial \hat{W}_T}{\partial c_2} \frac{\partial c_2}{\partial \theta^o} = \frac{1}{2} \frac{\partial \hat{W}_T}{\partial c_2} \tag{4.150}$$

and Eq. (4.149) may be replaced by

$$\partial \hat{W}_T / \partial c_2 = 0 \tag{4.151}$$

Consequently, if $\hat{M} = 0$, Eqs. (4.144) and (4.151) constitute a set of four equations for the constants p, q, c_1, and c_2. After solving these equations, the rotation may be found from Eq. (4.143). If Sep = 0, then $c_1 = 0$ and the equations

$$\partial \hat{W}_T / \partial p = 0 \quad , \quad \partial \hat{W}_T / \partial c_2 = 0 \tag{4.152}$$

yield the only remaining constants, p and c_2.

Finally, it should be mentioned that two generalizations using Lagrange multipliers have been tried. One consisted of allowing for a sign change in s_p over the interval $\theta_1 \leq \theta < \theta_c$, with the location of the sign change treated as a free parameter. The variational method predicted that the sign change occurs at one end of the interval; i.e., no sign change occurs. Another generalization introduced a thin layer of soil around the pipe in which the stresses were independent of radial location. The thickness of the layer was a free parameter; but it was subsequently predicted to be zero. While a more complex set of local displacements may lead to improved solutions, it appears that this

improvement cannot be achieved without a great deal of additional work and computer running time. Indeed, as the comparisons of theory and experiment made later in this report show, the solutions based on Eqs. (4.120)-(4.122) and (4.143) are entirely adequate for engineering purposes.

4.4.6 Loading for Proportional Movement: As a guide to developing normalization procedures for pipe loading which are helpful in representing large amounts of theoretical and experimental data compactly, we shall discuss so-called proportional movement. Namely, let $\hat{U}_i^o$ and θ^o depend on a common positive factor $\hat{U}$; for example, $\hat{U} = \hat{U}_R$ for elastic soil (cf. Eq. (4.108)) and $\hat{U} = \hat{V}_R$ for viscous soil (cf. Eq. (4.110)).

In the absence of gravity effects, i.e. $\hat{\gamma} = 0$ in Eq. (4.103), the dependence of pipe reactions on $\hat{U}$ is very simple and it will be discussed first. For this case $\hat{W}_T = \hat{W}_V$, where $\hat{W}_V$ is in Eq. (4.104). Moreover Eqs. (4.144) and (4.145), which are used to calculate the free constants, involve derivatives for fixed values of $\hat{U}_i^o$ and θ^o. Thus, the results are unaffected if $\hat{W}_T$ is replaced by $\hat{W}_V/\hat{U}^{1+N}$. Absorbing the divisor into the integrand, so that $e_e^o/\hat{U}$ replaces e_e^o, we see from Eqs. (4.133), (4.134), and (4.143) that $\hat{U}$ appears as a divisor of $\hat{U}_i^o$, θ^o, and c_1. Since $\hat{U}_i^o/\hat{U}$ and $\theta^o/\hat{U}$ are independent of $\hat{U}$, Eqs. (4.144) and (4.145) imply $c_1/\hat{U}$, p, and q are all independent of $\hat{U}$. As a consequence, the soil displacement distributions, Eqs. (4.120)-(4.122), are proportional to $\hat{U}$.

The dependence of the dimensionless reactions on $\hat{U}$ may be established by returning to Eq. (4.104) and differentiating under the integrals; e.g.

$$\frac{\partial \hat{W}_v}{\partial \hat{U}_1^o} = \int_{\theta_1}^{\theta_2} \int_{\hat{r}_1}^{\hat{r}_2} (e_e^o)^N \frac{\partial e_e^o}{\partial \hat{U}_1^o} F \hat{r} \, d\hat{r} \, d\theta \tag{4.153}$$

In view of the above results, we conclude that e_e^o is proportional to $\hat{U}$, $\partial e_e^o / \partial \hat{U}_1^o$ is independent $\hat{U}$, and consequently the energy derivative, Eq. (4.153), is proportional to $\hat{U}^N$. Applying this analysis to all reactions in Eq. (4.100), we find they are proportional to $\hat{U}^N$; namely,

$$\hat{F}_i \sim \hat{U}^N \quad \text{and} \quad \hat{M} \sim \hat{U}^N \tag{4.154}$$

For the case $\hat{M} = 0$, in which the free constants are derived from Eqs. (4.144) and (4.151) or (4.152) and the rotation from Eq. (4.143), a similar analysis yields

$$\hat{F}_i \sim \hat{U}^N \quad \text{and} \quad \theta^o \sim \hat{U} \tag{4.155}$$

Equations (4.154) and (4.155) imply we may use $\hat{U} = 1$ in all predictions of forces and pseudo displacements. Then for any $\hat{U} \neq 1$, by multiplying these forces and displacements by $\hat{U}^N$ and $\hat{U}$, respectively, the actual values may be found. Just the opposite process is to be followed in order to obtain a useful normalized form of experimental data. Namely, divide forces and pseudo displacements by $\hat{U}^N$ and $\hat{U}$, respectively, to express results in a form which may be conveniently compared to theory. If this normalization of exprimental data yields quantities which are independent of $\hat{U}$, a partial check of the theory is achieved.

Such simplicity in behavior does not exist if $\hat{\gamma}$ cannot be neglected. Nevertheless it is still helpful to normalize results in a similar way. This procedure leads to the use of a modified gravity parameter,

$$\hat{\gamma}_m \equiv \hat{\gamma}\hat{U}^{1-N} \tag{4.156}$$

Specifically, referring to Eqs. (4.102)-(4.104), and using the same arguments that lead to Eqs. (4.154) and (4.155), we obtain the same dependence on $\hat{U}$ if $\hat{\gamma}_m$, rather than $\hat{\gamma}$, is treated as a specified quantity.

4.4.7 Crack Growth Analysis: The development of separation between the pipe and soil and cracking within the soil may be analyzed using principles of fracture mechanics. Here we shall develop the equation needed to predict the extent of separation, as defined by the angle θ_c, for the Sep = 4 case in Fig. 4.5. For any particular value of θ_c, the pipe reactions may be found using the theory in Section 4.4.5.

This separation is viewed as a crack, in which the growth rate is

$$\dot{c} = -a\dot{\theta}_c \tag{4.157}$$

where $\dot{\theta}_c < 0$ during growth. The theory in [12] enables $\dot{c}$ to be predicted as a function of pipe movement through the driving force for crack growth, the "J_v integral". It will be assumed the crack tip zone of intense damage (in which Eq. (4.35) does not apply) is small compared to crack length and pipe diameter. Observations of the separation which occurs during testing support this assumption. For the case of a small crack tip damage zone, the J_v integral is equal to the "pseudo energy release rate", where the latter quantity is the change of pseudo strain energy with respect to crack area for fixed pseudo pipe displacements. With an increment in crack or separation area given by $-aLd\theta_c$, the separation rate may be expressed as the function,

$$\dot{c} = \dot{c}(J_v) \tag{4.158}$$

where

$$J_v = \frac{1}{aL} \frac{\partial W_T}{\partial \theta_c} \tag{4.159}$$

If J_v is less than a "critical value", J_c, then $\dot{c} = 0$, and when $J_v > J_c$ then $\dot{c}$ is an increasing function of J_v.

The function in Eq. (4.158) is not known for the sediment used in our investigations. However, observations of the separation process indicate that when it occurs, c usually grows very rapidly until some equilibrium size is reached. This behavior will be idealized here by supposing the resistance to crack growth is so small that $\dot{c}$ is very large when $J_v > 0$ and $\dot{c} = 0$ when $J_v = 0$. Numerical studies of the Sep = 4 case for horizontal movement indicate that $J_v > 0$ until the crack grows to a point on the bottom half of the pipe surface. Any virtual increase in separation beyond this point yields $J_v < 0$, and therefore the separation cannot actually extend beyond the point at which $J_v = 0$. Thus, for a soil with negligible resistance to cracking, the value of θ_c may be found from the condition

$$\partial \hat{W}_T / \partial \theta_c = 0 \tag{4.160}$$

where Eq. (4.99) for $\hat{W}_T$ has been used to obtain a dimensionless expression. This equation is analogous to the conditions used to derive the other free constants, such as Eq. (4.144).

Pressure may affect the value of J_v (e.g., by directly reducing the tensile stress at the crack tip) as well as the behavior of material at the crack tip (as characterized by the function in Eq. (4.158)). Consequences of pressure dependence on pipe loading are described in the experimental studies, Section 3.

4.5 Prediction of Sediment Displacements

4.5.1 Elastic Soil Model: Recall that for an elastic material the pseudo displacements are the physical displacements. Thus, by simply dropping the superscript "o" in Eqs. (4.120)-(4.122), the dimensionless soil displacements are obtained. As shown in Section 4.4.6, all displacements are proportional to the amount of pipe movement relative to the remote soil (in the absence of separation or cracking or for a fixed amount of separation). It should be emphasized that these displacements are based on small deformation theory for a nonlinear, elastic power law soil. Consequently, they certainly are not expected to be valid when relative pipe movement is not small compared to its diameter or after large changes in the mudline location occur.

The vertical displacement, u_2, of the mudline is a particularly useful quantity since it may be readily compared to laboratory or field observations. The dimensionless vertical displacement, $\hat{u}_2 = u_2/D$, may be derived by substituting Eqs. (4.120) and (4.121) into (4.147), and then introducing the values of θ and $\hat{r}$ which define the initial mudline.

4.5.2 Viscous Soil Model: The pseudo displacements in this case are equal to the soil particle velocity multiplied by the time constant t_c. Hence, integration of Eqs. (4.120)-(4.122) with respect to time yields the displacements; but it is necessary to account for the fact that $\hat{r}$ and θ define material points relative to a moving coordinate origin, the pipe's centerline. In order to illustrate the prediction of displacement we shall develop an expression for vertical movement of the mudline due to constant horizontal pipe velocity. Referring to Fig. 4.7, let x_o denote the initial horizontal location of a particle on the mudline relative to the initial position of the pipe's centerline. Then

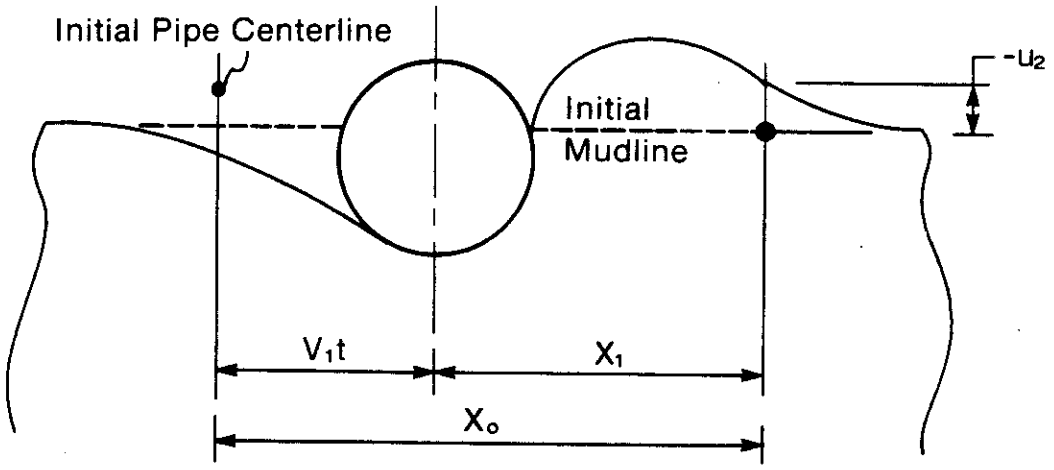

Figure 4.7 Coordinates for Predicting Mudline Displacements

with x_1 as the coordinate of this same material point relative to the instantaneous centerline, we may write

$$x_o = V_1 t + x_1 \tag{4.161}$$

Also, the displacement is

$$u_2 = \int_o^t \dot{u}_2 \, dt \tag{4.162}$$

where the integration is for fixed x_o. It is more convenient to integrate with respect to x_1 instead of t. For this change of variable, use Eq. (4.161) with $dx_o = 0$ to find

$$dt = -dx_1/V_1 \tag{4.163}$$

Thus, Eq. (4.162) becomes

$$u_2 = -\int_{x_o}^{x_1} \dot{u}_2 \, dx_1'/V_1 \tag{4.164}$$

where the prime is used to denote a variable of integration. The

approximate analysis in Section 4.4 uses dimensionless pseudo displacements, and therefore it is desirable to express the integral in terms of these quantities. Namely, substitute

$$u_2 = D\hat{u}_2 \ , \quad \dot{u}_2 = D\hat{u}_2^o/t_c \ , \quad V_1 = D\hat{V}_1/t_c \ , \quad x_1 = a\hat{x}_1 \ , \quad x_o = a\hat{x}_o \tag{4.165}$$

into Eq. (4.164) to find the dimensionless displacement,

$$\hat{u}_2 = -\frac{1}{2\hat{V}_1}\int_{\hat{x}_o}^{\hat{x}_1} \hat{u}_2^o \, d\hat{x}_1' \tag{4.166}$$

where

$$\hat{u}_2^o = \hat{u}_r^o \sin\theta + \hat{u}_\theta^o \cos\theta \tag{4.167}$$

and the pseudo displacements $\hat{u}_r^o$ and $\hat{u}_\theta^o$ are those in Eqs. (4.120) and (4.121); the coordinates θ and $\hat{r}$ are to be expressed in terms of the $\hat{x}_1$ coordinate, which becomes the variable of integration $\hat{x}_1'$ in Eq. (4.166).

In order to use Eq. (4.166) to calculate the displacement distribution at a fixed time, we have to eliminate $\hat{x}_o$ by means of the dimensionless form of Eq. (4.161),

$$\hat{x}_o = 2\hat{U}_1 + \hat{x}_1 \tag{4.168}$$

where

$$\hat{U}_1 \equiv V_1 t/D \tag{4.169}$$

The equation for displacement to the left of the pipe is the same as Eq. (4.166) but without the minus sign.

In most cases numerical integration is needed to predict the displacement, and the computer program contains a routine for this. However, when the pipe's centerline is at the mudline (h/D = 1/2),

analytical integration is possible. In this case the pseudo displacement of the mudline for $\hat{x}_1 \geq 1$ is simply

$$\hat{u}_2^o = c_2 \hat{x}_1^{-p} \tag{4.170}$$

which follows from the fact that $\theta = 0$, and thus $\hat{u}_2^o = \hat{u}_\theta^o$ and $\hat{x}_1 = \hat{r}$. Substitute Eq. (4.170) into (4.166), integrate, and then use Eq. (4.168). We find

$$\hat{u}_2 = \frac{c_2}{2\hat{V}_1(p-1)} \left[\hat{x}_1^{1-p} - (2\hat{U}_1 + \hat{x}_1)^{1-p} \right] \tag{4.171}$$

where $\hat{U}_1$ is a dimensionless pipe displacement, Eq. (4.169). It is to be observed that the displacement at the pipe, $\hat{x}_1 = 1$, is not necessarily zero because the analysis allows for partial slip at the mud-pipe interface.

4.6 Numerical Methods used in the Computer Program

4.6.1 Homogeneous Sediment: The computer program based on the foregoing theory was written for the Hewlett-Packard 9816 personal technical computer, and uses the language HP Basic 2.0 with Extensions AP2_0. A large amount of subprogramming has been employed in order to be able to program and debug the various components of the theory in Sections 4.4 and 4.5 individually. Here we shall comment briefly on the primary numerical techniques employed and what was done to assure their accuracy.

Numerical integration by Simpson's rule (subprogram Sim) is used to evaluate the total energy (subprogram FNW), Eqs. (4.102)-(4.104). The Newton-Raphson iteration method (subprograms Rt 1 through Rt 4) is employed to derive the free constants by requiring that certain derivatives vanish (e.g., Eqs. (4.144) or (4.145)); there may be from

one to four unknown constants, including rotation, and there is one subprogram for each case. All derivatives of total energy are evaluated numerically using sufficiently small finite differences. For homogeneous sediment the simple power-law dependence on radius of the pseudo effective shear strain, Eq. (4.133), permits analytical integration of Eq. (4.104) with respect to the radial coordinate; recall that F = 1 for homogeneous soil. Much of the computer program's complexity arises from the need to introduce the pipe and soil boundaries into the relationship of $\hat{r}_1$ and $\hat{r}_2$ (cf. Eq. (4.104)) to the polar angle θ.

Different numerical integration methods were studied (trapazoidal rule, Simpson's rule, and the so-called cautious adaptive Romberg extrapolation method available in the HP 98821A Numerical Analysis Library) and it was concluded that Simpson's rule provided the best combination of speed and accuracy in evaluating the energy. Displacements for the nonlinear viscous model, such as in Eq. (4.166), turn out to have a form (when expressed in terms of steps in pipe movement) which is evaluated most conveniently by the trapazoidal rule. All numerical methods employed in integrating, differentiating, and finding roots were studied thoroughly in order to make certain that all numerical errors have negligible effect on pipe loading and displacements. Also, when possible the results were compared with exact analytical solutions. In particular, it was found that numerical results using the energy method of analysis agreed very well with the exact solutions for pure rotation (Appendix 3) and pure axial displacement (Appendix 4). It was also possible to express an exact solution for combined rotation and axial movement in a form requiring

only numerical integration of a single integral; the energy solution was in excellent agreement with this problem as well.

Finally, we should comment on the dependence of the energy solution on the initial values assumed for the free constants and the rotation (if the torque or moment is given). In general, it was found that the solution was unique. That is, if convergence was achieved, the same solution was obtained regardless of the "guessed" initial values of the unknown constants. However, in the cases where there were three or four unknowns, convergence was sometimes not achieved (especially in the range $.5 \leq h/D \leq 1$) unless the initial values were within five or ten percent of the correct values. Nevertheless, this was not a major problem because one could start by obtaining a solution in a stable range of behavior (flow angle of 90° and $h/D \geq 2$) and then decrementing 5 degrees in flow angle and 0.075 in log (h/D); to speed up convergence a linear extrapolation method was used to estimate initial values from the previous two solutions. This is the procedure that was employed to generate the several thousand solutions used to plot the numerous theoretical curves which appear in the figures in Section 3 and Appendix 5.

4.6.2 Nonhomogeneous Sediment: The energy integral in Eq. (4.104) was integrated analytically with respect to $\hat{r}$ for a homogeneous soil ($F = 1$ and N constant). However, this is not usually possible when the sediment strength varies from point-to-point. It is anticipated that the time required to solve each problem on the computer would be increased by at least an order of magnitude if numerical double integration ($\hat{r}$ and θ) were used, as compared to numerical integration with respect to only θ. Also, the effect of numerical errors on convergence of solutions and accuracy of pipe loading predictions would

have to be studied anew. Considering these matters and the fact that it was not an objective of the project to develop a general purpose computer program, what was done was limited to three special cases with the following restrictions: (1) power law strength distribution with respect to x_2, $h/D = 1/2$, and moment = 0; (2) power law strength distribution with respect to x_2, $h/D \ll 1$, and moment = 0; and (3) the layered sediment shown in Fig. 4.8,

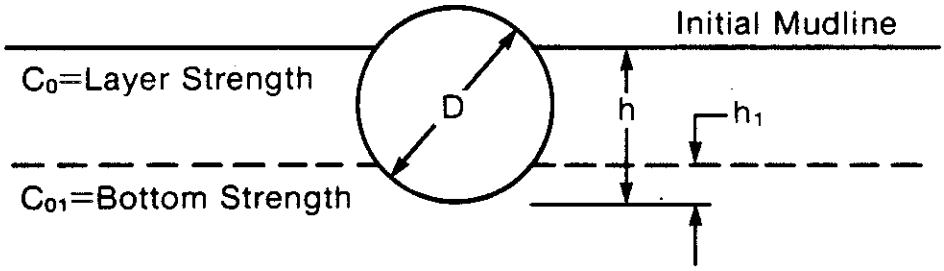

Figure 4.8. Layered Sediment Problem

$0 \leq h_1 \leq h$, and moment = 0.

The power law strength distribution may be written in the form

$$C_{op} = C_o \hat{x}_2^s \quad \text{and} \quad \hat{x}_2 = 2x_2/D \tag{4.172}$$

where s is a positive constant; it is expected that the values of s for sediment adjacent to the mudline will be in the range $0 \leq s \leq 1$. If $h/D = 1/2$, then $\hat{x}_2 = 1$ at the bottom of the pipe, and C_o is actually the strength at $x_2 = D/2$. By using C_o in the definition of g_i, Eq. (4.116), and changing to polar coordinates, Fig. 4.4, the factor F for $h/D = 1/2$ becomes

$$F = \hat{r}^s (\sin\theta)^s \quad \text{where} \quad 0 \leq \theta \leq \pi \tag{4.173}$$

Analytical integration of Eq. (4.104) with respect to $\hat{r}$ is clearly possible when Eqs. (4.133) and (4.173) are used. The computer program

(cf. Section 4.6.1) contains the case numbered (1) above, and thus the user may input values for s when h/D = 1/2 and moment = 0. The case (2) is discussed in Appendix 6, and is for a linear viscoelastic material.

Case (3) was solved for two problems studied experimentally in order to make a preliminary assessment of the theory's accuracy in predicting loading on pipes in nonhomogeneous sediment. The computer program for homogeneous sediment was easily adapted to the single layer case in the following manner. Referring to Fig. 4.8, let F_o and F_{ol} be the strength factors for the layer and bottom, respectively, to be used for F in Eq. (4.104), and assume N is the same for both materials. Then, it is easily found that the total energy, Eq. (4.102), is

$$\hat{W}_T = \hat{W}_s + F_{ol}\,\hat{W}_{vh} + (F_o - F_{ol})(\hat{W}_{vh} - \hat{W}_{lh}) \qquad (4.174)$$

where $\hat{W}_{vh}$ is the value of $\hat{W}_v$, Eq. (4.104), considering all of the sediment with F = 1; also, $\hat{W}_{lh}$ is $\hat{W}_v$ considering only the sediment below the layer and using F = 1. If, for example, the force coefficients g_i are derived by dividing forces by the bottom strength C_{ol}, then F_{ol} = 1 and F_o becomes the ratio of layer strength to that of the bottom. Thus, simply by using Eq. (4.174) for total energy and modifying the computer program accordingly, two-material problems may be solved.

5.0 COMPARISON OF THEORETICAL AND EXPERIMENTAL RESULTS

Predictions using one or more of the five cases in Fig. 4.5, designated by "Sep" numbers, have been made for all of the different experimental test conditions. They are plotted using continuous or broken lines in many of the figures in Section 3. The identification of each line type is given in Fig. 5.1.

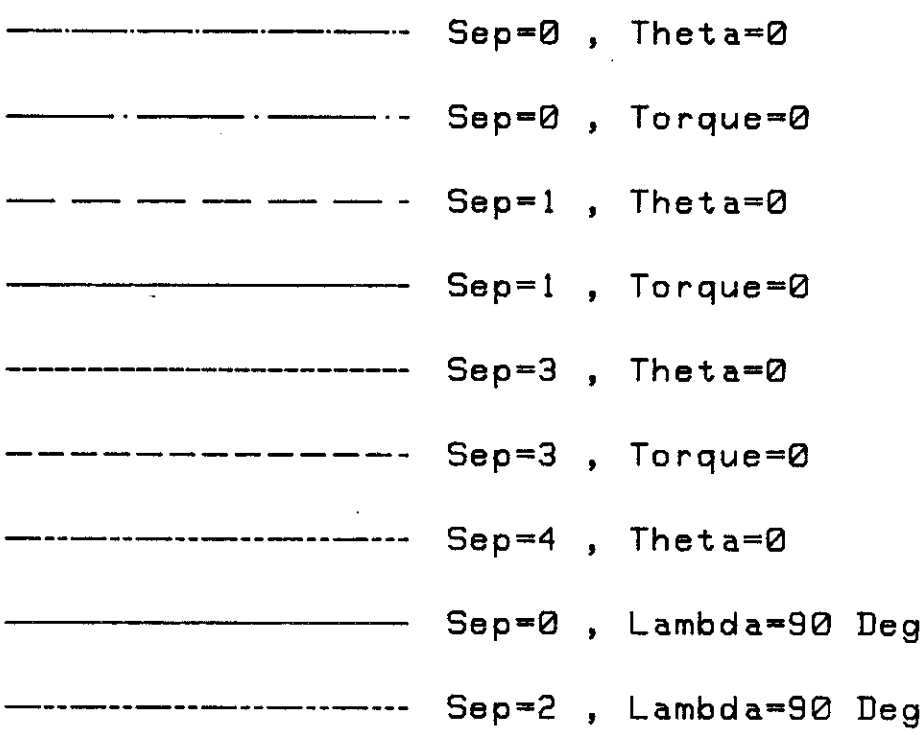

Figure 5.1 Key for Identifying Line Types in Section 3

The sediment is modeled as a nonlinear viscous body, and comparisons between theory and experiment are made in many cases at both the soil failure point (or pipe "breakaway" point) and a common value of large nondimensional displacement, U/D = 3. The same sediment properties, C_o and N, are used at both points, and for all comparisons N = 0.12. Unless shown otherwise, gravity effects are neglected by using $\hat{\gamma} = 0$. In Section 5.1 we summarize what the experimental data

appear to tell us about the applicability of each Sep model in Fig. 4.5, and then in Section 5.2 we discuss the applicability of the viscous soil model.

5.1 Changes in Sediment Geometry with Pipe Motion

For a nonlinear viscous material, the mud loading at any instant depends only on the current soil strain rates and current geometry of the mudline and cracks (if any). The only effect of pipe movement history enters through changes in soil geometry with time. Our approach to discussing the applicability of the idealized sediment geometry cases in Fig. 4.5 will be to state what we believe to be the sequence of events and then refer to many of the plots in Section 3 to support the conclusions.

The case Sep = 0 represents the starting point for all tests, in which the pipe may be fully submerged, $h/D > 1$, or partially exposed, $0 < h/D \leq 1$. For horizontal movement (or shallow penetration angles) and $0 < h/D \leq 1$, a shelf eventually forms behind the pipe, idealized as Sep = 1. However, before this and other more complex phenomena occur, the crack in Sep = 4 develops if $.5 \leq h/D \leq 2$.* In many cases the peak forces exist when the crack in Sep 4 is fully developed. Subsequent decay of the forces occurs as the crack opens and the mudline begins to take the shape of Sep = 1. In a few cases more extensive cracking may develop, which is modeled by using a deep vertical crack, Sep = 3. For downward movement which is vertical or at a steep angle, the type of cavity of Sep = 2 is formed if $h/D \leq 1$ initially. For $h/D \gtrsim 2$ initially and without external pressure, the type of cavity of Sep = 2 forms above the pipe, regardless of the direction of movement, as long as

*Thus, the plots in Section 3 for Sep = 4 extend only to h/D = 1/2.

there is a downward normal velocity component. However, under the weight of the mud above and adjacent to the cavity, it may close a short distance behind the pipe. For deep burial, h/D $\gtrsim$ 5, and with sufficient pressure on the mudline, little or no separation develops and therefore Sep = 0 is a good approximation regardless of the type of pipe movement.

This latter situation is supported by the data for deep burial in Figs. 3.99, 3.100, 3.120, and 3.121. Transition from Sep = 0 to Sep = 1 is illustrated for the moment coefficient in Figs. 3.61 and 3.62. The effect of h/D on the applicable Sep cases is implied in the logarithmic plots in Figs. 3.103-3.109 and 3.111-3.115. Although there is a significant spread in the data due to the effect of pressure, soil strength, rest period, and velocity, the overall behavior appears to be that described above, as illustrated in Figs. 3.111 and 3.114. For small initial recess depth, h/D = .25 and .50, Figs. 3.112 and 3.115 show there may be a significant increase in the "effective" depth of burial with pipe displacement. This is consistent with direct observations of the actual amount of mud pile-up at the front of the pipe. It should be added that the theory in Section 4.5.2 was used to calculate the mudline displacements, and it was found that limiting upward dimensionless movement at the pipe is less than or equal to the initial h/D values for h/D $\leq$ 1. Thus, for example, if the initial h/D is 0.25, the mudline at the front surface with large pipe motion may move up to h/D = 1/2. A few measurements indicate that the actual rise in the mudline ranges typically from this theoretical maximum amount to twice this amount for h/D $\leq$ 1.

The angle θ_c or β_c, which defines the crack tip location for Sep = 4, was studied theoretically for its change with respect to h/D at a flow angle of 90° and with horizontal pipe movement. It was found from

Eq. (4.160) that $\beta_c \simeq -30°$ ($\theta_c \simeq 120°$) for $h/D \geq .9$ and zero pipe rotation; for $.5 \leq h/D < .8$, the angle β_c was practically zero. In the case of zero moment or torque and $h/D \geq .5$, the angle β_c was predicted to be essentially zero (i.e., the crack tip is at the bottom of the pipe). These values of β_c (i.e. -30° and 0°) were used regardless of the flow angle in making the predictions shown in Section 3. Better agreement between theory and experiment for Sep = 4 with a flow angle α less than 90° would possibly be realized if a different β_c was calculated by means of Eq. (4.160) for each α and h/D. For $h/D < .5$, no interface crack was predicted to develop.

Considering all of the comparisons made for horizontal or nearly horizontal pipe motion, the least satisfying is that for the vertical force coefficient g_2 when $h/D > 1$. See, for example, Figs. 3.57, 3.70, and 3.85, in which negative values (downward acting force of the mud on the pipe) exist for $h/D > 1$. None of the different Sep cases predict negative g_2 for horizontal or downward motion of the pipe. However, we found that by allowing for shear failure of the soil on the aft surface of the pipe (interface shear stress = 0) down to an angle β_c, but without an open crack ($c_1 = 0$ in Eq. (4.134)), negative values of g_2 are predicted in many cases. This result may imply shear failure actually develops. Alternatively, negative g_2 values may be due to the weight of the sediment above the pipe which is not fully accounted for by using the methods described in Section 3, or due to a type of sediment cracking which is just more complex than that studied analytically. The pseudo energy release rate, Eq. (4.159), was found to be practically independent of the length of the shear crack, and therefore Eq. (4.160) could not be used to estimate β_c theoretically. It should be added that

the vertical force for Sep = 0 is always zero if the pipe motion is horizontal.

The tendency for a cavity to develop above a pipe which is pushed down is implied by the behavior illustrated in Figs. 3.66, 3.67, 3.71, and 3.72. Referring to Fig. 3.66a for vertical movement, the theoretical value of g_2 at large h/D for the Sep = 2 case is 0.8 of that for the top curve, Sep = 0. This factor of 0.8 should of course exist for horizontal movement of a deeply buried pipe if a trailing cavity exists. Earlier experimental studies of stronger sediment confirm this value of 0.8 for horizontal movement of pipes when there is no confining pressure [3]; the collapse of the cavity due to sediment weight was presumably less than in the present case because of the high soil strength. The behavior shown in the aforementioned figures (in which the measured force coefficients start low relative to the Sep = 0 case and then gradually approach this theoretical case without a cavity) is thus believed to reflect the early development of a cavity, which then closes with increasing weight of mud above it. The early, pre-failure segment of the curves in these figures is affected by elastic characteristics of the sediment; the soil elasticity is neglected in the theoretical model of viscous behavior. The amount of elastic-like deformation in the laboratory tests is dependent on the overall size of the drag box and pipe length, and therefore is not believed relevant to subsea pipeline analysis.

Theoretical and experimental results for the nonhomogeneous sediment problems, Figs. 3.90-3.95, are in relatively good agreement, especially at the soil failure points. The g-values shown were calculated by dividing force by the average sediment strength from the mudline to one pipe radius below the pipe, $y_a = h + 0.5D$. With this

choice of strength the resulting g_i values are close to those for homogeneous sediment. A separate theoretical study indicated that g_1 for each of the three layered-sediment problems equals that for homogeneous sediment if $y_a \simeq h + 0.3D$, and that g_2 is not nearly as sensitive to the strength of the top layer as g_1.

In all theoretical predictions for the layered sediment problems the case Sep = 1 with zero moment was used. Furthermore, c_1 was not calculated; but, instead, it was specified to be zero. This choice of conditions was made because they lead to relatively good agreement with experimental data on homogeneous sediment, as shown in Fig. 3.82a for $c_1 = 0$. The objective here was to obtain a preliminary check of the theory in predicting g_i for nonhomogeneous sediment, rather than to develop a general computer program for use in many different problems.

Finally, let us consider the effect of pipe size, as reflected in the value of the gravity parameter, $\hat{\gamma}_m$, Eq. (4.156). First, we must relate this parameter to test variables. Recall that for the viscous soil model $\hat{U}$ is $\hat{V}_R$, where $\hat{V}_R$ is the dimensionless resultant velocity in Eq. (4.111). Also, $\hat{\gamma}$ is defined by Eq. (4.97), in which $f = t/t_c$. The value of G_R is related to soil strength through Eq. (4.115). (The quantity $\hat{\gamma}_m$ is the variable "Grav" in the computer program.) These considerations yield

$$\text{Grav} \equiv \hat{\gamma}_m = \frac{\Delta\gamma U_R}{C_o}\left(\frac{2\dot{\theta}_{vo}}{N}\right)^N \left(\frac{V_R}{D}\right)^{-N} \tag{5.1}$$

where U_R is the time-dependent resultant pipe displacement, $V_R t$. The standard vane rotation rate is $\dot{\theta}_{vo} = 0.0143$ rad/sec. Also, for the test cases of interest N = 0.12 and $V_R/D = V_1/D = 0.015$ dia/sec. Since

water is not used, $\Delta\gamma \rightarrow \gamma_s$ where γ_s is the unit weight of sediment, 100 pcf. For the test results in Figs. 3.82 and 3.83, C_o = 20 psf, and therefore

$$\text{Grav} = 7.0\ U_R \qquad (U_R \text{ in feet}) \tag{5.2}$$

Predictions are shown in Figs. 3.82b and 3.83 for U_R = 1/14 ft. and U_R = 1/2 ft., respectively.

It should be noted that the theory is, strictly speaking, limited to small displacement (relative to pipe diameter) and therefore the second case is of questionable accuracy. It is likely that for large displacements a measure of the vertical mudline movement should be used in Eq. (5.1) instead of U_R. Nevertheless, the case Grav = 3.5 is shown for comparison purposes. Clearly, at the soil failure point, Fig. 3.82b, the theory predicts that gravity has a negligible effect.

5.2 Validity of the Viscous Soil Model

Results from the many tests that were conducted on deeply buried pipes with pressure on the mudline provide strong support for the viscous soil model at failure and at the large displacement point U/D = 3. For this situation the geometry of the mudline and sediment cracking are not significant factors. Figures 3.120 and 3.121 for soil failure are very encouraging considering that a complex multiaxial state of stress exists. The fact that practically all test results in Section 3 for deeply buried pipes are close to the predictions for the Sep = 0 case at the failure and U/D = 3 points leads us to conclude that the viscous model is entirely adequate for engineering purposes. As a consequence, it is believed the very complex type of behavior exhibited by g_i when $h/D \leq 2$ is due to sediment cracking, voids, and separation of

mud from the pipe. This conclusion about the viscous model may be contrasted with the behavior reported in [5], in which essentially the same sediment was studied in simple shear. Namely, it was found for constant strain rate tests that the shear stress is

$$\tau = t^{-n} f(\gamma) \tag{5.3}$$

where n is a positive constant and $f(\gamma)$ is a function of shear strain γ. Equation (5.3) is for a nonlinear elastic material with "aging". The function f increases with strain up to 6.6% and then slowly decreases. For a limited range of strain up to the maximum in f, this function may be approximated as a power law,

$$f = k\gamma^N \tag{5.4}$$

where k and N are positive constants. If we assume the multiaxial law in Eq. (4.35) is applicable, then for simple shear we obtain

$$\tau = \psi G_R \gamma^N \tag{5.5a}$$

and consequently

$$\psi G_R = k t^{-n} \tag{5.5b}$$

(It is of interest to point out that by using kt^{-n} in place of G_R in Eq. (4.96), and recalling that for elastic materials pseudo variables are equal to the physical variables, we may use the computer program for viscous mud to predict pipe force-displacement relationships prior to soil failure.) For constant velocity pipe motion without cracking, voids, or separation, one can show that all strain rates are constant (for small strains only if the pipe is not deeply buried). Equation (5.5), for example, becomes

$$\tau = k\dot{\gamma}^n \gamma^N / \gamma^n \tag{5.6}$$

If N = n,

$$\tau = k\dot{\gamma}^n \tag{5.7}$$

which is the constitutive relationship for a nonlinear viscous material. Consequently, one may interpret the nonlinear viscous model as a nonlinear, aging elastic material with N = n. Regardless of which interpretation is employed the predictions are the same for constant velocity motion of the pipe.

The function f actually exhibits a maximum point, and this is not accounted for in Eq. (5.4). Why a maximum in f does not reflect itself in pipe force-displacement curves which decay at large strains for deeply buried pipes is not known at this time. Possibly, wherever the strain at the maximum stress is exceeded in the soil mass a local increase in strain rate occurs and the stress returns to its peak value. The fact that some of the data points for g_1 shown in Section 3 (e.g., Fig. 3.104) are closer to the theoretical curve for zero moment than zero rotation (with a non-rotating pipe) at intermediate burial depths may be due to soil strength reduction at the high strain region near the pipe. However, the predicted values of g_1 for zero moment and zero rotation are relatively close, and thus one cannot use g_1 to argue for the existence of a weak layer of soil around the pipe. In some cases, such as in Figs. 3.63 and 3.64, the measured torque is noticeably less than predicted for the Sep = 1 case without rotation; indeed, if there is no slipping at the pipe-soil interface and the water content is constant, this behavior is likely due to a soil strength reduction at the high strains near the pipe.

6.0 REFERENCES

1. Anon, "Theoretical and Experimental Investigation of Mud Forces on Offshore Pipelines", Ernest L. Kistler & Associates, Inc., Report No. 2016; Phase I Final Report on AGA Project PR-149-113, August 1981.

2. H.S. Stevenson, "Vane Shear Determination of the Viscoelastic Shear Modulus of Submarine Sediments", M.S. Thesis, Civil Engineering Dept., Texas A&M University, December 1973.

3. J. Marti, "Lateral Loads Exerted on Offshore Piles by Subbottom Movements", Ph.D. Dissertation, Civil Engineering Dept., Texas A&M University, May 1976.

4. M. Riggins, "The Viscoelastic Characterization of Marine Sediment in Large-Scale Simple Shear," Ph.D. Dissertation, Civil Engineering Dept., Texas A&M University, May 1981.

5. R.A. Schapery and M. Riggins, "Development of Cyclic Nonlinear Viscoelastic Constitutive Equations for Submarine Sediment", In Numerical Models in Geomechanics, R. Dungar, G.N. Pande and J.A. Studer, Eds., A.A. Balkema/Rotterdam, 1982, pp. 172-182.

6. D. Broek, Elementary Fracture Mechanics, Third Revised Ed., Martinus-Nijhoff Pubs., 1982.

7. J.K. Mitchell, Fundamentals of Soil Behavior, John Wiley & Sons Inc., 1976.

8. R.F. Scott, Principles of Soil Mechanics, Addison-Wesley Pub. Co., 1963.

9. I.S. Sokolnikoff, Mathematical Theory of Elasticity, McGraw-Hill, 1956.

10. M.A. Biot, Mechanics of Incremental Deformations, Wiley & Sons, 1965.

11. R.A. Schapery, "On Viscoelastic Deformation and Failure Behavior of Composite Materials with Distributed Flaws", Pub. in 1981 Advances in Aerospace Structures and Materials, Pub. No. AD-01, S.S. Wang and W.J. Renton, Eds., ASME, 1981, pp. 5-20.

12. R.A. Schapery, "Correspondence Principles and a Generalized J Integral for Large Deformation and Fracture Analysis of Viscoelastic Media", Int. J. Fracture, July, 1984.

13. M.D. Greenberg, Foundations of Applied Mathematics, Prentice-Hall, 1978.

14. R.J. Roark, Formulas for Stress and Strain, McGraw-Hill Book Co., 1938.

Parameter Survey
Mud Forces on Offshore Pipelines

In the subject program (PR-149-113), a dimensional analysis is being performed which will be used to guide test parameter selection so that laboratory tests will be indicative of actual field conditions. Your assistance is requested in providing ranges of parameters listed below which are of interest to your company. Please respond to as many as you can, leaving blank those you do not have information on.

Pipe Parameters (List OD's of interest and corresponding ranges of parameters.)

OD* (in)	Range of** Specific Gravity	Range of*** Trench Depth (ft)	Range of Water Depths (ft)
22	1.25 - 1.4	-2 to 0	700-500
8	1.20 - 1.4	-1 to 0	200-300
10	1.20 - 1.4	3 to 5	100-200
14	1.20 - 1.4	3 to 5	100-200
8	1.20 - 1.4	3 to 5	100-200
24	1.25 - 1.4	-2 to 0	500-350

*Including weight coating.
**Relative to sea water at 64.0 lb/ft^3.
***Relative to top of pipeline.

Soil Parameters (list ranges of parameters)

Undrained Shear Strength (lb/in^2)	0.5 to 3.5
Unit Weight (lb/ft^3)	98 to 120
Mudflow Widths (ft)	____ to ____
Mudflow Velocity (ft/min)	____ to ____

Mudflow Types (Please describe below any mudflow features you are aware of, e.g. collapse depressions, gullies, etc., which have led to actual failures.)

Parameter Survey
Mud Forces on Offshore Pipelines

In the subject program (PR-149-113), a dimensional analysis is being performed which will be used to guide test parameter selection so that laboratory tests will be indicative of actual field conditions. Your assistance is requested in providing ranges of parameters listed below which are of interest to your company. Please respond to as many as you can, leaving blank those you do not have information on.

Pipe Parameters (List OD's of interest and corresponding ranges of parameters.)

OD* (in)	Range of** Specific Gravity	Range of*** Trench Depth (ft)	Range of Water Depths (ft)
* 12 3/4"	1.15 to 1.20	0' to 10'	150' to 250'

* 12 3/4" O.D. x .500" W.T. Pipe with 14 mils of fusion bond coating had a Specific Gravity of 1.15 in salt water.

*Including weight coating.
**Relative to sea water at 64.0 lb/ft^3.
***Relative to top of pipeline.

Soil Parameters (list ranges of parameters)

Undrained Shear Strength (lb/in^2)	0.417	to 0.972
Unit Weight (lb/ft^3)	85	to 102
Mudflow Widths (ft)	500	to 2000
Mudflow Velocity (ft/min)	--	to --

Mudflow Types (Please describe below any mudflow features you are aware of, e.g. collapse depressions, gullies, etc., which have led to actual failures.)

Mudslide Area - West Delta 109 to South Pass 77

Parameter Survey
Mud Forces on Offshore Pipelines

In the subject program (PR-149-113), a dimensional analysis is being performed which will be used to guide test parameter selection so that laboratory tests will be indicative of actual field conditions. Your assistance is requested in providing ranges of parameters listed below which are of interest to your company. Please respond to as many as you can, leaving blank those you do not have information on.

Pipe Parameters (List OD's of interest and corresponding ranges of parameters.)

OD* (in)	Range of** Specific Gravity	Range of*** Trench Depth (ft)	Range of Water Depths (ft)
11.0	1.1 - 1.3	Untrenched to 3' of cover	0 - 1000
12.75	1.1 - 1.3	Untrenched to 3' of cover	0 - 1000
15.75	1.3 - 1.8	Untrenched to 3' of cover	0 - 1000
18.3	1.1 - 1.4	Untrenched to 3' of cover	0 - 1000

*Including weight coating.
**Relative to sea water at 64.0 lb/ft^3.
***Relative to top of pipeline.

Soil Parameters (list ranges of parameters)

Undrained Shear Strength (lb/in^2)	0.24 to	1.0
Unit Weight (lb/ft^3)	75 to	120
Mudflow Widths (ft)	200 to	4000
Mudflow Velocity (ft/min)	____ to	____

Mudflow Types (Please describe below any mudflow features you are aware of, e.g. collapse depressions, gullies, etc., which have led to actual failures.)

Parameter Survey
Mud Forces on Offshore Pipelines

In the subject program (PR-149-113), a dimensional analysis is being performed which will be used to guide test parameter selection so that laboratory tests will be indicative of actual field conditions. Your assistance is requested in providing ranges of parameters listed below which are of interest to your company. Please respond to as many as you can, leaving blank those you do not have information on.

Pipe Parameters (List OD's of interest and corresponding ranges of parameters.)

OD* (in)	Range of** Specific Gravity	Range of*** Trench Depth (ft)	Range of Water Depths (ft)
24" (3½")	1.3	0' – 2'	200' to 400'
24" (2¾")	1.2	0' – 2'	200' to 400'
24" (2¾")	1.2	0' – 4'	150' to 200'
10¾" (0")	1.3	0' – 1'	200' to 400'
10¾" (0)	1.2	0' – 1'	200' to 400'
10¾" (0")	1.2	0' – 4'	150' to 200'

*Including weight coating.
**Relative to sea water at 64.0 lb/ft^3.
***Relative to top of pipeline.

Soil Parameters (list ranges of parameters)

Undrained (Vane) Shear Strength (lb/in^2)	50 lb/ft^2 to 100 lb/ft^2
Unit Weight (lb/ft^3)	85 lb/ft^3 to 90 lb/ft^3
Mudflow Widths (ft)	300' to ____
Mudflow Velocity (ft/min)	____ to ____

Mudflow Types (Please describe below any mudflow features you are aware of, e.g. collapse depressions, gullies, etc., which have led to actual failures.)

Parameter Survey
Mud Forces on Offshore Pipelines

In the subject program (PR-149-113), a dimensional analysis is being performed which will be used to guide test parameter selection so that laboratory tests will be indicative of actual field conditions. Your assistance is requested in providing ranges of parameters listed below which are of interest to your company. Please respond to as many as you can, leaving blank those you do not have information on.

Pipe Parameters (List OD's of interest and corresponding ranges of parameters.)

	OD* (in)	Range of** Specific Gravity	Range of*** Trench Depth (ft)	Range of Water Depths (ft)
8	10.9375	1.41	0 - 3	100 - 1000
12	15.0625	1.32	0 - 3	100 - 1000
	18.562	1.10		
16	20.562	1.30	0 - 3	100 - 1000
	29.063	1.10		
24	30.063	1.31	0 - 3	100 - 1000
	36.063	1.1		
30	36.063	1.3	0 - 3	100 - 1000
	41.562	1.1		
36	42.813	1.3	0 - 3	100 - 1000

*Including weight coating.
**Relative to sea water at 64.0 lb/ft^3.
***Relative to top of pipeline.

Soil Parameters (list ranges of parameters)

Undrained Shear Strength (lb/in^2)	0.07 to	1.0
Unit Weight (lb/ft^3)	80 to	130
Mudflow Widths (ft)	____ to	____
Mudflow Velocity (ft/min)	____ to	____

Mudflow Types (Please describe below any mudflow features you are aware of, e.g. collapse depressions, gullies, etc., which have led to actual failures.)

Parameter Survey
Mud Forces on Offshore Pipelines

In the subject program (PR-149-113), a dimensional analysis is being performed which will be used to guide test parameter selection so that laboratory tests will be indicative of actual field conditions. Your assistance is requested in providing ranges of parameters listed below which are of interest to your company. Please respond to as many as you can, leaving blank those you do not have information on.

Pipe Parameters (List OD's of interest and corresponding ranges of parameters.)

OD* (in)	Range of** Specific Gravity	Range of*** Trench Depth (ft)	Range of Water Depths (ft)
$10\frac{3}{4}$	1.30-1.35	0 – 8	50-1000
14	"	"	"
24	"	"	50 – 500
29	"	"	"
36	"	"	50 – 250
$8\frac{5}{8}$	"	"	50 – 1000

*Including weight coating.
**Relative to sea water at 64.0 lb/ft^3.
***Relative to top of pipeline.

Soil Parameters (list ranges of parameters) – NO INFORMATION

Undrained Shear Strength (lb/in^2)	_____ to _____
Unit Weight (lb/ft^3)	_____ to _____
Mudflow Widths (ft)	_____ to _____
Mudflow Velocity (ft/min)	_____ to _____

Mudflow Types (Please describe below any mudflow features you are aware of, e.g. collapse depressions, gullies, etc., which have led to actual failures.)

NONE AS OF THIS DATE

Parameter Survey
Mud Forces on Offshore Pipelines

In the subject program (PR-149-113), a dimensional analysis is being performed which will be used to guide test parameter selection so that laboratory tests will be indicative of actual field conditions. Your assistance is requested in providing ranges of parameters listed below which are of interest to your company. Please respond to as many as you can, leaving blank those you do not have information on.

Pipe Parameters (List OD's of interest and corresponding ranges of parameters.)

OD* (in)	Range of** Specific Gravity	Range of*** Trench Depth (ft)	Range of Water Depths (ft)
12	1.15 to 1.25	4'	150 to 350'
16	1.10 to 1.25	4½'	150 to 350
24	1.1 to 1.25	6'	100 to 400
30"	1.1 to 1.25	6½	100 to 450
36	1.1 to 1.25	8	100 to 450

*Including weight coating.
**Relative to sea water at 64.0 lb/ft^3.
***Relative to top of pipeline.

Soil Parameters (list ranges of parameters)

Undrained Shear Strength (lb/in^2)	.5	to 20
Unit Weight (lb/ft^3) (WET)	90	to 120
Mudflow Widths (ft)	50	to 3000
Mudflow Velocity (ft/min)	10	to 200

Mudflow Types (Please describe below any mudflow features you are aware of, e.g. collapse depressions, gullies, etc., which have led to actual failures.)

APPENDIX 2

Estimate of Mudline Pressure Changes

The pressure p_w^* in Eqs. (4.46) and (4.49) is negligible in many cases; conditions under which this simplification may be used are established in this appendix. We shall consider a two-dimensional problem of plane strain, in which $u_3 = 0$ and p_w^*, u_1, and u_2 are independent of x_3. Thus, from Eq. (4.15),

$$-\frac{\partial p_w^*}{\partial x_1} = \frac{\gamma_w}{g}\frac{\partial^2 u_1}{\partial t^2} , \tag{A.1a}$$

$$-\frac{\partial p_w^*}{\partial x_2} = \frac{\gamma_w}{g}\frac{\partial^2 u_2}{\partial t^2} . \tag{A.1b}$$

The incompressibility condition,

$$\partial u_1/\partial x_1 + \partial u_2/\partial x_2 = 0 , \tag{A.2}$$

gives the third field equation for the three dependent variables p_w^*, u_1, and u_2.

As a result of pipe and mud movement, waves are produced in the water which influence p_w^* in the interface condition, Eq. (4.46). We want to estimate the magnitude of the disturbance as a function of h_w, D, and pipe velocity. In general, the problem is a difficult one. However, we believe the essential features are taken into account by predicting the effect of a mudline displacement given as an infinitely

long sinusoidal, traveling wavetrain. The wave length is assumed to be the pipe diameter D (characteristic disturbance length), and the speed is that of the pipe, V_1. By predicting the effect of this disturbance, which is infinite in extent along the mudline, we should obtain an upper bound on the magnitude of p_w^* except possibly when the water is shallow and most of the pipe is above the mudline.

Water pressure and displacement wavetrain solutions which satisfy Eqs. (A.1) and (A.2) and contain two constants of integration A_1 and A_2 are

$$p_w^* = V_N^2 \gamma_w (-A_1 e^{-\ell x_2} + A_2 e^{\ell x_2}) \cos \phi \ , \tag{A.3}$$

$$u_1 = (-A_1 e^{-\ell x_2} + A_2 e^{\ell x_2}) \sin \phi \ , \tag{A.4}$$

$$u_2 = (A_1 e^{-\ell x_2} + A_2 e^{\ell x_2}) \cos \phi \ , \tag{A.5}$$

and from Eq. (4.16),

$$p_w = p_w^* + \gamma_w u_2 = \gamma_w [(1-V_N^2) A_1 e^{-\ell x_2} + (1+V_N^2) A_2 e^{\ell x_2}] \cos \phi \ , \tag{A.6}$$

where we have introduced the definitions,

$$\phi \equiv V_1 t/D - \ell x_1 \tag{A.7}$$

$$V_N \equiv V_1 / V_\infty \tag{A.8}$$

$$V_\infty \equiv (gD/2\pi)^{1/2} \tag{A.9}$$

$$\ell \equiv 2\pi/D \ . \tag{A.10}$$

The dimensionless ratio V_N is a "normalized" speed of disturbance, and is equal to the horizontal pipe speed divided by the speed of free surface waves, V_∞, of wave length D in infinitely deep water.

Denote the vertical displacement amplitude of disturbance at the mudline by U_2. Setting $x_2 = 0$ in Eq. (A.5) provides one condition for evaluating the constants A_1 and A_2:

$$A_1 + A_2 = U_2 \ . \tag{A.11}$$

The second condition is that the water surface, $x_2 = -h_w$, is stress free, $p_w = 0$ (except for a possible uniform initial pressure P_o); from Eq. (A.6),

$$(1 - V_N^2) e^{\ell h_w} A_1 + (1 + V_N^2) e^{-\ell h_w} A_2 = 0 \ , \tag{A.12}$$

and the solution of Eqs. (A.11) and (A.12) is

$$A_1 = \frac{U_2 (1 + V_N^2)(1 - V_{NR}^2)}{2(V_N^2 - V_{NR}^2)} \ , \quad A_2 = \frac{U_2 (1 - V_N^2)(1 + V_{NR}^2)}{2(V_{NR}^2 - V_N^2)} \ , \tag{A.13}$$

where

$$V_{NR} \equiv [\tanh(2\pi h_w/D)]^{1/2} \ . \tag{A.14}$$

It can be shown that V_{NR} is the ratio of the speed of a free surface wave in water of depth h_w (for which the water wave length is D and the bottom is rigid and flat) to that of a wave in infinitely deep water having the same wave length.

The water pressure acting on the mudline is given by Eq. (A.6) evaluated at $x_2 = 0$, and may be written in the form

$$p_w = P_w \cos \phi \ , \tag{A.15a}$$

where the amplitude P_w is

$$P_w = \gamma_w U_2 \left[\frac{1 - V_N^4}{1 - (V_N^2/V_{NR}^2)} \right] . \qquad \text{(A.15b)}$$

Another response quantity that may be of interest is the vertical displacement wave at the water surface, $x_2 = -h_w$,

$$u_2 = -U_w \cos \phi \ , \qquad \text{(A.16a)}$$

with amplitude

$$U_w = U_2 \frac{(1 - V_{NR}^4)^{1/2}}{\left[1 - (V_N^2/V_{NR}^2)\right]} \frac{V_N^2}{V_{NR}^2} . \qquad \text{(A.16b)}$$

The negative sign in Eq. (A.16a) implies the water surface wave is 180° out of phase with the mudline wave when $V_N < V_{NR}$.

Let us consider the physical significance of Eqs. (A.15) and (A.16). Observe that $P_w \to \infty$ and $U_w \to \infty$ when $V_N \to V_{NR}$; this behavior corresponds to a resonance in the sense that a small disturbance (U_2) is greatly magnified. When $V_N = V_{NR}$, the pipe speed is equal to the speed of a free surface wave for the given water depth. This free surface wave speed never exceeds that for very deep water since $0 \leq V_{NR} \leq 1$, according to Eq. (A.14); $V_{NR} \approx 0$ for shallow water ($h_w << D$) and $V_{NR} \approx 1$ for deep water ($h_w >> D$).

If $P_w \approx \gamma_w U_2$, the interface condition, Eq. (4.46), reduces to $s_{22} = -\gamma_w u_2$; this corresponds to the situation in which pressure due to inertia of the water (p_w^*) is negligible. In this case p_w^* can be neglected in the equivalent soil boundary condition, Eq. (4.49), at the

soil-water interface.

As a simple example consider the deep-water case, $V_{NR} = 1$. Then, from Eq. (A.15b),

$$P_w = \gamma_w U_2 (1+V_N^2) . \qquad (A.17)$$

If we require P_w to be within 10% of $\gamma_w U_2$, this result and Eq. (A.9) yield

$$V_1 \leq V_\infty/\sqrt{10} = (gD/20\pi)^{1/2} , \qquad (A.18a)$$

or, equivalently, in diameters per unit time,

$$V_1/D \leq V_\infty/\sqrt{10}D = (g/20\pi D)^{1/2} . \qquad (A.18b)$$

If, for example, D = 1 inch, the speed of the mudline disturbance is limited to

$$V_1 \leq 0.21 \text{ fps} \quad \text{or} \quad V_1/D \leq 2.5 \text{ dia/sec.} \qquad (A.19a)$$

and if D = 1 foot,

$$V_1 \leq 0.72 \text{ fps} \quad \text{or} \quad V_1/D \leq 0.72 \text{ dia/sec.} \qquad (A.19b)$$

The upper speed limit (for which $P_w \approx \gamma_w U_2$) is reduced with shallow water. Figure A.1 illustrates this point, in which $P_w/\gamma_w U_2$, Eq. (A.15b), V_{NR}^2, Eq. (A.14), and U_w/U_2, Eq. (A.16b), are plotted against the nondimensional water depth h_w/D. Clearly, for the present linear theory to be valid, we require the amplitude U_2 to be small compared to h_w; therefore, as a practical matter, especially for shallow water, the pipe recess depth, h (cf. Fig. 4.1) has to be large enough to not create excessive water displacements.

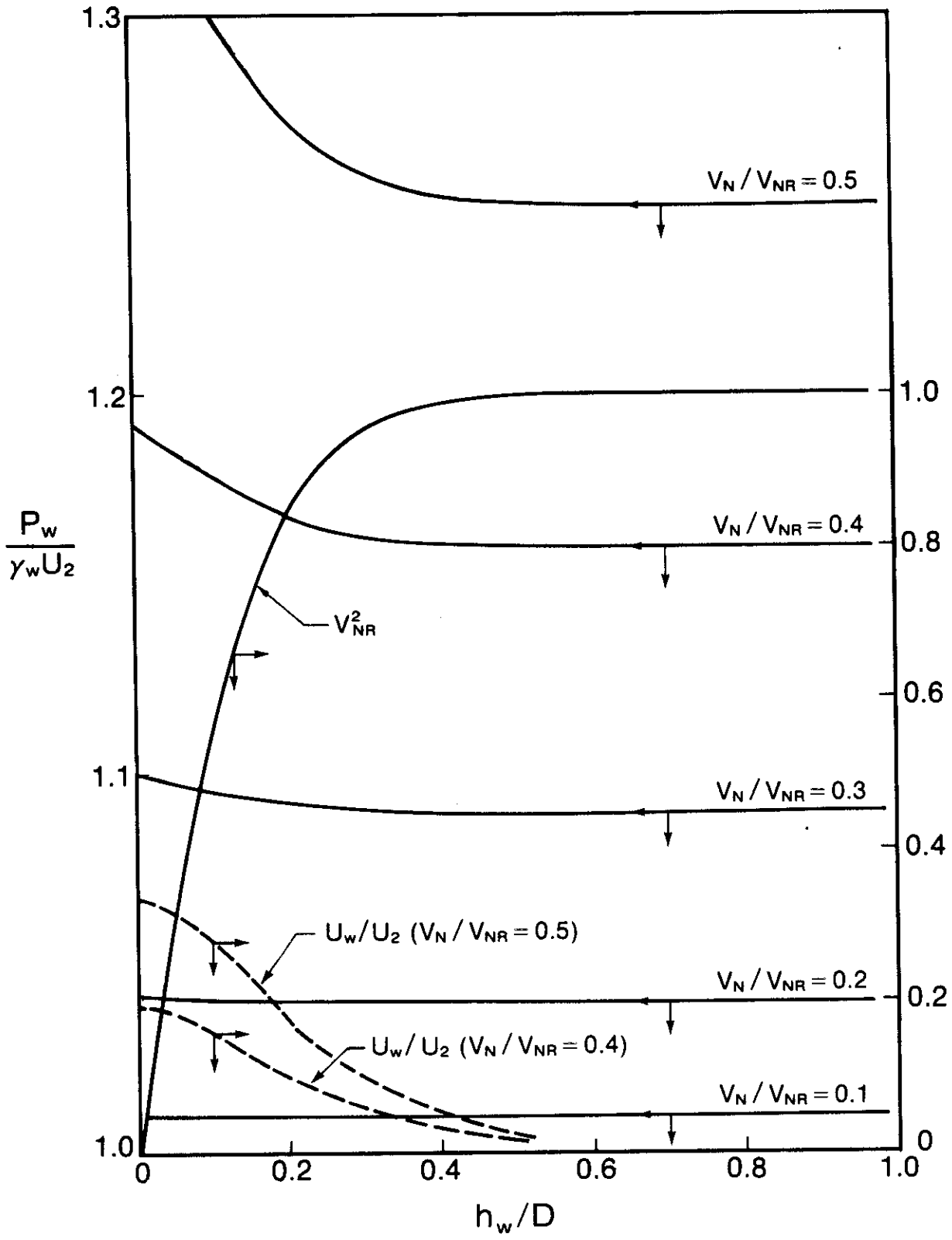

Figure A.1 Water Response to Traveling Wave at Mudline

Figure A.1 shows that except for extremely shallow water, $h_w/D < 0.2$ (say), the deep water solution for mudline pressure, Eq. (A.17), can be used to estimate the departure from the quasi-static bottom pressure solution, $P_w = \gamma_w U_2$.

APPENDIX 3

Circular Vane Analysis

The use of experimental measurements of torque and angle of rotation with bladed and circular vanes to obtain strength-strain rate relationships has been analyzed elsewhere [1,2]. The soil between blades was assumed to behave as a rigid body, and therefore both geometries were analyzed as rotating, rigid, circular pipes, Figure A.2

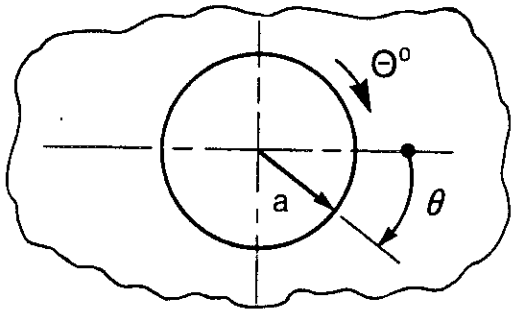

Figure A.2 Circular Vane

using standard theory. Here, we shall reproduce the theoretical analysis, but now employing the notation and theory of Section 4. Specifically, a relationship between soil shear stress and pseudo strain at the circular vane surface, r = a, is derived. This result is used in Section 4.4.4 to derive generalized force coefficients for a nonlinear viscous soil.

It is assumed the vane's length is very large compared to its diameter and that the surrounding soil mass (assumed homogeneous and isotropic) is great enough that there are no significant boundary effects. The latter condition is met in all of our laboratory tests. However, there may be small end effects because of the finite vane length; we suppose that any significant corrections have been made to the data so that the experimental results in Section 3 correspond to the

present mathematical model of an infinitely long circular vane. The experimental values are not needed for the theoretical analysis in Section 4.4.4, but they are required to obtain the appropriate generalized force coefficients which can be compared with theoretical values. Turning to the analysis of the rotating vane, we find that the governing equations for this problem may be satisfied if the only nonzero soil displacement is the tangential displacement, u_θ, and it depends at most on the independent variables of radius, r, and time, t. All pseudo strains in Eq. (4.129) vanish except for $e^o_{r\theta}$, which becomes

$$e^o_{r\theta} = \partial \hat{u}^o_\theta / \partial \hat{r} - \hat{u}^o_\theta / \hat{r} \quad . \tag{A.20}$$

The pseudo effective shear strain, Eq. (4.132), reduces to

$$e^o_e = 2e^o_{r\theta} \ , \tag{A.21}$$

where we have for simplicity assumed that the direction of vane rotation is such that $e^o_{r\theta} \geq 0$. In turn, after expressing the constitutive relationship, Eq. (4.35), in terms of cylindrical coordinate notation, we obtain the tangential shear stress

$$\sigma_{r\theta} = 2G_R (e^o_e)^{N-1} e^o_{r\theta} \ , \tag{A.22}$$

where, in keeping with the analysis in Section 4.4, the damage coefficient ψ has been assumed constant and absorbed into the modulus G_R. All other stresses are zero. Let τ_v be the shear stress acting along the vane surface $\hat{r} = 1$. Then by considering moment equilibrium of a soil mass between $\hat{r} = 1$ and any radius $\hat{r} > 1$, it is found that

$$\sigma_{r\theta} = \tau_v \hat{r}^{-2} \quad . \tag{A.23}$$

Substitute Eqs. (A.20), (A.21), and (A.23) into Eq. (A.22), and then solve the resulting differential equation,

$$\tau_v \hat{r}^{-2} = 2^N G_R \left[\partial \hat{u}_\theta^o/\partial \hat{r} - \hat{u}_\theta^o/\hat{r}\right]^N \quad . \tag{A.24}$$

The solution may be written in the form

$$\hat{u}_\theta^o = \frac{\theta_v^o}{2} \hat{r}^{-p} \quad , \tag{A.25a}$$

where

$$p = \frac{2}{N} - 1 \quad , \tag{A.25b}$$

and θ_v^o is the pseudo vane rotation. This rotation was introduced by recognizing that without slip at the vane-soil interface, $u_\theta(a,t) = a\theta_v$, and therefore $u_\theta^o(a,t) = a\theta_v^o$; furthermore, $\hat{u}_\theta^o \equiv u_\theta^o/D$. Equations (A.20) and (A.25a) yield the pseudo shear strain,

$$e_{r\theta}^o = -\frac{\theta_v^o}{N} \hat{r}^{-p-1} \quad . \tag{A.26}$$

Next, evaluate Eq. (A.24) at $\hat{r} = 1$ and find the primary result of interest

$$\tau_v = G_R(\gamma_v^o)^N \quad , \tag{A.27a}$$

where

$$\gamma_v^o = \left|2\theta_v^o/N\right| \tag{A.27b}$$

is the "engineering" pseudo shear strain, $2e_{r\theta}^o$, at $\hat{r} = 1$. The absolute value notation, $|\ |$, is used in Eq. (A.27b) because θ_v^o has to be negative if $e_{r\theta}^o$ is to be positive (as assumed). The condition $\theta_v^o < 0$ is satisfied, for example, if the vane is rotated counterclockwise at a constant rate. Had the condition $e_{r\theta}^o > 0$ not been imposed, the results would be the same except stress would be negative when pseudo strain is negative.

APPENDIX 4

Axial Flow Analysis

It is possible to derive an exact, closed-form solution to the problem in which the relative movement between pipe and soil is parallel to the pipe axis when $h/D = \infty$ and $h/D = 1/2$. We shall consider the former case first, and predict the generalized drag factor, g_3. The drag factor for $h/D = 1/2$ is then easily argued to be one-half of that for the deeply embedded pipe.

All of the governing equations are found to be satisfied using soil displacements $u_r = u_\theta = 0$ (cf. Fig. 4.4) and axial displacement $u_z = u_z(r,t)$. From Eq. (4.129),

$$e^o_{rz} = \partial \hat{u}^o_z / \partial \hat{r} \quad , \tag{A.28}$$

and all other strains are zero. The pseudo effective shear strain, Eq. (4.132), becomes

$$e^o_e = 2e^o_{rz} \quad , \tag{A.29}$$

in which, for simplicity, the direction of axial flow is assumed to be such that $e^o_{rz} > 0$. Using cylindrical coordinate notation with the variables in Eq. (4.35) for the stresses, the axial shear stress becomes

$$\sigma_{rz} = 2G_R (e^o_e)^{N-1} e^o_{rz} \quad , \tag{A.30}$$

where, as before, the constant damage factor ψ is absorbed into the modulus G_R. All other stresses are zero. The only equilibrium equation which is not automatically satisfied is that for the axial direction. Its solution may be obtained directly by considering axial equilibrium of a cylindrical mass of soil between $\hat{r} = 1$ and any $\hat{r} > 1$; thus,

$$\sigma_{rz} = \tau_3 \hat{r}^{-1} \quad , \tag{A.31}$$

where $\tau_3 = \sigma_{rz}(a,t)$ is the shear stress along the pipe-soil interface.

Substitute Eqs. (A.28), (A.29), and (A.31) into (A.30) to obtain a differential equation for $\hat{u}_z^o$,

$$\tau_3 \hat{r}^{-1} = 2^N G_R (\partial \hat{u}_z^o / \partial \hat{r})^N \quad . \tag{A.32}$$

Let us introduce the no-slip condition, $u_z = U_3$ at $\hat{r} = 1$, where U_3 is the axial pipe displacement; in terms of dimensionless pseudo displacements, this condition for $\hat{r} = 1$ is $\hat{u}_z^o = \hat{U}_3^o$. The solution to Eq. (A.32) may then be written as

$$\hat{u}_z^o = \hat{U}_3^o \hat{r}^{-p} \quad , \tag{A.33a}$$

where

$$p = \frac{1}{N} - 1 \quad , \tag{A.33b}$$

which is a positive exponent since $0 \leq N < 1$. The axial pseudo shear strain follows from Eqs. (A.28) and (A.33a),

$$e_{rz}^o = -p \hat{U}_3^o \hat{r}^{-p-1} \quad , \tag{A.34}$$

which shows that $\hat{U}_3^o < 0$ if e_{rz}^o is to be positive (as assumed).

The axial shear stress τ_3 at the pipe-soil interface, $\hat{r} = 1$, may be written in a form which is analogous to Eq. (A.27). First, introduce the engineering" pseudo shear strain at $\hat{r} = 1$,

$$\gamma_3^o \equiv 2e_{rz}^o(1,t) \quad . \tag{A.35}$$

Then evaluate Eq. (A.32) at $\hat{r} = 1$ by using Eqs. (A.33)-(A.35) and find

$$\tau_3 = G_R (\gamma_3^o)^N \quad , \tag{A.36a}$$

where

$$\gamma_3^o = 2\left(\frac{1}{N} - 1\right)\left|\hat{U}_3^o\right| \quad . \tag{A.36b}$$

The axial pipe force, F_3, may be obtained directly from Eq. (A.36) since

$$F_3 = -\pi D L \tau_3 \tag{A.37}$$

where $F_3 < 0$ because $\hat{U}_3^o < 0$; note that $\alpha = 180°$, according to Fig. 4.6. The dimensionless force is (cf. Eq. (4.96)),

$$\hat{F}_3 = -\pi(\gamma_3^o)^N = -2^N \pi\left(\frac{1}{N} - 1\right)^N \left|\hat{U}_3^o\right|^N \quad . \tag{A.38}$$

The axial generalized force coefficient, g_3, for a nonlinear viscous soil is of particular interest. For a viscous material,

$$\left|\hat{U}_3^o\right| = t_c V_3 / D \quad , \tag{A.39}$$

where V_3 is the magnitude of the axial pipe velocity (assuming the far-field mud is at rest); this result follows from Eq. (4.111) after using V_3 for the resultant velocity V_R. Equations (4.115)-(4.117) serve to define g_3, which, together with Eqs. (A.36), (A.37), and (A.39) yield

$$g_3 = -\pi(1-N)^N(\dot{\theta}_{vo})^{-N} \quad . \tag{A.40}$$

Recall that $\dot{\theta}_{vo}$ is the vane rotation rate (in radians per unit time) used to measure the soil strength, C_o.

Equation (A.40) is the generalized drag factor for a deeply embedded pipe, $h/D = \infty$. For the case $h/D = 1/2$ the stress, strain, and displacement are the same as for $h/D = \infty$, but they of course apply only to the range $0^o \leq \theta \leq 180°$. That these solutions are valid here may be seen by noting that the only difference in the two problems is the existence of the mudline for $h/D = 1/2$, which is traction free (apart from a possible uniform pressure which has no effect on the assumed

incompressible mud). Because $\sigma_\theta = \sigma_{\theta r} = \sigma_{\theta z} = 0$ for the above solution, the traction-free condition is indeed satisfied. Inasmuch as the axial shear stress along the pipe, τ_3, acts on only the lower half, the axial force and drag factor are one-half of the values in Eqs. (A.37) and (A.40), respectively.

Clearly, g_3 in Eq. (A.40) is negative because e^o_{rz} was taken to be positive. As noted above this choice corresponds to $\alpha = 180°$ in Fig. 4.6. Had we assumed $e^o_{rz} < 0$, the analysis would be for $\alpha = 0$ and the drag factor would be that in Eq. (A.40) but positive.

APPENDIX 5

Theoretical Curves of Generalized Force Coefficients for Various Parameter Values

Notes

- Figures 1-15 are for no gravity effect (GRAV = 0).
- Figures 16-18 show effects of gravity.
- All figures, with exception of Figure 18, are for horizontal movement.
- Figure 18 is for downward vertical movement.

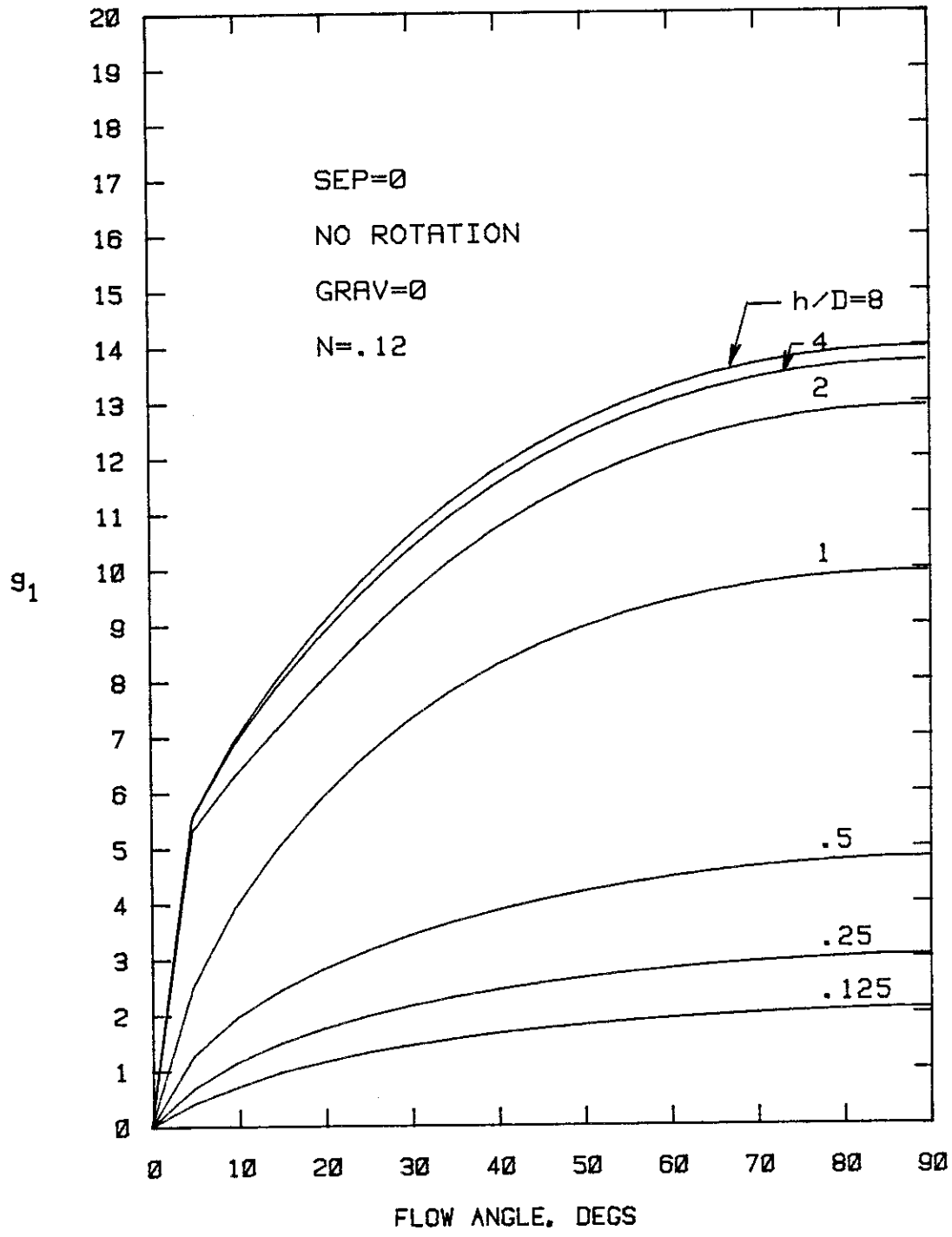
SEP=0
NO ROTATION
GRAV=0
N=.12
h/D=8
4
2
1
.5
.25
.125
g_1
FLOW ANGLE, DEGS
0
10
20
30
40
50
60
70
80
90
0
1
2
3
4
5
6
7
8
9
10
11
12
13
14
15
16
17
18
19
20

Figure 1

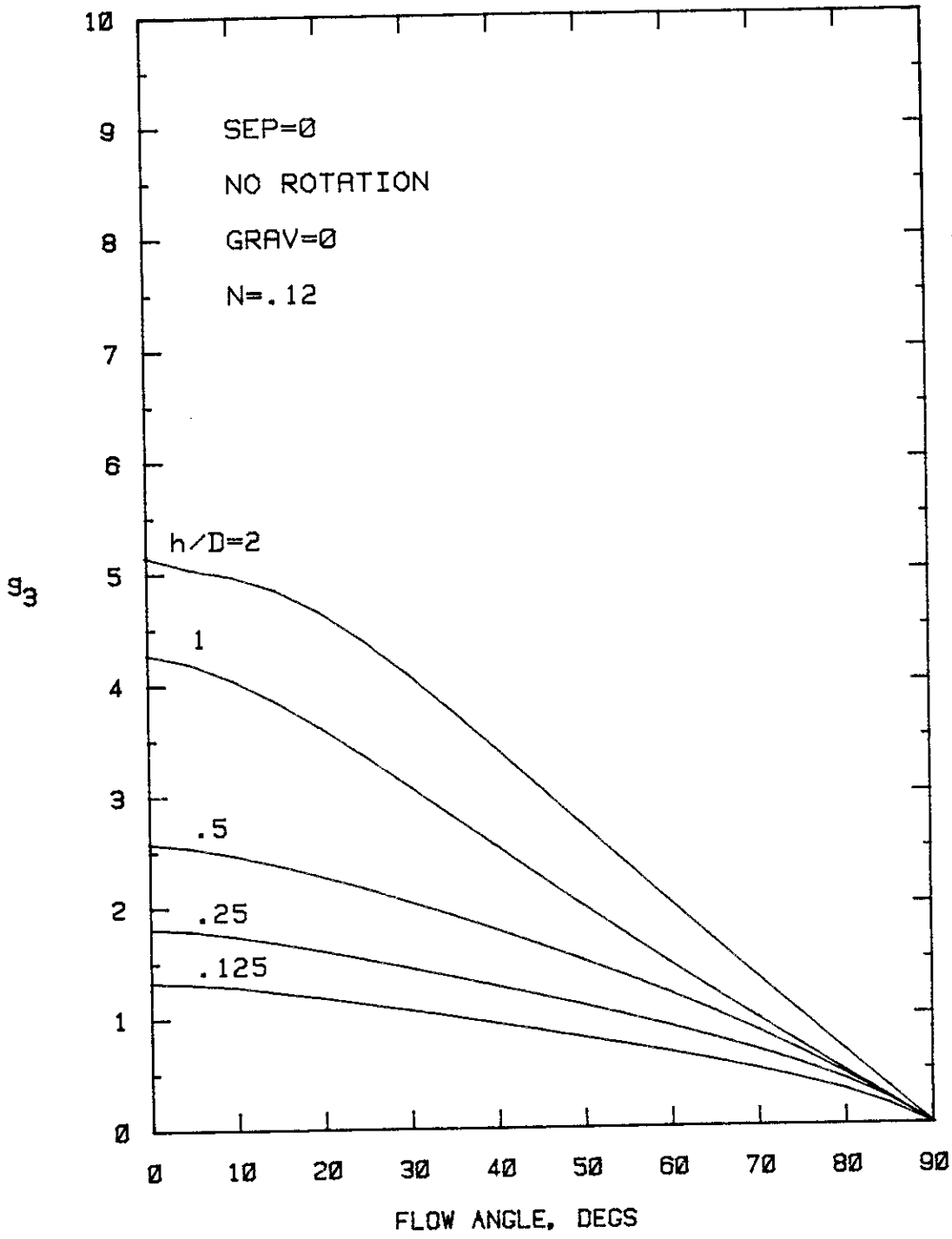
SEP=0
NO ROTATION
GRAV=0
N=.12
h/D=2
1
.5
.25
.125
g_3
0
1
2
3
4
5
6
7
8
9
10
0
10
20
30
40
50
60
70
80
90
FLOW ANGLE, DEGS

Figure 2

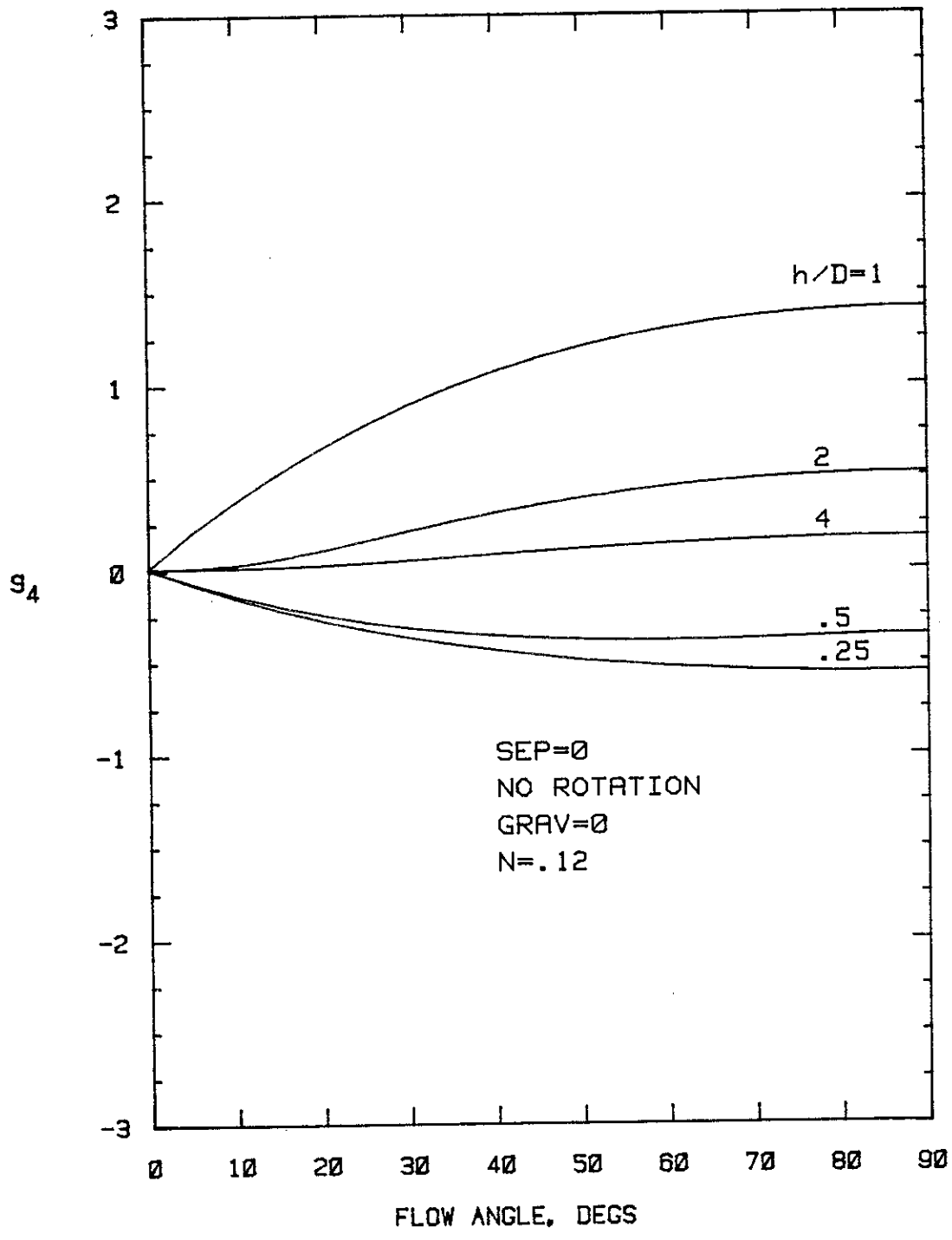
3
2
1
0
-1
-2
-3
g_4
h/D=1
2
4
.5
.25
SEP=0
NO ROTATION
GRAV=0
N=.12
0
10
20
30
40
50
60
70
80
90
FLOW ANGLE, DEGS

Figure 3

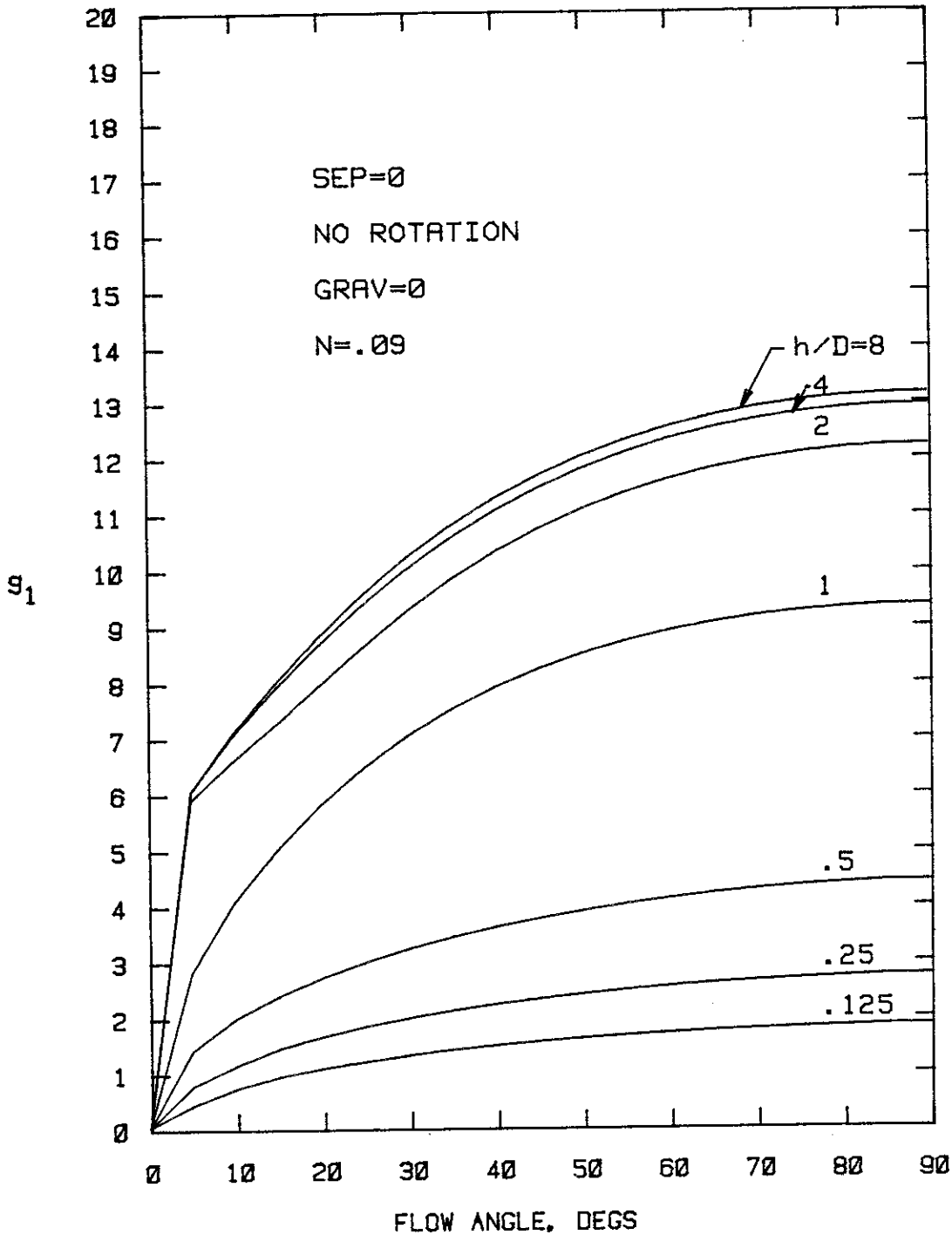
SEP=0
NO ROTATION
GRAV=0
N=.09
h/D=8
4
2
1
.5
.25
.125
g_1
FLOW ANGLE, DEGS
0
1
2
3
4
5
6
7
8
9
10
11
12
13
14
15
16
17
18
19
20
0
10
20
30
40
50
60
70
80
90

Figure 4

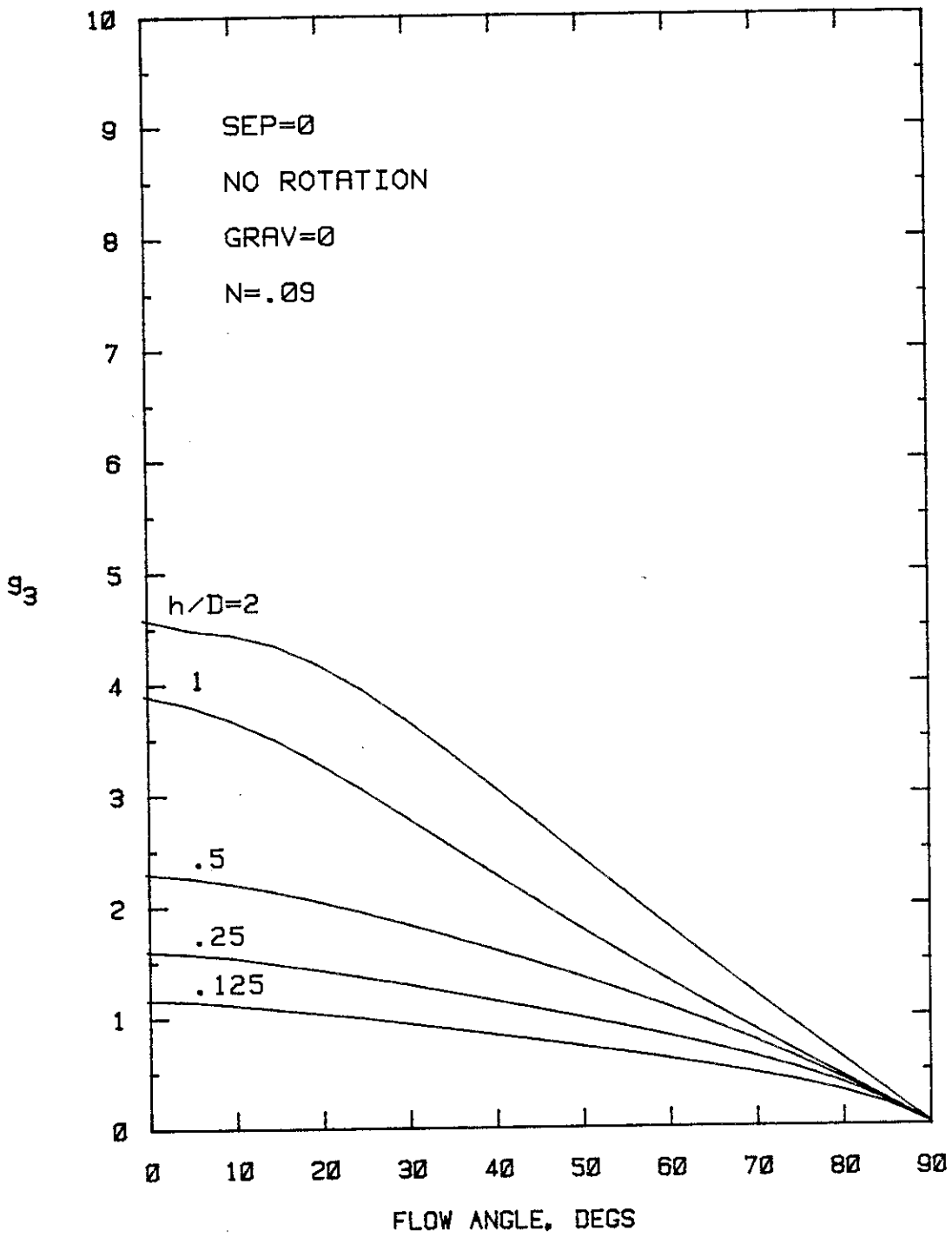
10
9
8
7
6
5
4
3
2
1
0
SEP=0
NO ROTATION
GRAV=0
N=.09
g_3
h/D=2
1
.5
.25
.125
0
10
20
30
40
50
60
70
80
90
FLOW ANGLE, DEGS

Figure 5

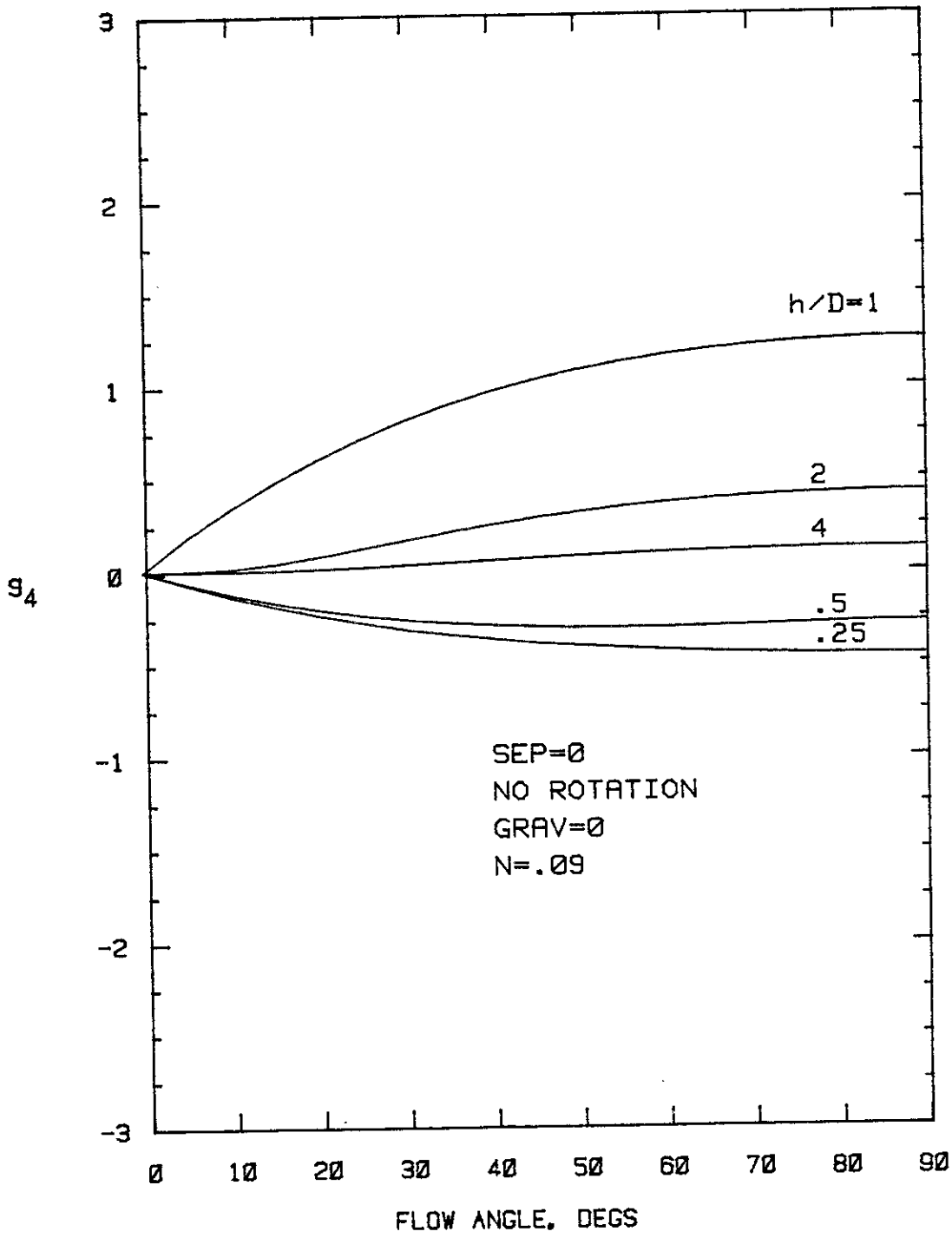
3
2
1
0
-1
-2
-3
g_4
h/D=1
2
4
.5
.25
SEP=0
NO ROTATION
GRAV=0
N=.09
0
10
20
30
40
50
60
70
80
90
FLOW ANGLE, DEGS

Figure 6

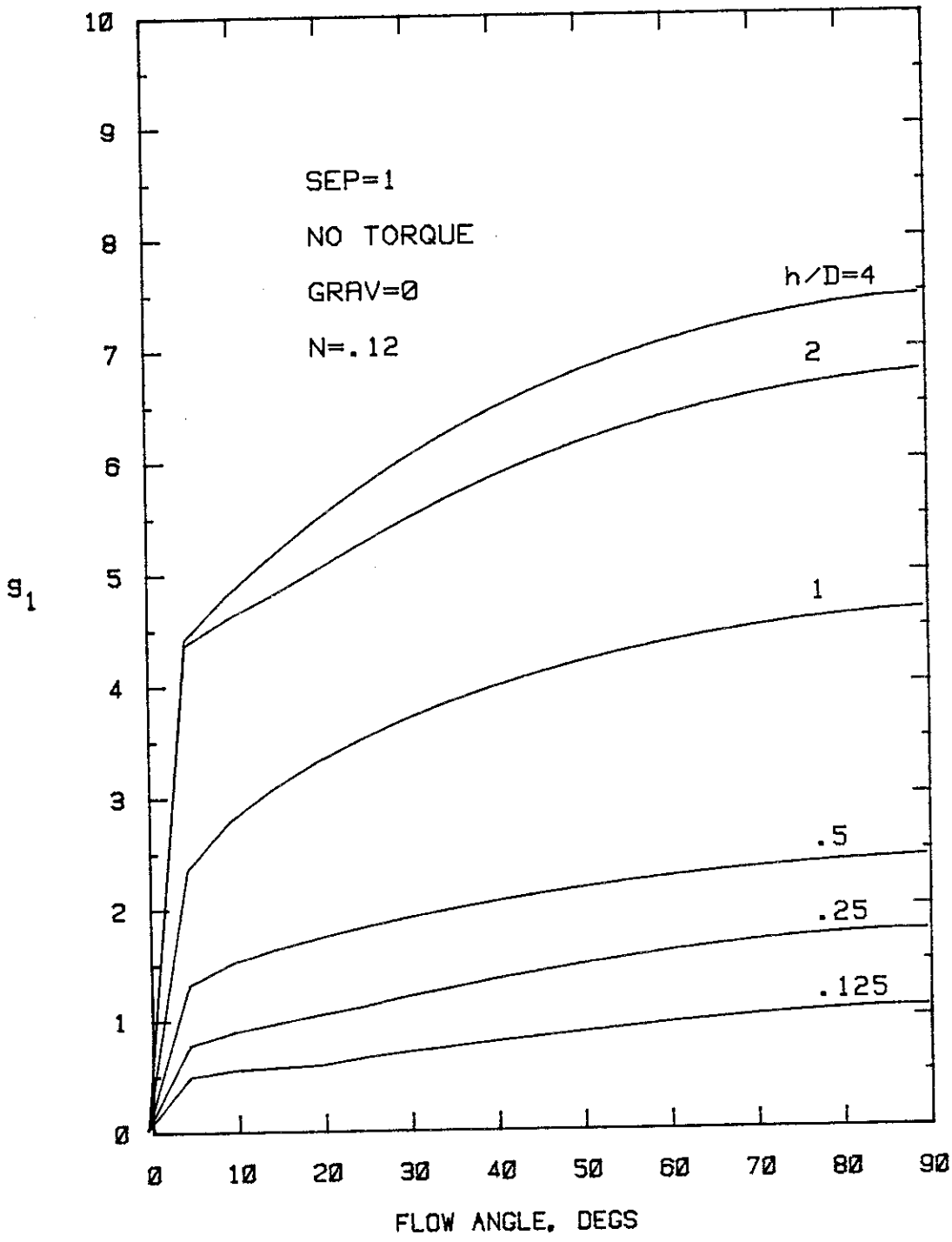
SEP=1
NO TORQUE
GRAV=0
N=.12
h/D=4
2
1
.5
.25
.125
g_1
0
1
2
3
4
5
6
7
8
9
10
0
10
20
30
40
50
60
70
80
90
FLOW ANGLE, DEGS

Figure 7

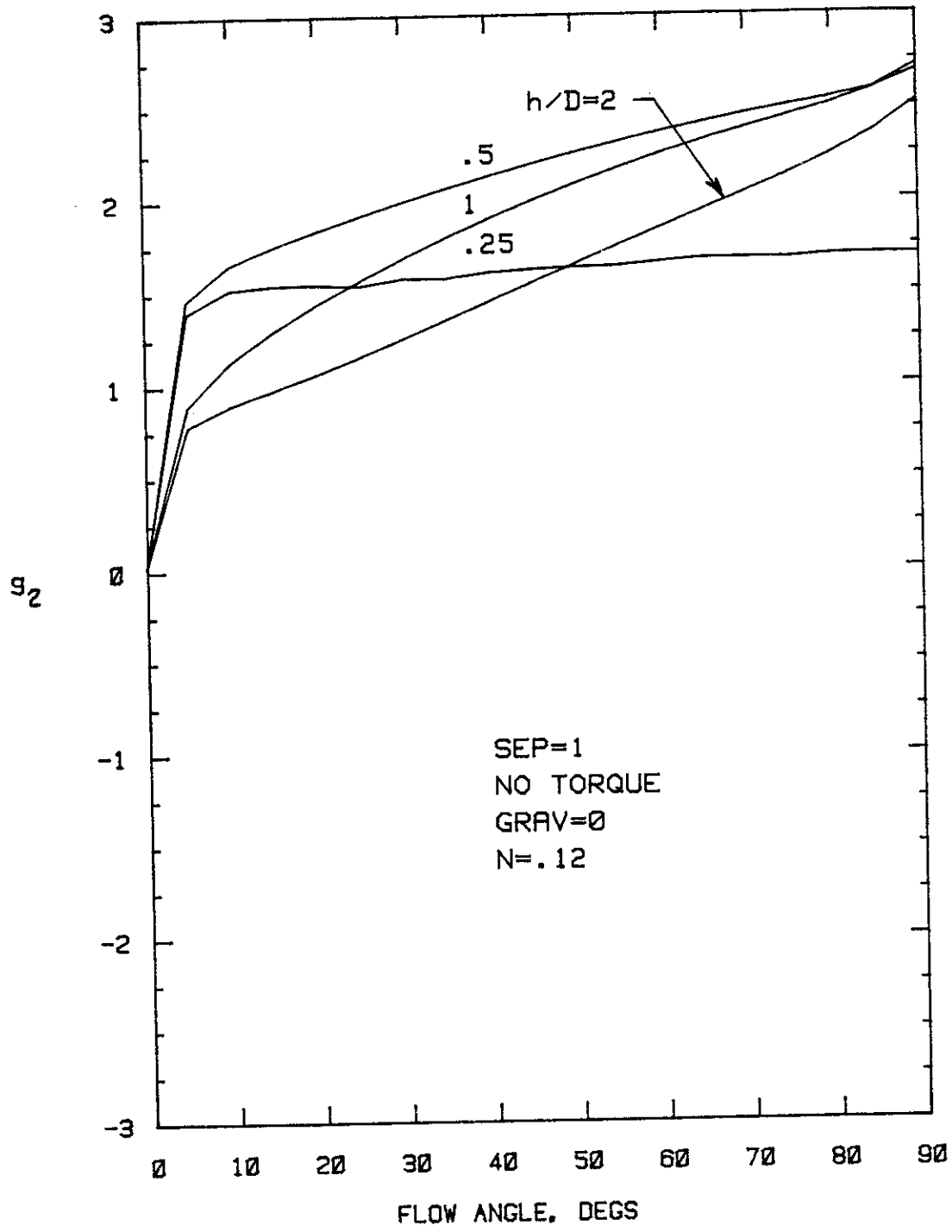
3
2
1
0
-1
-2
-3
g_2
h/D=2
.5
1
.25
SEP=1
NO TORQUE
GRAV=0
N=.12
0
10
20
30
40
50
60
70
80
90
FLOW ANGLE, DEGS

Figure 8

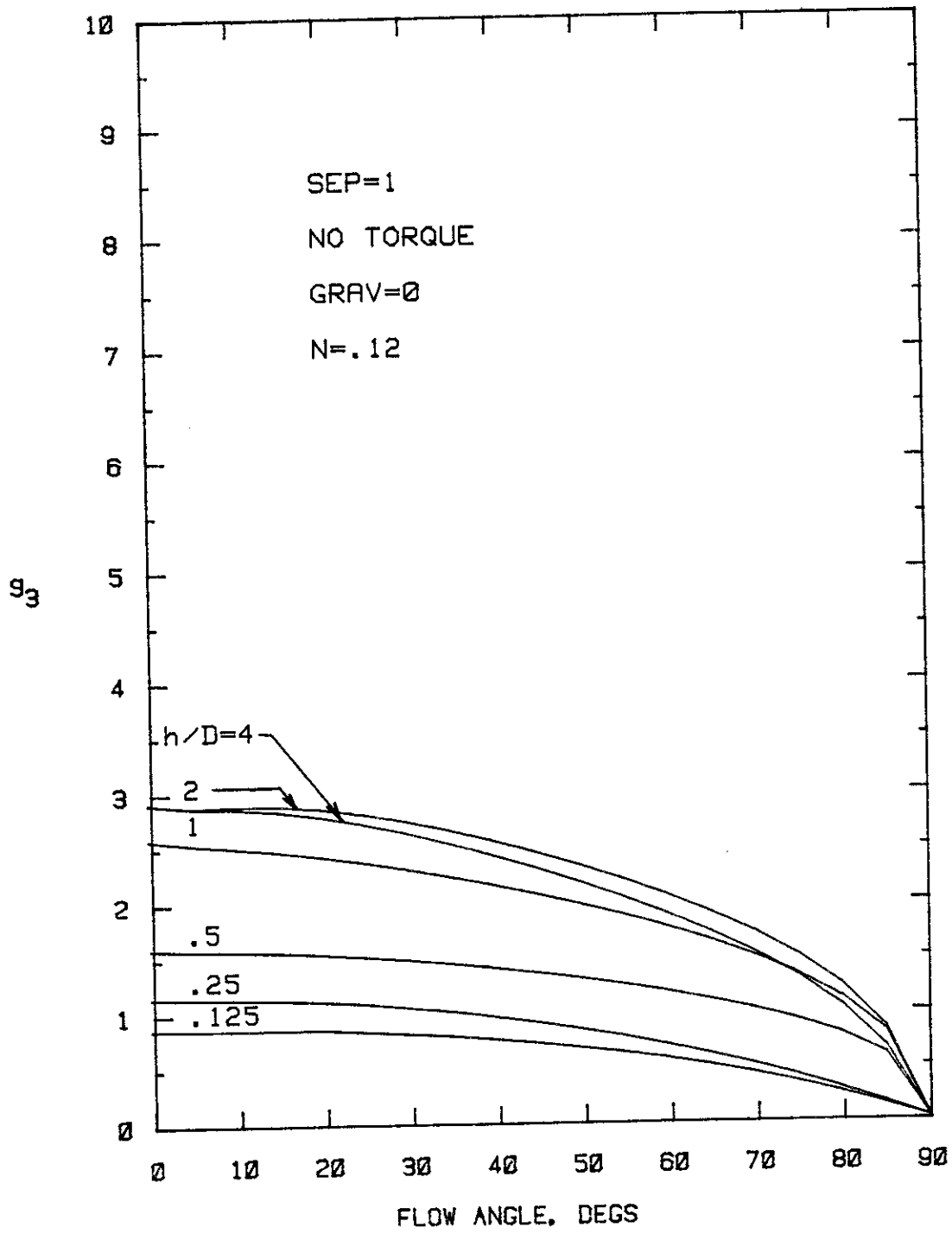
SEP=1
NO TORQUE
GRAV=0
N=.12
g_3
h/D=4
2
1
.5
.25
.125
10
9
8
7
6
5
4
3
2
1
0
0
10
20
30
40
50
60
70
80
90
FLOW ANGLE, DEGS

Figure 9

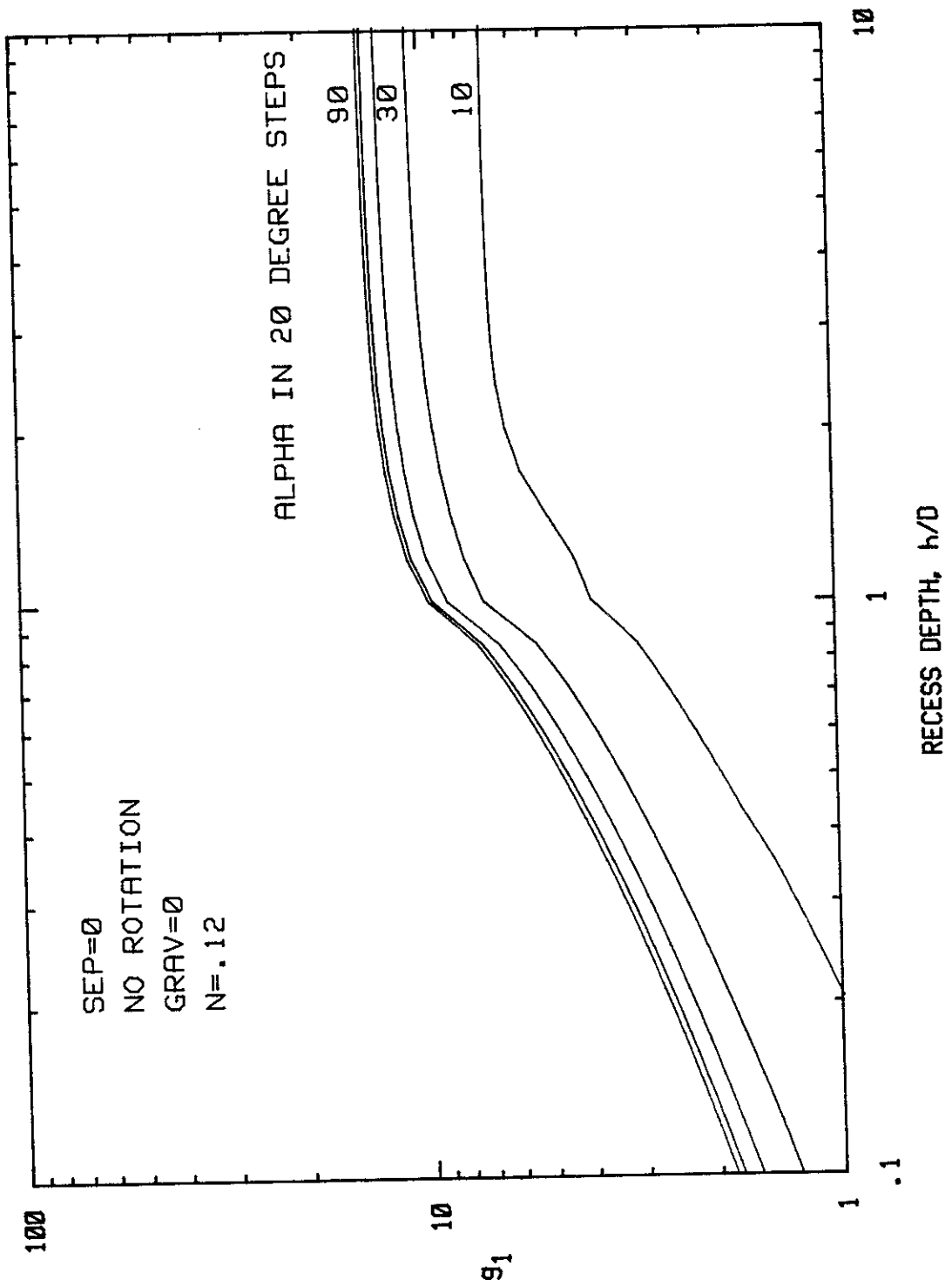
ALPHA IN 20 DEGREE STEPS
90
30
10
SEP=0
NO ROTATION
GRAV=0
N=.12
100
10
1
g_1
10
1
.1
RECESS DEPTH, h/D

Figure 10

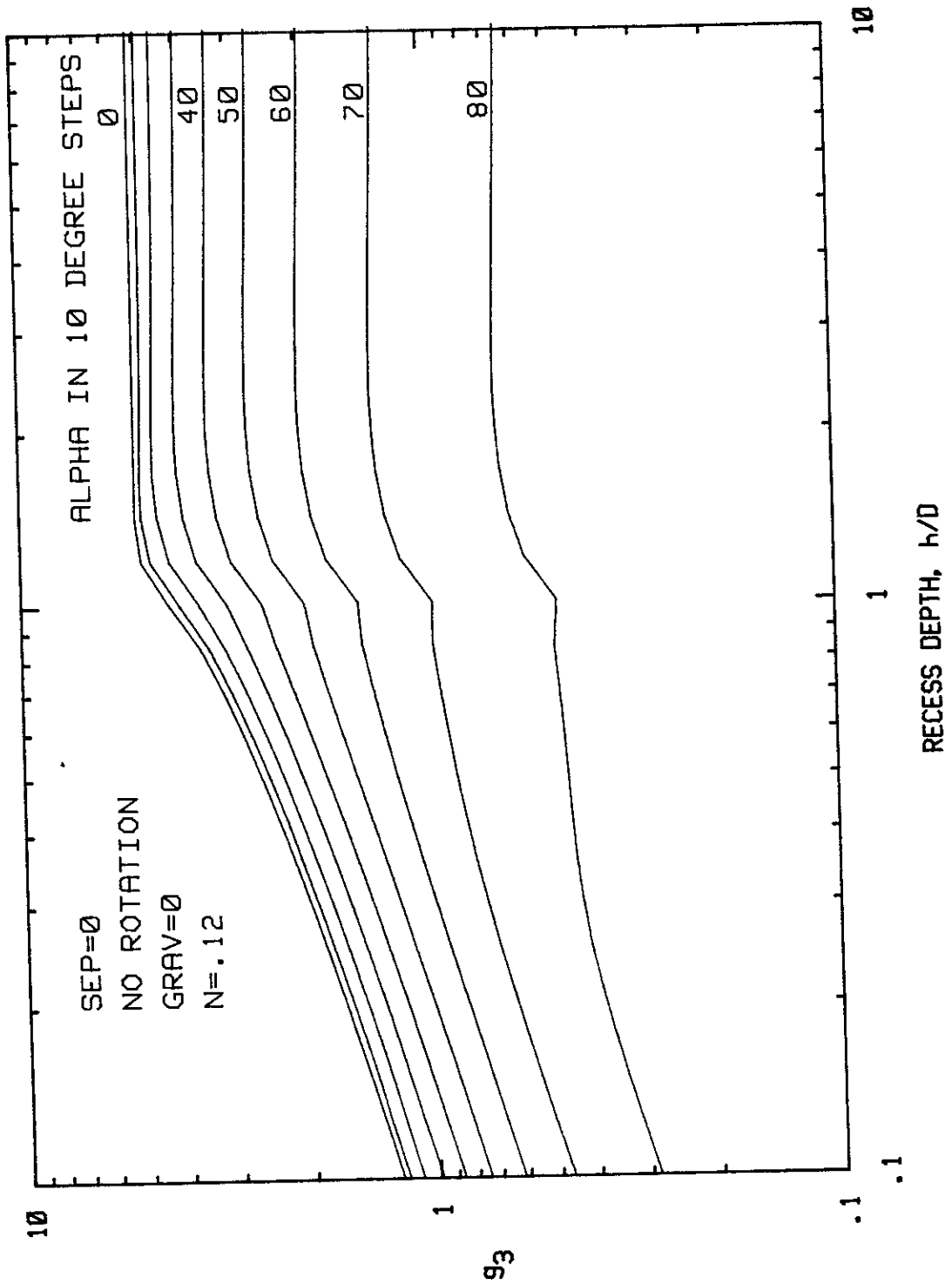
ALPHA IN 10 DEGREE STEPS
0
40
50
60
70
80
SEP=0
NO ROTATION
GRAV=0
N=.12
10
1
.1
g_3
.1
1
10
RECESS DEPTH, h/D

Figure 11

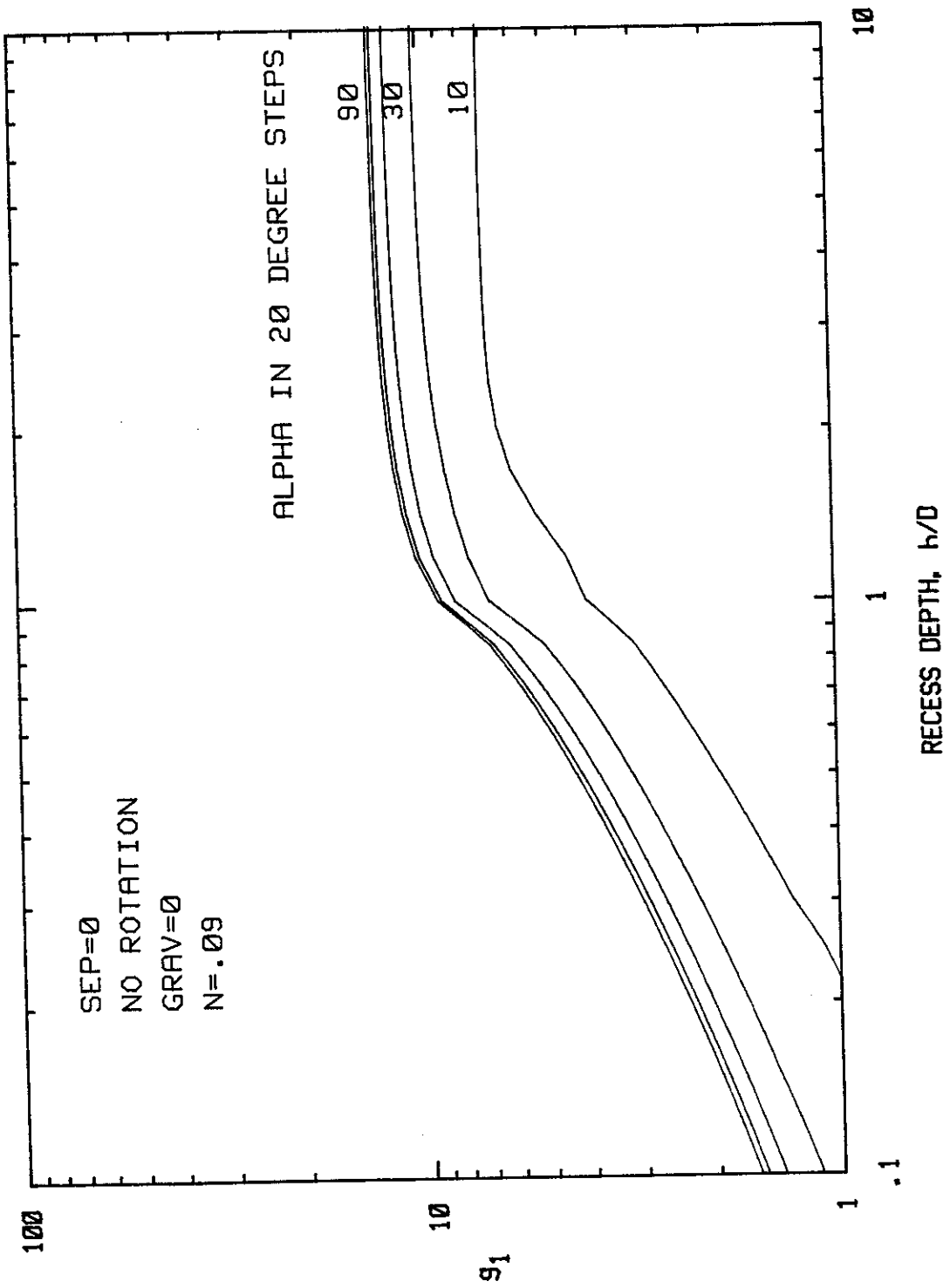
ALPHA IN 20 DEGREE STEPS
90
30
10
SEP=0
NO ROTATION
GRAV=0
N=.09
100
10
1
g_1
.1
1
10
RECESS DEPTH, h/D

Figure 12

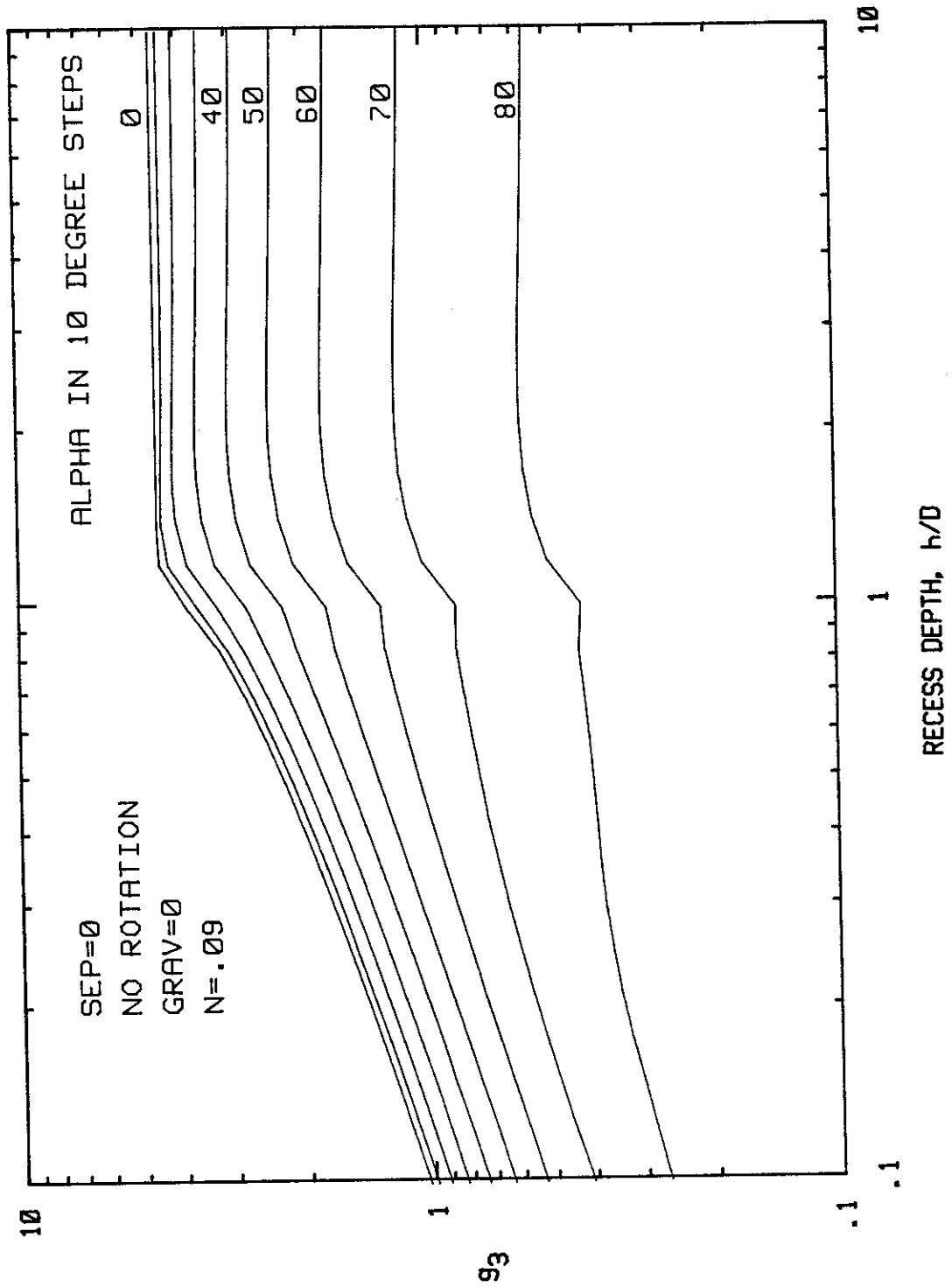
ALPHA IN 10 DEGREE STEPS
0
40
50
60
70
80
SEP=0
NO ROTATION
GRAV=0
N=.09
10
1
.1
g_3
10
1
.1
RECESS DEPTH, h/D

Figure 13

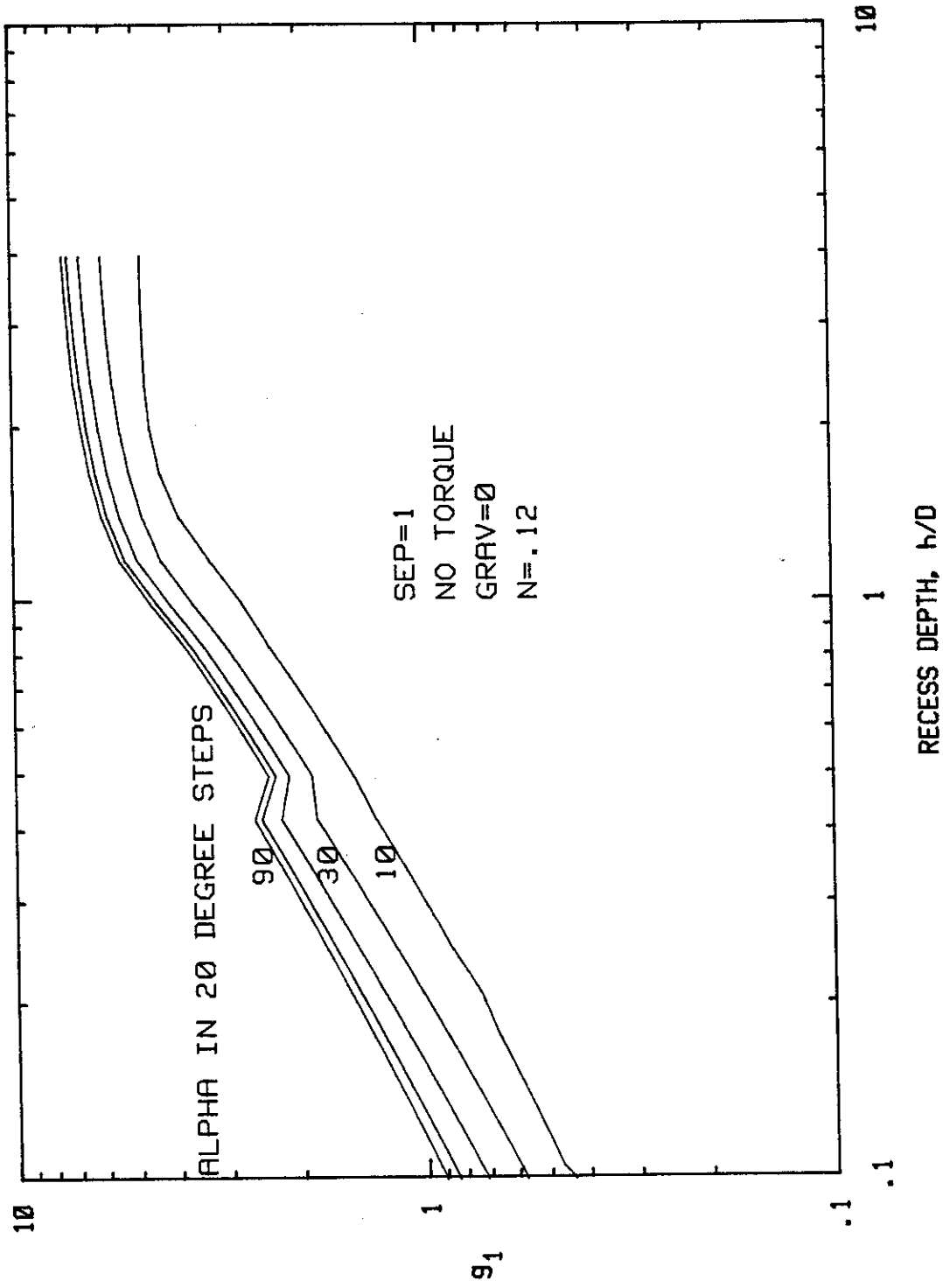
ALPHA IN 20 DEGREE STEPS
90
30
10
SEP=1
NO TORQUE
GRAV=0
N=.12
10
1
.1
g_1
10
1
.1
RECESS DEPTH, h/D

Figure 14

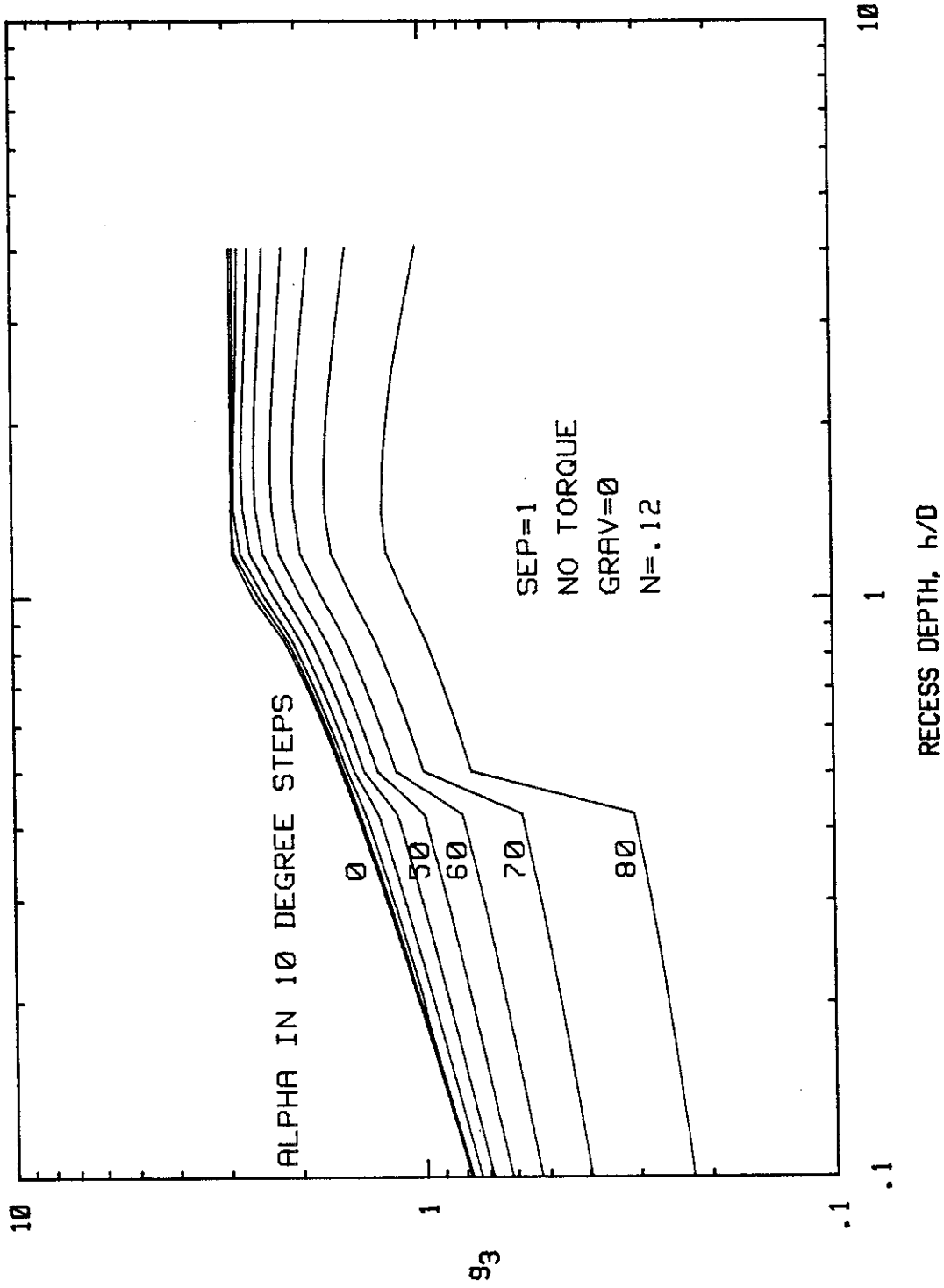
10
1
.1
g_3
.1
1
10
RECESS DEPTH, h/D
ALPHA IN 10 DEGREE STEPS
0
50
60
70
80
SEP=1
NO TORQUE
GRAV=0
N=.12

Figure 15

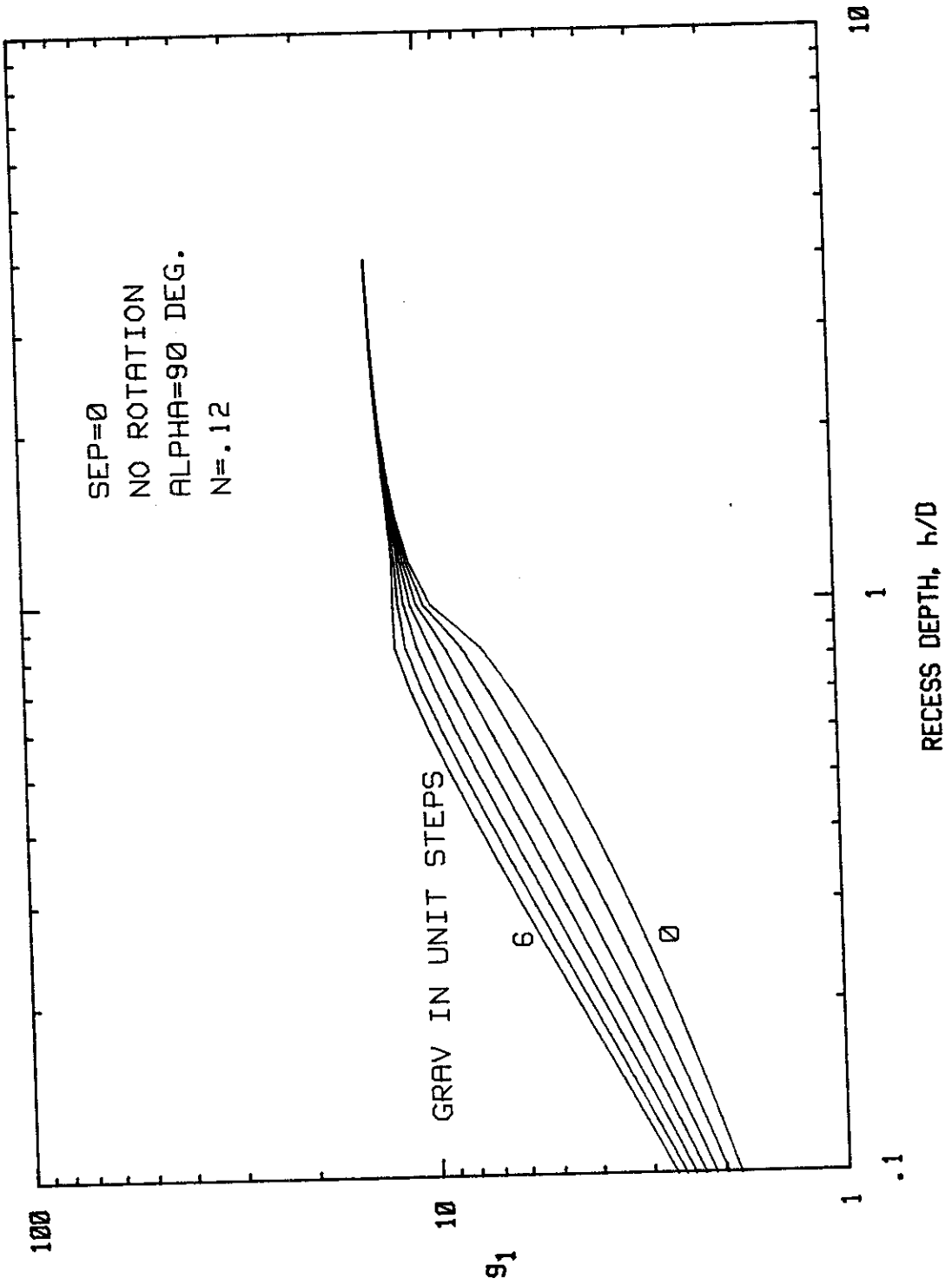
SEP=0
NO ROTATION
ALPHA=90 DEG.
N=.12
GRAV IN UNIT STEPS
6
0
100
10
1
g_1
10
1
.1
RECESS DEPTH, h/D

Figure 16

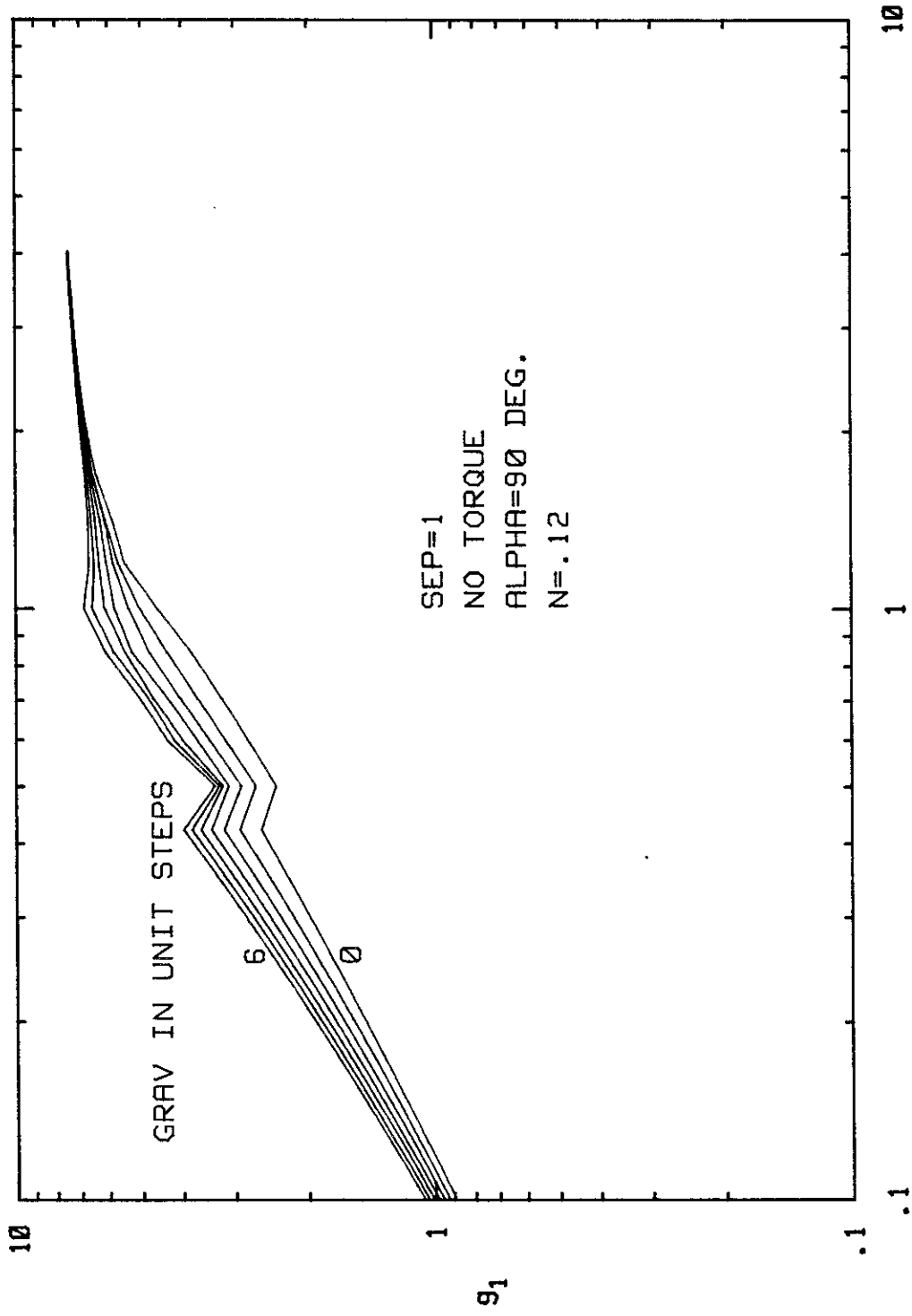
10
1
.1
g_1
GRAV IN UNIT STEPS
6
0
SEP=1
NO TORQUE
ALPHA=90 DEG.
N=.12
.1
1
10
RECESS DEPTH, h/D

Figure 17

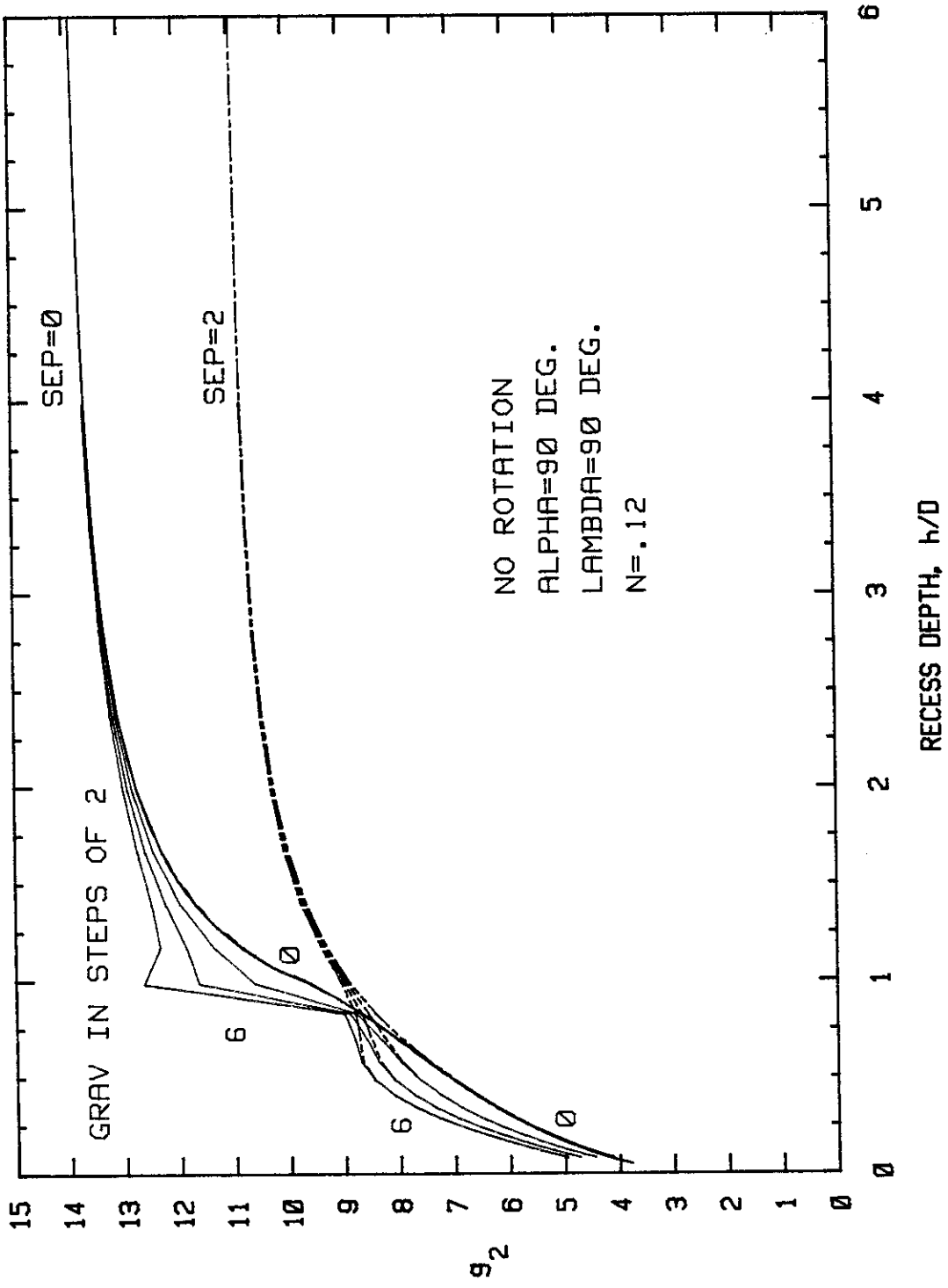
SEP=0
SEP=2
NO ROTATION
ALPHA=90 DEG.
LAMBDA=90 DEG.
N=.12
GRAV IN STEPS OF 2
0
6
6
0
g_2
RECESS DEPTH, h/D
0 1 2 3 4 5 6
0 1 2 3 4 5 6 7 8 9 10 11 12 13 14 15

Figure 18

APPENDIX 6

Pipe Sliding Over Surface of a Linearly Viscoelastic Sediment

Final Report of Work Completed by Jay R. Walton

on A.G.A. Project for E.L. Kistler and Associates

TABLE OF PARAMETERS

$G = G(t,y) = G_c(y/y_c)^n(t/t_c)^{-m}$ - viscoelastic shear modulus of mud

G_c - value of G at characteristic depth and time

y_c - characteristic depth

t_c - characteristic time

ν - Poisson's ratio

R - pipe radius

D - pipe diameter

h - pipe depth (see figure 1)

v - speed of pipe over mud

$q \equiv [(1 + n)(1 - n/(1 - \nu))]^{1/2}$

$I \equiv 2^n(n + 2)\Gamma((n + q + 3)/2)\Gamma((n - q + 3)/2)/\Gamma(n + 3)$

$\Gamma(\cdot)$ - gamma function

$\delta \equiv (k/q)(1 + n)\cot(n\pi/2)$

k - Coulomb friction constant

$w = (2/\pi)\tan^{-1}(\delta)$

$\gamma \equiv (1 + n - w - 2m)/2$, $\gamma' \equiv (w + n + 1)/2$

(a,b) - interval of contact between pipe and mud

λ - weight/length of pipe on mud

F_H - horizontal force/length on pipe due to assymmetrical piling up of mud under pipe

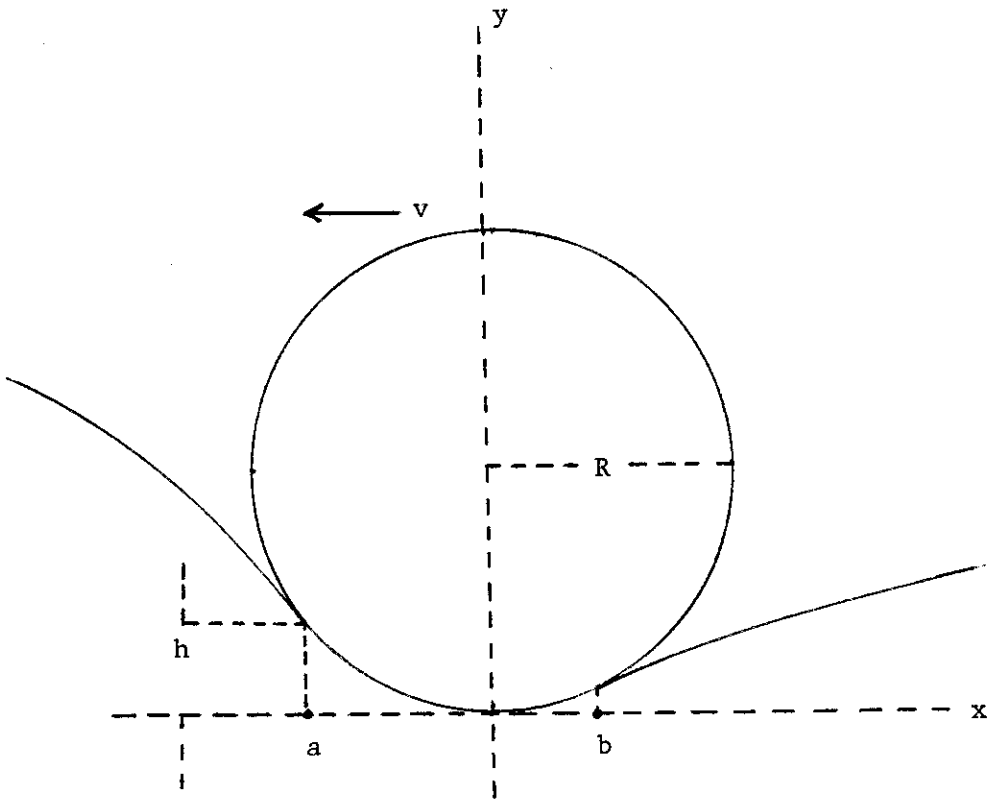

Figure 1.

1. Problem Description and Solution

This report describes the results of an analysis of an idealized mathematical model of a pipe sliding with constant speed across the mud surface. The mud is assumed to be inhomogeneous with a shear modulus that is depth dependent. The effect of gravity is not considered here since it introduces considerable extra mathematical difficulties that preclude finding a simple closed form solution. The purpose of this effort was to construct a closed form solution to the model problem in order to:

a. enhance an understanding of the combined effects of mud viscoelasticity and inhomogeneity in pipe force predictions;

b. provide test solutions against which the numerical procedures to be used on more realistic models could be checked and calibrated.

In the model considered here, the mud is characterized as a linearly viscoelastic solid with a constant Poisson's ratio, ν, and a shear modulus of the form

$$G = G(t,y) = G_c(y/y_c)^n(t/t_c)^{-m}, \quad y,t > 0 \qquad (1)$$
$$0 \le n \le 1, \quad 0 \le m < 1.$$

In (1), G_c, y_c and t_c are characteristic modulus, depth and time, respectively. The specific boundary value problem describing the model is that for sliding contact with Coulomb friction, that is,

$$\sigma_{ij,j} = 0, \quad -\infty < x_1 < \infty, \quad x_2 > 0 \qquad (2)$$

$$\sigma_{ij} = 2G * d\varepsilon_{ij} + \delta_{ij} \frac{2\nu}{1-2\nu} G * d\varepsilon_{kk} \qquad (3)$$

$$\sigma_{12}(x_1,0) = -k\sigma_{22}(x_1,0) \qquad (4)$$

$$\left.\begin{aligned} &\sigma_{22}(x_1,0) = 0 \quad x_1 < a - vt \quad \text{or} \quad x_1 > b - vt \\ &u_{2,1}(x_1,0) = -(x_1 + vt)/R. \end{aligned}\right\} \qquad (5)$$

Line (2) contains the equilibrium equations, (3) the constitutive equations, (4) the Coulomb friction condition and (5) the standard contact boundary conditions. In the above equations, σ_{ij} and ε_{ij} denote the viscoelastic stresses and strains, respectively, and $f*d\varepsilon$ denotes the Riemann-Stieltyes convolution

$$f*d\varepsilon = \int_{-\infty}^{\infty} f(x - s)d\varepsilon(s).$$

The construction of the solution to (2) - (5) is facilitated by adoption of the Galilean variable $x = x_1 + vt$ and the change of variables $y = y_1$, $\sigma_{11} = \sigma_{xx}$, $\sigma_{12} = \sigma_{xy}$, etc. A Fourier transform technique may now be applied to solve the boundary value problem.

A key step in the solution of (2) - (5) is the derivation of the transfer function, $T(p)$, relating $\hat{u}_y(p)$ and $\hat{\sigma}_{yy}(p)$, the Fourier transform with respect to x of $u_y(x,0)$ and $\sigma_{yy}(x,0)$. From the viscoelastic correspondence principle and the transfer function for an elastic half-plane with power-law depth dependence (see [1]), it can be shown that

$$T(p) = \frac{-q(1 - \nu)I \sin(q\pi/2)y_c^n(ip)^{-m}|p|^{n-1}(1 - i\delta \operatorname{sgn}(p))}{G_c(vt_c)^m\Gamma(1 - m)\Gamma(n + 2)\cos(n\pi/2)}$$

where $\hat{u}_y = T(p)\hat{\sigma}_{yy}$. (6)

Fourier inversion of (6) produces a generalized Abel integral equation which may be solved in a manner similar to that employed in [2]. It may then be shown that on the interval of contact, (a,b), the normal stress, $\sigma_{yy}(x,0)$, is given by

$$\frac{\sigma_{yy}(x,0)}{G_c D(vt_c/D)^m} = C_1((x - a)/D)^{\gamma}((b - x)/D)^{\gamma'} \qquad (7)$$

where $\gamma = (1 + n - w - 2m)/2$, $\gamma' = (w + n + 1)/2$

and

$$C_1 = \frac{-\Gamma(1-m)\,\Gamma(n+2)\cos(n\pi/2)\cos(w\pi/2)(y_c/D)^{-n}}{(D/2)\,\Gamma(2+n-m)\cos((n+w)\pi/2)\sin(q\pi/2)q(1-\nu)I[1+\tan^{-1}((n+w)\pi/2)^2]^{1/2}}.$$

From (7) all physical quantities of interest can be computed. Two such parameters are

$$\lambda \equiv \int_a^b \sigma_{yy}(x,0)\,dx \tag{8}$$

$$F_H \equiv \int_a^b \sigma_{yy}(x,0)\,u_{y,x}(x,0)\,dx. \tag{9}$$

λ is the total load per unit length of pipe on the mud due to the weight of the pipe and F_H is the horizontal force per unit length of pipe due to the assymmetrical piling up of mud in front of the pipe (i.e. ignoring friction).

Substitution of (7) into (8) and (9) and the fact that, on (a,b), $u_{y,x}(x,0) = -x/R$ yields

$$\frac{\lambda}{G_c D(vt_c/D)^m} = DC_1 B((3+n-w-2m)/2,\ (3+w+n)/2)((b-a)/D)^{2+n-m} \tag{10}$$

$$F_H = 2\lambda\,\frac{(2+n-m)(m+w)}{(3+n-m)(1+n-m)}\quad (b-a)/D. \tag{11}$$

The determination of the contact interval and the depth of penetration follows easily from (10) and the analysis leading to (7). Specifically,

$$a = \frac{-(b-a)}{2}\quad (1+n+w)/(1+n-m),$$

$$b = \frac{(b-a)}{2}\quad (1+n-w-2m)/(1+n-m)$$

and $$h/D = (1/4)((b-a)/D)^2(1+n+w)^2/(1+n-m)^2. \tag{12}$$

Moreover, from (7) it can be shown that the maximum value of $\sigma_{yy}(x,0)$ occurs at $x = \bar{x}$ where

$$\bar{x} = -(b-a)(m+w)/(1+n-m). \tag{13}$$

Obviously then, either the maximum stress under the pipe occurs at $x = a$ or $a < \bar{x} < b$. Hence, from (13) it is clear that the maximum stress occurs at $x = a$ whenever $w + 2m \geq 1 + n$ and at a point strictly between a and b otherwise. The details of the derivation of the above results may be found in the paper "The sliding with Coulomb friction of a rigid indentor over a power-law inhomogeneous linearly viscoelastic half-plane," which was recently published [3].

This report concludes with a section describing the results of numerical calculations illustrating the theoretical results. Of particular interest is the question of the magnitude of the effect on force predictions from the assumption of mud inhomogeneity.

2. Sample Calculations

The principle focus of the numerical study of the theoretical results was the following problem: Find an "effective depth", y_1, so that the force on a pipe predicted by the inhomogeneous mud model equals the force predicted for a homogeneous mud model with shear modulus equal to the inhomogeneous modulus evaluated at $y = y_1$. Hence, the value of the modulus of the mud at depth $y = y_1$ can be thought of as an "effective modulus" for pipe force predictions. The question can be answered quite easily. For the sake of simplicity it will be assumed that there is no Coulomb frictional force, i.e. $w = 0$. (Actually the Coulomb friction assumption is probably not a very accurate model of the resistance on a pipe due to the adhesion of mud to the pipe. It was included in the theoretical study mostly for mathematical completeness.) Moreover, h/D will

be taken as input parameter since it is what is most easily controlled in drag box experiments of a pipe sliding over mud. From (10), (11) and (12) it is seen that, assuming mud inhomogeneity,

$$\frac{F_H}{G_c D(vt_c/D)^m} = C_2(n,m)((b-a)/D)^{3+n-m} \qquad (14)$$

and $(b-a)/D = 2(h/D)^{1/2}(1+n-m)/(1+n)$ (15)

where $C_2(n,m)$ is a constant depending on n and m. Now assume a homogeneous mud model with modulus given by the inhomogeneous model at an effective depth, y_1, that is, for which the shear modulus has the form

$$G(t) = G_c(y_1/y_c)^n(t/t_c)^{-m} \equiv G_h(t/t_c)^{-m}. \qquad (16)$$

The predicted force in this case follows from lines (14) and (15) by substituting G_h for G_c and putting $n = 0$. Hence,

$$\frac{F_H}{G_h D(vt_c/D)^m} = C_2(0,m)((b-a)/D)^{3-m} \qquad (17)$$

and $(b-a)/D = 2(h/D)^{1/2}(1-m)$. (18)

Finally, equating F_H in both (14) and (17) and making use of (14), (15), (17) and (18) it is seen that

$$(y_1/y_c)^n = G_h/G_c = \frac{C_2(n,m)}{C_2(0,m)} \frac{2^n(1+n-m)^{3+n-m}}{(1-m)^{3-m}} (h/D)^{n/2}. \qquad (19)$$

To illustrate the result (19), the value of $(G_h/G_c)(D/h)^{n/2}$, with $(y_c/D) = 1$, for various values of n, m and ν were computed and are displayed in the following graphs. It should be noted that $n = 1$ and $\nu = 1/2$ is a singular limit in that $(G_n/G_c)(D/h)^{n/2}$ becomes infinitely large as n and ν tend to 1 and 1/2 respectively.

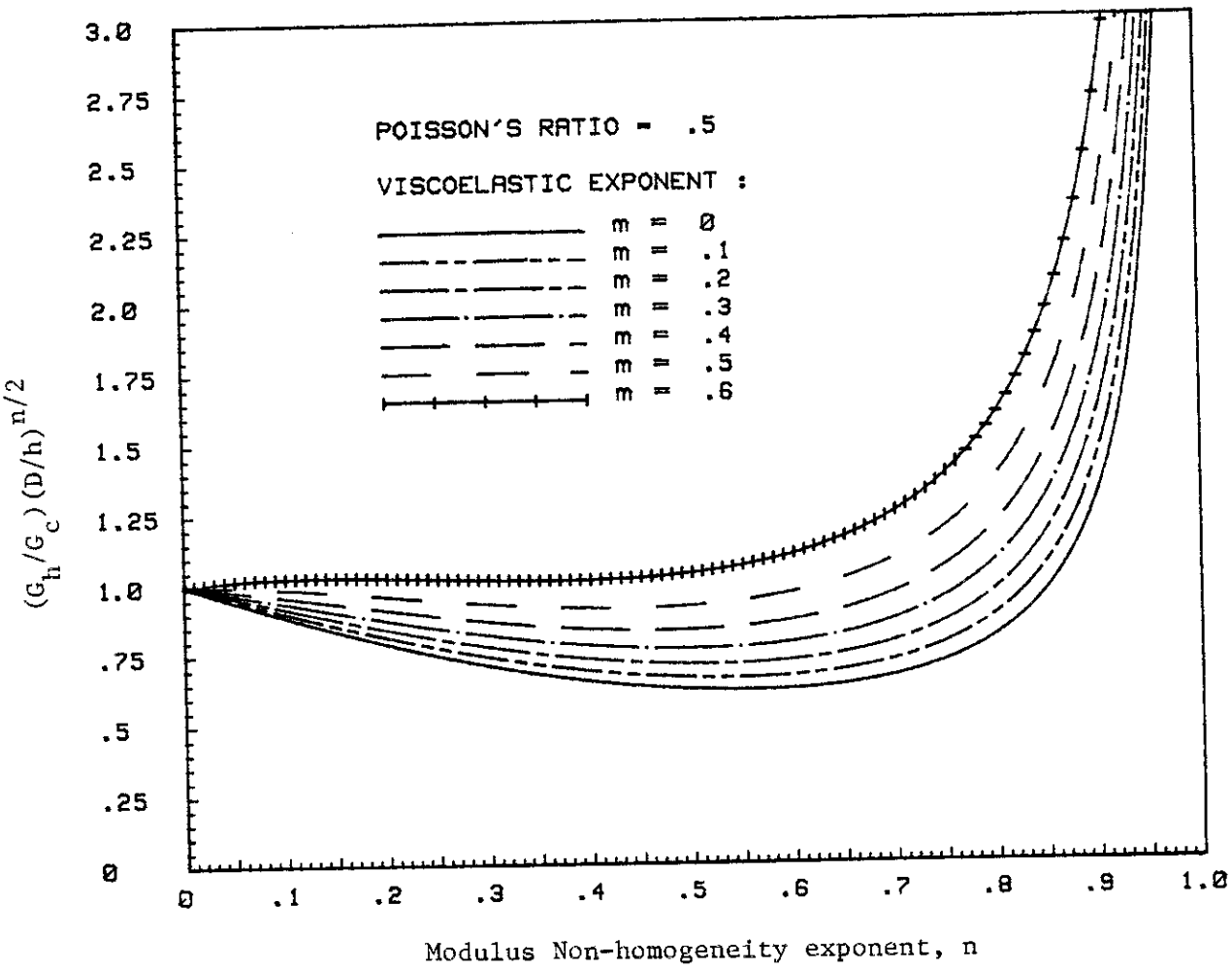
POISSON'S RATIO = .5
VISCOELASTIC EXPONENT :
m = 0
m = .1
m = .2
m = .3
m = .4
m = .5
m = .6
$(G_h/G_c)(D/h)^{n/2}$
3.0
2.75
2.5
2.25
2.0
1.75
1.5
1.25
1.0
.75
.5
.25
0
0
.1
.2
.3
.4
.5
.6
.7
.8
.9
1.0
Modulus Non-homogeneity exponent, n

Figure 2

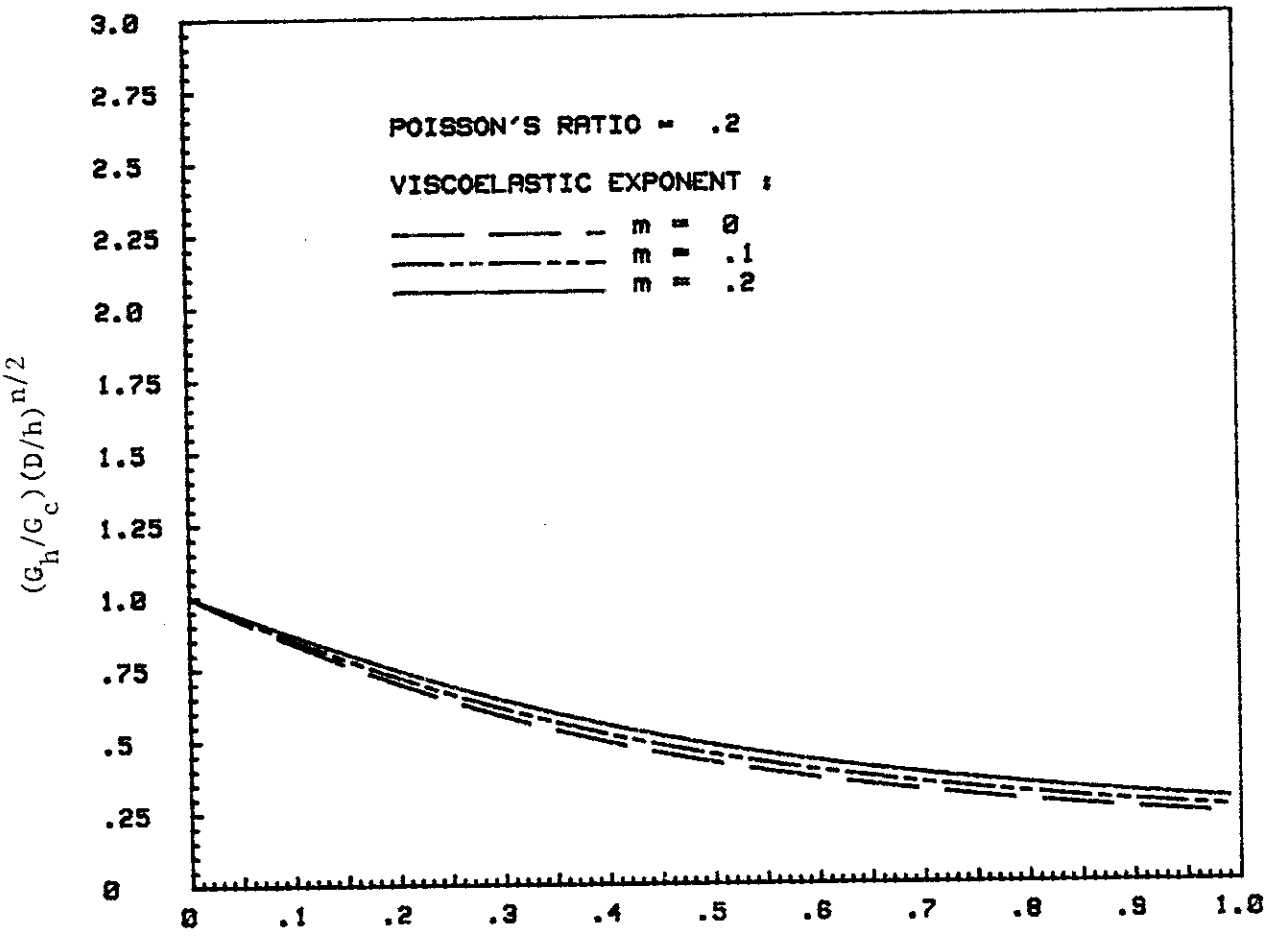
POISSON'S RATIO = .2
VISCOELASTIC EXPONENT :
m = 0
m = .1
m = .2
$(G_h/G_c)(D/h)^{n/2}$
3.0
2.75
2.5
2.25
2.0
1.75
1.5
1.25
1.0
.75
.5
.25
0
0
.1
.2
.3
.4
.5
.6
.7
.8
.9
1.0
Modulus Non-homogeneity exponent, n

Figure 3

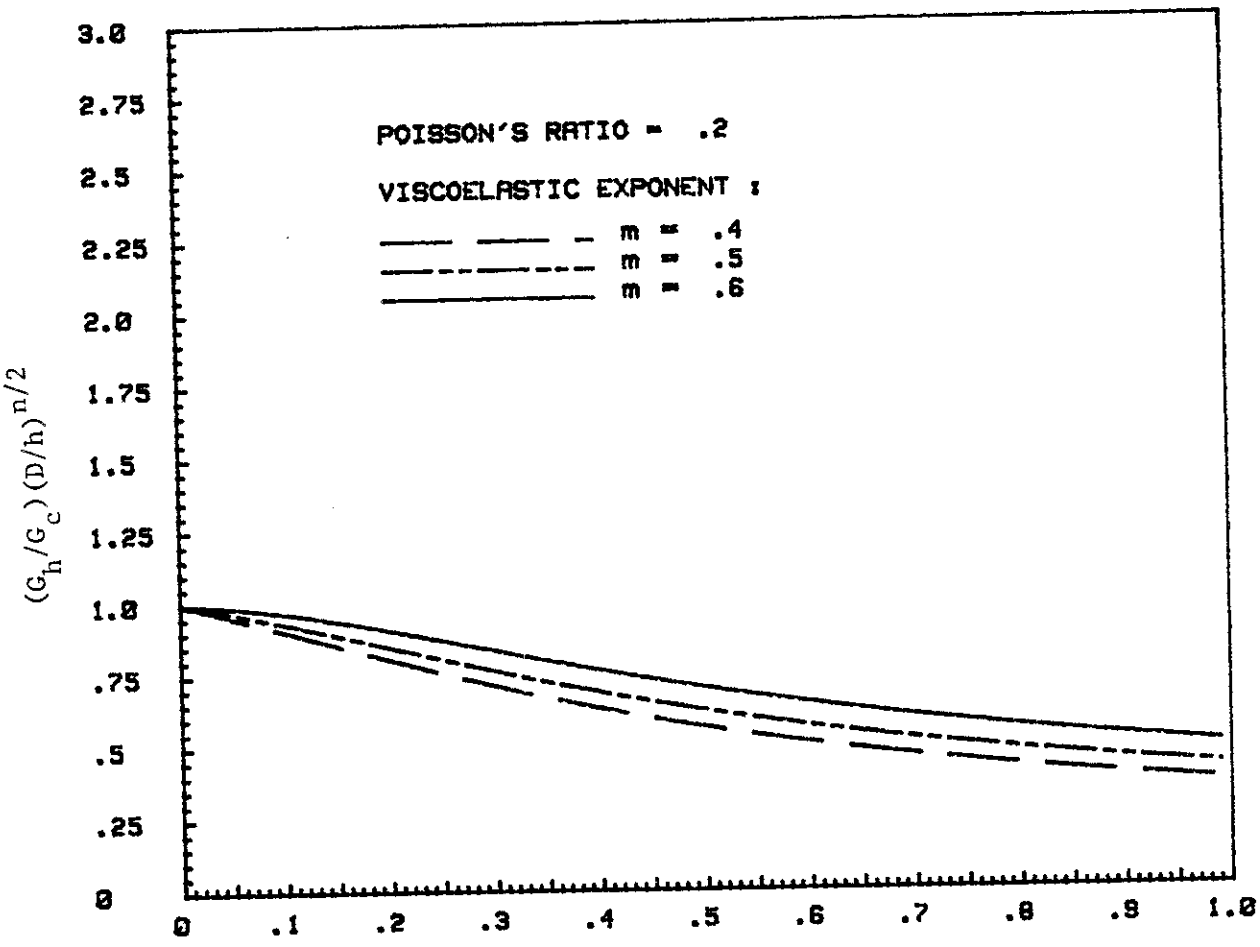
POISSON'S RATIO = .2
VISCOELASTIC EXPONENT :
m = .4
m = .5
m = .6
$(G_h/G_c)(D/h)^{n/2}$
3.0
2.75
2.5
2.25
2.0
1.75
1.5
1.25
1.0
.75
.5
.25
0
0
.1
.2
.3
.4
.5
.6
.7
.8
.9
1.0
Modulus Non-homogeneity exponent, n

Figure 4

REFERENCES

[1] G. M. L. Gladwell, Contact problems in the classical theory of elasticity, Sijthoff and Noordhoff, Germantown, Maryland, 1980.

[2] J. R. Walton, A. Nachman and R. A. Schapery, "The sliding of a rigid indentor over a power-law viscoelastic half-space," Q. J. Mech. Appl. Math. (31) No. 3, 1978, pp. 295-321.

[3] J. R. Walton, "The sliding with Coulomb friction of a rigid indentor over a power-law inhomogeneous linearly viscoelastic half-plane," J. Applied Mech. (51), 1984, pp. 289-293.